

Kinematic mapping and control scheme design of telemanipulation systems

Wang, Heng

2008

Wang, H. (2008). Kinematic mapping and control scheme design of telemanipulation systems. Doctoral thesis, Nanyang Technological University, Singapore.

<https://hdl.handle.net/10356/5273>

<https://doi.org/10.32657/10356/5273>

Nanyang Technological University

Downloaded on 13 Mar 2024 15:02:15 SGT



**NANYANG
TECHNOLOGICAL
UNIVERSITY**

**KINEMATIC MAPPING AND CONTROL
SCHEME DESIGN OF TELEMANIPULATION
SYSTEMS**

**WANG HENG
SCHOOL OF MECHANICAL & AEROSPACE ENGINEERING
2008**

Kinematic Mapping And Control Scheme Design of Telemanipulation Systems

Wang Heng

School of Mechanical & Aerospace Engineering

A thesis submitted to the Nanyang Technological University
in fulfilment of the requirement for the degree of
Doctor of Philosophy

2008

Abstract

This thesis presents two parts of work in the area of telemanipulation, which are the kinematic mapping of master-slave hand systems and the bilateral control scheme design.

In a master-slave hand system, the motion of the slave robot hand is determined according to that of the human hand by the mapping algorithm. Previous works mainly focus on the systems with an anthropomorphic or semi-anthropomorphic robot hand. To enrich the study on mapping, the system with a three-fingered non-anthropomorphic robot hand is considered. The widely used fingertip position mapping is first applied, and the inefficiency is shown by the mapping results. A virtual circle mapping method is then proposed. The basic idea is to express the operator's motion by a virtual circle determined by his/her three fingertips. The mapping results show that the proposed method is more effective for tele-controlling the non-anthropomorphic robot hands.

The second part of the thesis focuses on the control scheme design. A combined impedance/direct control scheme is first proposed, which is then applied to design the bilateral controller for the teleoperation systems. An investigation on impedance control shows that the force tracking performance decreases when there is disturbances and environmental impedance uncertainties. A combined impedance/direct control is then proposed. If compared to impedance control, the proposed controller is more robust to environment uncertainties and disturbances. Moreover, it is not required to switch the control modes when the end-effector moves from free space to contact conditions, or vice versa. Finally, by applying the combined impedance/direct control scheme, a two-channel bilateral controller is proposed. The proposed bilateral control scheme has the following features. Firstly, perfect transparency can be achieved. Secondly, it does not need to switch the control modes during the transition of motion. A limitation is that the environment impedance is required to be known in order for perfect transparency.

Acknowledgement

First of all, I would like to express my sincere and utmost gratitude to my supervisor, Professor Kin Huat Low, for his invaluable support, advices, and encouragement throughout the research.

I would like to thank Professors Feng Gong and Michael Yu Wang, for their support and insightful suggestions. I would also like to acknowledge Professors Kim Meow Liew and Yiyu Cai for their support on the construction of the test-bed for kinematic mapping.

I am grateful that Nanyang Technological University (NTU) has provided the research scholarship for my Ph.D study.

I owe a special thank to my lab colleague, Leong Yeo Wai, who has given me great help in using various software. I will also miss the coffee break routine with him. I would also like to thank Kiang Hock Tan, who helped draw the mechanical drawings of the robot hand and assembled the prototype. I also appreciate the valuable technical support from the technicians of Robotics Research Center of NTU: Mr. Eng Cheng Lim, Mrs. Tan Agnes, Mr. Kim San You, and Miss Yen Mei Toh.

I have received all kinds of support from a number of knowledgeable and friendly people in NTU. They have also shared great fun with me. I would like to thank Shuxiang Jiao, Jialin Su, Xiaopeng Liu, Whu Ken Loh, and all other lab colleagues and various project team members.

Last but not the least, I would like to thank my family. They have been with me every step of the way and I could not have done it without them.

Table of Contents

Abstract	i
Acknowledgement	ii
Table of Contents	iii
List of Figures	vii
List of Tables	xiii
List of Symbols	xiv
Chapter 1 Introduction	1
1.1 Research Motivation	3
1.2 Objective and Scope	4
1.3 Thesis Outline	4
Chapter 2 Literature Review	7
2.1 Mapping of Single Manipulator Systems	7
2.2 Mapping of Hand Systems	8
2.2.1 Conventional Methods	8
2.2.1.1 Direct Joint Mapping	8
2.2.1.2 Pose Mapping	9
2.2.1.3 Fingertip Position Mapping	10
2.2.2 Virtual Object Based Mapping	11
2.3 Force Control of Robot Manipulators	12
2.3.1 Hybrid Position/Force Control	13
2.3.2 Impedance Control	13
2.4 Bilateral Telemanipulation	15
2.4.1 Two-Port Network Model	15

2.4.2	Four-Channel Architecture	16
2.4.3	Two-Channel Architectures	18
PART I: KINEMATIC MAPPING		20
Chapter 3 Investigation on Fingertip Position Mapping		21
3.1	System Description	21
3.1.1	Human Hand Model	22
3.1.2	Robot Hand	23
3.2	Mapping Implementation	24
3.3	Mapping Results	25
3.3.1	Discussion	25
3.4	Summary	27
Chapter 4 Virtual Circle Mapping		29
4.1	Virtual Circle Mapping Concept	29
4.2	Parameters Describing the Human Hand Circle	30
4.2.1	Circle Radius and Central Angles	32
4.2.2	Circle Center Position	32
4.2.3	Circle Orientation	36
4.3	Human-to-Robot Transformation	37
4.3.1	Transformation of Circle Radius and Central Angles	37
4.3.2	Transformation of Circle Orientation	39
4.3.3	Transformation of Circle Center Position	41
4.4	Computation for Robot Positions	42
4.5	Mapping Results	45
4.5.1	Discussion	46
4.6	Experiments	48
4.7	Concluding Remarks	51
PART II: CONTROL SCHEME DESIGN		52
Chapter 5 Investigation on Impedance Control		53
5.1	Robot Dynamic Equations	53
5.2	Performance Analysis of Impedance Control	55

5.2.1	Impedance Control Implementation	55
5.2.2	Effects of External Disturbances	58
5.2.3	Effects of Environment Stiffness Uncertainty	60
5.3	Computer Simulations	62
5.3.1	Effects of External Disturbances	63
5.3.2	Effects of Environment Stiffness Uncertainty	66
5.4	Concluding Remarks	68
Chapter 6	Combined Impedance/Direct Control of Robot Manipulators	69
6.1	Scheme I: Direct Error Based Compensation	70
6.2	Scheme II: Indirect Error Based Compensation	72
6.2.1	Time-Delay Control (TDC) Based Estimation	73
6.2.2	Controller Design	74
6.3	Stability Analysis	78
6.4	Computer Simulations	80
6.4.1	Results of Control Scheme I	80
6.4.2	Results of Control Scheme II	81
6.5	Experiments	85
6.5.1	Experimental Platform	86
6.5.2	Experimental Results	89
6.5.2.1	Results of Position Tracking	89
6.5.2.2	Results of Force Control	93
6.5.2.3	Results of Transition of Motion	96
6.6	A Comparison of the Control Schemes	97
6.7	Concluding Remarks	99
Chapter 7	Bilateral Control Scheme Design	103
7.1	Transparency Conditions of Two-Channel Systems	104
7.2	Bilateral Control Scheme Design	106
7.2.1	F-P Architecture in Constrained Condition	107
7.2.1.1	Master and Slave Controller Design	107
7.2.1.2	Transparency Analysis	110
7.2.1.3	Stability Analysis	112
7.2.2	P-P Architecture in Unconstrained Condition	113
7.2.3	Transition of Motion	114

7.3	Experimental Study	115
7.3.1	Experimental Platform	115
7.3.2	Results of Constrained Motion	117
7.3.3	Results of Transition of Motion	118
7.4	Concluding Remarks	119
Chapter 8 Conclusions and Future Work		125
8.1	Structures Combining Mapping and Control	125
8.1.1	Structure I	125
8.1.2	Structure II	126
8.2	Summary of Contributions	127
8.3	Suggestions for Future Work	128
8.4	Conclusions	130
Bibliography		131
Appendix A - A Mechatronic Approach to Manipulator Controller Design		143
A.1	Introduction	143
A.2	Hardware and Software	144
A.3	Modeling and Control	145
A.3.1	Transfer Function Model for Joint R_{lower}	145
A.3.2	Controller Design by Simulation	147
A.3.3	Control System Implementation	149
Appendix B - Kinematics and Dynamics of the Parallel Manipulator		151
B.1	Kinematics	151
B.1.1	Forward Kinematics	152
B.1.2	Differential Kinematics	153
B.1.3	Inverse Kinematics	153
B.2	Dynamics	154

List of Figures

1.1	Schematic of the telemanipulation system.	2
1.2	Framework of the thesis.	4
2.1	Examples of non-anthropomorphic robot hands. (a) A two fingered hand by Stanford Univ. [110]; (b) A three-fingered hand by Univ. LAVAL [111]; (c) A three-fingered hand by Kyushu Univ. [112].	12
2.2	Network model of telemanipulation systems.	16
2.3	Four-channel bilateral telemanipualtion block diagram.	17
3.1	Human hand and its simplified kinematic model with human base frame $\{\mathcal{H}_0\}$ attached (Right hand. Finger 0: thumb; Finger 1: index finger; Finger 2: middle finger).	22
3.2	The robot hand.	23
3.3	Mapping results of human thumb (finger 0) and middle finger (finger 2) by fingertip position mapping.	25
3.4	Mapping results of human index finger (finger 1) by fingertip position mapping.	26
4.1	The concept of virtual circle mapping.	30
4.2	Procedure of virtual circle mapping.	31
4.3	Plane for projection of the motions of fingers 0 and 2.	31
4.4	Graphical illustration of the circle radius and central angles.	33
4.5	Graphical illustration of shifting the circle center of the human hand (Finger 1 is not shown for clarity).	34
4.6	Graphical illustration of determining the bounds of parameter λ	35
4.7	Graphical illustration of the circle orientation of the human hand (Finger 1 is not shown for clarity).	36

4.8	Circles of the human hand (smaller one) and the robot hand (larger one) in the same orientation.	38
4.9	Possible strategies for choosing K	39
4.10	Graphical illustration of transforming the circle orientation and circle center.	39
4.11	Graphical illustration of finding the value ϕ	40
4.12	Definition of the pinch-points of human and robot hands.	41
4.13	Graphical illustration of computing the fingertip positions of the robot hand (The middle finger is not shown for clarity).	43
4.14	Flow chart of virtual circle mapping.	44
4.15	Mapping results of human thumb (finger 0) and middle finger (finger 2) by virtual circle mapping.	45
4.16	Mapping results of human index finger (finger 1) by virtual circle mapping.	47
4.17	The developed test-bed for mapping.	48
4.18	A comparison of typical human-robot correspondences by fingertip position mapping and virtual circle mapping.	49
4.19	Two additional examples of the human-robot correspondences by virtual circle mapping.	49
4.20	Hand grasp geometries (Adapted from [16]).	50
5.1	The impedance control structure.	56
5.2	The robot finger model for simulation.	63
5.3	Simulation results of impedance control with parameter setting $\mathbf{K}_e = \text{diag}[10^2, 0]$, $\mathbf{B}_e = \text{diag}[2, 0.1]$, $\mathbf{M}_t = \text{diag}[1, 1]$, $\mathbf{B}_t = \text{diag}[40, 30]$, and $\mathbf{K}_t = \text{diag}[200, 10^4]$ verifying Remark 1.	64
5.4	Simulation results of impedance control with parameter setting $\mathbf{K}_e = \text{diag}[10^3, 0]$, $\mathbf{B}_e = \text{diag}[2, 0.1]$, $\mathbf{M}_t = \text{diag}[1, 1]$, $\mathbf{B}_t = \text{diag}[50, 30]$, $\mathbf{K}_t = \text{diag}[200, 10^4]$, $\mathbf{F}_{dist} = [2, 2]^T$ verifying Remark 2.	64
5.5	Simulation results of impedance control verifying Remark 3. The parameters are set as $\mathbf{K}_e = \text{diag}[10^3, 0]$, $\mathbf{B}_e = \text{diag}[2, 0.1]$, $\mathbf{B}_t = \text{diag}[50, 30]$, and $\mathbf{F}_{dist} = [2, 2]^T$	65
5.6	Simulation results of impedance control with parameter setting $\mathbf{B}_e = \text{diag}[2, 0.1]$, $\mathbf{M}_t = \text{diag}[1, 1]$, $\mathbf{B}_t = \text{diag}[50, 30]$, $\mathbf{K}_t = \text{diag}[200, 10^4]$, $\mathbf{F}_{dist} = [2, 2]^T$ verifying Remark 4.	66

5.7	Simulation results of impedance control verifying Remark 5. The environment stiffness is estimated 20% higher than the real value. The parameters are set as $\mathbf{K}_e = \text{diag}[10^2, 0]$, $\mathbf{B}_e = \text{diag}[2, 0.1]$, $\mathbf{M}_t = \text{diag}[1, 1]$, $\mathbf{B}_t = \text{diag}[40, 30]$, $\mathbf{K}_t = \text{diag}[200, 10^4]$, and $\mathbf{F}_{dist} = [0, 0]^T$.	67
5.8	Simulation results of impedance control verifying Remark 6. The environment stiffness is estimated 20% higher than the real value. The parameters are set as $\mathbf{K}_e = \text{diag}[10^2, 0]$, $\mathbf{B}_e = \text{diag}[2, 0.1]$, $\mathbf{M}_t = \text{diag}[1, 1]$, $\mathbf{B}_t = \text{diag}[50, 30]$, $\mathbf{F}_{dist} = [0, 0]^T$, and $\mathbf{F}_d = [10^2, 0]^T$	67
6.1	A manipulator approaching the environment.	70
6.2	Control structure of the combined impedance/direct control Scheme I. .	73
6.3	Control structure of the combined impedance/direct control Scheme II. .	77
6.4	Responses of the combined impedance/direct control Scheme I in the case of constant external disturbances ($\mathbf{K}_e = \text{diag}[10^3, 0]$, $\mathbf{B}_e = \text{diag}[2, 0.1]$, $\mathbf{M}_t = \text{diag}[1, 1]$, $\mathbf{B}_t = \text{diag}[50, 30]$, $\mathbf{K}_t = \text{diag}[200, 10^4]$, $\mathbf{K}_p = \text{diag}[50, 50]$, $\mathbf{K}_i = \text{diag}[10, 10]$, $\mathbf{F}_{dist} = [2, 2]^T$).	81
6.5	Responses of the combined impedance/direct control Scheme I in the case of hard environments and random disturbances ($\mathbf{K}_e = \text{diag}[10^4, 0]$, $\mathbf{B}_e = \text{diag}[2, 0.1]$, $\mathbf{M}_t = \text{diag}[1, 1]$, $\mathbf{B}_t = \text{diag}[10^3, 30]$, $\mathbf{K}_t = \text{diag}[200, 10^4]$, $\mathbf{K}_p = \text{diag}[50, 50]$, $\mathbf{K}_i = \text{diag}[10, 10]$, $\mathbf{F}_{dist} = [r, r]^T$, where r is a random function with the amplitude of 10).	82
6.6	Responses of the combined impedance/direct control Scheme I in the case of environmental stiffness uncertainty ($\mathbf{K}_e = \text{diag}[10^2, 0]$ with 50% estimation uncertainty, $\mathbf{B}_e = \text{diag}[2, 0.1]$, $\mathbf{M}_t = \text{diag}[1, 1]$, $\mathbf{B}_t = \text{diag}[100, 30]$, $\mathbf{K}_t = \text{diag}[300, 10^4]$, $\mathbf{K}_p = \text{diag}[50, 50]$, $\mathbf{K}_i = \text{diag}[10, 10]$, $\mathbf{F}_{dist} = [0, 0]^T$).	82
6.7	Responses of the combined impedance/direct control Scheme II in the case of constant external disturbances ($\mathbf{B}_e = \text{diag}[2, 0.1]$, $\mathbf{M}_t = \text{diag}[1, 1]$, $\mathbf{B}_t = \text{diag}[50, 30]$, $\mathbf{K}_t = \text{diag}[200, 10^4]$, $\mathbf{K}_p = \text{diag}[100, 100]$, and $\mathbf{K}_i = \text{diag}[80, 80]$, $\mathbf{F}_{dist} = [2, 2]^T$).	83
6.8	Responses of the combined impedance/direct control Scheme II in the case of a pulse external disturbance ($\mathbf{B}_e = \text{diag}[2, 0.1]$, $\mathbf{M}_t = \text{diag}[1, 1]$, $\mathbf{B}_t = \text{diag}[200, 30]$, $\mathbf{K}_t = \text{diag}[800, 10^4]$, $\mathbf{K}_p = \text{diag}[100, 100]$, and $\mathbf{K}_i = \text{diag}[80, 80]$, $\mathbf{F}_{dist} = [p, 0]^T$, where p is a pulse function with the amplitude of 10 between $t = 1$ s and $t = 1.5$ s).	84

6.9	Responses of the combined impedance/direct control Scheme II in the case of the soft environment and random disturbances ($\mathbf{K}_e = \text{diag}[10, 0]$, $\mathbf{B}_e = \text{diag}[2, 0.1]$, $\mathbf{M}_t = \text{diag}[1, 1]$, $\mathbf{B}_t = \text{diag}[200, 30]$, $\mathbf{K}_t = \text{diag}[800, 10^4]$, $\mathbf{K}_p = \text{diag}[100, 100]$, and $\mathbf{K}_i = \text{diag}[80, 80]$, $\mathbf{F}_{dist} = [r, r]^T$, where r is a random function with the amplitude of 10).	85
6.10	Responses of the combined impedance/direct control Scheme II in the case of the hard environment and random disturbances ($\mathbf{K}_e = \text{diag}[10^4, 0]$, $\mathbf{B}_e = \text{diag}[2, 0.1]$, $\mathbf{M}_t = \text{diag}[1, 1]$, $\mathbf{B}_t = \text{diag}[200, 30]$, $\mathbf{K}_t = \text{diag}[800, 10^4]$, $\mathbf{K}_p = \text{diag}[100, 100]$, and $\mathbf{K}_i = \text{diag}[80, 80]$, $\mathbf{F}_{dist} = [r, r]^T$, where r is a random function with the amplitude of 10).	86
6.11	Responses of the combined impedance/direct control Scheme II in the case of environmental stiffness uncertainty (50% k_e uncertainty, $\mathbf{B}_e = \text{diag}[2, 0.1]$, $\mathbf{M}_t = \text{diag}[1, 1]$, $\mathbf{B}_t = \text{diag}[100, 30]$, $\mathbf{K}_t = \text{diag}[300, 10^4]$, $\mathbf{K}_p = \text{diag}[100, 100]$, and $\mathbf{K}_i = \text{diag}[80, 80]$, $\mathbf{F}_{dist} = [0, 0]^T$).	87
6.12	The experimental platform.	87
6.13	Structure of the parallel manipulator.	88
6.14	Typical position tracking results in free space motion. The control parameters are set as $\mathbf{M}_t = \text{diag}[1, 1] \text{ N} \cdot \text{s}^2/\text{m}$, $\mathbf{B}_t = \text{diag}[30, 30] \text{ N} \cdot \text{s}/\text{m}$, and $\mathbf{K}_t = \text{diag}[10^4, 10^4] \text{ N}/\text{m}$.	90
6.15	Responses to step force input $f_d = 2 \text{ N}$ in contact condition by Scheme I. The control parameters are set as $\mathbf{M}_t = \text{diag}[1, 1] \text{ N} \cdot \text{s}^2/\text{m}$, $\mathbf{B}_t = \text{diag}[30, 30] \text{ N} \cdot \text{s}/\text{m}$, $\mathbf{K}_t = \text{diag}[10^4, k_t] \text{ N}/\text{m}$, $\mathbf{K}_p = \text{diag}[1, 1]$, and $\mathbf{K}_i = \text{diag}[1, 1]$.	91
6.16	Responses to step force input $f_d = 2 \text{ N}$ in contact condition by Scheme II. The control parameters are set as $\mathbf{M}_t = \text{diag}[1, 1] \text{ N} \cdot \text{s}^2/\text{m}$, $\mathbf{B}_t = \text{diag}[30, 300] \text{ N} \cdot \text{s}/\text{m}$, $\mathbf{K}_t = \text{diag}[10^4, k_t] \text{ N}/\text{m}$, $\mathbf{K}_p = \text{diag}[100, 100]$, and $\mathbf{K}_i = \text{diag}[80, 80]$.	92
6.17	Force tracking results by Scheme I with environment impedance uncertainties. The control parameters are set as $\mathbf{M}_t = \text{diag}[1, 1] \text{ N} \cdot \text{s}^2/\text{m}$, $\mathbf{B}_t = \text{diag}[30, 30] \text{ N} \cdot \text{s}/\text{m}$, $\mathbf{K}_t = \text{diag}[10^4, 10^4] \text{ N}/\text{m}$, $\mathbf{K}_p = \text{diag}[1, 1]$, and $\mathbf{K}_i = \text{diag}[1, 1]$.	94
6.18	Force tracking results by Scheme II with environment impedance uncertainties. The control parameters are set as $\mathbf{M}_t = \text{diag}[1, 1] \text{ N} \cdot \text{s}^2/\text{m}$, $\mathbf{B}_t = \text{diag}[30, 30] \text{ N} \cdot \text{s}/\text{m}$, $\mathbf{K}_t = \text{diag}[10^4, 10^4] \text{ N}/\text{m}$, $\mathbf{K}_p = \text{diag}[100, 100]$, and $\mathbf{K}_i = \text{diag}[80, 80]$.	95

6.19	Typical results of transition between the free space motion and the constrained motion by Scheme I. The environment stiffness is $k_e = 3000\text{N/m}$, which is estimated to be $\hat{k}_e = 2000\text{ N/m}$. The control parameters are set as $\mathbf{M}_t = \text{diag}[1, 1]\text{ N} \cdot \text{s}^2/\text{m}$, $\mathbf{B}_t = \text{diag}[30, 30]\text{ N} \cdot \text{s}/\text{m}$, $\mathbf{K}_t = \text{diag}[10^4, 10^4]\text{ N/m}$, $\mathbf{K}_p = \text{diag}[1, 1]$, and $\mathbf{K}_i = \text{diag}[1, 1]$	100
6.20	Typical results of transition between the free space motion and the constrained motion by Scheme II. The environment stiffness is $k_e = 3000\text{N/m}$, which is estimated to be $\hat{k}_e = 2000\text{ N/m}$. The control parameters are set as $\mathbf{M}_t = \text{diag}[1, 1]\text{ N} \cdot \text{s}^2/\text{m}$, $\mathbf{B}_t = \text{diag}[30, 30]\text{ N} \cdot \text{s}/\text{m}$, $\mathbf{K}_t = \text{diag}[10^4, 10^4]\text{ N/m}$, $\mathbf{K}_p = \text{diag}[50, 50]$, and $\mathbf{K}_i = \text{diag}[40, 40]$	101
6.21	Typical results of transition between the free space motion and the constrained motion by Scheme II. The environment stiffness is $k_e = 1.2 \times 10^4\text{ N/m}$, which is estimated to be $\hat{k}_e = 2 \times 10^4\text{ N/m}$. The control parameters are set as $\mathbf{M}_t = \text{diag}[1, 1]\text{ N} \cdot \text{s}^2/\text{m}$, $\mathbf{B}_t = \text{diag}[30, 30]\text{ N} \cdot \text{s}/\text{m}$, $\mathbf{K}_t = \text{diag}[10^4, 10^4]\text{ N/m}$, $\mathbf{K}_p = \text{diag}[50, 50]$, and $\mathbf{K}_i = \text{diag}[40, 40]$	102
7.1	Four-channel architecture with local force feedback [37, 55].	105
7.2	Block diagram of the proposed bilateral control scheme (Refer to Fig. 6.3 for the details of the combined impedance/direct control block).	115
7.3	Telemanipulation experimental platform.	116
7.4	Slider crank mechanism used in the experiments.	116
7.5	Results of the quasi transparent system without integral term of position error at the master. The environment impedance parameters are $k_e = 400\text{ N/m}$, $m_e = 0.14\text{ kg}$, and b_e unknown. The control parameters are set as $m_{ts} = 1\text{ N} \cdot \text{s}^2/\text{m}$, $b_{ts} = 10\text{ N} \cdot \text{s}/\text{m}$, $k_{ts} = 3000\text{ N/m}$, $k_{ps} = 90$, $k_{is} = 80$, $k_{pm} = 1.8 \times 10^4$, and $k_{vm} = 10$	120
7.6	Results of the quasi transparent system with integral term of position error at the master. The environment impedance parameters are $k_e = 400\text{ N/m}$, $m_e = 0.14\text{kg}$, and b_e unknown. The control parameters are set as $m_{ts} = 1\text{ N} \cdot \text{s}^2/\text{m}$, $b_{ts} = 10\text{ N} \cdot \text{s}/\text{m}$, $k_{ts} = 3000\text{ N/m}$, $k_{ps} = 90$, $k_{is} = 80$, $k_{pm} = 1.8 \times 10^4$, $k_{vm} = 10$, and $k_{im} = 10^4$	121

7.7	Results of nontransparent system with integral term of position error at the master. The environment impedance parameters are $k_e = 400$ N/m, $m_e = 0.14$ kg, and b_e unknown. The control parameters are set as $m_{ts} = 1$ N · s ² /m, $b_{ts} = 10$ N · s/m, $k_{ts} = 1.8 \times 10^4$ N/m, $k_{ps} = 90$, $k_{is} = 80$, $k_{pm} = 1.8 \times 10^4$, $k_{vm} = 10$, and $k_{im} = 10^4$	122
7.8	Results in the case that the environment stiffness is estimated with error. The environment impedance parameters are $k_e = 400$ N/m, $m_e = 0.14$ kg, and b_e unknown. k_e is estimated as $\hat{k}_e = 2500$ N/m. The control parameters are set as $m_{ts} = 1$ N · s ² /m, $b_{ts} = 10$ N · s/m, $k_{ts} = 1.8 \times 10^4$ N/m, $k_{ps} = 90$, $k_{is} = 80$, $k_{pm} = 1.8 \times 10^4$, $k_{vm} = 10$, and $k_{im} = 10^4$	123
7.9	Results of an operation including transition between the free space motion and the constrained motion. The environment impedance parameters are $k_e = 400$ N/m, $m_e = 0.14$ kg, and b_e unknown. k_e is known. The control parameters are set as $m_{ts} = 1$ N · s ² /m, $b_{ts} = 10$ N · s/m, $k_{ts} = 1.8 \times 10^4$ N/m, $k_{ps} = 90$, $k_{is} = 80$, $k_{pm} = 0$ (free space motion) or 1.5×10^4 (constrained motion), $k_{vm} = 10$, and $k_{im} = 0$ (free space motion) or 10^4 (constrained motion).	124
A.1	Control system architecture of the test-bed for mapping.	144
A.2	The input-output relation of joint R_{lower}	146
A.3	Bode plot of experimental data and system model $P(s)$	148
A.4	Block scheme of joint R_{lower} with PID controller for simulation.	148
A.5	Step input response of joint R_{lower} by simulation.	149
A.6	Block scheme of joint R_{lower} with real system in the loop.	149
A.7	Step input response of real system and simulation.	150
A.8	Sine wave (2 Hz) response of real system and simulation.	150
B.1	Kinematic structure of the parallel manipulator.	151
B.2	Kinematic structure for deriving the inverse kinematics and dynamics equations.	154

List of Tables

6.1	Comparison of the control schemes.	98
-----	--	----

List of Symbols

$\mathcal{H}_j \mathbf{P}_i$	Position vector of i -th finger of the human hand defined in frame \mathcal{H}_j , $i = 0, 1, 2$; $j = 0, 1, 2$
$\mathcal{R}_0 \mathbf{P}_{right}$	Position vector of robot right finger defined in frame \mathcal{R}_0
$\mathcal{R}_0 \mathbf{P}_{left}$	Position vector of robot left finger defined in frame \mathcal{R}_0
$\mathcal{R}_0 \mathbf{P}_{middle}$	Position vector of robot middle finger defined in frame \mathcal{R}_0
\mathbf{u}_{ij}	Vectors defined by position vectors of the human fingertips, $i, j = 0, 1, 2$
r_{human}	Radius of the human circle
r_{robot}	Radius of the robot circle
$\mathbf{P}_{Human-pinch}$	Position of the human pinch point
$\mathbf{P}_{Robot-pinch}$	Position of the robot pinch point
\mathbf{P}_{hc}	Circle center position of the human hand
$\mathbf{P}_{hc,shift}$	Shifted circle center position of the human hand
$\mathbf{P}_{hc,shift,rel}$	Shifted circle center position of the human hand relative to the human pinch-point
$\mathbf{P}_{rc}, \mathbf{P}_{rc,original}$	Circle center position of the robot hand
$\mathcal{R}_0 \mathbf{P}_{H1ORG}$	Origin of frame \mathcal{H}_1 defined in frame \mathcal{R}_0
$\mathcal{R}_c \mathbf{P}_{right-to-rc}$	Robot right finger position defined in frame \mathcal{R}_c
$\mathcal{R}_c \mathbf{P}_{left-to-rc}$	Robot left finger position defined in frame \mathcal{R}_c
$\mathcal{R}_c \mathbf{P}_{middle-to-rc}$	Robot middle finger position defined in frame \mathcal{R}_c
$\mathbf{P}_{02,mid-point}$	Position of the mid-point of chord 02
\mathbf{P}_{int}	Intermediate vector defined by $\mathbf{P}_{rc,original}$ and $\mathbf{P}_{02,mid-point}$
$\mathbf{R}_x(\theta)$	Rotational matrix by frame rotation about x-axis for angle θ
\mathbf{q}	Vectors of joint angles of the manipulator
\mathbf{X}	Vectors of the positions/orientations of the end-effector expressed in Cartesian space

\mathbf{X}_r	Reference trajectory of the impedance controller
\mathbf{X}_{eo}	Initial environment position
$\mathbf{D}(\mathbf{q}) \in \mathbb{R}^{n \times n}$	Inertia matrix of the robot dynamics
$\mathbf{C}(\mathbf{q}, \dot{\mathbf{q}})\dot{\mathbf{q}} \in \mathbb{R}^n$	Coriolis and centrifugal torque of the robot dynamics
$\mathbf{G}(\mathbf{q}) \in \mathbb{R}^n$	Gravitational torque of the robot dynamics
\mathbf{D}_x	Inertia matrix in Cartesian space
\mathbf{C}_x	Coriolis and centrifugal torque in Cartesian space
\mathbf{G}_x	Gravitational torque in Cartesian space
\mathbf{H}_x	Combination of \mathbf{C}_x and \mathbf{G}_x
$\hat{\mathbf{D}}_x, \hat{\mathbf{H}}_x$	Estimation of \mathbf{D}_x and \mathbf{H}_x , respectively
$\Delta \mathbf{D}_x$	Difference between \mathbf{D}_x and $\hat{\mathbf{D}}_x$
$\Delta \mathbf{H}_x$	Difference between \mathbf{H}_x and $\hat{\mathbf{H}}_x$
\mathbf{H}'_x	Defined as $\Delta \mathbf{D}_x \ddot{\mathbf{X}} + \mathbf{H}_x$
τ	Actuator joint torque
τ_e	Force exerted by the end effector to the environment expressed in joint space
τ_{dist}	External disturbance force acted on the end-effector expressed in joint space
$\mathbf{J}(\mathbf{q})$	Jacobian matrix
\mathbf{F}_e	Force exerted by the end effector to the environment
\mathbf{F}_{ess}	Robot-environment interaction force at steady state
\mathbf{F}_{dist}	External disturbance force acted on the end-effector
\mathbf{F}'_{dist}	Model uncertainty and external disturbance related disturbance force defined by Eq. (5.32)
\mathbf{F}''_{dist}	Model uncertainty and external disturbance related disturbance force defined by Eq. (6.29)
\mathbf{F}_d	Desired force between the end-effector and the environment
\mathbf{E}_f	Force tracking error
\mathbf{E}_{fss}	Steady state force tracking error
\mathbf{E}_x	Position error, defined as the difference between \mathbf{X}_r and \mathbf{X}
\mathbf{K}_p	Diagonal matrix representing the P type compensator
\mathbf{K}_i	Diagonal matrix representing the I type compensator
\mathbf{M}_t	Target inertia in impedance control
\mathbf{B}_t	Target damping in impedance control

\mathbf{K}_t	Target stiffness in impedance control
\mathbf{M}_e	Environment inertia
\mathbf{B}_e	Environment damping
\mathbf{K}_e	Environment stiffness
$\hat{\mathbf{K}}_e$	Estimate of \mathbf{K}_e
\mathbf{K}_{eq}	Equivalent stiffness defined by \mathbf{K}_t and \mathbf{K}_e
$\hat{\mathbf{K}}_{eq}$	Estimate of \mathbf{K}_{eq}
\mathbf{M}_h	Operator inertia
\mathbf{B}_h	Operator damping
\mathbf{K}_h	Operator stiffness
\mathbf{Z}_h	Impedance of the operator
\mathbf{V}_h	Velocity of the operator
\mathbf{M}_{ts}	Target inertia in impedance control of slave robot
\mathbf{B}_{ts}	Target damping in impedance control of slave robot
\mathbf{K}_{ts}	Target inertia in impedance control of slave robot
\mathbf{K}_{eqs}	Equivalent stiffness of slave robot
\mathbf{D}_{xm}	Inertia matrix of the master in Cartesian space
\mathbf{D}_{xs}	Inertia matrix of the slave in Cartesian space
\mathbf{H}_{xm}	Coriolis and centrifugal, and gravitational force of the master in Cartesian space
\mathbf{H}_{xs}	Coriolis and centrifugal, and gravitational force of the slave in Cartesian space
\mathbf{X}_m	Master position
\mathbf{X}_s	Slave position
\mathbf{X}_{rs}	Slave reference position
\mathbf{K}_{ps}	P type compensator for slave robot
\mathbf{K}_{is}	I type compensator for slave robot
\mathbf{K}_{pm}	P type compensator for master robot
\mathbf{K}_{im}	I type compensator for master robot
\mathbf{K}_{vm}	D type compensator for master robot
\mathbf{X}_{md}	Desired master position
\mathbf{F}_h^*	Operator exogenous input force
\mathbf{F}_h	Force exerted on the master by the operator

\mathbf{F}_{ed}	Desired force applied on the environment by the slave
\mathbf{F}_{mc}	Control input of the master
\mathbf{F}_{sc}	Control input of the slave
\mathbf{E}_{fs}	Force error between the slave and the environment
\mathbf{E}_{xs}	Position error between the slave reference position and the actual position
\mathbf{E}_{xm}	Position error between the slave (desired master position) and the master

Chapter 1

Introduction

Telemanipulation refers to an action where the human operator controls the *slave* manipulator, end effector, or robotic hand through a *master* device to explore the remote environment, or manipulate the remote objects. A telemanipulation system enables humans to perform tasks in dangerous (e.g., nuclear radioactive spots [56]), or difficult-to-access (e.g., outer space [105]) environments, or delicate tasks (e.g., microsurgery [91]) by robots while taking advantage of the human abilities in spatial reasoning, task planning, and adaptation.

As shown in Fig. 1.1, the telemanipulation system generally consists of five components, which are the human operator, the master, the slave, the environment, and the communication channel. In the most common telemanipulation architecture, the human operator operates the local master device. Motion commands are measured on the master and transmitted through the communication channel to the remote slave robot, which executes these commands by tracking the motion of the master. The interaction force information between the slave robot and the environment is then fed back to the master such that the human operator feels as if he himself is interacting with the remote environment. This type of two-channel (one communication link in each direction) architecture is often referred to as the “position-force” architecture. In the more general four-channel architecture, both positions (or velocities) and forces are communicated bilaterally. In addition, the visual and aural information can also be fed back from the slave to the master to aid the human operator in planning and reasoning.

The master and the slave are basically two electronically instrumented robotic mechanisms. The slave robot is usually a manipulator, or a robotic hand. The master device, which is often referred to as the *haptic interface*, takes many forms, such as joysticks, exoskeletons, data gloves, etc. Some of the master devices are designed to be mounted

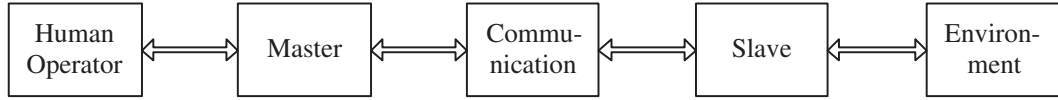


Figure 1.1: Schematic of the telemanipulation system.

on a table, ceiling, or the ground, while others are designed to be worn by the human operators. In this way, the master mechanisms can be categorized into non-portable and portable devices. Two review works on master devices can be found in [6] and [39]. Some examples of the non-portable master devices are the joysticks [61], the desk-grounded pen-based haptic interface PHANTOM [70], the pantograph haptic device Mk-II [7], and the arm-hand-integrated Gifu Haptic Interface [51]. Some examples of the portable master devices are the Rutgers Master II [5], the exoskeleton-glove-combined CyberGrasp [108, 109], and the hand exoskeletons [13, 97].

An explicit requirement for a telemanipulation system is that the slave robot can follow the motion of the master device faithfully as expected by the human operator. In the first telemanipulation system (developed by Goertz [28]), the slave motion was solely determined by the mechanical linkages between the master and the slave due to the fact that the system was mechanically coupled. Shortly after, the linkage connections were replaced by electric servomotors allowing for a much greater distance from remote environments [29]. Most of the current telemanipulation systems are electronically coupled. As a result, a specific rule is required for each system, such that the motion of the slave robot can be determined according to that of the master device. The study on this issue falls into the research of *kinematic mapping* between the master and the slave. The functions of mapping are twofold. One is to produce optimal workspace matching between the master and the slave. The other is to provide high degree of intuitiveness to the human operator in terms of the master-slave pose correspondences.

The most fundamental requirement for a telemanipulation system is on the stability and performance of the control system. A sophisticated bilateral control scheme can provide better system performance with less hardware and computing resources. The research work on the area of the telemanipulation control scheme design in the last two decades can be classified into two branches in general. In one branch, the robots are usually simplified to be single degree-of-freedom (DOF) systems, and the network theory

and all aspects of the control theories are employed thoroughly¹, e.g., the two-port network model [34], the passivity [82], wave variable [90], and H_∞ optimization [102] techniques. In the other branch, the control architectures are designed by taking advantage of the well developed single manipulator control schemes, e.g., the hybrid position/force control [55], the impedance control [12, 26, 32, 79, 89], the parallel force/position control [36], and the Naturally Transitioning Rate-to-Force Control [99].

The advances in both areas of the kinematic mapping and the control scheme design can improve the *telepresence* of the system, which means that the operator receives sufficient information from the remote environment displaying in a sufficiently natural way, such that the operator feels physically present at the remote site [87]. With a good mapping scheme, the visual feedback from the slave site presents the remote scene with a natural pose of the slave robot just as expected by the operator; with a good bilateral controller, the human operator gains the feeling of the environment impedance with high fidelity. The term *transparency* is widely used to describe the level of matching between the environment impedance and the impedance perceived by the human operator [60].

1.1 Research Motivation

The master-slave mapping problem includes the mapping between two single manipulators, and that between a hand master and a slave robotic hand. Mapping schemes for the former form the basis of those for the latter. The previous work has addressed several mapping methods. However, they are not applicable or cannot result in satisfactory performance if the slave is a multi-fingered non-anthropomorphic robot hand. Therefore, the development of an effective mapping method for this kind of slave robots appears to be necessary.

Several manipulator control schemes have been developed in the last three decades. Each of them possesses specific advantages and deficiencies. It is of significance to keep putting effort on the research of manipulator control. Since these control schemes take most dynamic effects into account, and are readily applicable to the multi-DOF manipulators, it is advantageous to develop bilateral telemanipulation controllers by utilizing these available schemes. A major concern is then how to design a stable control architecture with high level of transparency when the individual control laws (one for the master, and the other for the slave) are integrated into the single network of the telemanipulation framework.

¹The term *teleoperation* is more often used than telemanipulation in these work.

1.2 Objective and Scope

The objective of this work is to develop schemes and methods for telemanipulation systems, such that the *telepresence* of the system can be improved. Toward this end, this thesis presents the work in both kinematic mapping and control scheme design, aiming to improve the performance of the telemanipulation system.

The scope of the thesis includes two areas of work, which are the kinematic mapping and the control scheme design. Firstly, the rules of the mapping are explored in part I. The previous methods are first investigated, followed by the presentation of the developed virtual circle mapping method. Part II deals with two issues in telemanipulation systems, which are the system transparency and the smooth transition of motion between the constrained and unconstrained conditions. Specifically, the impedance control is investigated, and a combined impedance/direct control scheme for single manipulator control is proposed, which is then applied to the telemanipulation systems. The overall framework of the thesis is shown in Fig. 1.2.

1.3 Thesis Outline

The thesis consists of eight chapters and two appendices. This chapter has provided the background of, and motivation for, the research in kinematic mapping and control scheme design of the telemanipulation systems. The outline of the thesis is given as follows.

Chapter 2: Literature Review Previous research and background in the area of telemanipulation and robot manipulator control is discussed. The previous mapping methods for master-slave systems are first reviewed. The two classical manipulator control

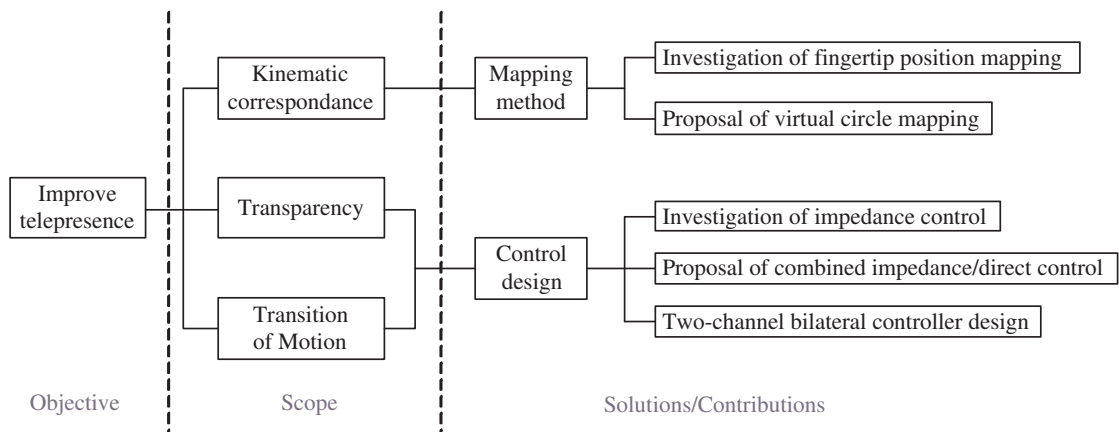


Figure 1.2: Framework of the thesis.

schemes, i.e., hybrid position/force control and impedance control, are then reviewed. Finally, the background of the modeling method of the telemanipulation systems and control architecture design are addressed.

Chapter 3: Investigation on Fingertip Position Mapping This chapter investigates the performance of the fingertip position mapping in the case of a non-anthropomorphic slave hand. In particular, a three-fingered robot hand having a symmetric structure with 7 DOFs is used in the investigation. The investigation shows that, for non-anthropomorphic slave hands, the fingertip position mapping method fails to provide satisfactory degree of telepresence and workspace matching between the master and the slave hands.

Chapter 4: Virtual Circle Mapping A virtual circle mapping method dealing with the three-fingered robot hands is presented in this chapter. The proposed method is developed based on the basic geometry theorem, which states that three points (if they are not in a line) define a unique circle. The fundamental idea is to construct a corresponding relationship between two virtual circles defined by the human fingertips and the robot fingertips, respectively. As a result, a corresponding relationship between the Cartesian positions of the human fingers and those of the robot fingers can be constructed. The mapping from master to slave can thus be achieved. In this chapter, the concept of the virtual circle mapping is first introduced. The detailed implementation of the idea is then presented, followed by the simulation results and the experimental validation. Finally, the results and the discussions are concluded.

Chapter 5: Investigation on Impedance Control The force tracking performance of impedance control is investigated in this chapter. Firstly, the robot dynamics model considering the external disturbances is given. The detailed implementation of the impedance control technique is then presented, followed by the analysis of the force tracking performance. Simulations are next conducted. Finally, the insights obtained from the investigation are summarized.

Chapter 6: Combined Impedance/Direct Control of Robot Manipulators A combined impedance/direct control scheme for control of robot manipulators is proposed in this chapter. The fundamental idea is to form a single controller along all the degrees of freedom by combining the reference trajectory characterized impedance control with the force error based PI-type compensator. It is not required to switch the control modes when the end-effector moves from free space to contact conditions, or vice

versa. In addition, the proposed controller is more robust to environment uncertainties and disturbances than impedance control. In this chapter, the idea of the combined impedance/direct control is first given. Next, the stability analysis is performed. Computer simulations are then performed to verify the effectiveness of the proposed controller, followed by the comprehensive experiments. Finally, the concluding remarks are addressed.

Chapter 7: Bilateral Control Scheme Design A two-channel bilateral controller is proposed for telemanipulation systems by applying the combined impedance/direct control scheme. A control architecture is constructed considering both the free space motion and the constrained motion. Specifically, the F-P architecture is applied in the constrained motion, while the P-P architecture is applied in the free space motion. Perfect transparency can be achieved in theory. In addition, it does not need to switch the control modes of the master and the slave controllers during the transition of motion. In this chapter, the transparency conditions of two-channel control architectures are first reviewed. The bilateral controller is then proposed with transparency and stability analysis. Next, the experimental results is presented. The concluding remarks are finally addressed.

Chapter 8: Conclusions and Future Work The work presented in this thesis and the contributions made are summarized. Suggestions for future work are also discussed.

Chapter 2

Literature Review

2.1 Mapping of Single Manipulator Systems

As addressed in Chapter 1, the telemanipulation system necessitates a mapping algorithm. This section focuses on the mapping of the systems, in which the master and the slave are two manipulators (or a joystick and a manipulator, respectively). For systems that the master and the slave possess similar kinematic chains, joint positions could be commanded from the master to the slave directly. While in situations where the kinematic chains differ in structure or in number of joints, the joint spaces are not identical and the mapping is fulfilled in the Cartesian space.

The Cartesian space mapping can be defined by [19]

$$U : \mathbb{R}^6 \rightarrow \mathbb{R}^6 \quad (2.1)$$

where U may be written as a set of six equations

$$x_{si} = U(x_{m1}, x_{m2}, \dots, x_{m6}), \quad i = 1 \dots 6 \quad (2.2)$$

and $\mathbf{x}_m = [x_{m1}, x_{m2}, \dots, x_{m6}]^T$ is the master Cartesian position, and $\mathbf{x}_s = [x_{s1}, x_{s2}, \dots, x_{s6}]^T$ is the slave Cartesian position. These equations map the tip position vector \mathbf{x}_m in the master space to the tip position vector \mathbf{x}_s in the slave space. The forward kinematics of the master is used to compute \mathbf{x}_m according to the joint positions of the master device, and the inverse kinematics of the slave is used to compute the commanded joint angles from \mathbf{x}_s .

The mapping can also be achieved in the velocity domain. A Jacobian relating the

velocities of the master and the slave may be defined as

$$\mathbf{J} = \frac{\partial \mathbf{x}_s}{\partial \mathbf{x}_m} \quad (2.3)$$

Thus, given a mapping U , the slave velocity may be obtained from the master velocity according to

$$\frac{d\mathbf{x}_s}{dt} = \mathbf{J} \frac{d\mathbf{x}_m}{dt} \quad (2.4)$$

Based on the above scheme, several variable position/velocity mapping methods have been developed [19, 27, 67]. Although most other literature on telemanipulation do not address the detailed implementation, the above mapping scheme forms the foundation of mapping of master-slave hand systems.

2.2 Mapping of Hand Systems

In a master-slave hand system, a kinematic mapping algorithm is used to transform the motion of the operator's fingers (master) to the robot hand frame to command the motion of the robot fingers (slave). The motion of the operator's fingers is measured by the sensors of the master device. For the portable master devices, such as the data gloves [108, 109] and the hand exoskeletons [13, 97], the sensor readings of the hand master are usually applied to a kinematic model of the human hand to obtain its joint angles and the fingertip positions. The mapping algorithm is then used to transform the finger positions (or joint angles) to suitable robot finger positions (or joint angles).

2.2.1 Conventional Methods

Three mapping methods have been developed for the master-slave hand systems in general, namely direct joint mapping, pose mapping, and fingertip position mapping.

2.2.1.1 Direct Joint Mapping

For systems with exactly the same or nearly identical kinematics between the master and the slave hands, a simple direct joint mapping (joint-to-joint mapping) can be used. Bouzit [4] developed a robot hand with almost the same structure as that of the human hand when it was equipped with the LRP exoskeleton hand master. Besides the main links, which mimic the human fingers, an exoskeleton type mechanism is also attached to each of the robot fingers. For both the hand master and the robot hand, the position sensors and the actuators were attached on the exoskeletons. In this case, the sensor

readings of the LRP hand master can be directly treated as the motion commands to the robot hand, such that the motion of the human hand was mapped to that of the robot hand in joint space. A similar mapping strategy is applicable to the master slave system introduced by Yokokohji *et al.* [103], where the master device (hand and arm) is non-portable and has exactly the same structure as the robot hand and arm.

In another system, Kyriakopoulos *et al.* [57] employed a linear equation ($\theta_R = k\theta_H + b$) to each of the pairs between the human hand joint θ_H and the corresponding robot hand (Anthrobot, an anthropomorphic hand) joint θ_R . A modified Exos Dexterous Hand Master was used as the master device and worn on the back of the hand to measure its motions. The slave hand, Anthrobot, is anthropomorphic in that it is designed for anatomical consistency with the human hand. This includes not only the number of fingers, but also the placement and motion of the thumb, the proportions of the link lengths, and the shape of the palm. These features make the joint-to-joint mapping feasible. The slope k , and the y-intercept b are determined according to each finger's maximum extension and minimum flexion and the corresponding robot finger's motion range.

There are also some works on direct joint mapping done to the systems with less anthropomorphic (semi-anthropomorphic) slave hands, such as the Utah-MIT Dexterous Hand. However, the resulted performances were usually unsatisfactory. For example, Rohling and Hollerbach [81] reported that a direct joint mapping between Utah Dexterous Hand Master and Utah/MIT Dexterous Hand generated roughly similar human and robot motions, but was unsatisfactory because the kinematic dissimilarities between the human and robot hands required the operator to make contorted hand poses to achieve the desired robot hand motions.

2.2.1.2 Pose Mapping

The pose mapping, which was first developed by Pao and Speeter [76], is a special indirect joint mapping method. In this method, a set of representative poses of the human hand that span the range of the hand motion was defined. Also, another set of poses of the robot hand, which corresponds to that of the human hand, was also defined. A pose, of either the human or robot hand, is defined by a row vector with the joint angles as its components. All the vectors were then stacked into a matrix \mathbf{H} . Similarly, matrix \mathbf{R} representing the poses of the robot hand was also formed. The basic idea is to find a transformation matrix \mathbf{T} , defined as $\mathbf{HT} = \mathbf{R}$, to match poses of the human hand with those of the robot hand. The transformation matrix was found through pseudo-inversion,

which was then used to calculate robot joint angles from the arbitrary measured human hand configuration using interpolation technique. It was reported by the authors that the experiment of this algorithm on the Utah/MIT dexterous hand resulted in smooth and functionally related transformations of human hand positions, although the transformation is sensitive to the specific poses chosen to define the transformation matrix. An advantage of this method is its extensibility to various master/slave configurations. A drawback was reported by Rohling and Hollerbach [81] that the method produced unpredictable movement of the robot fingers and thus suffered from providing enough confidence to the operator.

Recently, pose mapping has been applied to the systems with non-anthropomorphic robot hands. Liu and Zhang [63] developed a pose mapping strategy for a three-fingered symmetric robot hand. Wojtara *et al.* [100] constructed pose correspondences between human hand and a four-fingered symmetric robot hand by a trained neural network. The two systems are sufficient for relatively simple tasks since all the possible poses of the human hand are mapped into several grasp poses (five in [63], and three in [100]) of the robot hand.

2.2.1.3 Fingertip Position Mapping

Compared to the above two methods, The fingertip position mapping (point-to-point) is more popular. It is applicable to all the anthropomorphic and semi-anthropomorphic robot hands and results in predictable motions of the robot fingertips. In this method, the fingertip positions of the human hand are first computed by virtue of forward kinematics according to the sensor readings of the hand master. A conversion algorithm is then used to transform the fingertip positions of the human hand to those of the robot hand. The conversion can be expressed by

$${}^R\mathbf{P}_k = \mathbf{G}\mathbf{R}^H\mathbf{P}_k + \mathbf{P}_o \quad (2.5)$$

where ${}^H\mathbf{P}_k$ and ${}^R\mathbf{P}_k$ represent the human fingertip position and the robot fingertip position, respectively; \mathbf{R} and \mathbf{P}_o are rotational matrix and translation vector, respectively; \mathbf{G} is the scaling gain matrix. Finally, the commanded joint angles of the robot hand are computed by virtue of inverse kinematics.

Fingertip position mapping has been used in several systems. Fischer *et al.* [21] developed a fingertip position mapping method using only a translation and linear scaling with a constant factor in all three degrees of freedom to map the information gathered from CyberGlove to the anthropomorphic DLR robot hand. Wright and Stanisic [101]

presented the kinematic mapping between the EXOS hand master exoskeleton and the Utah/MIT hand. Hong and Tan [41] developed a system to control the Utah/MIT robot hand by the VPL data glove. Hu *et al.* [43] recently applied the fingertip position mapping to tele-control the HIT/DLR hand by using CyberGlove.

Rohling and Hollerbach [81] tested the above three mapping methods, which are direct joint angle mapping, pose mapping and fingertip position mapping, by using Utah Dexterous Hand Master to control Utah/MIT Hand. They reached the conclusion that without addressing fingertip orientation or workspace differences, the operator felt more comfortable during telemanipulation when using fingertip position mapping method, as direct control of the distance between fingertips appears to be essential for performance of grasping tasks.

Several other mapping methods [30, 49, 50] have been developed for the purpose of programming the robot by human demonstration. In these methods, the contact points on the object of the human fingertips are observed by using data gloves or vision systems. The fingertip positions and grasp pose of the robot hand are then determined based on a certain index function, such as maximizing the manipulability of the robot hand, on the condition that the robot grasps the object at the teaching contact points.

2.2.2 Virtual Object Based Mapping

Previous work focused on tele-controlling an anthropomorphic or semi-anthropomorphic robot hand, such as the Utah/MIT Hand [41, 81, 101] and the KH Hand type S [73]. An unaddressed situation is that the robot hand is non-anthropomorphic. Most of the non-anthropomorphic hands have symmetric structure, and all the fingers are identical. Some examples are shown in Fig. 2.1. Using CyberGlove as the master device, Griffin [31] recently developed a virtual object based method to map the motion of the human thumb and index finger to the two-fingered planar non-anthropomorphic hand shown in Fig. 2.1(a). The fundamental idea is to assume that motions of the human fingers are imparting motions to a virtual sphere held between the fingers. The parameters describing the planar virtual object are then mapped to the robot hand frame such that the robot motions intuitively match the hand motions. Compared with the fingertip position mapping, the virtual object based method achieved better workspace matching and produced higher intuitiveness for the operator during the operation. The method is extensible to other planar two-fingered hands.

The previous work has not addressed the situation that the slave hand is a multi-fingered non-anthropomorphic robot hand. To enrich the study on mapping, the first part

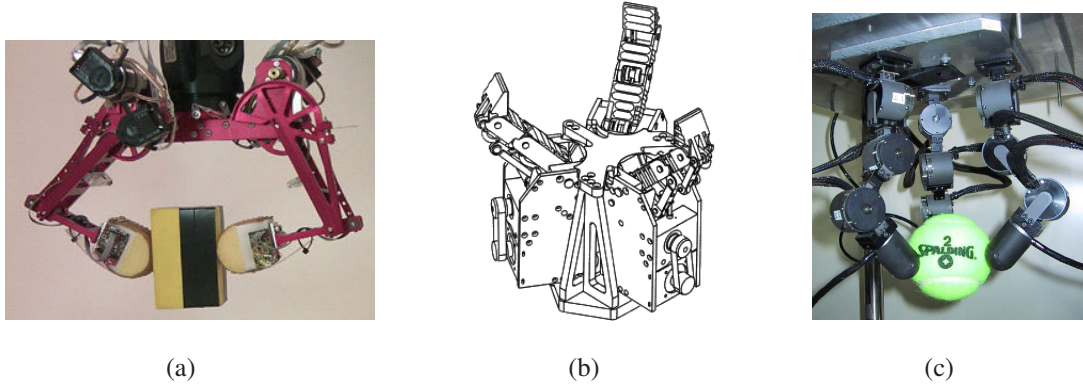


Figure 2.1: Examples of non-anthropomorphic robot hands. (a) A two fingered hand by Stanford Univ. [110]; (b) A three-fingered hand by Univ. LAVAL [111]; (c) A three-fingered hand by Kyushu Univ. [112].

of the thesis focuses on the mapping between the human hand and the three-fingered non-anthropomorphic robot hand. In particular, Chapter 3 investigates the performance of the fingertip position mapping, and a virtual circle mapping method is proposed in Chapter 4.

2.3 Force Control of Robot Manipulators

As introduced in Chapter 1, the research work on the telemanipulation control scheme design can be classified into two branches in general. This work follows the branch in which the bilateral controllers are designed by utilizing the well developed manipulator control schemes. In particular, special emphasis is laid on the constrained motion control of robot manipulators, where the interaction between the robot and the environment is involved.

The advances in robot force control have been well summarized in [11] and [107]. In particular, two fundamental ideas have been developed dealing with the issue of constrained motion control, which are the direct position/force control [10, 22, 36, 54, 72, 80, 86, 95, 98, 106] and the compliant control (assigning a dynamic relationship between position and force variables) [9, 20, 40, 46, 47, 48, 52, 58, 71, 83, 84, 94]. Specifically, two control approaches have been well established. They are the hybrid position/force control, which was first proposed by Raibert and Craig [80], and the impedance control, which was first proposed by Hogan [40].

2.3.1 Hybrid Position/Force Control

The hybrid position/force control was constructed based on the work of task analysis by Mason [69], a major result from which is that the whole task space is partitioned into two orthogonal subspaces, the position controlled subspace and the force controlled subspace. The controller for each subspace takes care of the own artificial constraints (position or force) while ignoring the other. The actual implementation utilizes a compliance selection matrix to determine the subspaces for which the force or position is to be controlled. In this way, the force and position control actions are decoupled. The control laws for each degree of freedom can be designed independently, so that different position and force trajectory tracking commands regarding to each degree of freedom are simultaneously realized. The variables of both the position and the force are usually controlled directly by PID controllers. The scheme of directly controlling the position and force variables makes the system more robust to model and environment uncertainties than impedance control.

A major drawback of the hybrid position/force control is that the control structure has to be changed during the switches between different tasks or in each phase of the same task. Whenever the task coordinate is changed, or one of the position controlled coordinate is switched to the force controlled one or vice versa, the partition of the task space must be re-performed. As a result, the control structure needs to be changed to account for the altered partition of the task space.

2.3.2 Impedance Control

The impedance control technique provides a unified approach to all aspects of manipulation. It is a compliance control strategy for manipulators in both unconstrained and constrained motions. It is therefore not required to switch the control modes when the end-effector moves from free space to contact conditions. Unlike the hybrid position/force control approach, impedance control does not attempt to track motion and force trajectories but rather to regulate the pre-specified target impedance model, which is the dynamic relationship between the end-effector's position and the interaction force with the environment. Therefore, the manipulator-environment interaction force can only be controlled indirectly by an appropriate selection of the reference trajectory for the target impedance.

As stated by Jung *et al.* [48], the reference trajectory is calculated from known environment stiffness. One of the major practical difficulties is that the environment

stiffness is usually not known precisely, and therefore accurate reference trajectory cannot be designed to achieve accurate force control. To solve this problem, two types of strategies have generally been used. One is to update the reference trajectory dynamically by certain appropriate design methods. Lasky and Hsia [58] employed the steepest descent algorithm to update the reference trajectory. Seraji and Colbaugh [84] presented a direct adaptive control scheme to generate the reference trajectory on-line as a function of the force-tracking error. The other is to estimate the stiffness of the environment. Several environment stiffness/impedance estimation techniques can be found in [47, 48, 64, 77, 84, 96].

The optimal reference trajectory alone cannot guarantee satisfactory force tracking performance. The parameters of the target impedance should also be selected properly. For example, according to the duality principle [2], the manipulator should be hard by choosing a large value for the target stiffness when interacting with soft environments, and be soft by choosing a small value for the target stiffness when the environment is hard. Many attempts have been made on adjusting the target impedance parameters both on-line and off-line. Some representative work can be found in [2, 18, 20, 40, 71, 94].

Another important concern is the uncertainties in robot dynamics. If the nonlinear robot dynamics cannot be accurately compensated for, the designed target impedance will be deteriorated and has error, and thus the system performance will be degraded. Many schemes have been proposed to solve this problem. Park and Cho [78] defined an impedance error vector, according to which the stiffness matrix of the target impedance is adjusted. Cheah and Wang [9] proposed an iterative learning impedance controller, which reduces the impedance error as the operations are repeated. The controllers proposed by Jung and Hsia [47], and Huang *et al.* [45] minimized the impedance tracking error by utilizing the neural network technique. To deal with the parametric uncertainties of flexible robot arms, Jiang [46] derived an adaptive scheme, such that the motion of the system converges and remains to the ideal manifold, which is designed to prescribe desirable performance of the system.

The advantage of the impedance control is that it is not required to switch the control modes between the unconstrained motion and the constrained motion. However, the strategies dealing with the environmental and robot dynamic uncertainties in the structure of the impedance control are usually complex. Moreover, when the external disturbances exist, it is difficult to maintain the designed target impedance or to eliminate the target impedance error, even the nonlinear compensation schemes (such as the neural network technique used in [47]) are applied, in that the external disturbances are

unpredictable by nature.

The impedance control can be implemented in the hybrid position/force control structure. Anderson and Spong [2] used the systems approach to analyze the robot-environment interaction, based on which the position controlled impedance controller and the force controlled impedance controller were developed independently. The task space was then partitioned into position controlled and force controlled subsystems, as in the hybrid position/force control. The two controllers were then combined into the hybrid control structure, and the resulted control law is known as the hybrid impedance control. The control mode switch is necessary during the transition of motion.

Liu and Goldenberg also proposed a hybrid impedance control law [62]. In this scheme, the target impedance of the basic impedance control law was redefined by including the commanded force and a selection matrix, which was used to partition the position and force controlled subsystems. Furthermore, the acceleration error based feedback controller was also included into the control law. The scheme is recently applied to a kinematically redundant manipulator [85]. A possible difficulty is the measurement of the acceleration, since most manipulators use digital encoders to measure the joint angles.

2.4 Bilateral Telemanipulation

2.4.1 Two-Port Network Model

The circuit expression is often used to model the telemanipulation system, which consists of three interacting subsystems. As shown in Fig. 2.2 [34], the operator and environment are represented by two one-port network models, whereas the master, slave and communication-channel are lumped into a two-port network model. Z_h and Z_e are impedances of the human operator and the environment, respectively, F_h is the force applied to the master by the operator, F_e is the force applied to the environment by the slave, V_h and V_e are the velocities of the master and the slave, respectively.

The two-port model can be used to quantitatively describe the transparency of the system. Define the impedance felt by the operator at the master interface as the transmitted impedance Z_t , i.e., $F_h = Z_t V_h$, then the telemainipulation system is completely transparent if $Z_t = Z_e$. The two-port model can be described by the following hybrid

matrix formulation [34],

$$\begin{Bmatrix} F_h \\ -V_e \end{Bmatrix} = \begin{bmatrix} h_{11} & h_{12} \\ h_{21} & h_{22} \end{bmatrix} \begin{Bmatrix} V_h \\ F_e \end{Bmatrix} \quad (2.6)$$

in which, h_{ij} is an expression involving the master impedance, Z_m , and the slave impedance, Z_s , and may become very complicated. Solving for F_h and V_h in terms of V_e and F_e , and combining $F_e = Z_e V_e$ and eliminating V_e yields the following expression,

$$F_h = (h_{11} - h_{12}Z_e)(h_{21} - h_{22}Z_e)^{-1}V_h \quad (2.7)$$

So the transmitted impedance is

$$Z_t = (h_{11} - h_{12}Z_e)(h_{21} - h_{22}Z_e)^{-1} \quad (2.8)$$

A fundamental insight to be derived from Eq. (2.8) is that a perfect transparency condition to satisfy $Z_t = Z_e$ is achieved if

$$\mathbf{H} = \begin{bmatrix} h_{11} & h_{12} \\ h_{21} & h_{22} \end{bmatrix} = \begin{bmatrix} 0 & 1 \\ -1 & 0 \end{bmatrix} \quad (2.9)$$

holds [34, 60].

2.4.2 Four-Channel Architecture

In general, both positions (or velocities) and forces can be communicated bilaterally between the master and the slave. Figure 2.3 shows a block diagram of a general four-channel telemanipulation system including master, slave, bilateral communication, as well as operator and environment dynamics developed by Lawrence [60], in which, a one DOF system is considered. To simplify the stability and transparency analysis, it is

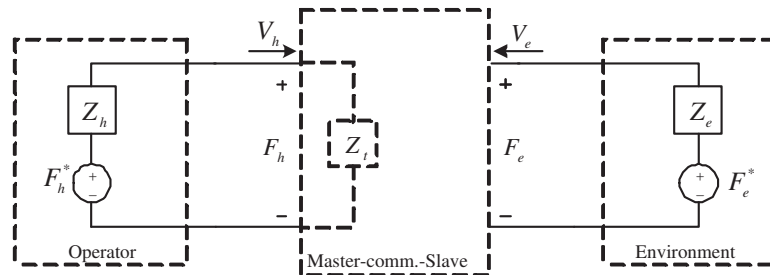


Figure 2.2: Network model of telemanipulation systems.

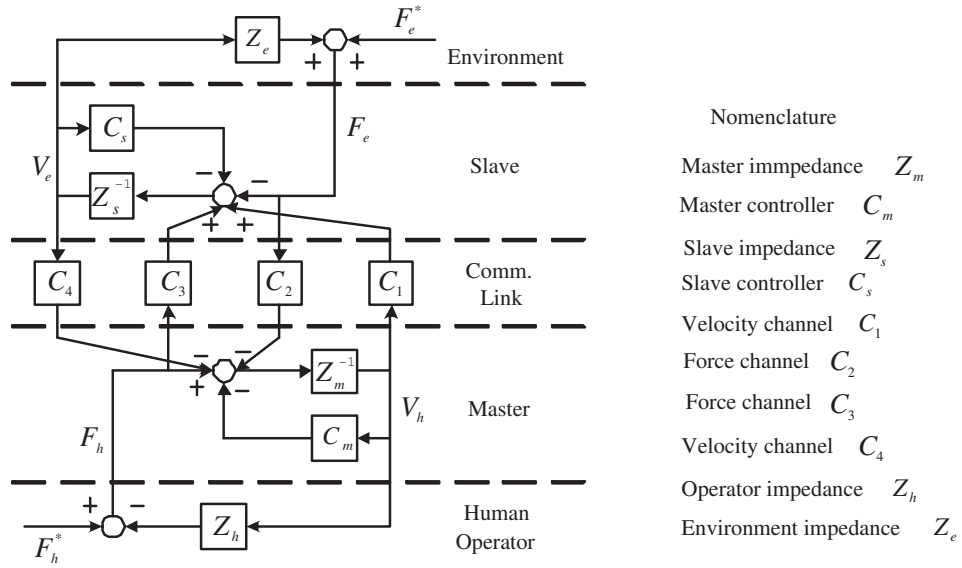


Figure 2.3: Four-channel bilateral telemanipulation block diagram.

assumed that the contact with an environment is maintained. By linearizing the system, the system blocks can be represented in the frequency domain using the Laplace transform. In this architecture, compensators C_m and C_s are included in a local feedback loop for the master and slave systems. The communication blocks, C_i ($i = 1, 2, 3, 4$), depend on the type of architecture and can include filtering blocks, modeled delays, and compensators. The external forces F_e^* and F_h^* are independent of the telemanipulator system behavior.

It has been proven that, in theory, the ideal performance can be achieved by transmitting both master and slave positions and forces [60, 104]. It is claimed that this achievement is due to the use of all four channels of data transmission, especially the transfer of the hand force [60]. On the contrary, in [37], it is shown that only three data channels can result in perfect transparency by employing local force feedback.

Yokokohji and Yoshikawa [104] focused on developing a system with perfect transparency and showed that in the absence of time delay a system could also be passive. To implement such a system, the master and slave parameters must be known exactly and the position, velocity, and acceleration measurements must be available without time delay. Using a well characterized one DOF experimental set-up with the necessary sensors, a high degree of transparency was achieved. However, in practice, because the plant models were not known exactly, the dynamics could not be fully canceled without causing instability, thus reducing the transparency.

By extending the idea of parallel force/position control for single robot compliance

control [10], Hashtrudi-Zaad and Salcudean [36] proposed a four-channel bilateral parallel force/position controller as a simple solution for enhanced performance. In the controller, higher priority is given to position control at the master side and to force control at the slave side. Although the analysis and the experiments were performed for the linear single DOF system, this controller can improve the force and position tracking performance in the presence of system parameter and dynamic uncertainties.

2.4.3 Two-Channel Architectures

Given the complexity and hardware requirements of four-channel bilateral systems, Some research has focused on the two-channel architectures, which can be obtained by suitable specialization of the subsystem dynamics of the four-channel architecture. On the basis of the transferred information type, two-channel architectures can be classified into four types, i.e., position-position (P-P), where the position signals are transmitted bilaterally, position-force (P-F), where the master position commands are sent to the slave and the force information is fed back from the slave to the master, force-position (F-P), where the master force commands are sent to the slave and the slave position signals are transmitted to the master, and force-force (F-F), where the force signals are transmitted bilaterally. In [55], the transparency attainability of each type of two-channel architectures are given using hybrid parameters.

In the P-P architecture, the position error between the master and the slave is used to derive the corresponding motion for the slave and the force feedback information for the master. Therefore, the position error has to be non-zero to generate the actuating force. As a result, to achieve transparency in theory, the control gains have to be infinitely large. This in return makes the system feel sluggish in free motion as large reaction forces, caused by the lag between the master and slave positions, are supplied to the operator [60]. While in [59], Lau and Wai showed that, in free space motion, the P-P architecture resulted in better performance than the P-F architecture. Lawrence [60] showed that, with linear time-invariant controllers, the P-P architecture provides poor transparency. To improve transparency, the position controllers should be adjusted when the dynamics at the slave site changes, such as hitting a hard object. Ni and Wang [74] recently presented a gain-switching control scheme to improve the transparency of a position-error-based bilateral teleoperation system. The advantage of the P-P architecture is that no force/torque sensor is required.

The P-F architecture has been widely used, e.g., [17, 32, 33], and it has been shown

that the P-F architecture performs better than the P-P architecture under the contact motion [59, 60]. However, this architecture is also prone to stability and transparency problems [34]. Similar to other architectures, the network-based concepts were uniformly incorporated to address the transparency [55, 60], and the stability is addressed by incorporating passivity or absolute stability concepts [12, 82]. Rather than using the network theory, Fite *et al.* [23, 24] addressed the performance and stability of the P-F two-channel system from a frequency-domain loop-shaping perspective, which enables the use of classical compensation techniques. It was shown that the transparency and stability robustness can be simultaneously improved in a bilateral telemanipulation system, which contests the previous result that stability and transparency are conflicting design objectives.

A bilateral controller in the framework of the F-F architecture was proposed by Kazerouni *et al.* in [53]. It has been found that, although the communication bandwidth can be increased, the entire system may still suffer from a positional error buildup between the master and the slave. Another F-F architecture controller has been developed in [75], in which the transmitted force signals are utilized to realize a desired impedance at the master. The positional error problem still affects the performance of this controller. By use of the impedance control with an added position error correction channel, a controller was developed in [68], which solved the problem of positional error buildup associated with the F-F architecture.

PART I

KINEMATIC MAPPING

Chapter 3

Investigation on Fingertip Position Mapping

Suppose a data glove is worn by the human operator. The motion of the robot hand is then determined by that of the human hand, which is measured by the data glove. Mapping algorithms are necessary to compute the slave position/configuration according to the master position/configuration. The objective is to provide the human operator intuitive feeling on the slave motion, and at the same time good workspace matching between the human hand (master) and the robot hand (slave).

Most previous master-slave hand systems adopted an anthropomorphic robot hand. However, in practice, a non-anthropomorphic robot hand with less dexterity is sufficient to perform many tasks. An immediate benefit of these systems is the cost reduction in the aspects of design, fabrication, and actuation of the robot hand. As stated in Chapter 2, pose mapping usually results in unsatisfactory performance. Due to the differences in the kinematics of the human hand and the slave robot hand, the direct joint mapping is not possible. An initial solution to these systems is thus the fingertip position mapping. This chapter aims to investigate the performance of the fingertip position mapping in the case of a non-anthropomorphic slave hand. In particular, a three-fingered robot hand having a symmetric structure with 7 DOFs is used in the investigation. The *5DT Data Glove I6-W* [109] was used as the hand master. Correspondingly, a three-fingered human hand model is developed.

3.1 System Description

This section introduces the master-slave hand system. The mapping algorithm is implemented on a three-fingered human hand model and a three-fingered non-anthropomorphic

robot hand.

3.1.1 Human Hand Model

The human hand is a remarkably complex mechanism. Its skeletal system is composed of more than 20 bone segments, constituting palm and fingers. The hand movement is produced by the muscles and tendons attached to the bones. Researchers have made various approximations when modeling it, depending on the application.

Based on the anatomic structure of the human hand [66] and the models developed by Rohling and Hollerbach [81], Bouzit [4], and Turner [92], a three-fingered (thumb, index finger and middle finger) kinematic model is developed by making some proper approximations on the anatomic structure. As shown in Fig. 3.1, the human hand (right hand) is converted to a mechanical linkage with 4 DOFs for each finger. The bone segments (as the links) are connected by pin joints. Note that frame $\{\mathcal{H}_0\}$ shown in the

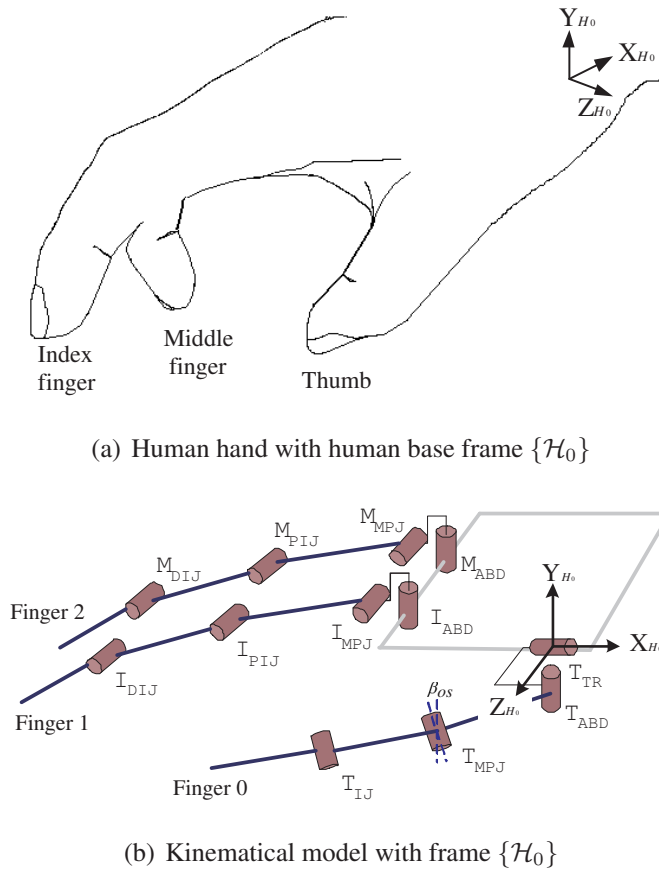


Figure 3.1: Human hand and its simplified kinematic model with human base frame $\{\mathcal{H}_0\}$ attached (Right hand. Finger 0: thumb; Finger 1: index finger; Finger 2: middle finger).

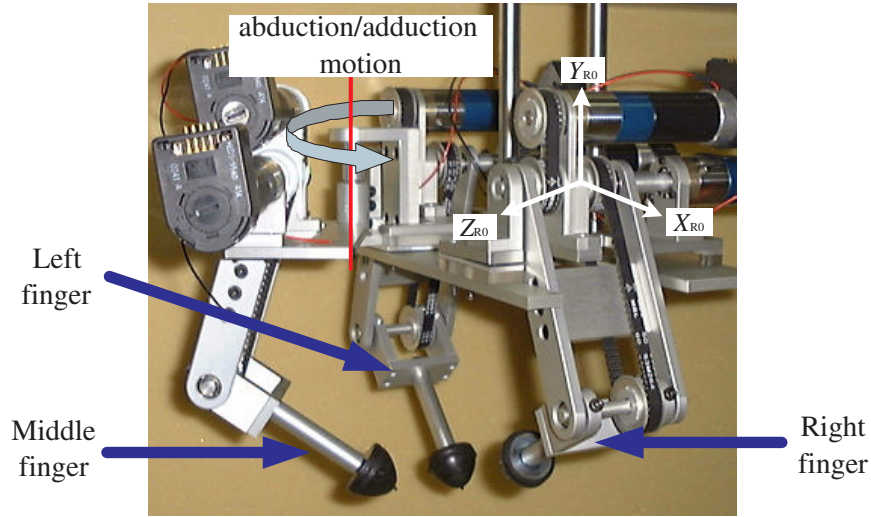


Figure 3.2: The robot hand.

figure is the human base frame, which is located at the thumb rotation joint T_{TR} . The X -axis points away from the index metacarpal bone, the Y -axis is directed outward from a flat open palm, and the Z -axis is defined by the right hand rule.

In the model, the index metacarpophalangeal joint has two orthogonal collocated degrees of freedom, abduction (I_{ABD}) and flexion (I_{MPJ}). The I_{MPJ} , I_{PIJ} and I_{DIJ} joints are all defined such that the axes of rotation are parallel. The middle finger are kinematically identical to the index finger, with the bases of the fingers offset along the z -axis. Modeling the thumb is more challenging due to the complex thumb structure. The T_{TR} joint is located at the base of the thumb with the axis of rotation along the index metacarpal. The T_{ABD} joint is collocated and orthogonal to the T_{TR} joint. The T_{MPJ} and T_{IJ} joints are parallel to each other, and their axes have an offset angle β_{os} to that of the T_{ABD} joint.

For clarity in the following presentation, the human thumb, index finger and middle finger are represented by finger 0, finger 1 and finger 2, respectively.

3.1.2 Robot Hand

As shown in Fig. 3.2, the slave robot hand in our system is a three-fingered non-anthropomorphic robot hand with 7 DOFs. Each of the planar lateral fingers (right finger and left finger) has 2 DOFs. Besides the same 2 DOFs, the middle finger has one additional DOF accounting for the abduction/adduction movement. Particularly, the structure and dimension of the last two links (upper link and lower link) of the middle finger are the same as those of the lateral fingers. The lengths for the upper and lower links of the three fingers are both 96 mm long.

The problem is now reduced to map the motion of the 12-DOF human hand model to those of the 7-DOF robot hand. Naturally, the motions of fingers 0, 1, and 2 are corresponding to those of robot right finger, middle finger and left finger, respectively (refer to Figs. 3.1 and 3.2).

3.2 Mapping Implementation

The measured glove data are applied to the kinematic model to produce 3-D fingertip positions of fingers 0, 1 and 2. For each finger, this Cartesian based mapping can be expressed as

$${}^{\mathcal{R}_0}\mathbf{P} = \begin{bmatrix} g_x & 0 & 0 \\ 0 & g_y & 0 \\ 0 & 0 & g_z \end{bmatrix} [\mathbf{R}_x(\gamma_3)\mathbf{R}_z(\gamma_2)\mathbf{R}_y(\gamma_1)]^{-1} {}^{\mathcal{H}_0}\mathbf{P} + \mathbf{P}_o \quad (3.1)$$

in which the human position vector ${}^{\mathcal{H}_0}\mathbf{P}$ undergoes a series of rotation $\mathbf{R}(\cdot)$, scaling by factors g_x , g_y , and g_z for each of the three components, respectively, and translation \mathbf{P}_o ($\mathbf{P}_o = [p_{ox}, p_{oy}, p_{oz}]^T$) to be mapped to the robot position ${}^{\mathcal{R}_0}\mathbf{P}$. Here the vector rotation is performed by means of frame rotation. The rotational matrix $\mathbf{R}_x(\gamma_3)\mathbf{R}_z(\gamma_2)\mathbf{R}_y(\gamma_1)$ is obtained by rotating the human frame $\{\mathcal{H}_0\}$ about axis \mathbf{Y} by angle γ_1 , then about the new axis \mathbf{Z} by angle γ_2 , and finally about the new axis \mathbf{X} by angle γ_3 , respectively, such that the the resulted frame is in the same orientation as the robot frame $\{\mathcal{R}_0\}$. Note that the sequence of rotation is basically arbitrary. The \mathbf{Y} - \mathbf{Z} - \mathbf{X} sequence is adopted because $\mathbf{R}_y(\gamma_1)$ (representing the first rotation) accounts for the major difference in orientation between frames $\{\mathcal{H}_0\}$ and $\{\mathcal{R}_0\}$. The scaling factors, g_x , g_y and g_z , are chosen to enlarge the operator's finger motions to account for the larger workspace of the robot fingers. The rotated and scaled position vectors are finally translated by \mathbf{P}_o such that most mapped positions are within the workspace of the robot fingers.

Thus, nine parameters are used in the fingertip position mapping, which are g_x , g_y , g_z , γ_1 , γ_2 , γ_3 , p_{ox} , p_{oy} and p_{oz} . Same scaling gains, rotational angles, and translation vector should be applied to each finger such that the robot fingertips gather at a certain point when the operator brings his/her fingertips together (This property is defined as fingertip-to-fingertip correspondence). Note that the computed robot left and right fingertip positions should be projected onto the plane defined by axes \mathbf{X}_{R_0} and \mathbf{Y}_{R_0} of frame $\{\mathcal{R}_0\}$ (refer to Fig. 3.2) to account for the planar nature of the two fingers.

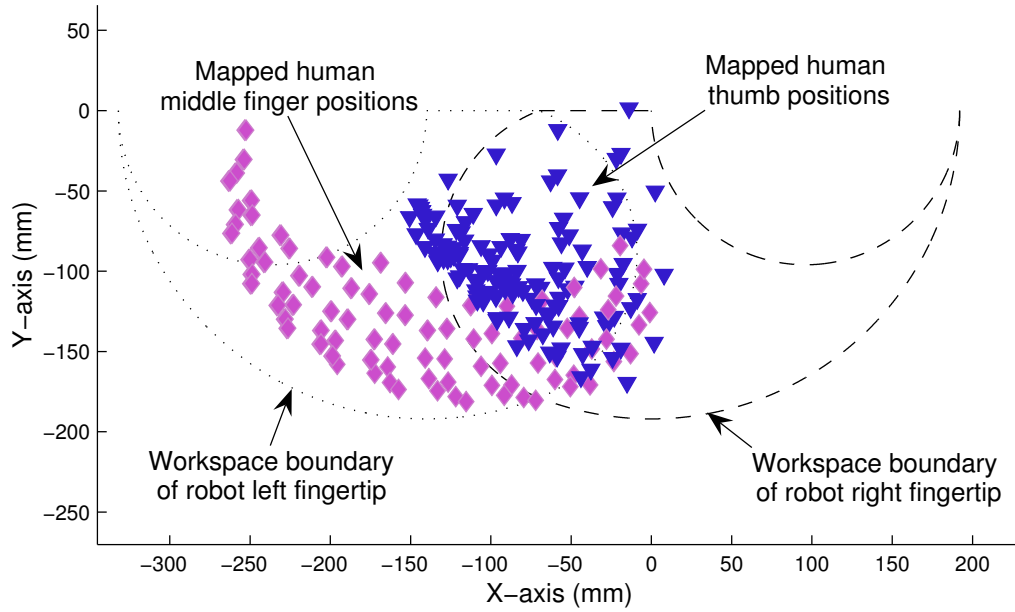


Figure 3.3: Mapping results of human thumb (finger 0) and middle finger (finger 2) by fingertip position mapping.

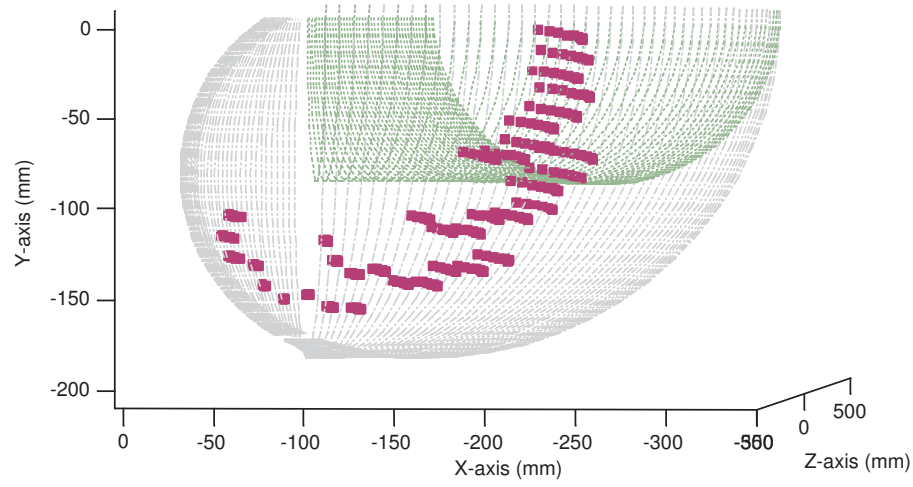
3.3 Mapping Results

The mapping results by simulation, which were obtained by programming the mapping algorithm in MATLABTM, are presented in this section. The value of each joint angle of the human hand was chosen randomly over its motion range. The parameter values were chosen by trial-and-error as $g_x = 1.6$; $g_y = 1.2$; $g_z = 1.6$; $\gamma_1 = -23^\circ$; $\gamma_2 = -8^\circ$; $\gamma_3 = 0^\circ$; $p_{ox} = 32$; $p_{oy} = -44$; $p_{oz} = 63$.

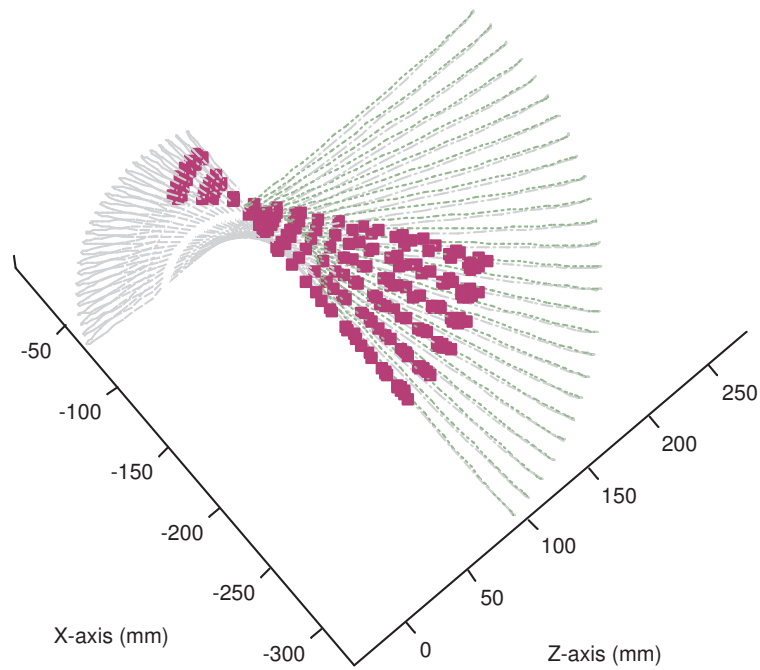
Figure 3.3 shows a typical result of finger 0 and finger 2, the motions of which are mapped into the workspace of the robot right and left fingers, respectively. Figure 3.4 shows the result of finger 1 in two perspectives, the motion of which is mapped into the workspace of the robot middle finger. The curves represent the workspace boundaries of the robot fingers, while the points represent the mapped positions of the human fingertips.

3.3.1 Discussion

As shown in Fig. 3.3, the motion of finger 2 is relatively well mapped to the workspace of the robot left finger. It is mainly due to the kinematic similarities between the two fingers, plus the abduction/adduction motion of finger 2 is much smaller compared to the



(a) Viewpoint 1



(b) Viewpoint 2

Figure 3.4: Mapping results of human index finger (finger 1) by fingertip position mapping.

flexion/extension motion. Moreover, when the human hand is grasping an object, finger 2 always maintains the abduction/adduction angle at a certain value, which roughly constrains the motion of finger 2 to a plane. The motion range of the robot left finger also corresponds well with the flexion/extension range of finger 2, yielding a similar workspace shape. Therefore, the operator is capable of using a large percentage of workspace of the robot left finger.

However, the result of finger 0 is somewhat non-satisfactory. The achievable positions of the finger are mapped to a relatively small region. Despite the large 3-D motion range of finger 0, its projected tip positions are approximately confined to a small region spanning the left part of the workspace of the robot right finger. It is mainly due to the great kinematic dissimilarities between finger 0 and the robot right finger. Firstly, finger 0 is shorter than finger 2, while robot right and left fingers are identical. Secondly, the relative location of fingers 0 and 2 is different from that of robot right and left fingers.

Similarly, the achievable positions of finger 1 are also mapped to a relatively small region of the corresponding robot workspace, i.e., the workspace of the robot middle finger. As shown in Fig. 3.4, only half of the abduction/adduction motion of the robot middle finger can be used by the human operator.

To improve the achievable mapped positions of fingers 0 and 1, one could simply increase the gains for the two fingers' transformation. However, because it is desired that the mapping has the fingertip-to-fingertip correspondence, all the gains and offsets must be the same for all the three fingers. To prevent a large portion of finger 2's mapped positions from falling outside of the workspace and large velocities of all the three fingers, the gains can not be increased to an over large value.

3.4 Summary

The results shown in Figs. 3.3 and 3.4 imply the en-effectiveness of the fingertip position mapping in the case that the slave robot hand is non-anthropomorphic. Firstly, the human fingertips' position can not be mapped into the whole robot workspace, such that the large workspace of the robot hand cannot be fully utilized. Secondly, the mismatch between the mapped human finger positions and the corresponding robot workspace will provide low intuitiveness to the operator due to the poor grasp pose correspondence. For instance, according to Fig. 3.3, when the operator opens his/her hand with the thumb fully extended, the robot right finger cannot extend as expected, which tends to frustrate the operator. This is tested by the experiments and will be addressed in Sec. 4.6 as a

comparison with the virtual circle mapping method presented in Chapter 4.

In a word, the investigation in this chapter shows that, for non-anthropomorphic slave hand, the fingertip position mapping method fails to provide satisfactory degree of telepresence and workspace matching between the master and the slave hands.

Chapter 4

Virtual Circle Mapping

For three-fingered non-anthropomorphic robot hands, the previous developed methods are not applicable or cannot result in satisfactory performance. By extending Griffin's virtual object based method [31], which was developed particularly for 2-D cases, this chapter focuses on 3-D cases and presents a virtual circle mapping method dealing with the three-fingered robot hands.

The mapping algorithm presented in this chapter is developed particularly for the three-fingered non-anthropomorphic robot hand introduced in Chapter 3. The general idea of the method is applicable for other three-fingered robot hands. In the following sections, the concept of the virtual circle mapping is first introduced. The detailed implementation of the idea is then presented, followed by the simulation results and the experimental validation. Finally, the work and the results presented are concluded.

4.1 Virtual Circle Mapping Concept

The virtual circle mapping method is developed based on the basic geometry theorem, which states that three points (if they are not in a line) define a unique circle. The fundamental idea is to construct a corresponding relationship between two virtual circles defined by the human fingertips and the robot fingertips, respectively. As a result, a corresponding relationship between the Cartesian positions of the human fingers and those of the robot fingers can be constructed. The mapping from master to slave can thus be achieved. Figure 4.1 shows the concept of the proposed method, where the virtual circle is described by four sets of parameters. They are

- Circle radius
- Central angles
- Circle center position

- Circle orientation

Note that the circle radius and central angles are scalars; the circle center position is expressed by a vector; and the circle orientation is represented by a frame attached to the circle plane.

Different from the fingertip position mapping, which transfers the absolute Cartesian positions of the fingertips, the virtual circle method defines and transfers the information of the relative positions between the fingertips. The virtual circle actually carries the relative-position information. The mapping procedure is depicted in Fig. 4.2, in which three steps are performed in sequence. Firstly, the four sets of parameters describing the virtual circle of the human hand are derived according to the fingertip Cartesian positions. Secondly, the parameters are transformed to the robot frame such that the virtual circle of the robot hand is constructed. Finally, the robot fingertip positions are computed according to the transformed parameters describing the robot virtual circle.

4.2 Parameters Describing the Human Hand Circle

A major difference between the human hand and the robot hand is the inability of robot left and right fingers' abduction/adduction motion. Therefore, it is necessary to find a suitable plane, onto which the tip positions of fingers 0 and 2 are projected to account for the planar nature of the robot right and left fingers. In fact, there exists a plane that contains most motions of fingers 0 and 2 when the operator opens and closes his/her grasp naturally. As shown in Fig. 4.3(a), frame $\{\mathcal{H}_1\}$, which means human frame 1, is defined to locate the plane for projection. By observation, frame $\{\mathcal{H}_1\}$ can be found

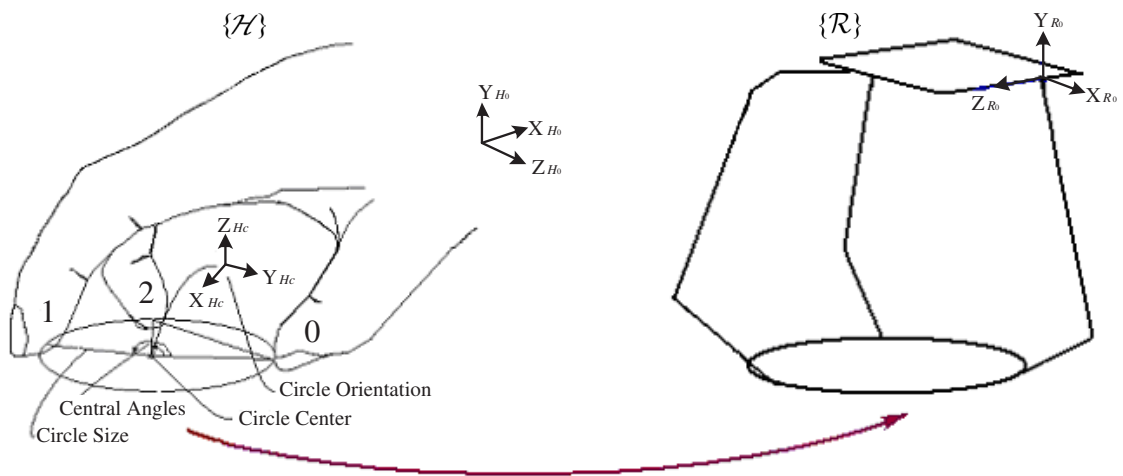


Figure 4.1: The concept of virtual circle mapping.

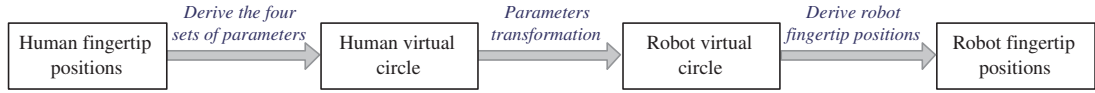


Figure 4.2: Procedure of virtual circle mapping.

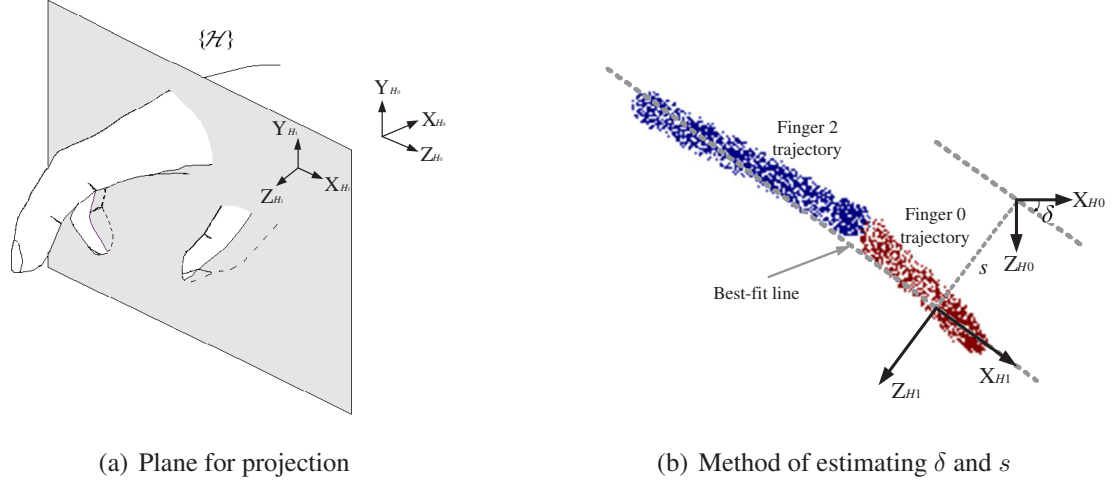


Figure 4.3: Plane for projection of the motions of fingers 0 and 2.

by first rotating frame $\{H_0\}$ about \mathbf{Y} -axis by an angle δ and then translating the rotated frame along its \mathbf{Z} -axis by a distance s . The best values of δ and s can be obtained by an estimate-and-tune process.

Figure 4.3(b) shows the method of estimating the values of δ and s . Firstly, the operator is asked to open and close his/her grasp naturally. The tip positions of fingers 0 and 2 are then recorded and projected onto $\mathbf{X}_{H_0}\mathbf{Z}_{H_0}$ plane. Secondly, the best-fit line of the tip trajectories is computed. Finally, the estimation of value δ is found as the angle between \mathbf{X}_{H_0} -axis and the best-fit line. The estimated value of s is the distance from the origin of frame $\{H_0\}$ to the best-fit line. Although the estimated values are reasonable and close to the optimal ones, it is better to fine tune them by the operator himself/herself. The major reason is that whether the resulted robot pose is intuitive or not is basically subjective. Therefore, the operator should have the right to tune the value by a small amount around the estimated values.

By applying the sensor readings to the kinematic model of the human hand, the fingertip positions are obtained by virtue of forward kinematics. After the motion projection of fingers 0 and 2, the three tip positions can be expressed in frame $\{H_1\}$ as

$${}^{\mathcal{H}_1}\mathbf{P}_i = [{}^{\mathcal{H}_1}x_i \ {}^{\mathcal{H}_1}y_i \ {}^{\mathcal{H}_1}z_i]^T, \quad i = 0, 1, 2 \quad (4.1)$$

where ${}^{\mathcal{H}_1}z_0 = {}^{\mathcal{H}_1}z_2 = 0$. The superscript \mathcal{H}_1 denotes frame $\{H_1\}$. The four sets of

parameters are then derived in the following sections.

4.2.1 Circle Radius and Central Angles

Three vectors \mathbf{u}_{01} , \mathbf{u}_{02} , and \mathbf{u}_{12} are defined and expressed in frame $\{\mathcal{H}_1\}$ respectively by

$${}^{\mathcal{H}_1}\mathbf{u}_{01} = {}^{\mathcal{H}_1}\mathbf{P}_1 - {}^{\mathcal{H}_1}\mathbf{P}_0, \quad {}^{\mathcal{H}_1}\mathbf{u}_{02} = {}^{\mathcal{H}_1}\mathbf{P}_2 - {}^{\mathcal{H}_1}\mathbf{P}_0, \quad {}^{\mathcal{H}_1}\mathbf{u}_{12} = {}^{\mathcal{H}_1}\mathbf{P}_2 - {}^{\mathcal{H}_1}\mathbf{P}_1 \quad (4.2)$$

As shown in Fig. 4.4 with the circle center denoted by C_h (center of the human circle), there are two possible cases of the resulted circle, which are $\angle 012 \leq \pi/2$ (Fig. 4.4(b)) and $\angle 012 > \pi/2$ (Fig. 4.4(c)). For both cases, the internal angles $\angle 012$ and $\angle 021$ of the triangle composed by the three fingertips are computed firstly using the Cosine Law as

$$\angle 012 = \cos^{-1} \frac{\|\mathbf{u}_{01}\|^2 + \|\mathbf{u}_{12}\|^2 - \|\mathbf{u}_{02}\|^2}{2\|\mathbf{u}_{01}\| \cdot \|\mathbf{u}_{12}\|} \quad (4.3)$$

$$\angle 021 = \cos^{-1} \frac{\|\mathbf{u}_{02}\|^2 + \|\mathbf{u}_{12}\|^2 - \|\mathbf{u}_{01}\|^2}{2\|\mathbf{u}_{02}\| \cdot \|\mathbf{u}_{12}\|} \quad (4.4)$$

Define anti-clockwise as the positive direction, the central angles $\angle 0C_h1$ and $\angle 0C_h2$ are then obtained

$$\angle 0C_h1 = 2\pi - 2\angle 021 \quad (4.5)$$

$$\angle 0C_h2 = 2\angle 012 \quad (4.6)$$

For both cases shown in Fig. 4.4, the radius of the circle is computed by

$$r_{human} = \frac{\|\mathbf{u}_{02}\|}{2 \sin \angle 012} \quad (4.7)$$

4.2.2 Circle Center Position

The circle center is used to describe the location of the circle. Express the circle center position of the human hand in frame $\{\mathcal{H}_1\}$ as ${}^{\mathcal{H}_1}\mathbf{P}_{hc} = [{}^{\mathcal{H}_1}x_{hc}, {}^{\mathcal{H}_1}y_{hc}, {}^{\mathcal{H}_1}z_{hc}]^T$, where the subscript hc means “human circle center”. According to the geometry theories that the distances from the center to each point of the circle are equal, and the three fingertips and the center are in the same plane, the following three equations are obtained:

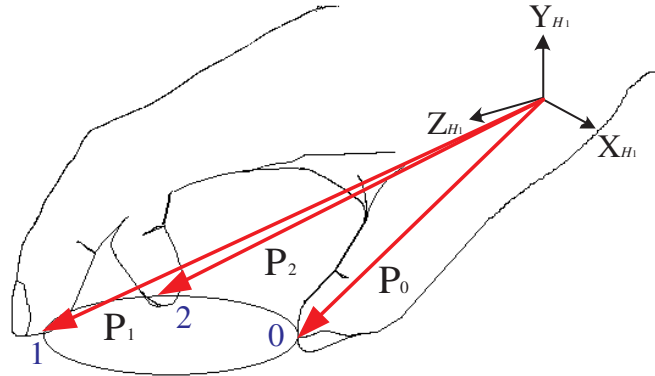
$$\|{}^{\mathcal{H}_1}\mathbf{P}_{hc} - {}^{\mathcal{H}_1}\mathbf{P}_0\| = \|{}^{\mathcal{H}_1}\mathbf{P}_{hc} - {}^{\mathcal{H}_1}\mathbf{P}_1\| \quad (4.8)$$

$$\|\mathcal{H}_1 \mathbf{P}_{hc} - \mathcal{H}_1 \mathbf{P}_0\| = \|\mathcal{H}_1 \mathbf{P}_{hc} - \mathcal{H}_1 \mathbf{P}_2\| \quad (4.9)$$

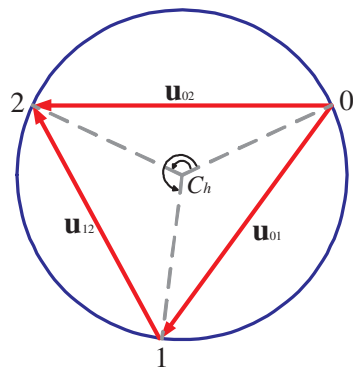
$$\det \begin{pmatrix} \mathcal{H}_1 x_{hc} & \mathcal{H}_1 y_{hc} & \mathcal{H}_1 z_{hc} & 1 \\ \mathcal{H}_1 x_0 & \mathcal{H}_1 y_0 & \mathcal{H}_1 z_0 & 1 \\ \mathcal{H}_1 x_1 & \mathcal{H}_1 y_1 & \mathcal{H}_1 z_1 & 1 \\ \mathcal{H}_1 x_2 & \mathcal{H}_1 y_2 & \mathcal{H}_1 z_2 & 1 \end{pmatrix} = 0 \quad (4.10)$$

which can then be used to solve for $\mathcal{H}_1 x_{hc}$, $\mathcal{H}_1 y_{hc}$ and $\mathcal{H}_1 z_{hc}$ and thus the circle center can be obtained and is expressed as $\mathcal{H}_1 \mathbf{P}_{hc,original}$ in frame $\{\mathcal{H}_1\}$.

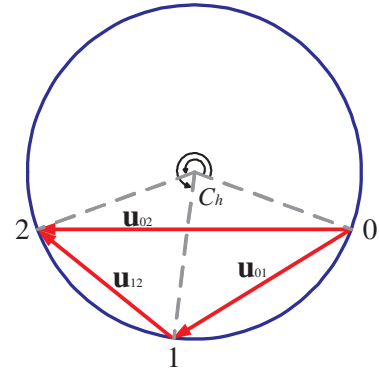
The original circle center should be shifted along two directions, respectively. Firstly, the motions of fingers 0 and 2 during a natural grasp are asymmetric. The workspace of finger 0 is smaller than that of finger 2 in terms of the motions within the $\mathbf{X}_{H_1} \mathbf{Y}_{H_1}$ plane. While the right and left fingers of the robot hand, the counterparts of fingers 0 and 2, have the same kinematic structure and thus symmetric motions during a natural grasp. As a



(a) Fingertip positions defined in frame $\{\mathcal{H}_1\}$



(b) $\angle 012 \leq \frac{\pi}{2}$ (i.e. $\angle 0C_h 2 \leq \pi$)



(c) $\angle 012 > \frac{\pi}{2}$ (i.e. $\angle 0C_h 2 > \pi$)

Figure 4.4: Graphical illustration of the circle radius and central angles.

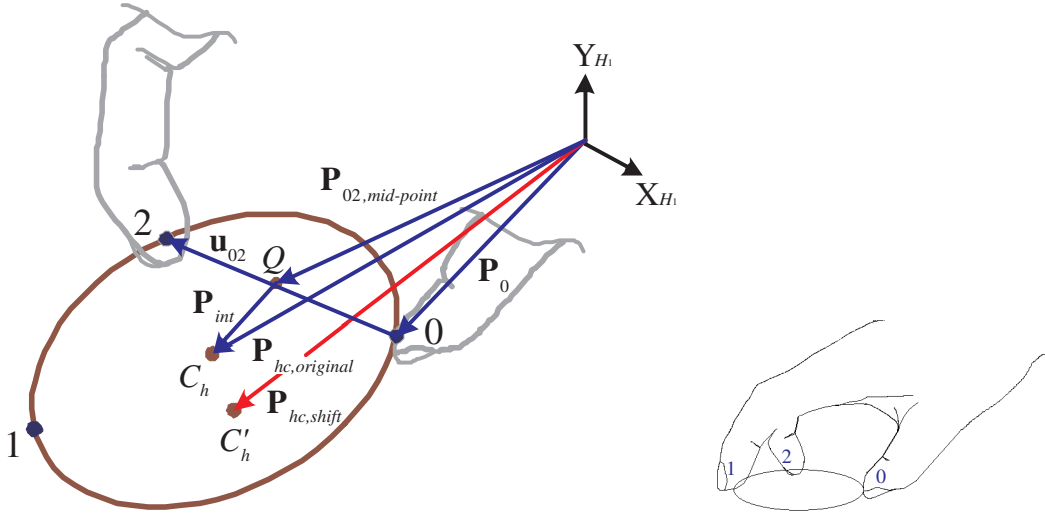


Figure 4.5: Graphical illustration of shifting the circle center of the human hand (Finger 1 is not shown for clarity).

result, if the operator opens his/her grasp from the pinch-point ($\mathbf{P}_{human-pinch}$) naturally (refer to Fig. 4.12 for the definitions of human and robot pinch-points), the mid-point of chord 02 (refer to Fig. 4.5) will shift toward finger 2. While the desired robot motion has its pinch-point ($\mathbf{P}_{robot-pinch}$) as the constant mid-point of the line segment determined by robot right and left fingers. To account for the asymmetric motions by fingers 0 and 2 of the human hand, the circle center should be shifted towards finger 0, as claimed by Griffin in his virtual object based method[31]. Secondly, the robot circle is larger than its corresponding human circle due to the larger dimension of the robot hand. Also, the $\mathbf{X}_{H_1}\mathbf{Y}_{H_1}$ plane is corresponding to the plane containing the motions of robot left and right fingers. Therefore, if the two planes are located such that they coincide with each other, it is easy to find that a shift of the human circle center away from the $\mathbf{X}_{H_1}\mathbf{Y}_{H_1}$ plane is necessary. Actually, the $\mathbf{X}_{H_1}\mathbf{Y}_{H_1}$ plane is used as the reference plane, and in the following derivations, it is assumed that the corresponding plane of the robot hand coincides with that of the human hand. As shown in Fig. 4.5, the position of the mid-point of chord 02 can be expressed in frame $\{\mathcal{H}_1\}$ by

$$\mathbf{P}_{02,mid-point} = \mathbf{P}_0 + \frac{1}{2}\mathbf{u}_{02} \quad (4.11)$$

where the vector \mathbf{u}_{02} is defined by Eq. (4.2). Define an “intermediate” vector \mathbf{P}_{int} as

$$\mathbf{P}_{int} = \mathbf{P}_{hc,original} - \mathbf{P}_{02,mid-point} \quad (4.12)$$

Note that vectors \mathbf{P}_{int} and \mathbf{u}_{02} are orthogonal. The position of the shifted circle center can now be expressed in frame $\{\mathcal{H}_1\}$ as

$$\mathbf{P}_{hc,shift} = \mathbf{P}_0 + \lambda \mathbf{u}_{02} + \mu \mathbf{P}_{int} \quad (4.13)$$

where λ represents the shifting ratio of the mid-point of chord 02, and μ represents the stretch ratio of the intermediate vector, \mathbf{P}_{int} . Although the above derivation is based on the case shown in Fig. 4.4(b), the derived formulas are valid for the case shown in Fig. 4.4(c). The statement to the scheme of determining μ is deferred to Sec. 4.3.1, and that of λ is discussed here.

Similar to locating the projection plane, the determination of the value of λ can also be performed through an estimate-and-tune process. The operator is asked to open and close his/her grasp naturally. The tip positions of fingers 0 and 2 are then recorded and projected onto $\mathbf{X}_{H_1}\mathbf{Z}_{H_1}$ plane, as shown in Fig. 4.6(a). Further, the tip positions are projected onto \mathbf{X}_{H_1} -axis. At the initial stage of opening the grasp, the tip positions of fingers 0 and 2 ($\mathbf{P}_{0-initial}$ and $\mathbf{P}_{2-initial}$) are nearly symmetric with respect to the pinch-point (refer to Fig. 4.6(a)). In other words, the mid-point of the line segment determined by the two tips coincides with the pinch-point. This situation gives the upper bound of λ , which is $\lambda_{max} = 0.5$. When the fingers reach the ends of their workspace (represented by \mathbf{P}_{0-max} and \mathbf{P}_{2-max} in Fig. 4.6(b)), the mid-point shifts toward finger 2 for a small amount. This situation gives the lower bound of λ , which is $\lambda_{min} = \frac{d_{0p-max}}{d_{02-max}}$, where d_{0p-max} is the magnitude of vector $(\mathbf{P}_{human-pinch} - \mathbf{P}_{0-max})$ projected onto \mathbf{X}_{H_1} -axis, and d_{02-max} is the magnitude of vector $(\mathbf{P}_{2-max} - \mathbf{P}_{0-max})$ projected onto \mathbf{X}_{H_1} -axis.

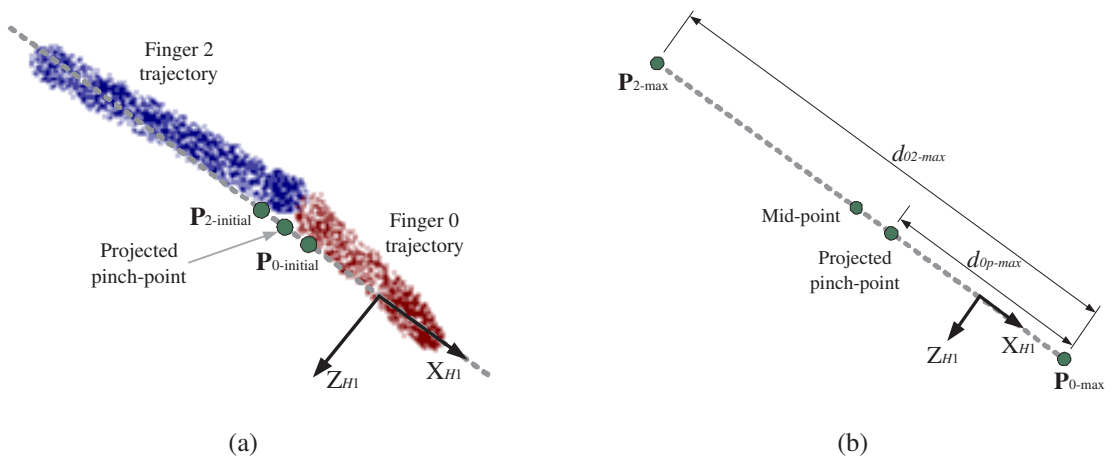


Figure 4.6: Graphical illustration of determining the bounds of parameter λ .

Therefore, the value of λ should satisfy

$$\frac{d_{0p-max}}{d_{02-max}} \leq \lambda \leq 0.5 \quad (4.14)$$

When implementing the method, the initial value can be set as $\frac{1}{2}(\lambda_{min} + \lambda_{max})$. The operator then fine tunes the value before the operation. Note that different operators usually choose different value for λ due to two reasons. Firstly, human hands are different and thus result in different values for $\frac{d_{0p-max}}{d_{02-max}}$. Secondly, the operator tunes the value based on his/her own standard of intuitiveness.

4.2.3 Circle Orientation

The circle orientation is described by a frame, say frame $\{\mathcal{H}_c\}$, which means ‘‘Human’s circle’’, attached to the circle, as shown in Fig. 4.7. Note that the two possible cases due to the relative positions between the fingertips are shown in Fig. 4.7(a) and Fig. 4.7(b), respectively. In both cases, the origin of the frame $\{\mathcal{H}_c\}$ lies in the original circle center for convenience, although the location of the frame is arbitrary. The three components of the frame are defined as

$$\mathbf{X}_{H_c} = \begin{cases} \frac{\mathbf{P}_{int}}{\|\mathbf{P}_{int}\|} & \text{if } \angle 0C_h2 \leq \pi \\ \frac{-\mathbf{P}_{int}}{\|\mathbf{P}_{int}\|} & \text{if } \angle 0C_h2 > \pi \end{cases} \quad (4.15)$$

$$\mathbf{Y}_{H_c} = \frac{-\mathbf{u}_{02}}{\|\mathbf{u}_{02}\|} \quad (4.16)$$

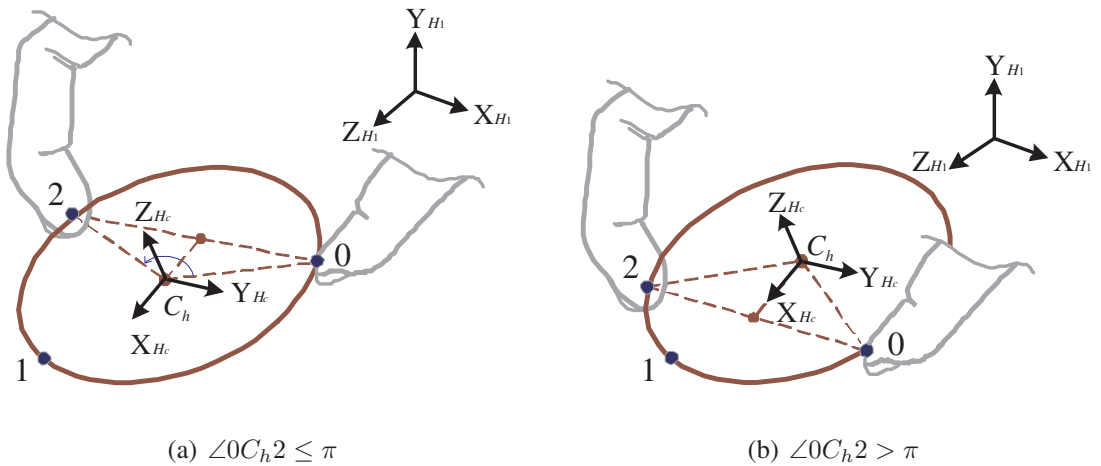


Figure 4.7: Graphical illustration of the circle orientation of the human hand (Finger 1 is not shown for clarity).

$$\mathbf{Z}_{H_c} = \mathbf{X}_{H_c} \times \mathbf{Y}_{H_c} \quad (4.17)$$

Note that vector \mathbf{X}_{H_c} is defined such that it always points to the direction of finger 1. The definition is depending on $\angle 0C_h2$, which is measured about axis \mathbf{Z}_{H_c} . Vectors \mathbf{X}_{H_c} and \mathbf{Y}_{H_c} are orthogonal since vectors \mathbf{P}_{int} and \mathbf{u}_{02} are orthogonal.

By expressing the three unit vectors in frame $\{\mathcal{H}_1\}$, they can be written into a rotational matrix, ${}^{\mathcal{H}_1}_{\mathcal{H}_c}\mathbf{R}$, to describe the orientation of frame $\{\mathcal{H}_c\}$ relative to frame $\{\mathcal{H}_1\}$ as

$${}^{\mathcal{H}_1}_{\mathcal{H}_c}\mathbf{R} = \begin{bmatrix} {}^{\mathcal{H}_1}\mathbf{X}_{H_c} & {}^{\mathcal{H}_1}\mathbf{Y}_{H_c} & {}^{\mathcal{H}_1}\mathbf{Z}_{H_c} \end{bmatrix} \quad (4.18)$$

The four sets of parameters describing the virtual circle of the human hand have been obtained. They are the circle radius r_{human} , the central angles $\angle 0C_h1$ and $\angle 0C_h2$, the center position ${}^{\mathcal{H}_1}\mathbf{P}_{hc,shift}$, and the circle orientation ${}^{\mathcal{H}_1}_{\mathcal{H}_c}\mathbf{R}$. Next, the parameters in the human frame should be transformed into the robot frame.

4.3 Human-to-Robot Transformation

By transforming the derived four sets of parameters of the human circle into robot frame, a corresponding virtual circle of the robot hand can then be constructed. While the formulas obtained in this section are valid for both cases of the human circle shown in Fig. 4.4, the following analysis is based on the case shown in Fig. 4.4(b), where the three fingers enclosing the circle.

4.3.1 Transformation of Circle Radius and Central Angles

To achieve the desired correspondence in poses between the human hand and the robot hand, the central angles of the robot circle are maintained the same as of the human circle. The explanation is given next. Suppose the virtual circle of the robot hand is constructed, and frame $\{\mathcal{R}_c\}$ is attached to the origin of the circle to describe its orientation. Locate the two circles as shown in Fig. 4.8(a), such that frames $\{\mathcal{R}_c\}$ and $\{\mathcal{H}_c\}$ coincide, where C_r and C_h represent the centers of the robot circle and the human circle, respectively. Refer to Fig. 4.8(a), the way to maintain the relative positions between the fingertips in the circle plane is to keep $\triangle 012$ similar to $\triangle RML$, which requires

$$\angle RC_rL = \angle 0C_h2 \quad (4.19)$$

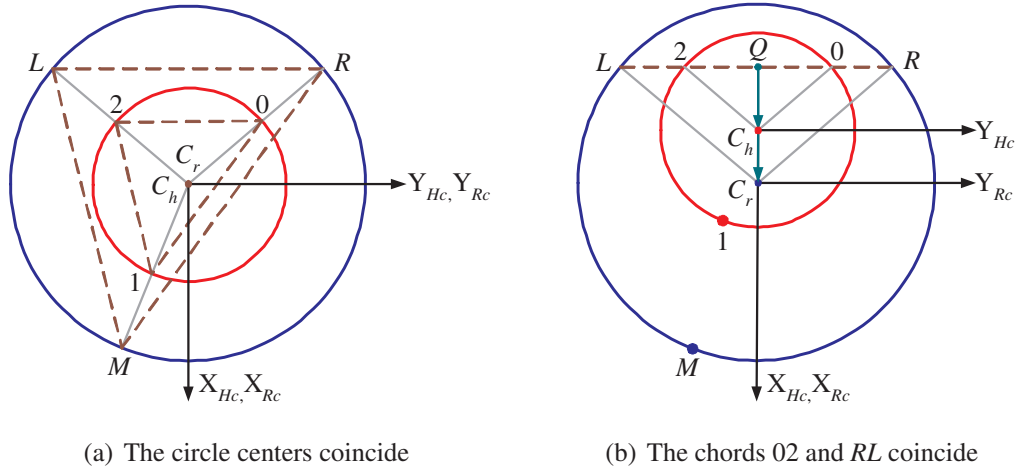


Figure 4.8: Circles of the human hand (smaller one) and the robot hand (larger one) in the same orientation.

$$\angle RC_r M = \angle 0C_h 1 \quad (4.20)$$

where L , R and M represent the robot left, right and middle fingertips, respectively.

To account for the larger workspace of the robot hand, the circle radius is scaled by

$$r_{robot} = K r_{human} \quad (4.21)$$

where r_{robot} is the radius of the robot circle. A useful observation is that the optimal value for the scaling ratio K is equal to the stretch ratio μ in Eq. (4.13), i.e.

$$K = \mu \quad (4.22)$$

Refer to Fig. 4.8(b), which is obtained by moving the human circle shown in Fig. 4.8(a) along $-\mathbf{X}_{Rc}$, such that chord 02 coincides with chord RL . Then vector \mathbf{P}_{int} defined in Eq. (4.12) and Fig. 4.5 is actually the vector $\overrightarrow{QC_h}$ shown in Fig. 4.8(b), where Q is the mid-point of chords 02 and RL . It is known that $\triangle 0C_h 2$ and $\triangle RC_r L$ are isosceles triangles and $\triangle 0C_h 2$ is similar to $\triangle RC_r L$. Thus $\triangle 0QC_h$ is similar to $\triangle RQC_r$. We then have

$$K = \frac{r_{robot}}{r_{human}} = \frac{\|RC_r\|}{\|0C_h\|} = \frac{\|\overrightarrow{QC_r}\|}{\|\overrightarrow{QC_h}\|} = \mu \quad (4.23)$$

The determination of parameter K (and μ) is again an estimate-and-tune process. The radius of the circle should be scaled such that the maximum span of the human pose matches the maximum grasp that the robot can achieve. Refer to Fig. 4.6(b), d_{02-max}

represents the maximum span of fingers 0 and 2. If d_{RL-max} is used to represent the maximum span that the robot right and left fingers can reach, K should then satisfy

$$K \leq K_{max} = \frac{d_{RL-max}}{d_{02-max}} \quad (4.24)$$

Based on the estimation, the value can then be fine tuned by the operator given the value of K_{max} . Figure 4.9 shows three possible strategies for choosing K .

4.3.2 Transformation of Circle Orientation

The orientation of the robot circle should be maintained the same as the human circle with respect to the world coordinate. Set frame $\{\mathcal{R}_0\}$ as the world coordinate. Locate the two circles (human and robot) as shown in Fig. 4.10(a), such that the circle center of the robot hand coincides with the shifted circle center of the human hand, and frame $\{\mathcal{H}_c\}$ has the same orientation as frame $\{\mathcal{H}_c\}$. Then frame $\{\mathcal{R}_0\}$ has different location and orientation from frame $\{\mathcal{H}_1\}$. The circle orientation should be expressed with respect to frame $\{\mathcal{R}_0\}$. The task is reduced to find the orientational relationship between frame

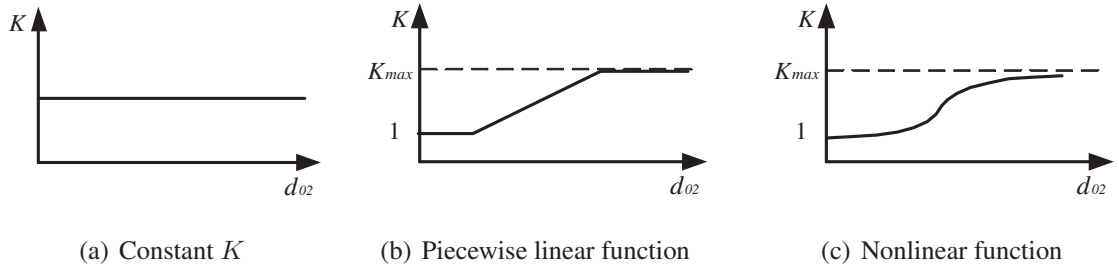


Figure 4.9: Possible strategies for choosing K .

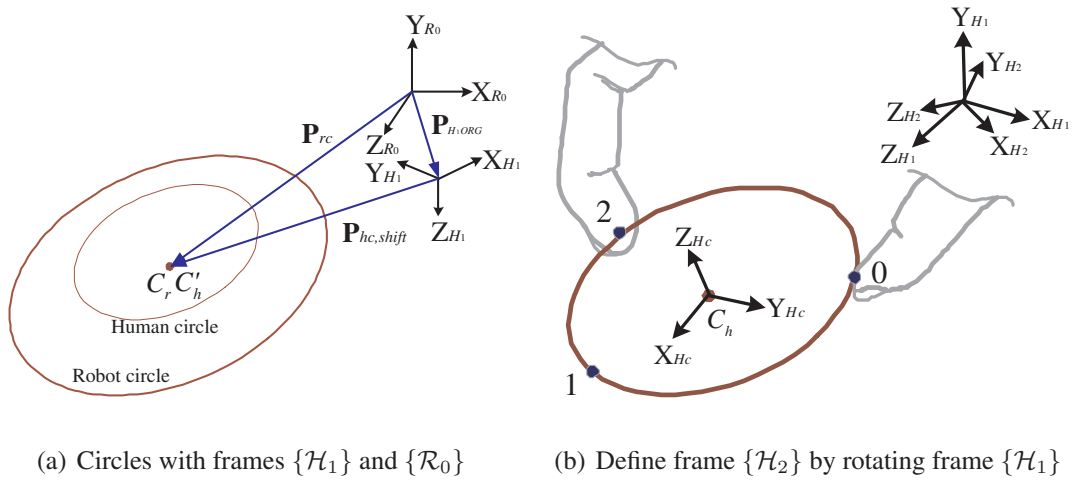


Figure 4.10: Graphical illustration of transforming the circle orientation and circle center.

$\{\mathcal{H}_1\}$ and frame $\{\mathcal{R}_0\}$.

Frame $\{\mathcal{H}_2\}$ is then introduced, as shown in Fig. 4.10(b), which has the same orientation as frame $\{\mathcal{R}_0\}$. A full rotation can be obtained through rotating of frame $\{\mathcal{H}_1\}$ by the **Y-X-Z** Cardan angles [65]. While the rotation about axis \mathbf{Y}_1 is not necessary since the function of this rotation has been obtained when locating the projection plane (i.e., defining frame $\{\mathcal{H}_1\}$). Therefore, the orientation of frame $\{\mathcal{H}_2\}$ with respect to frame $\{\mathcal{H}_1\}$ can be expressed as

$${}^{\mathcal{H}_1}_{\mathcal{H}_2}\mathbf{R} = \mathbf{R}_x(\theta)\mathbf{R}_z(\phi) \quad (4.25)$$

where θ and ϕ are rotational angles about axes \mathbf{X} and \mathbf{Z} , respectively. Normally, the value of θ is set as zero. The reason of introducing this parameter is to give the operator more freedom to tune the algorithm. The values of ϕ can be obtained by the estimate-and-tune process. Recall the method used to find the value of λ (Sec. 4.2 and Fig. 4.3), the tip trajectories of fingers 0 and 2 are now projected onto $\mathbf{X}_{H_1}\mathbf{Y}_{H_1}$ plane, as shown in Fig. 4.11. The best-fit line is then computed. If the robot opens its grasp, the tip trajectories of the right and left fingers will be symmetric, and parallel to \mathbf{X}_{R_0} -axis. Therefore, the angle between the best-fit line shown in Fig. 4.11 and \mathbf{X}_{H_1} -axis should be the optimal estimation of ϕ . Again, this value can be fine tuned by the operator according to his/her own feelings on intuitiveness.

Since frame $\{\mathcal{H}_2\}$ has the same orientation as the robot base frame $\{\mathcal{R}_0\}$, the orientation of the transformed virtual circle with respect to frame $\{\mathcal{R}_0\}$ can then be computed by

$${}^{\mathcal{R}_0}_{\mathcal{R}_c}\mathbf{R} = {}^{\mathcal{H}_2}_{\mathcal{H}_c}\mathbf{R} = {}^{\mathcal{H}_1}_{\mathcal{H}_2}\mathbf{R}^{-1} {}^{\mathcal{H}_1}_{\mathcal{H}_c}\mathbf{R} \quad (4.26)$$

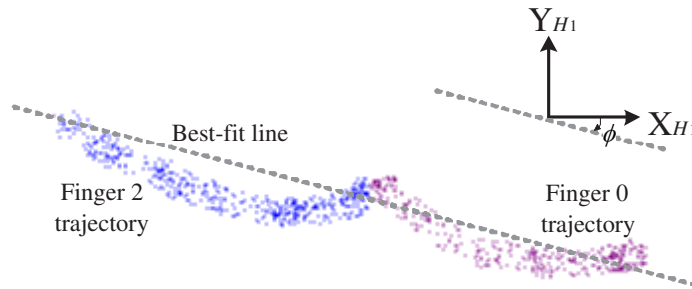


Figure 4.11: Graphical illustration of finding the value ϕ .

where ${}^{\mathcal{H}_1}_{\mathcal{H}_c}\mathbf{R}$ is given by Eq. (4.18); ${}^{\mathcal{H}_1}_{\mathcal{H}_2}\mathbf{R}^{-1}$ is the inverse of ${}^{\mathcal{H}_1}_{\mathcal{H}_2}\mathbf{R}$, which is given by Eq. (4.25).

4.3.3 Transformation of Circle Center Position

To address the transformation of the circle center, it is convenient to locate the two circles (human and robot) as shown in Fig. 4.10(a). The task now is to express the position of the shifted circle center of the human hand (C'_h) in frame $\{\mathcal{R}_0\}$. Two methods can be used to accomplish this task.

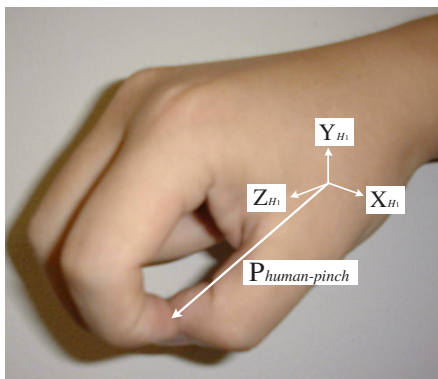
Refer to Fig. 4.10(a), the transformed circle center, i.e., circle center of the robot hand, can be expressed in frame $\{\mathcal{R}_0\}$ as

$${}^{\mathcal{R}_0}\mathbf{P}_{rc} = {}^{\mathcal{H}_1}_{\mathcal{R}_0}\mathbf{R}^{-1} {}^{\mathcal{H}_1}\mathbf{P}_{hc,shift} + {}^{\mathcal{R}_0}\mathbf{P}_{H_1ORG} \quad (4.27)$$

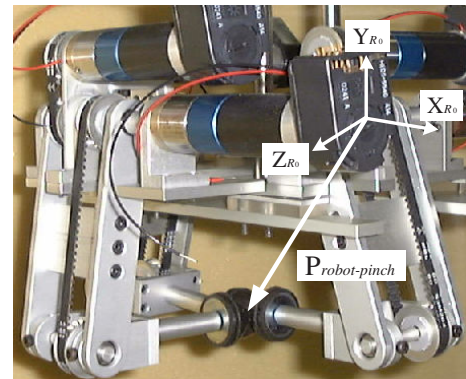
where ${}^{\mathcal{H}_1}_{\mathcal{R}_0}\mathbf{R} = {}^{\mathcal{H}_1}_{\mathcal{H}_2}\mathbf{R}$ is given by Eq. (4.25). The value for ${}^{\mathcal{R}_0}\mathbf{P}_{H_1ORG}$ can be obtained by an estimate-and-tune process.

A problem of applying Eq. (4.27) is that estimating the value for the vector ${}^{\mathcal{R}_0}\mathbf{P}_{H_1ORG}$ is not as straightforward as that for scalars. To avoid estimating a vector, the technique of defining the pinch-points of human and robot hands as the reference points, which was introduced in Griffin's work [31], is used in this work. As shown in Fig. 4.12, the pinch-points of the human hand and the robot hand are defined in such a way that the robot pinch-point should give the operator intuitive feeling that it is the counterpart of his/her pinch-point. Note that the human pinch-point should be projected to $\mathbf{X}_{H_1}\mathbf{Y}_{H_1}$ plane, since the robot pinch-point is in $\mathbf{X}_{R_0}\mathbf{Y}_{R_0}$ plane.

A new vector describing the shifted circle center position of the human hand relative



(a) Human pinch-point



(b) Robot pinch-point

Figure 4.12: Definition of the pinch-points of human and robot hands.

to the human pinch-point is then defined by

$$\mathbf{P}_{hc,shift,rel} = \mathbf{P}_{hc,shift} - \mathbf{P}_{human-pinch} \quad (4.28)$$

where the subscript “*rel*” means *relative*. The transformed circle center (i.e., circle center of the robot hand) can then be expressed in frame $\{\mathcal{R}_0\}$ as

$${}^{\mathcal{R}_0}\mathbf{P}_{rc} = {}^{\mathcal{H}_1}\mathbf{R}_0^{-1} {}^{\mathcal{H}_1}\mathbf{P}_{hc,shift,rel} + {}^{\mathcal{R}_0}\mathbf{P}_{robot-pinch} \quad (4.29)$$

where ${}^{\mathcal{H}_1}\mathbf{R}_0 = {}^{\mathcal{H}_1}\mathbf{R}$ is given by Eq. (4.25). It can be seen that defining the pinch-points instead of estimating the value for ${}^{\mathcal{R}_0}\mathbf{P}_{H_1ORG}$ in Eq. (4.27) simplifies the task.

The four sets of parameters have now been transformed to the robot frame. They are the circle radius r_{robot} , the central angles $\angle RC_rL$ and $\angle RC_rM$, the center position ${}^{\mathcal{R}_0}\mathbf{P}_{rc}$, and the orientation ${}^{\mathcal{R}_0}\mathbf{R}$. The last step is to compute the robot fingertip positions according to the transformed parameters.

4.4 Computation for Robot Positions

The positions of the robot fingertips are computed by two steps. Firstly, the positions with respect to frame $\{\mathcal{R}_c\}$ are computed. They are then computed with respect to frame $\{\mathcal{R}_0\}$.

Two possible cases of the resulted robot circles are shown in Figs. 4.13(a) and 4.13(b), respectively. The position vector of the robot right fingertip with respect to frame $\{\mathcal{R}_c\}$, $\mathbf{P}_{right-to-rc}$, is defined as shown in the figure. The subscript “*right-to-rc*” means “right fingertip relative to robot’s center”. Similarly, position vectors $\mathbf{P}_{left-to-rc}$ and $\mathbf{P}_{middle-to-rc}$ are defined. For both cases,

$${}^{\mathcal{R}_c}\mathbf{P}_{right-to-rc} = \begin{Bmatrix} r_{robot} \cos(\pi - \frac{1}{2}\angle RC_rL) \\ r_{robot} \sin(\pi - \frac{1}{2}\angle RC_rL) \\ 0 \end{Bmatrix} \quad (4.30)$$

$${}^{\mathcal{R}_c}\mathbf{P}_{left-to-rc} = \begin{Bmatrix} r_{robot} \cos(\pi + \frac{1}{2}\angle RC_rL) \\ r_{robot} \sin(\pi + \frac{1}{2}\angle RC_rL) \\ 0 \end{Bmatrix} \quad (4.31)$$

$${}^{\mathcal{R}_c}\mathbf{P}_{middle-to-rc} = \begin{Bmatrix} r_{robot} \cos(\pi - \frac{1}{2}\angle RC_rL + \angle RC_rM) \\ r_{robot} \sin(\pi - \frac{1}{2}\angle RC_rL + \angle RC_rM) \\ 0 \end{Bmatrix} \quad (4.32)$$

As illustrated in Fig. 4.13(c), the position of the robot right fingertip with respect to frame $\{\mathcal{R}_0\}$, \mathbf{P}_{right} , can then be computed and expressed in frame $\{\mathcal{R}_0\}$ by

$${}^{\mathcal{R}_0}\mathbf{P}_{right} = {}^{\mathcal{R}_0}\mathbf{R} {}^{\mathcal{R}_c}\mathbf{P}_{right-to-rc} + {}^{\mathcal{R}_0}\mathbf{P}_{rc} \quad (4.33)$$

Similarly,

$${}^{\mathcal{R}_0}\mathbf{P}_{left} = {}^{\mathcal{R}_0}\mathbf{R} {}^{\mathcal{R}_c}\mathbf{P}_{left-to-rc} + {}^{\mathcal{R}_0}\mathbf{P}_{rc} \quad (4.34)$$

$${}^{\mathcal{R}_0}\mathbf{P}_{middle} = {}^{\mathcal{R}_0}\mathbf{R} {}^{\mathcal{R}_c}\mathbf{P}_{middle-to-rc} + {}^{\mathcal{R}_0}\mathbf{P}_{rc} \quad (4.35)$$

The three fingertip positions of the robot hand are now obtained, and the flow chart of the algorithm is shown in Fig. 4.14. It is worth to point out that the optimal values

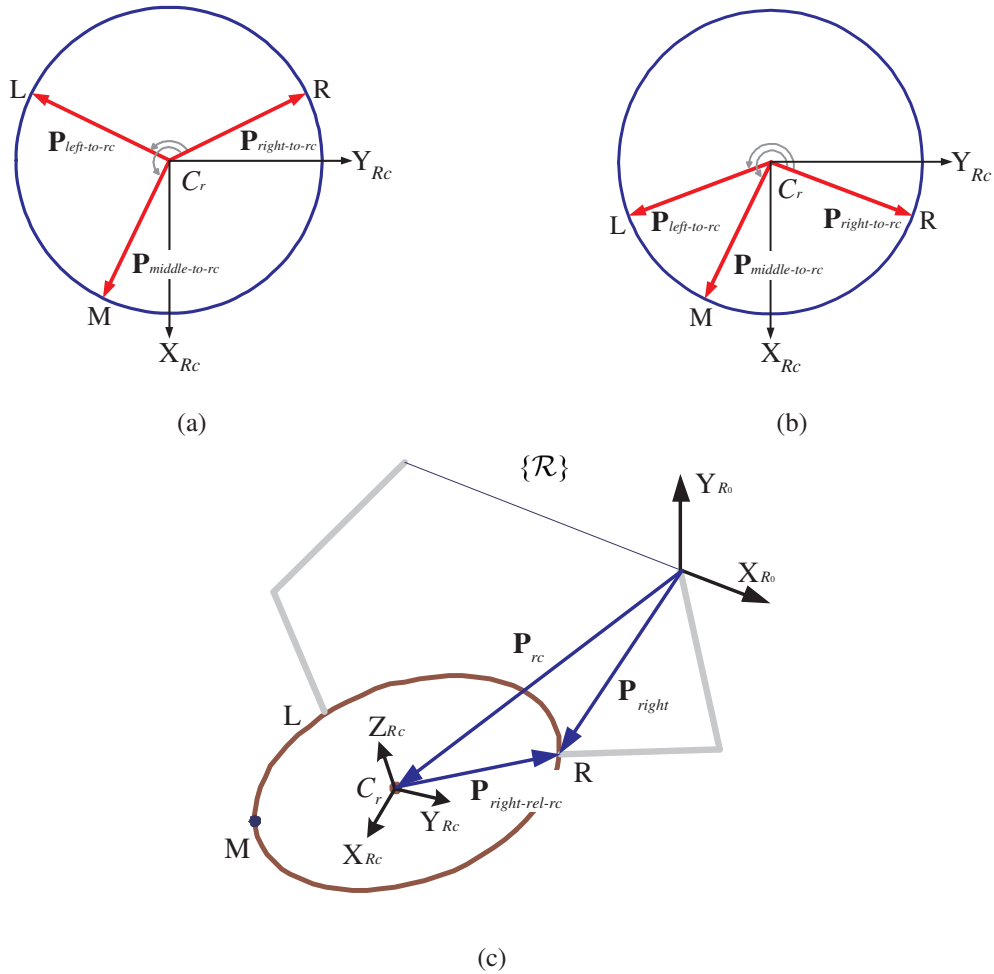


Figure 4.13: Graphical illustration of computing the fingertip positions of the robot hand (The middle finger is not shown for clarity).

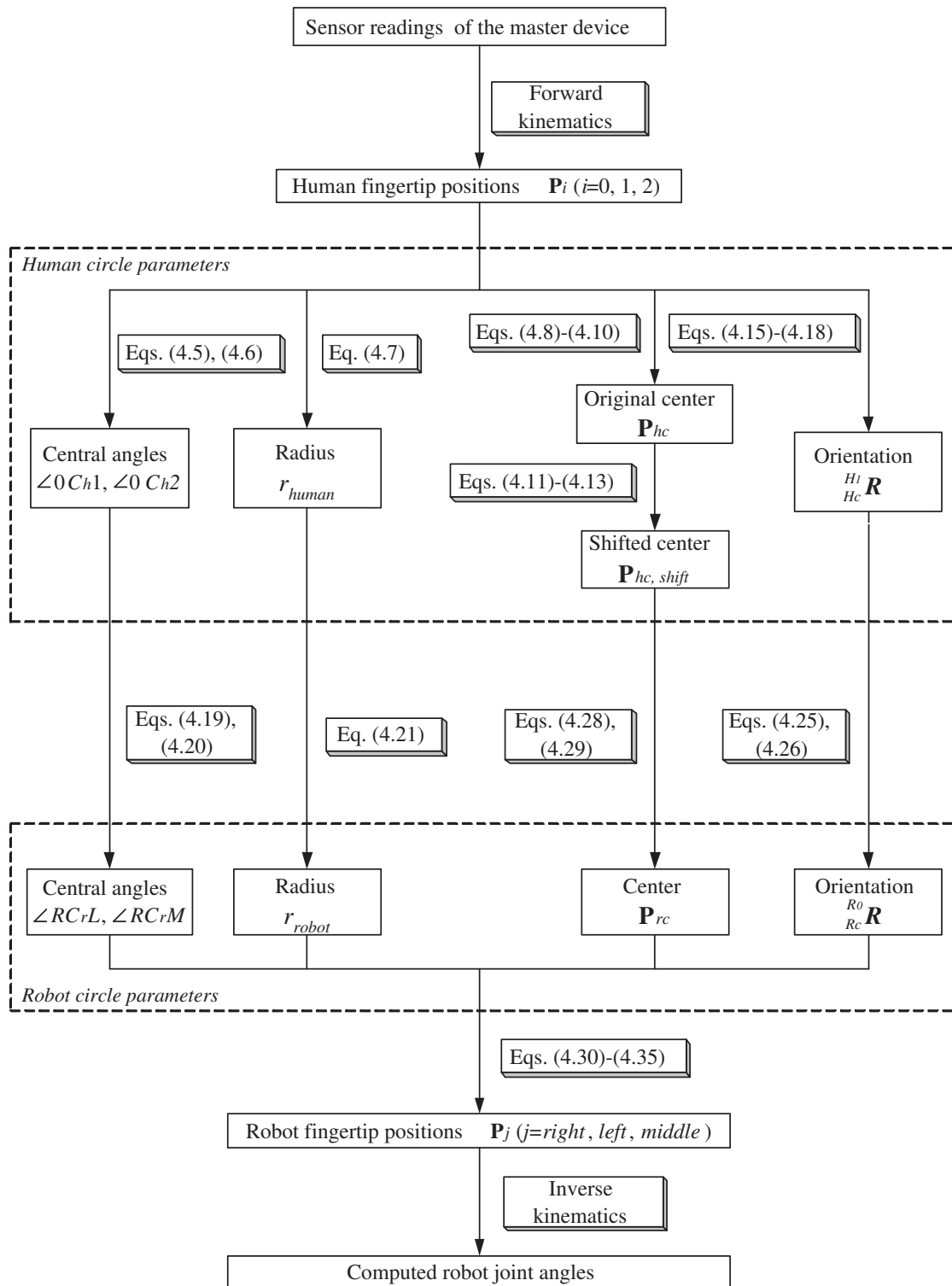


Figure 4.14: Flow chart of virtual circle mapping.

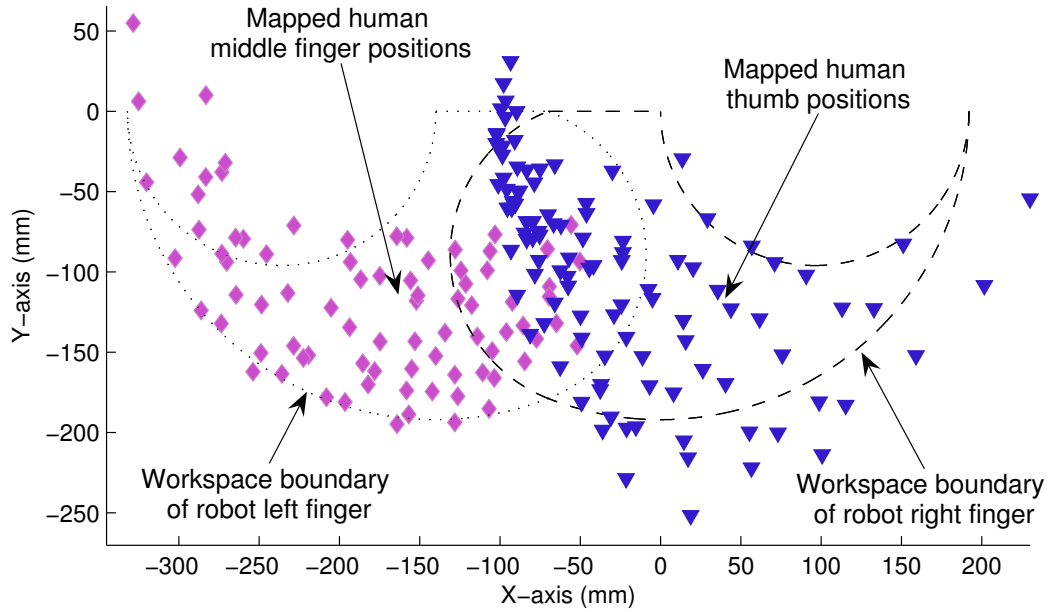


Figure 4.15: Mapping results of human thumb (finger 0) and middle finger (finger 2) by virtual circle mapping.

for the parameters of the virtual circle mapping usually vary for different operators by a small value, due to the subjectivity of the operators.

4.5 Mapping Results

The mapping results by simulation are presented in this section to show the advantages of the virtual circle mapping method when the robot hand is non-anthropomorphic. The results were obtained by programming the proposed algorithm in MATLABTM. The value of each joint angle of the human hand was chosen randomly over its motion range. The values of the parameters were chosen as $\delta = 43^\circ$; $s = 37mm$; $\lambda = 0.45$; $\phi = -12^\circ$; $\theta = 0$; and the strategy shown in Fig. 4.9(b) was used for K (so and μ) with $K_{max} = 2.85$. They were obtained by performing the estimation processes stated in previous sections on a specific operator, whose hand dimensions were used as the hand model parameters.

Figure 4.15 shows a set of mapping results of finger 0 and finger 2, the motions

of which are mapped into the workspace of the robot right and left fingers, respectively. Figure 4.16 shows the results of finger 1 in two perspectives, the motion of which is mapped into the workspace of the robot middle finger. The curves represent the workspace boundaries of the robot fingers, and the points represent the mapped positions of the human fingertips.

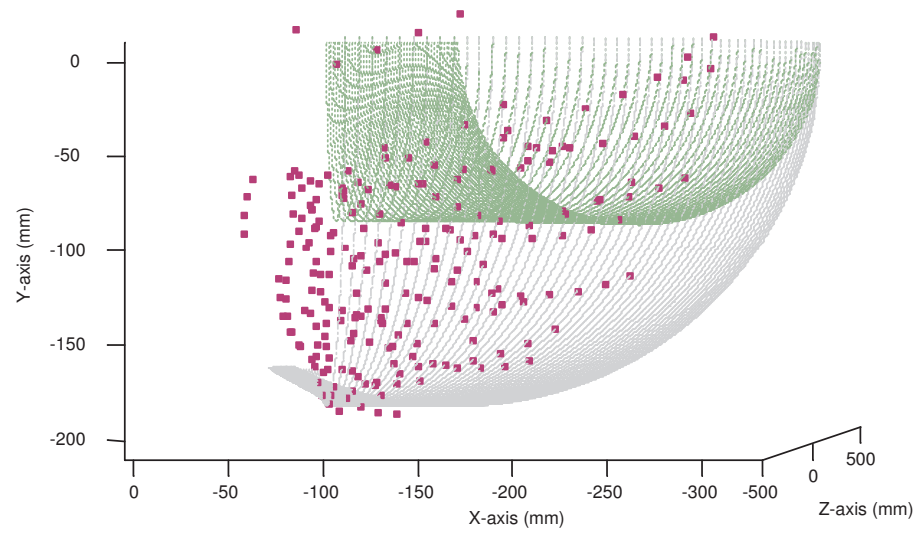
4.5.1 Discussion

The investigation performed in Chapter 3 has demonstrated that the achievable mapped positions of finger 0 can only be mapped to a relatively small region. While for both finger 0 and finger 2, the motions of the mapped positions are greatly expanded, and match the robot workspace much better by the virtual circle mapping method, as shown in Fig. 4.15. This feature will not only allow the operator to better utilize the robot's large workspace, but also provide the operator a higher degree of intuitiveness.

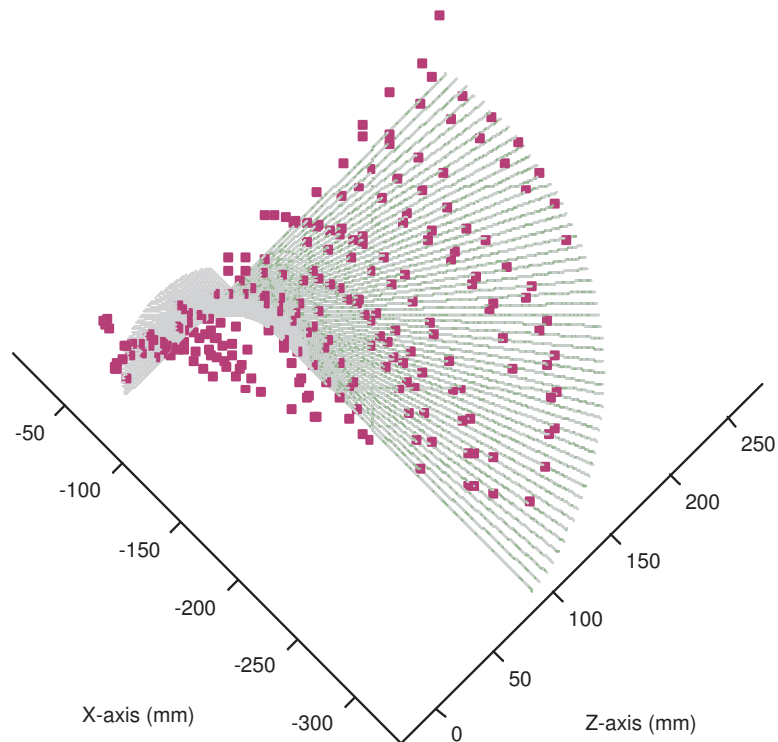
As addressed in Chapter 3, the motion of finger 1 is also mapped into a small region of the corresponding robot workspace by fingertip position mapping. While by virtual circle mapping, the motion is mapped into a much larger region, as shown in Fig. 4.16. One advantage is the better usage of the abduction/adduction motion of the robot middle finger (refer to Fig. 3.2). The other is the extension of the mapped positions along axis \mathbf{Z}_{R_0} . Similar to the mapping of finger 0, this feature will provide the operator a higher degree of intuitiveness compared to that by the fingertip position mapping.

Note that the workspace of the robot hand shown in Fig. 3.4 is different from that shown in Fig. 4.16. This is because of an assumption for virtual circle mapping, which is that the tip position of finger 1 remains away from $\mathbf{X}_{H_1}\mathbf{Y}_{H_1}$ plane (refer to Fig. 4.3) during the operation. Consequently, the tip position of the robot middle finger remains away from $\mathbf{X}_{R_0}\mathbf{Y}_{R_0}$ plane (refer to Fig. 3.2). As a result, the workspace of the robot middle finger is restricted by $\mathbf{X}_{R_0}\mathbf{Y}_{R_0}$ plane, as shown in Fig. 4.16. Since the virtual circle couples the three fingertip positions, this assumption was made to avoid considering the situations that the three tip positions are in a line and that the tip position of finger 1 locates behind $\mathbf{X}_{H_1}\mathbf{Y}_{H_1}$ plane. Actually, the assumption makes sense since the robot middle finger seldom pierces through $\mathbf{X}_{R_0}\mathbf{Y}_{R_0}$ plane during the grasp and manipulation tasks. However, the assumption was not made when applying the fingertip position mapping, because each finger was mapped independently.

Note that some of the mapped positions fall outside of the robot workspace. For a real operational system, extra algorithm should be developed to deal with this situation. A possible method is to find a suitable point within the workspace to substitute for each



(a) Viewpoint 1



(b) Viewpoint 2

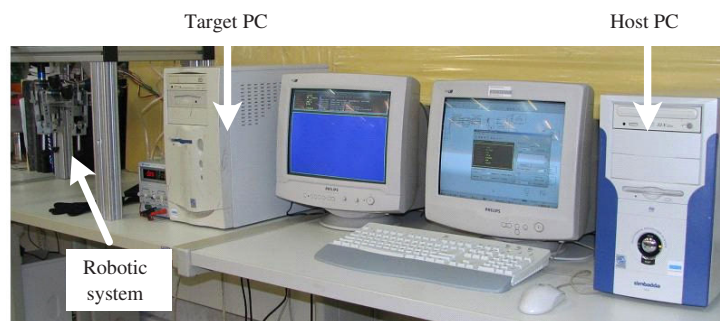
Figure 4.16: Mapping results of human index finger (finger 1) by virtual circle mapping.

out-of-workspace point.

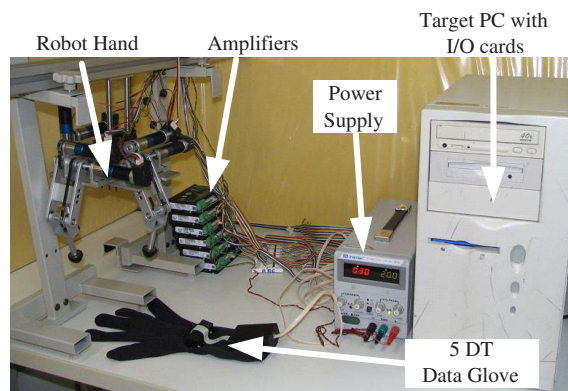
4.6 Experiments

By using xPC Target, a toolbox of MATLABTM, a real time motion control system was developed for experimental study of the mapping methods. xPC Target provides a high-performance, host-target prototyping environment that enables us to connect the Simulink models to physical systems and execute them in real time on PC compatible hardware.

The *5DT Data Glove 16-W* [109] was used as the hand master. The links of the robot hand were driven by DC motors with power amplifiers. The angular position of the joints were measured by encoders attached to the shafts of the motors. The I/O boards were plugged into the PCI bus of the target PC to read the encoder data and output analog signals to the amplifiers to control the motors. The developed test-bed is shown in Fig. 4.17. The detailed development of the test-bed is addressed in Appendix A, where a mechatronic approach is applied to construct the real time motion control system.



(a) The developed real time control system.



(b) The robotic system.

Figure 4.17: The developed test-bed for mapping.

Firstly, the experiments were performed to study the pose correspondence between the human hand and the robot hand. The experiment on the fingertip position mapping was first performed. Figure 4.18(a) shows a typical pose of the robot hand resulted from that of the human hand. As shown in the figure, when the human operator opened his grasp and extended the thumb, the robot right finger (corresponding to human thumb) was not able to move to the right position as expected. This conforms to the simulation result shown in Fig. 3.3. As seen, fingertip position mapping tends to supply little confidence to and thus frustrate the operator. The virtual circle mapping method was then applied. As shown in Fig. 4.18(b), for a similar human hand pose to the one shown in Fig. 4.18(a), the virtual circle mapping resulted a better robot hand pose with better pose similarities. Therefore, the virtual circle mapping produces higher degree of intuitiveness for the human operator. Two more examples of the pose correspondences by virtual circle mapping are shown in Fig. 4.19.

Next, the mapping results are discussed considering the grasping strategies. According to the work by Cutkosky and Howe [16], the human grasp can be categorized into power grasp and precision grasp (refer to Fig. 4.20). In power grasp, the object is



Figure 4.18: A comparison of typical human-robot correspondences by fingertip position mapping and virtual circle mapping.



Figure 4.19: Two additional examples of the human-robot correspondences by virtual circle mapping.

grasped by the whole hand. In other words, the force is applied on the object by some or all of the finger segments and the metacarpus. In precision grasp, the object is grasped by the fingertips. The precision grasp has higher level of dexterity, and is usually performed in the central area of the workspace. As such, both the fingertip position mapping and the virtual circle mapping are capable of the precision grasp. However, according to the results shown in Fig. 4.18(a), the robot hand by fingertip position mapping will fail to grasp large objects by power grasp, such as the circular prehensile power grasp as shown in Fig. 4.20, since the robot right finger cannot extend to the desired position as commanded by the human thumb. In contrast, Fig. 4.18(b) shows that the robot hand by virtual circle mapping is capable of power grasping a large object. The above analysis is also supported by the mapping results shown in Figs. 3.3 and 4.15. Therefore, besides the telemanipulation, the proposed virtual circle mapping has potential applications in the areas of the grasp/posture recognition, and the programming robot by demonstration, etc.

Finally, The computational time was investigated. The Pentium 4-1.8G CPU was used to perform the computation. If the whole mapping algorithm has the master sensor readings as the inputs, and the computed robot joint angles as the outputs, the measured computing time for one set of inputs was averagely 0.00112 s. The speed is fast enough for our system and other digitally controlled robotic systems.

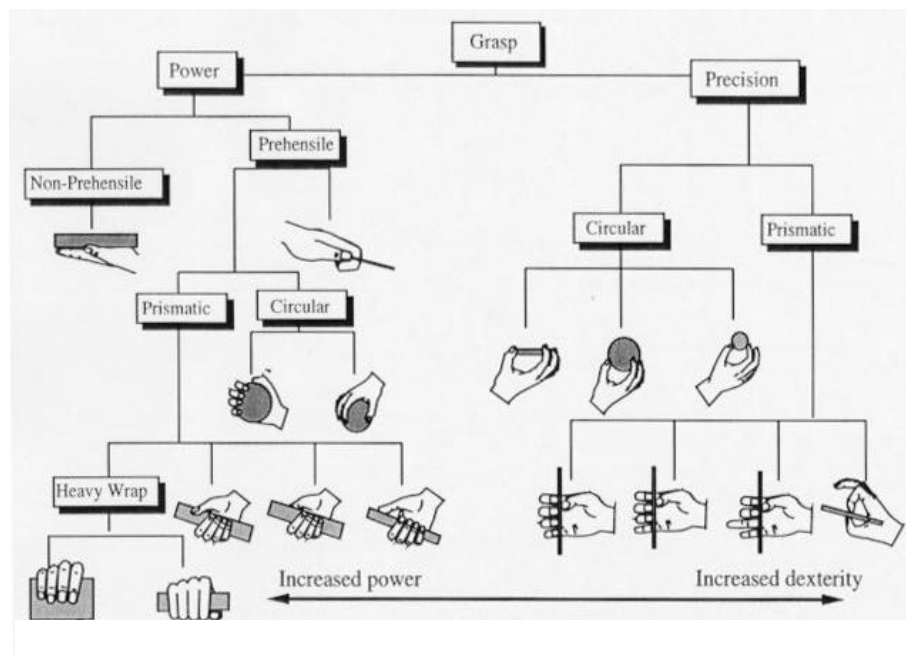


Figure 4.20: Hand grasp geometries (Adapted from [16]).

4.7 Concluding Remarks

A virtual circle mapping method is proposed for three-fingered master-slave hand systems. The concept of the method has first been introduced. The basic idea is to express the operator's motion by a virtual circle determined by his/her three fingertips. Four sets of parameters are used to describe the circle. The information of relative positions between the fingertips is delivered from the master to the slave by transforming the four sets of parameters from the human frame to the robot frame. The robot fingertip positions are then computed according to the transformed parameters. An algorithm for a specific three-fingered robot hand has been presented. The simulation results of the workspace matching have shown that the proposed method can account for the dissimilarities between the human hand and the robot hand, and therefore more effective for tele-controlling the non-anthropomorphic robot hands. The experiments demonstrated the feasibility of the proposed method.

Although the presented algorithm is specific for the non-anthropomorphic robot hand introduced in Sec. 3.1.2, the idea of virtual circle mapping is applicable for all kinds of three-fingered robot hands, both anthropomorphic and non-anthropomorphic. Since the manipulation tasks of some master-slave systems do not require the robot hand as complicated as the anthropomorphic hand, it is possible to replace the anthropomorphic robot hand in the system by a three-fingered non-anthropomorphic hand and apply the virtual circle method for mapping. By doing this, the cost of the system can be reduced.

PART II

CONTROL SCHEME DESIGN

Chapter 5

Investigation on Impedance Control

As addressed in Chapter 2, in the impedance control structure, it is not required to switch the control modes during the transition between the free space motion and the constrained motion. Many schemes have been proposed to deal with the problem of environment impedance uncertainties [48, 58, 64, 77, 84, 96] and robot dynamics uncertainties [9, 45, 46, 47, 78]. However, to our best knowledge, the force tracking performance in the case of external disturbances remains unaddressed. In fact, when the external disturbances exist, it is difficult to maintain the designed target impedance or to eliminate the target impedance error, even the nonlinear compensation schemes (such as the neural network technique used in [47]) are applied, in that the external disturbances are unpredictable by nature. Therefore, it is necessary to study the effects of the external disturbances to the force tracking performance.

This chapter investigates the force tracking performance of impedance control. In the following sections, the robot dynamic model considering the external disturbances is first given. The detailed implementation of the impedance control is then presented, followed by the analysis of the force tracking performance. The results are next verified by simulations. Finally, the insights obtained from the investigation are concluded.

5.1 Robot Dynamic Equations

The dynamic equation of an n -DOF manipulator is expressed in joint space as [15]

$$\mathbf{D}(\mathbf{q})\ddot{\mathbf{q}} + \mathbf{C}(\mathbf{q}, \dot{\mathbf{q}})\dot{\mathbf{q}} + \mathbf{G}(\mathbf{q}) = \boldsymbol{\tau} \quad (5.1)$$

where the vectors $\mathbf{q}, \dot{\mathbf{q}}, \ddot{\mathbf{q}} \in \mathbb{R}^n$ denote the joint angles, angular velocities, and angular accelerations, respectively, $\mathbf{D}(\mathbf{q}) \in \mathbb{R}^{n \times n}$ is the symmetric positive-definite inertia

matrix, $\mathbf{C}(\mathbf{q}, \dot{\mathbf{q}})\dot{\mathbf{q}} \in \mathbb{R}^n$ is the Coriolis and centrifugal torque, $\mathbf{G}(\mathbf{q}) \in \mathbb{R}^n$ is the gravitational torque, and $\tau \in \mathbb{R}^n$ is the actuator joint torque.

If considering the contact force with the environment and the external disturbances, the robot dynamics can be expressed as

$$\mathbf{D}(\mathbf{q})\ddot{\mathbf{q}} + \mathbf{C}(\mathbf{q}, \dot{\mathbf{q}})\dot{\mathbf{q}} + \mathbf{G}(\mathbf{q}) = \tau - \tau_e + \tau_{dist} \quad (5.2)$$

where $\tau_e \in \mathbb{R}^n$ represents the force exerted by the end-effector to the environment expressed in joint space, $\tau_{dist} \in \mathbb{R}^n$ denotes the external disturbance force acted on the end-effector expressed in joint space.

It is well known that when the end-effector contacts the environment, a task space coordinate system defined with reference to the environment is convenient for the study of contact motion. Let $\mathbf{X} \in \mathbb{R}^6$ be the task space vector representing the Cartesian position/orientation of the end-effector, which is defined by [40]

$$\mathbf{X} = L(\mathbf{q}) \quad (5.3)$$

where $L(\cdot) \in \mathbb{R}^n \rightarrow \mathbb{R}^6$ is the forward kinematics transformation describing the relation between the joint and task spaces. Then, the derivatives of \mathbf{X} are given as

$$\dot{\mathbf{X}} = \mathbf{J}(\mathbf{q})\dot{\mathbf{q}} \quad (5.4)$$

$$\ddot{\mathbf{X}} = \mathbf{J}(\mathbf{q})\ddot{\mathbf{q}} + \dot{\mathbf{J}}(\mathbf{q})\dot{\mathbf{q}} \quad (5.5)$$

where $\mathbf{J} = \partial L(\cdot)/\partial \mathbf{q} \in \mathbb{R}^{6 \times n}$ is the Jacobian matrix. Here it is assumed that \mathbf{J} is square and nonsingular (otherwise, pseudoinverse may be used to compute the inverse of the Jacobian matrix). The equation of motion can therefore be expressed in the task space as [15]

$$\mathbf{D}_x(\mathbf{q})\ddot{\mathbf{X}} + \mathbf{C}_x(\mathbf{q}, \dot{\mathbf{q}})\dot{\mathbf{X}} + \mathbf{G}_x(\mathbf{q}) = \mathbf{F} - \mathbf{F}_e + \mathbf{F}_{dist} \quad (5.6)$$

where

$$\mathbf{D}_x = \mathbf{J}^{T^{-1}} \mathbf{D} \mathbf{J}^{-1} \quad (5.7)$$

$$\mathbf{C}_x = \mathbf{J}^{T^{-1}} \left(\mathbf{C} \dot{\mathbf{q}} - \mathbf{D} \dot{\mathbf{J}}^{-1} \dot{\mathbf{q}} \right) \quad (5.8)$$

$$\mathbf{G}_x = \mathbf{J}^{T^{-1}} \mathbf{G} \quad (5.9)$$

$$\mathbf{F} = \mathbf{J}^{T^{-1}} \boldsymbol{\tau} \quad (5.10)$$

and $\mathbf{F}_e \in \mathbb{R}^6$ is the force exerted by the end-effector to the environment, $\mathbf{F}_{dist} \in \mathbb{R}^6$ denotes the external disturbance force acted on the end-effector. Note that the arguments are dropped for clarity. By defining

$$\mathbf{H}_x = \mathbf{C}_x + \mathbf{G}_x \quad (5.11)$$

Equation (5.6) becomes

$$\mathbf{D}_x \ddot{\mathbf{X}} + \mathbf{H}_x = \mathbf{F} - \mathbf{F}_e + \mathbf{F}_{dist} \quad (5.12)$$

Note that \mathbf{D}_x and \mathbf{H}_x in Eq. (5.12) can be estimated with a certain accuracy, while \mathbf{F}_{dist} is usually unpredictable.

In the following derivation and analysis, it is assumed that the robot is force controlled along all the degrees of freedom in the task space. Let \mathbf{F}_d denote the desired force input, then the function of the force tracking controller is to regulate the force \mathbf{F}_e to follow the desired value of \mathbf{F}_d , while the end-effector is interacting with the environment.

5.2 Performance Analysis of Impedance Control

5.2.1 Impedance Control Implementation

Impedance control is based on specifying a desired dynamic relationship between the position (or velocity) of the end-effector and the robot-environment interaction force¹ [40]. The impedance controller discussed in this work applies the target impedance as

$$\mathbf{M}_t \ddot{\mathbf{E}}_x + \mathbf{B}_t \dot{\mathbf{E}}_x + \mathbf{K}_t \mathbf{E}_x = \mathbf{F}_e \quad (5.13)$$

where $\mathbf{M}_t, \mathbf{B}_t, \mathbf{K}_t \in \mathbb{R}^{6 \times 6}$ are positive definite diagonal matrices representing the target inertia, damping, and stiffness, respectively; \mathbf{E}_x is the position error, which is given by

$$\mathbf{E}_x = \mathbf{X}_r - \mathbf{X} \quad (5.14)$$

¹The dynamic relationship in some works (e.g. [71]) was enforced between the position of the end-effector and the force error between the actual interaction force and the desired force.

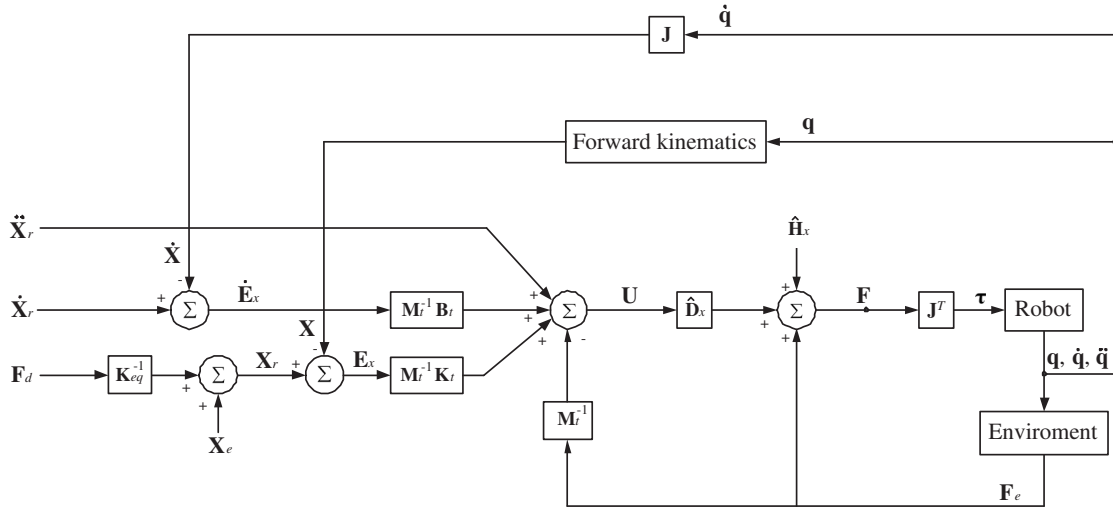


Figure 5.1: The impedance control structure.

with $\mathbf{X}_r \in \mathbb{R}^6$ denoting the reference trajectory input to the impedance controller. Equation (5.13) specifies a desired dynamic relationship between the position, velocity, and acceleration of the end-effector and the force exerted by the end-effector to the environment.

By virtue of the model-based computed torque technique, the impedance control law \mathbf{F} can be obtained by combining Eqs. (5.12), (5.13), and (5.14), which yields

$$\mathbf{F} = \hat{\mathbf{D}}_x \left[\ddot{\mathbf{X}}_r + \mathbf{M}_t^{-1} \left(\mathbf{B}_t \dot{\mathbf{E}}_x + \mathbf{K}_t \mathbf{E}_x - \mathbf{F}_e \right) \right] + \hat{\mathbf{H}}_x + \mathbf{F}_e \quad (5.15)$$

where $\hat{\mathbf{D}}_x$ and $\hat{\mathbf{H}}_x$ are the estimates of \mathbf{D}_x and \mathbf{H}_x , respectively; The value of \mathbf{F}_e is obtained by the force sensor. Note that the control law does not include \mathbf{F}_{dist} in view of its unpredictable nature. The control structure is shown in Fig. 5.1.

Substituting Eq. (5.15) into Eq. (5.12) yields the closed-loop position tracking error dynamic equation

$$\ddot{\mathbf{E}}_x + \mathbf{M}_t^{-1} \left(\mathbf{B}_t \dot{\mathbf{E}}_x + \mathbf{K}_t \mathbf{E}_x - \mathbf{F}_e \right) = \hat{\mathbf{D}}_x^{-1} \left(\Delta \mathbf{D}_x \ddot{\mathbf{X}} + \Delta \mathbf{H}_x - \mathbf{F}_{dist} \right) \quad (5.16)$$

where

$$\Delta \mathbf{D}_x = \mathbf{D}_x - \hat{\mathbf{D}}_x \quad (5.17)$$

$$\Delta \mathbf{H}_x = \mathbf{H}_x - \hat{\mathbf{H}}_x \quad (5.18)$$

It is easy to verify that the manipulator will behave to satisfy the target impedance specified by Eq. (5.13) if $\Delta \mathbf{D}_x = \Delta \mathbf{H}_x = \mathbf{F}_{dist} = \mathbf{0}$.

To regulate \mathbf{F}_e to track the desired force \mathbf{F}_d , \mathbf{X}_r should be properly designed, such that $\mathbf{F}_e = \mathbf{F}_d$ is achieved at steady state. The optimal value of \mathbf{X}_r is basically decided by the target impedance parameters and the environment stiffness. The environment dynamics is generally modeled as a linear system

$$\mathbf{F}_e = \mathbf{M}_e \ddot{\mathbf{X}} + \mathbf{B}_e \dot{\mathbf{X}} + \mathbf{K}_e (\mathbf{X} - \mathbf{X}_{eo}) \quad (5.19)$$

where $\mathbf{X}_{eo} \in \mathbb{R}^6$ is the known initial environment position, $\mathbf{M}_e, \mathbf{B}_e, \mathbf{K}_e \in \mathbb{R}^{6 \times 6}$ are positive definite diagonal matrices representing the environmental inertia, damping, and stiffness, respectively. In the following derivation, it is assumed that the end-effector maintains contact with the environment.

Combining Eqs. (5.13), (5.14), and (5.19) yields the dynamic equation regarding \mathbf{X}_r and \mathbf{X} as

$$\mathbf{M}_t (\ddot{\mathbf{X}}_r - \ddot{\mathbf{X}}) + \mathbf{B}_t (\dot{\mathbf{X}}_r - \dot{\mathbf{X}}) + \mathbf{K}_t (\mathbf{X}_r - \mathbf{X}) = \mathbf{M}_e \ddot{\mathbf{X}} + \mathbf{B}_e \dot{\mathbf{X}} + \mathbf{K}_e (\mathbf{X} - \mathbf{X}_{eo}) \quad (5.20)$$

At steady state, we have

$$\mathbf{K}_t (\mathbf{X}_r - \mathbf{X}) = \mathbf{K}_e (\mathbf{X} - \mathbf{X}_{eo}) \quad (5.21)$$

Solve Eq. (5.21) for \mathbf{X}

$$\mathbf{X} = (\mathbf{K}_t + \mathbf{K}_e)^{-1} (\mathbf{K}_t \mathbf{X}_r + \mathbf{K}_e \mathbf{X}_{eo}) \quad (5.22)$$

Considering the control objective $\mathbf{F}_e = \mathbf{F}_d$ and Eq. (5.13) at steady state, we have

$$\mathbf{F}_d = \mathbf{K}_t (\mathbf{X}_r - \mathbf{X}) \quad (5.23)$$

Substituting Eq. (5.22) into Eq. (5.23) and solving for \mathbf{X}_r yields the matrix form expression of the reference trajectory \mathbf{X}_r as²

$$\mathbf{X}_r = \mathbf{X}_{eo} + \mathbf{K}_e^{-1} (\mathbf{K}_e + \mathbf{K}_t) \mathbf{K}_t^{-1} \mathbf{F}_d \quad (5.24)$$

²The reference trajectory of a single degree of freedom, i.e., the scalar expression, has been given in [48] and [88].

5.2.2 Effects of External Disturbances

This section investigates the force tracking performance of the impedance controller with the presence of disturbances. Some insights are gained, which may guide the force tracking impedance controller design. More importantly, the analysis shows some inefficiencies of the impedance control if the robot is subject to uncertainties and external disturbances.

The force tracking error \mathbf{E}_f is first defined by

$$\mathbf{E}_f = \mathbf{F}_d - \mathbf{F}_e \quad (5.25)$$

A stiffness matrix \mathbf{K}_{eq} , called the equivalent matrix, is defined as

$$\mathbf{K}_{eq} = \mathbf{K}_t (\mathbf{K}_e + \mathbf{K}_t)^{-1} \mathbf{K}_e \quad (5.26)$$

Substituting Eqs. (5.25) and (5.26) into Eq. (5.24) yields

$$\mathbf{X}_r = \mathbf{X}_{eo} + \mathbf{K}_{eq}^{-1} (\mathbf{F}_e + \mathbf{E}_f) \quad (5.27)$$

Combining Eqs. (5.14), (5.16), (5.19), and (5.27) yields the force tracking error equation as

$$\begin{aligned} \mathbf{E}_f = & \left(\mathbf{K}_t \mathbf{K}_{eq}^{-1} \right)^{-1} \left[\left(\mathbf{M}_t + \mathbf{M}_e - \mathbf{K}_t \mathbf{K}_{eq}^{-1} \mathbf{M}_e + \mathbf{M}_t \hat{\mathbf{D}}_x^{-1} \Delta \mathbf{D}_x \right) \ddot{\mathbf{X}} \right. \\ & + \left(\mathbf{B}_t + \mathbf{B}_e - \mathbf{K}_t \mathbf{K}_{eq}^{-1} \mathbf{B}_e \right) \dot{\mathbf{X}} + \left(\mathbf{K}_t + \mathbf{K}_e - \mathbf{K}_t \mathbf{K}_{eq}^{-1} \mathbf{K}_e \right) (\mathbf{X} - \mathbf{X}_{eo}) \\ & \left. + \mathbf{M}_t \hat{\mathbf{D}}_x^{-1} (\Delta \mathbf{H}_x - \mathbf{F}_{dist}) \right] \end{aligned} \quad (5.28)$$

in which the condition of $\ddot{\mathbf{X}}_r = \dot{\mathbf{X}}_r = \mathbf{0}$ is assumed. Since matrices \mathbf{K}_t and \mathbf{K}_e are both diagonal by definition, it is easy to prove that

$$\mathbf{K}_t \mathbf{K}_{eq}^{-1} \mathbf{K}_e = \mathbf{K}_t \mathbf{K}_e^{-1} (\mathbf{K}_e + \mathbf{K}_t) \mathbf{K}_t^{-1} \mathbf{K}_e = \mathbf{K}_t + \mathbf{K}_e \quad (5.29)$$

Equation (5.28) is then simplified to

$$\mathbf{E}_f = \left(\mathbf{K}_t \mathbf{K}_{eq}^{-1} \right)^{-1} \left[\left(\mathbf{M}_t + \mathbf{M}_e - \mathbf{K}_t \mathbf{K}_{eq}^{-1} \mathbf{M}_e + \mathbf{M}_t \hat{\mathbf{D}}_x^{-1} \Delta \mathbf{D}_x \right) \ddot{\mathbf{X}} + \left(\mathbf{B}_t + \mathbf{B}_e - \mathbf{K}_t \mathbf{K}_{eq}^{-1} \mathbf{B}_e \right) \dot{\mathbf{X}} + \mathbf{M}_t \hat{\mathbf{D}}_x^{-1} \left(\Delta \mathbf{H}_x - \mathbf{F}_{dist} \right) \right] \quad (5.30)$$

Substituting Eq. (5.26) into Eq. (5.30) and setting all the time derivatives to zero yields the steady state force tracking error \mathbf{E}_{fss} as

$$\mathbf{E}_{fss} = \left[\mathbf{K}_e^{-1} \left(\mathbf{K}_e + \mathbf{K}_t \right) \right]^{-1} \mathbf{M}_t \mathbf{F}'_{dist} \quad (5.31)$$

with

$$\mathbf{F}'_{dist} = \hat{\mathbf{D}}_x^{-1} (\Delta \mathbf{H}_x - \mathbf{F}_{dist}) \quad (5.32)$$

Since $\hat{\mathbf{D}}_x$ is non-diagonal, and the values of its elements are dependent on \mathbf{q} , Eq. (5.32) implies the following two remarks.

Remark 1. The external disturbance force in any direction affects the force tracking error along the other degrees of freedom.

Remark 2. For the same parametric uncertainties of the robot model and external disturbances, the steady state force tracking error varies for different ending positions of the end-effector.

In practical situations, the external disturbances often exist. Remarks 1 and 2 reveal certain deficiencies of the impedance control in dealing with the external disturbances. For example, suppose the end-effector is commanded to move along a flat environment while maintaining the contact force. The surface of the environment most likely has different property at different locations. Therefore, according to Remark 1, the frictions along the position controlled degrees of freedom (which are treated as disturbances) always change and affect the force tracking performance along the force controlled degrees of freedom. In addition, Remark 2 shows that the force tracking error changes during the motion of the end-effector even the disturbances are constant.

Equation (5.31) implies the way to restrict the force tracking error within an acceptable range by appropriately selecting the values of the parameters \mathbf{K}_t and \mathbf{M}_t . Next let us examine Eq. (5.31). Since matrices \mathbf{M}_t , \mathbf{K}_t and \mathbf{K}_e are all diagonal, the force tracking error along a single degree of freedom can be expressed as

$$e_{fss} = \frac{m_t k_e}{k_e + k_t} f'_{dist} = \frac{m_t}{1 + \frac{k_t}{k_e}} f'_{dist} \quad (5.33)$$

where e_{fss} , m_t , k_t , k_e , and f'_{dist} are respectively the elements of \mathbf{E}_{fss} , \mathbf{M}_t , \mathbf{K}_t , \mathbf{K}_e , and \mathbf{F}'_{dist} , corresponding to a certain degree of freedom. Equation (5.33) implies Remarks 3 and 4 as follows.

Remark 3. To reduce the steady state force tracking error caused by the robot dynamics uncertainties and the external disturbances, larger values for the elements of \mathbf{K}_t and smaller values for the elements of \mathbf{M}_t are desirable.

Remark 4. For the same target impedance parameters of \mathbf{K}_t and \mathbf{M}_t , the environment with a different stiffness results in a different steady state force tracking error due to the robot dynamics uncertainties and external disturbances. The harder the environment, the larger the steady state error.

It is known that a small value for the target stiffness should be chosen when the end-effector is interacting with hard environments [2, 71]. However, Remarks 3 and 4 imply that when interacting with hard environments, with the presence of model uncertainties and external disturbances, the controller with a small value for the target stiffness may result in large steady state force tracking error. The conflicting design guidelines for choosing the target stiffness may bring the designer into a dilemma. It is therefore necessary to find an alternative means to reduce the force tracking error, rather than relying on adjusting the values of \mathbf{K}_t and \mathbf{M}_t . The control scheme proposed in Chapter 6 will solve the problem.

5.2.3 Effects of Environment Stiffness Uncertainty

The effects of the external disturbances to the force tracking performance is analyzed assuming that the environment stiffness is known or precisely estimated. In most cases, however, the environment stiffness is unknown or cannot be precisely estimated. The uncertainty of the environment stiffness also affects the force tracking performance of impedance control. Let $\hat{\mathbf{K}}_e$ denote the estimate of \mathbf{K}_e . According to Eq. (5.27), the reference trajectory is now calculated by

$$\mathbf{X}_r = \mathbf{X}_{eo} + \hat{\mathbf{K}}_{eq}^{-1}(\mathbf{F}_e + \mathbf{E}_f) \quad (5.34)$$

where

$$\hat{\mathbf{K}}_{eq} = \mathbf{K}_t \left(\hat{\mathbf{K}}_e + \mathbf{K}_t \right)^{-1} \hat{\mathbf{K}}_e \quad (5.35)$$

By virtue of Eq. (5.28), and setting $\Delta \mathbf{H}_x = \mathbf{F}_{dist} = \mathbf{0}$, the force tracking error equation in the case of imprecise environment stiffness is then obtained as

$$\begin{aligned} \mathbf{E}_f = & \left(\mathbf{K}_t \hat{\mathbf{K}}_{eq}^{-1} \right)^{-1} \left[\left(\mathbf{M}_t + \mathbf{M}_e - \mathbf{K}_t \hat{\mathbf{K}}_{eq}^{-1} \mathbf{M}_e + \mathbf{M}_t \hat{\mathbf{D}}_x^{-1} \Delta \mathbf{D}_x \right) \ddot{\mathbf{X}} \right. \\ & \left. + \left(\mathbf{B}_t + \mathbf{B}_e - \mathbf{K}_t \hat{\mathbf{K}}_{eq}^{-1} \mathbf{B}_e \right) \dot{\mathbf{X}} + \left(\mathbf{K}_t + \mathbf{K}_e - \mathbf{K}_t \hat{\mathbf{K}}_{eq}^{-1} \mathbf{K}_e \right) \left(\mathbf{X} - \mathbf{X}_{eo} \right) \right] \end{aligned} \quad (5.36)$$

At steady state, $\ddot{\mathbf{X}} = \dot{\mathbf{X}} = \mathbf{0}$, and the force tracking error in steady state is

$$\mathbf{E}_{fss} = \hat{\mathbf{K}}_{eq} \mathbf{K}_t^{-1} \left(\mathbf{K}_t + \mathbf{K}_e - \mathbf{K}_t \hat{\mathbf{K}}_{eq}^{-1} \mathbf{K}_e \right) \left(\mathbf{X} - \mathbf{X}_{eo} \right) \quad (5.37)$$

According to Eq. (5.19), the interaction force between the end-effector and the environment at steady state \mathbf{F}_{ess} is determined by

$$\mathbf{F}_{ess} = \mathbf{K}_e (\mathbf{X} - \mathbf{X}_{eo}) \quad (5.38)$$

Since

$$\mathbf{F}_{ess} = \mathbf{F}_d - \mathbf{E}_{fss} \quad (5.39)$$

combining Eqs. (5.38) and (5.39) yields

$$\mathbf{X} - \mathbf{X}_{eo} = \mathbf{K}_e^{-1} (\mathbf{F}_d - \mathbf{E}_{fss}) \quad (5.40)$$

The substitution of Eqs. (5.35) and (5.40) into (5.37) then yields the steady state force tracking error as

$$\mathbf{E}_{fss} = \mathbf{K}_t \left(\mathbf{K}_t \mathbf{K}_e^{-1} + \mathbf{I} \right)^{-1} \left(\mathbf{K}_e^{-1} - \hat{\mathbf{K}}_e^{-1} \right) \mathbf{F}_d \quad (5.41)$$

Since matrices \mathbf{K}_t , \mathbf{K}_e , and $\hat{\mathbf{K}}_e$ are all diagonal, the force tracking error along a single

degree of freedom can be expressed as

$$e_{fss} = \frac{\frac{1}{k_e} - \frac{1}{\hat{k}_e}}{\frac{1}{k_e} + \frac{1}{k_t}} f_d \quad (5.42)$$

where e_{fss} , k_t , k_e , \hat{k}_e , and f_d are respectively the elements of \mathbf{E}_{fss} , \mathbf{K}_t , \mathbf{K}_e , $\hat{\mathbf{K}}_e$, and \mathbf{F}_d , corresponding to a single degree of freedom. Equation (5.42) implies Remarks 5 and 6 as follows.

Remark 5. The force tracking error caused by the environment stiffness uncertainty increases when the force command \mathbf{F}_d increases.

Remark 6. To reduce the steady state force tracking error caused by the environment stiffness uncertainty, smaller values for the elements of \mathbf{K}_t are desirable.

An immediate observation is that Remark 6 implies a conflicting design guideline to the one implied by Remark 3. That is, to reduce the steady state force tracking error, higher value should be assigned to \mathbf{K}_t to reduce the effects of disturbances; however, higher values of \mathbf{K}_t increases the error caused by the environment stiffness uncertainty. Therefore, in the impedance control structure, it is not easy to select the right values for the components of \mathbf{K}_t in the case that both the disturbances and the environment uncertainties exist. To solve the problem, a combined impedance/direct control scheme is proposed in Chapter 6, which will be shown to be more robust to environment uncertainties and disturbances.

5.3 Computer Simulations

The computer simulations validate Remarks 1-6 given in Section 5.2. The simulations are performed for the model of a two degrees of freedom planar robotic finger with two rotational joints, $\mathbf{q} = [q_1, q_2]^T$. The units used in the simulations are: mN for force, mm for length/distance, mN·mm for torque, N/m for stiffness, N·s/m for damping coefficient, N·s²/m for target inertia, and radian for angle. The units are omitted in the following presentation for clarity. The robot dynamics is given in Eq. (5.2) with

$$\mathbf{D} = \begin{bmatrix} 955 & 285 \cos(q_1 - q_2) \\ 285 \cos(q_1 - q_2) & 208 \end{bmatrix} \quad (5.43)$$

$$\mathbf{C} = \begin{bmatrix} 285\dot{q}_2^2 \sin(q_1 - q_2) \\ 285\dot{q}_1^2 \sin(q_1 - q_2) \end{bmatrix} \quad (5.44)$$

$$\mathbf{G} = \begin{bmatrix} -109.196 \cos q_1 \\ -29.123 \cos q_2 \end{bmatrix} \times 10^3 \quad (5.45)$$

$$\mathbf{J} = \begin{bmatrix} -96 \sin q_1 & -96 \sin q_2 \\ -96 \cos q_1 & -96 \cos q_2 \end{bmatrix} \quad (5.46)$$

The modeled environment and the robotic finger are shown in Fig. 5.2. The reaction surface is oriented normal to the x -axis and is located such that $\mathbf{X}_{eo} = [0, 0]^T$. A spring-damper model is used for the environment along the x -axis. While along the y -axis, a damper model is used to simulate the friction force when the fingertip moves along the surface. The initial robot configuration is assigned to be $\mathbf{q} = [0.9515, 2.1686]^T$ (which corresponds to the Cartesian position $\mathbf{X} = [0, 0]^T$), and $\dot{\mathbf{q}} = [0, 0]^T$, such that the fingertip contacts with the surface with zero initial velocity and force.

5.3.1 Effects of External Disturbances

All the tasks in this section require the exertion of a desired contact force $\mathbf{F}_d = [100, 0]^T$ while maintaining the y -axis position, except that for validating *Remark 2*, which tracks a position trajectory.

The controller by Eq. (5.15) is simulated, and it is assumed that the robot dynamics is accurately estimated, i.e. $\Delta \mathbf{D}_x = \mathbf{0}$ and $\Delta \mathbf{H}_x = \mathbf{0}$. This assumption will not affect

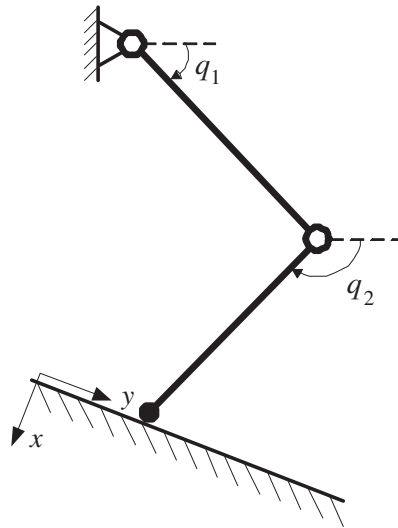


Figure 5.2: The robot finger model for simulation.

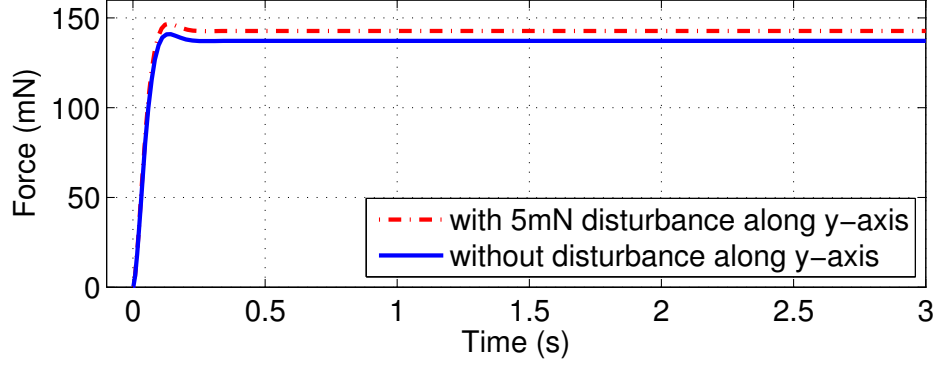


Figure 5.3: Simulation results of impedance control with parameter setting $\mathbf{K}_e = \text{diag}[10^2, 0]$, $\mathbf{B}_e = \text{diag}[2, 0.1]$, $\mathbf{M}_t = \text{diag}[1, 1]$, $\mathbf{B}_t = \text{diag}[40, 30]$, and $\mathbf{K}_t = \text{diag}[200, 10^4]$ verifying Remark 1.

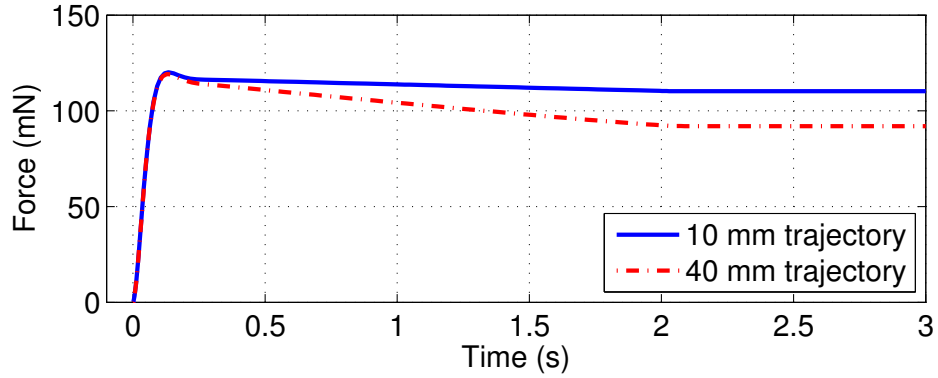
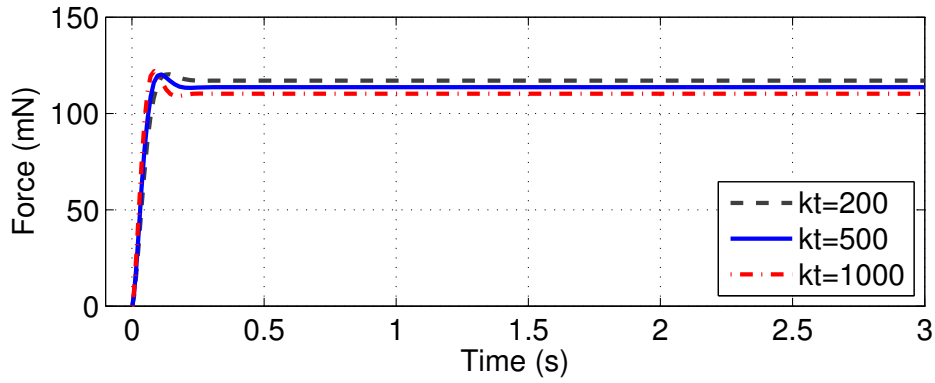
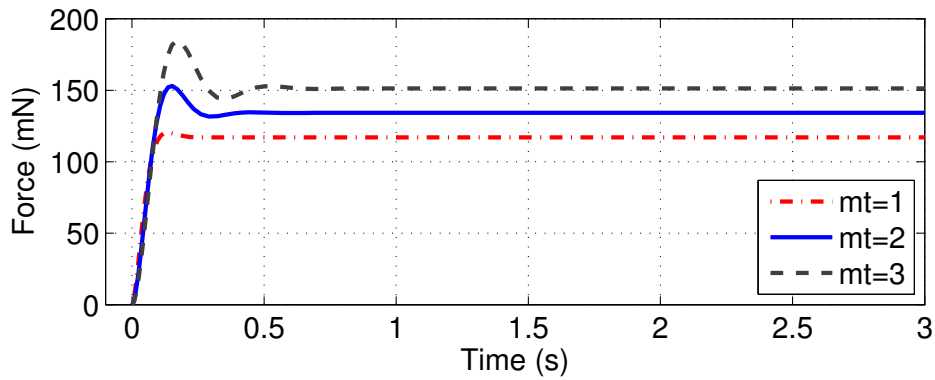


Figure 5.4: Simulation results of impedance control with parameter setting $\mathbf{K}_e = \text{diag}[10^3, 0]$, $\mathbf{B}_e = \text{diag}[2, 0.1]$, $\mathbf{M}_t = \text{diag}[1, 1]$, $\mathbf{B}_t = \text{diag}[50, 30]$, $\mathbf{K}_t = \text{diag}[200, 10^4]$, $\mathbf{F}_{dist} = [2, 2]^T$ verifying Remark 2.



(a) x -axis component of \mathbf{K}_t varied



(b) x -axis component of \mathbf{M}_t varied

Figure 5.5: Simulation results of impedance control verifying Remark 3. The parameters are set as $\mathbf{K}_e = \text{diag}[10^3, 0]$, $\mathbf{B}_e = \text{diag}[2, 0.1]$, $\mathbf{B}_t = \text{diag}[50, 30]$, and $\mathbf{F}_{dist} = [2, 2]^T$.

the validity of the simulations, since the effects of the estimated dynamics error is represented together with the external disturbance \mathbf{F}_{dist} in the simulation. Several results are shown in Figs. 5.3 to 5.6.

Figure 5.3 shows two force tracking curves with the disturbances to be $\mathbf{F}_{dist} = [5, 0]^T$ and $\mathbf{F}_{dist} = [5, 5]^T$, respectively. The parameters are chosen as $\mathbf{K}_e = \text{diag}[10^3, 0]$, $\mathbf{B}_e = \text{diag}[2, 0.1]$, $\mathbf{M}_t = \text{diag}[1, 1]$, $\mathbf{B}_t = \text{diag}[50, 30]$, and $\mathbf{K}_t = \text{diag}[200, 10^4]$. It can be seen that the existence of y -axis disturbance affects the force tracking performance along the x -axis, which conforms to Remark 1. With the same values of the parameters, Fig. 5.4 shows the results when the fingertip moves along the y -axis for 10 mm and 40 mm, respectively, with a ramp followed by a constant as the position command. The constant disturbance $\mathbf{F}_{dist} = [2, 2]^T$ is assumed. The results show that a different ending position results in a different force tracking error, as stated in Remark 2. For the same environment model, and setting $\mathbf{F}_{dist} = [2, 2]^T$, $\mathbf{M}_t = \text{diag}[1, 1]$, $\mathbf{B}_t = \text{diag}[60, 50]$,

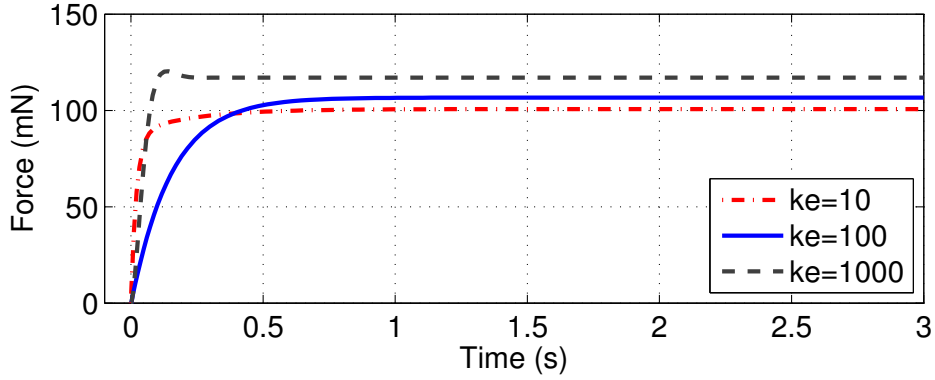


Figure 5.6: Simulation results of impedance control with parameter setting $\mathbf{B}_e = \text{diag}[2, 0.1]$, $\mathbf{M}_t = \text{diag}[1, 1]$, $\mathbf{B}_t = \text{diag}[50, 30]$, $\mathbf{K}_t = \text{diag}[200, 10^4]$, $\mathbf{F}_{dist} = [2, 2]^T$ verifying Remark 4.

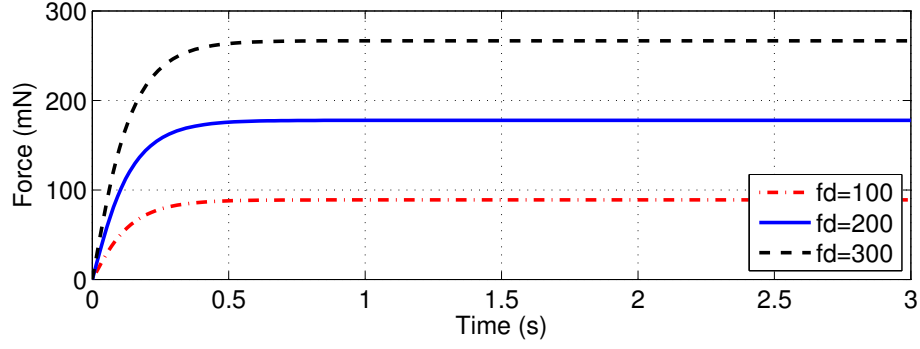
Fig. 5.5(a) shows three curves with different target stiffness. It can be seen that higher value of the target stiffness results in lower steady state force tracking error. In Fig. 5.5(b), the target stiffness is set as $\mathbf{K}_t = \text{diag}[200, 10^4]$, and the target inertia is varied. The curves show that a lower value of the target inertia results in a lower steady state force tracking error. Remark 3 is thus validated. In Fig. 5.6, the values of the parameters are set the same as in Fig. 5.3 except that \mathbf{K}_e is varied. As stated in Remark 4, the harder the environment, the larger the steady state error.

5.3.2 Effects of Environment Stiffness Uncertainty

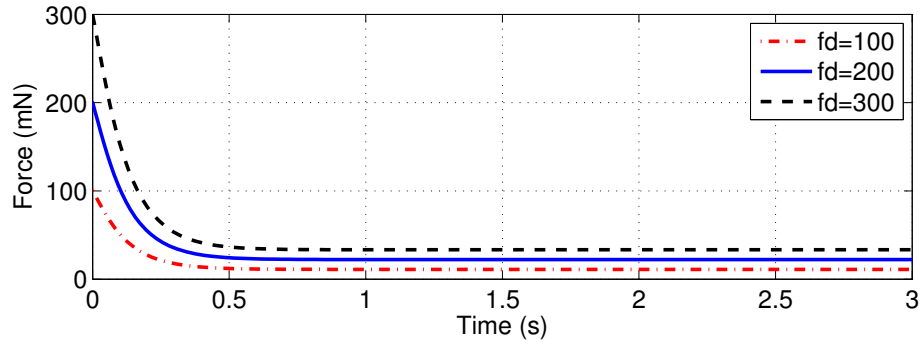
In this section, the effects of the environment stiffness uncertainty are studied by simulations, and thus Remarks 5 and 6 are verified. The controller by Eq. (5.15) is simulated, and it is assumed that no external disturbances exist, and the robot dynamics is accurately estimated, i.e. $\Delta \mathbf{D}_x = \Delta \mathbf{H}_x = \mathbf{F}_{dist} = \mathbf{0}$. The tasks in this section require the exertion of a desired contact force along the x -axis, while maintaining the position along the y -axis.

Figure 5.7 shows the responses to the three input force commands $\mathbf{F}_d = [100, 0]^T$, $\mathbf{F}_d = [200, 0]^T$, and $\mathbf{F}_d = [300, 0]^T$, respectively. The parameters are chosen as $\mathbf{K}_e = \text{diag}[10^2, 0]$, $\mathbf{B}_e = \text{diag}[2, 0.1]$, $\mathbf{M}_t = \text{diag}[1, 1]$, $\mathbf{B}_t = \text{diag}[40, 30]$, and $\mathbf{K}_t = \text{diag}[200, 10^4]$. The environment stiffness is supposed to be estimated 20% higher than the real value. It can be seen from Fig. 5.7(b) that when the force command is increased from 100 to 300, the steady state force tracking error also increases, which verifies Remark 5.

Setting the parameters as $\mathbf{K}_e = \text{diag}[10^2, 0]$, $\mathbf{B}_e = \text{diag}[2, 0.1]$, $\mathbf{M}_t = \text{diag}[1, 1]$,



(a) The force tracking curves



(b) The tracking error curves

Figure 5.7: Simulation results of impedance control verifying Remark 5. The environment stiffness is estimated 20% higher than the real value. The parameters are set as $\mathbf{K}_e = \text{diag}[10^2, 0]$, $\mathbf{B}_e = \text{diag}[2, 0.1]$, $\mathbf{M}_t = \text{diag}[1, 1]$, $\mathbf{B}_t = \text{diag}[40, 30]$, $\mathbf{K}_t = \text{diag}[200, 10^4]$, and $\mathbf{F}_{dist} = [0, 0]^T$.

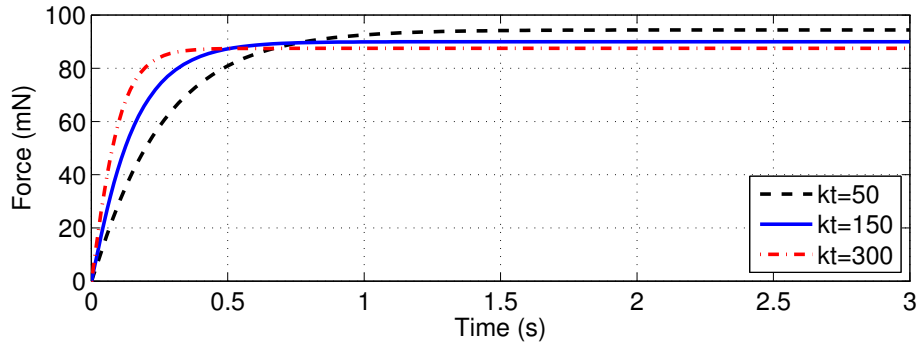


Figure 5.8: Simulation results of impedance control verifying Remark 6. The environment stiffness is estimated 20% higher than the real value. The parameters are set as $\mathbf{K}_e = \text{diag}[10^2, 0]$, $\mathbf{B}_e = \text{diag}[2, 0.1]$, $\mathbf{M}_t = \text{diag}[1, 1]$, $\mathbf{B}_t = \text{diag}[50, 30]$, $\mathbf{F}_{dist} = [0, 0]^T$, and $\mathbf{F}_d = [10^2, 0]^T$.

and $\mathbf{B}_t = \text{diag}[40, 30]$, Fig. 5.8 shows the responses to the force command $\mathbf{F}_d = [100, 0]^T$ with the target stiffness \mathbf{K}_t set as $\text{diag}[50, 10^4]$, $\text{diag}[150, 10^4]$, and $\text{diag}[300, 10^4]$, respectively. The results show that the response with $\mathbf{K}_t = \text{diag}[50, 10^4]$ has the lowest steady state force tracking error. When the value of the target stiffness is increased, the steady state error also increases. Remark 6 is thus verified.

It can also be observed from Fig. 5.8 that for the soft environment, e.g., $\mathbf{K}_e = \text{diag}[10^2, 0]$ in the simulation, a relatively large value of the target stiffness has a faster response. However, the negative effects due to the environment stiffness uncertainty prevents using a high target stiffness parameter.

5.4 Concluding Remarks

In this chapter, the force tracking performance of impedance control is investigated. In particular, the effects to the performance by the disturbances, and environmental uncertainties are studied. Several insights have been obtained and summarized in Remarks 1 to 6, which have been verified by simulations. These observations can provide some guides for the impedance controller design on the one hand. On the other hand, the deficiency of the force tracking performance gives rise to the development of a more robust control scheme. Moreover, it is desired to keep the advantage of impedance control, i.e., no need to switch the control modes for all task execution.

Chapter 6

Combined Impedance/Direct Control of Robot Manipulators

The investigation of impedance control presented in Chapter 5 has shown that large force tracking error may be present in the case of disturbances and the environment dynamics uncertainty. Equation (5.15) shows that, in the impedance control structure, the force feedback \mathbf{F}_e in the controller is used to realize the designed target impedance, in addition to compensating for the physically generated interaction force. We believe that the robustness to the disturbances and uncertainties of impedance control can be improved by further usage of the interaction force information than is used in the basic impedance control structure.

Before the presentation of the combined impedance/direct control, the problem of the control mode switch is first addressed by the example shown in Fig. 6.1, where the manipulator is approaching the environment along the x-axis of the task space. In the structure of the hybrid position/force control, the controller for the free space motion is different from that for the contact condition. The controller for the free space motion control is formulated by the PD control according to the position error, while the controller in contact condition is formulated by the PD control according to the force error. Once the end-effector starts to contact the environment from the free space motion, the controller is switched through a selection matrix, namely \mathbf{S} . In the structure of impedance control, the free space and the contact condition are treated in a unified way, such that a single controller is designed without the need to switch the control modes at any time.

This chapter presents a combined impedance/direct control scheme for control of robot manipulators. simulation and experimental results show that the proposed control

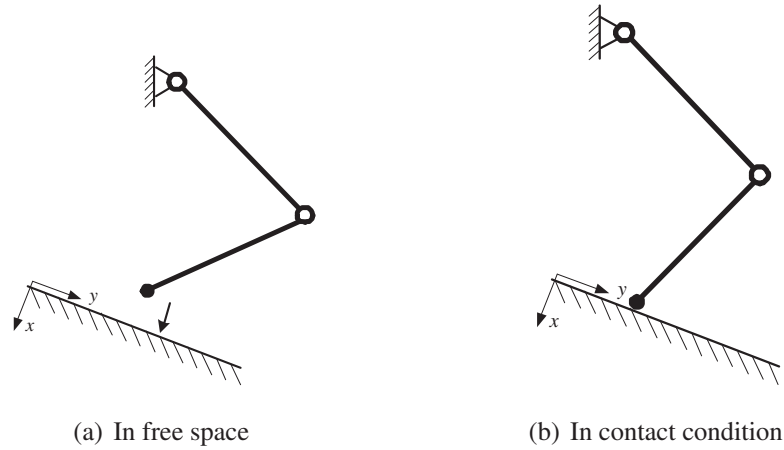


Figure 6.1: A manipulator approaching the environment.

scheme is more robust to robot model uncertainties, disturbance force and environment uncertainties than impedance control. In addition, unlike the hybrid position/force control, switching the control modes is not needed when the end-effector moves from free space to contact conditions, or vice versa.

In the following sections, the idea of combined impedance/direct control is first given, together with two implementing schemes. In particular, the time-delay control (TDC) based estimation technique is integrated into the second scheme for estimating the unknown dynamics. Next, a sufficient stability condition is given. Computer simulations are then conducted to demonstrate the superiority of the proposed control scheme over the impedance control, followed by the comprehensive experiments. Finally, the concluding remarks are addressed.

6.1 Scheme I: Direct Error Based Compensation

According to the above analysis, an immediate solution to the force tracking control is to incorporate an error based compensator into the basic impedance controller (shown in Eq. (5.15)), which can be expressed as

$$\mathbf{F} = \hat{\mathbf{D}}_x \mathbf{U} + \hat{\mathbf{H}}_x + \mathbf{F}_e + \mathbf{K}_p \mathbf{E}_f \quad (6.1)$$

in which

$$\mathbf{U} = \ddot{\mathbf{X}}_r + \mathbf{M}_t^{-1} (\mathbf{B}_t \dot{\mathbf{E}}_x + \mathbf{K}_t \mathbf{E}_x - \mathbf{F}_e) \quad (6.2)$$

where the force error \mathbf{E}_f has been defined in Eq. (5.25), the position error \mathbf{E}_x is defined

in Eq. (5.14), \mathbf{X}_r is the reference trajectory computed by Eq. (5.24), \mathbf{M}_t , \mathbf{B}_t , \mathbf{K}_t are the target parameters of impedance control, $\hat{\mathbf{D}}_x$ and $\hat{\mathbf{H}}_x$ are the estimates of \mathbf{D}_x and \mathbf{H}_x in the robot dynamics equation (5.12), and \mathbf{K}_p is a diagonal matrix.

Substituting Eq. (6.1) into Eq. (5.12) yields the closed loop system equation as

$$\mathbf{D}_x \left(\mathbf{U} - \ddot{\mathbf{X}} \right) + \mathbf{K}_p \mathbf{E}_f + \mathbf{F}_{dist} = \Delta \mathbf{D}_x \mathbf{U} + \Delta \mathbf{H}_x \quad (6.3)$$

where $\Delta \mathbf{D}_x$ and $\Delta \mathbf{H}_x$ have been given in Eqs. (5.17) and (5.18), respectively.

Combining Eqs. (5.14), (5.19), (5.25), (5.26), (5.27), (6.2), and (6.3), and assuming the condition $\ddot{\mathbf{X}}_r = \dot{\mathbf{X}}_r = \mathbf{0}$, we obtain the force tracking error equation of the proposed controller by Eq. (6.1) as

$$\begin{aligned} \mathbf{E}_f = & \left(\mathbf{K}_t \mathbf{K}_{eq}^{-1} + \mathbf{K}_p \mathbf{M}_t \hat{\mathbf{D}}_x^{-1} \right)^{-1} \left[\left(\mathbf{M}_t + \mathbf{M}_e - \mathbf{K}_t \mathbf{K}_{eq}^{-1} \mathbf{M}_e + \mathbf{M}_t \hat{\mathbf{D}}_x^{-1} \Delta \mathbf{D}_x \right) \ddot{\mathbf{X}} \right. \\ & \left. + \left(\mathbf{B}_t + \mathbf{B}_e - \mathbf{K}_t \mathbf{K}_{eq}^{-1} \mathbf{B}_e \right) \dot{\mathbf{X}} + \mathbf{M}_t \hat{\mathbf{D}}_x^{-1} \left(\Delta \mathbf{H}_x - \mathbf{F}_{dist} \right) \right] \end{aligned} \quad (6.4)$$

Let us examine the steady state force tracking error. Substituting Eq. (5.26) into Eq. (6.4), and setting $\ddot{\mathbf{X}} = \dot{\mathbf{X}} = \mathbf{0}$ yields the steady state force tracking error \mathbf{E}_{fss} as

$$\mathbf{E}_{fss} = \left[\mathbf{K}_e^{-1} \left(\mathbf{K}_e + \mathbf{K}_t \right) + \mathbf{K}_p \mathbf{M}_t \hat{\mathbf{D}}_x^{-1} \right]^{-1} \mathbf{M}_t \mathbf{F}'_{dist} \quad (6.5)$$

Where \mathbf{F}'_{dist} is given in Eq. (5.32). Equations (6.5) and (5.31) are then compared. In principle, since matrix $\hat{\mathbf{D}}_x$ is generally non-diagonal, it is not always true that the magnitudes of the components of \mathbf{E}_{fss} in Eq. (6.5) are smaller than those in Eq. (5.31). However, it should be pointed out that \mathbf{K}_p can be chosen with certain freedom. Therefore, a relative large value for the components of \mathbf{K}_p can be chosen such that the values of the components of the term $\mathbf{K}_p \mathbf{M}_t \hat{\mathbf{D}}_x^{-1}$ are always much larger than their corresponding components of the term $\mathbf{K}_e^{-1} (\mathbf{K}_e + \mathbf{K}_t)$, and as a result

$$\mathbf{K}_e^{-1} \left(\mathbf{K}_e + \mathbf{K}_t \right) + \mathbf{K}_p \mathbf{M}_t \hat{\mathbf{D}}_x^{-1} \approx \mathbf{K}_p \mathbf{M}_t \hat{\mathbf{D}}_x^{-1} \quad (6.6)$$

In this case, the steady state error can then be expressed as

$$\mathbf{E}_{fss} \approx \left(\mathbf{K}_p \mathbf{M}_t \hat{\mathbf{D}}_x^{-1} \right)^{-1} \mathbf{M}_t \mathbf{F}'_{dist} = \mathbf{K}_p^{-1} \hat{\mathbf{D}}_x \mathbf{F}'_{dist} \quad (6.7)$$

It can be seen that if the components of \mathbf{K}_p are large enough, the resulting steady state error by the proposed controller can be smaller than that by the impedance controller.

The oscillatory transient response may be induced, if an over large value is assigned to \mathbf{K}_p . In this case, a higher value of \mathbf{B}_t can be applied to increase damping to the system.

Furthermore, an integral term of the force tracking error can be introduced. The controller can then be expressed as

$$\mathbf{F} = \hat{\mathbf{D}}_x \mathbf{U} + \hat{\mathbf{H}}_x + \mathbf{F}_e + \mathbf{K}_p \mathbf{E}_f + \mathbf{K}_i \int_0^t \mathbf{E}_f dt \quad (6.8)$$

where the control parameter $\mathbf{K}_i \in \mathbb{R}^{6 \times 6}$ is again a diagonal matrix, and \mathbf{U} is given in (6.2). In the above analysis, $\ddot{\mathbf{X}}_r$ and $\dot{\mathbf{X}}_r$ are simply designed to be $\mathbf{0}$, while in a more general form, $\ddot{\mathbf{X}}_r$ and $\dot{\mathbf{X}}_r$ are included in the controller by (6.8).

Note that in the above analysis, it is assumed that the manipulator is force controlled along all the degrees of freedom. If position is required to be controlled along certain degrees of freedom, it is only needed to assign \mathbf{X}_d to \mathbf{X}_r , and $\mathbf{F}_d = \mathbf{0}$ for the components of the position controlled degrees of freedom, where \mathbf{X}_d is the desired position. Therefore, ideally, Eq. (6.8) holds for all cases since $\mathbf{E}_f = \mathbf{0}$ for the position controlled degrees of freedom.

A consideration is that, in the practical situation, friction may exist in the position controlled degrees of freedom. If the friction is large, the performance of the controller may be affected due to the term $(\mathbf{K}_p \mathbf{E}_f + \mathbf{K}_i \int_0^t \mathbf{E}_f dt)$ in Eq. (6.8). A possible strategy to solve the problem is that, the components of \mathbf{F}_e in the position controlled degrees of freedom are measured and assigned to the corresponding components of \mathbf{F}_d , such that $\mathbf{E}_f = \mathbf{0}$ always holds in the position controlled degrees of freedom.

The combined impedance/direct control law given in Eq. (6.8) (i.e., Scheme I) is composed of two parts, namely the direct force control action and the impedance control action. Besides the indirect regulation of the reference trajectory, the model uncertainties and the external disturbances are at the same time handled directly by the PI-type compensator. The control structure is shown in Fig. 6.2. On the other hand, since $\mathbf{E}_f = \mathbf{0}$ holds in free space motion, the controller becomes a pure impedance controller during the unconstrained motion. Therefore, it does not need to switch the control modes when the end-effector transmits between the unconstrained and constrained motions.

6.2 Scheme II: Indirect Error Based Compensation

This section proposes the second scheme of the combined impedance/direct control. By examining the steady state force tracking error by the impedance controller combined

Note that $\mathbf{D}_x = \hat{\mathbf{D}}_x + \Delta\mathbf{D}_x$ is used. From Eq. (6.9), \mathbf{H}'_x at time t can be represented as

$$\mathbf{H}'_x(t) = \mathbf{F}(t) - \hat{\mathbf{D}}_x(t)\ddot{\mathbf{X}}(t) - \mathbf{F}_e(t) \quad (6.11)$$

By assuming that the value of \mathbf{H}'_x does not change much during two consecutive sampling instances, the estimate of \mathbf{H}'_x , represented by $\hat{\mathbf{H}}'_x$, at time t , can be expressed as

$$\hat{\mathbf{H}}'_x(t) = \mathbf{F}(t - \delta) - \hat{\mathbf{D}}_x(t - \delta)\ddot{\mathbf{X}}(t - \delta) - \mathbf{F}_e(t - \delta) \quad (6.12)$$

Where δ is the sampling period, and $\ddot{\mathbf{X}} = \mathbf{J}\dot{\mathbf{q}} + \mathbf{J}\ddot{\mathbf{q}}$. The estimation relies on the previous values of \mathbf{F} , \mathbf{F}_e , $\hat{\mathbf{D}}_x$, \mathbf{q} and its derivatives. A shorter sampling period enables a more accurate estimation. Note that the proposed TDC estimator in Eq. (6.12) requires to estimate \mathbf{D}_x in advance, which can be achieved by the well established system identification techniques. Note that the acceleration sensors may be needed to measure the joint accelerations. If there are no acceleration sensors available, additional algorithm may be necessary to generate the estimated values of the joint accelerations, such as the central difference algorithm [42].

6.2.2 Controller Design

Although the TDC estimator can provide estimation of the nonlinear dynamics with less robot model information, it is not sufficient to guarantee the force tracking performance, especially when the external disturbance exists. The external disturbance force is changing randomly by nature, both the magnitude and direction. A controller with an compensator added to the impedance controller of Eq. (5.15) is proposed in this section to reject both the external (\mathbf{F}_{dist}) and the robot dynamics related ($\Delta\mathbf{H}_x$) disturbances.

The proposed control law can be expressed as

$$\mathbf{F} = \hat{\mathbf{D}}_x \mathbf{U} + \hat{\mathbf{H}}'_x + \mathbf{F}_e + \Phi \quad (6.13)$$

where Φ is the newly introduced compensator, and \mathbf{U} and $\hat{\mathbf{H}}'_x$ are given in Eqs. (6.2) and (6.12), respectively.

Substituting Eq. (6.13) into Eq. (5.12) yields the closed-loop equation as

$$\hat{\mathbf{D}}_x \mathbf{U} - \mathbf{D}_x \ddot{\mathbf{X}} + \Phi + \mathbf{F}_{dist} = \mathbf{H}_x - \hat{\mathbf{H}}'_x \quad (6.14)$$

From Eq. (6.10), We have

$$\begin{aligned}\hat{\mathbf{H}}'_x(t) &= \Delta \mathbf{D}_x(t - \delta) \ddot{\mathbf{X}}(t - \delta) + \mathbf{H}_x(t - \delta) \\ &= \Delta \mathbf{D}_x(t - \delta) \ddot{\mathbf{X}}(t - \delta) + \hat{\mathbf{H}}_x(t)\end{aligned}\quad (6.15)$$

Then $\mathbf{H}_x - \hat{\mathbf{H}}'_x$ at time t can be expressed as

$$\mathbf{H}_x - \hat{\mathbf{H}}'_x = \Delta \mathbf{H}_x - \Delta \mathbf{W}_x \quad (6.16)$$

where

$$\Delta \mathbf{W}_x(t) = \Delta \mathbf{D}_x(t - \delta) \ddot{\mathbf{X}}(t - \delta) \quad (6.17)$$

At steady state, $\Delta \mathbf{W}_x = \mathbf{0}$. Next, substituting Eq. (6.16) and $\mathbf{D}_x = \hat{\mathbf{D}}_x + \Delta \mathbf{D}_x$ into Eq. (6.14) yields

$$\hat{\mathbf{D}}_x \left(\mathbf{U} - \ddot{\mathbf{X}} + \mathbf{F}'_{dist} \right) - \Delta \mathbf{D}_x \ddot{\mathbf{X}} + \Phi + \Delta \mathbf{W}_x = \mathbf{0} \quad (6.18)$$

where \mathbf{F}'_{dist} is given in Eq. (5.32). Combining Eqs. (5.19), (5.24), (6.2), and (6.18), and assuming the condition $\ddot{\mathbf{X}}_r = \dot{\mathbf{X}}_r = \mathbf{0}$, we have

$$\begin{aligned}\mathbf{M}_t^{-1} \mathbf{K}_t \mathbf{K}_{eq}^{-1} \mathbf{E}_f + \hat{\mathbf{D}}_x^{-1} \Phi &= \mathbf{M}_t^{-1} \left(\mathbf{M}_t + \mathbf{M}_e - \mathbf{K}_t \mathbf{K}_{eq}^{-1} \mathbf{M}_e + \mathbf{M}_t \hat{\mathbf{D}}_x^{-1} \Delta \mathbf{D}_x \right) \ddot{\mathbf{X}} \\ &\quad + \mathbf{M}_t^{-1} \left(\mathbf{B}_t + \mathbf{B}_e - \mathbf{K}_t \mathbf{K}_{eq}^{-1} \mathbf{B}_e \right) \dot{\mathbf{X}} \\ &\quad - \hat{\mathbf{D}}_x^{-1} \Delta \mathbf{W}_x + \mathbf{F}'_{dist}\end{aligned}\quad (6.19)$$

where \mathbf{K}_{eq} is given in Eq. (5.26).

In order to derive a proper error based compensator Φ , we examine the steady state closed loop equation by setting $\ddot{\mathbf{X}} = \dot{\mathbf{X}} = \Delta \mathbf{W}_x = \mathbf{0}$ in Eq. (6.19), which yields

$$\mathbf{M}_t^{-1} \mathbf{K}_t \mathbf{K}_{eq}^{-1} \mathbf{E}_f + \hat{\mathbf{D}}_x^{-1} \Phi = \mathbf{F}'_{dist} \quad (6.20)$$

Substituting Eq. (5.26) into Eq. (6.20) yields

$$\mathbf{M}_t^{-1} \mathbf{K}_e^{-1} (\mathbf{K}_e + \mathbf{K}_t) \mathbf{E}_f + \hat{\mathbf{D}}_x^{-1} \Phi = \mathbf{F}'_{dist} \quad (6.21)$$

By observing the form of Eq. (6.21), and considering the control objective, which is to reduce the force tracking error caused by the disturbances, the error based compensator Φ can then be design as

$$\Phi = \mathbf{K}_p \hat{\mathbf{D}}_x \mathbf{E}_f \quad (6.22)$$

Substituting Eq. (6.22) back into Eq. (6.21) yields the steady state force tracking error as

$$\mathbf{E}_{fss} = \left[\mathbf{M}_t^{-1} \mathbf{K}_e^{-1} (\mathbf{K}_e + \mathbf{K}_t) + \mathbf{K}_p \right]^{-1} \mathbf{F}'_{dist} \quad (6.23)$$

where \mathbf{F}'_{dist} is given in Eq. (5.32). According to Eq. (6.23), the steady state force tracking error for a single degree of freedom can be expressed as

$$e_{fss} = \frac{m_t}{1 + \frac{k_t}{k_e} + k_p m_t} f'_{dist} \quad (6.24)$$

Comparing Eq. (6.24) with Eq. (5.33), we can find that the steady state force tracking error induced by the dynamic uncertainties and external disturbances can be reduced by introducing the compensator $\Phi = \mathbf{K}_p \hat{\mathbf{D}}_x \mathbf{E}_f$. As stated in Sec. 5.2.2, for the basic impedance control, a large error may be present in the case of contacting hard environments. While the proposed control law of Eq. (6.13) can greatly reduce the steady state error by assigning proper values to the components of \mathbf{K}_p .

It is known that, for the basic impedance control, the reference trajectory is computed according to the stiffness of the environment. As a result, if the environmental stiffness cannot be estimated accurately enough, a large force tracking error may be induced, which has been demonstrated in Chapter 5. While due to the error based compensator Φ , the proposed control law is more robust to the environment uncertainties than impedance control, which will be shown by simulations and experiments.

The compensator by Eq. (6.22) is basically a P-type compensator. An I-type compensator can also be introduced. Now the compensator Φ is rewritten as

$$\Phi = \hat{\mathbf{D}}_x \left(\mathbf{K}_p \mathbf{E}_f + \mathbf{K}_i \int_0^t \mathbf{E}_f dt \right) \quad (6.25)$$

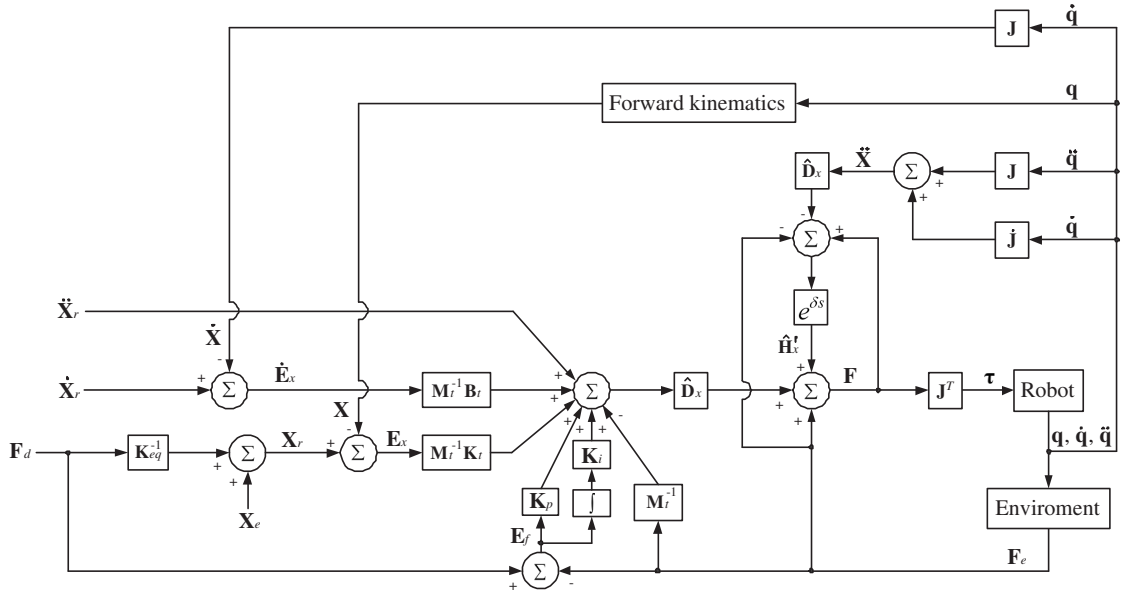


Figure 6.3: Control structure of the combined impedance/direct control Scheme II.

Substituting Eq. (6.25) into Eq. (6.13) yields the control law

$$\mathbf{F} = \hat{\mathbf{D}}_x \left(\mathbf{U} + \mathbf{K}_p \mathbf{E}_f + \mathbf{K}_i \int_0^t \mathbf{E}_f dt \right) + \hat{\mathbf{H}}'_x + \mathbf{F}_e \quad (6.26)$$

where \mathbf{E}_f , \mathbf{U} , and $\hat{\mathbf{H}}'_x$ are given in Eqs. (5.25), (6.2), and (6.12), respectively, and the interaction force \mathbf{F}_e is given by the readings of the force/torque sensor. Note that if the TDC estimation is not applied, Eq. (6.26) becomes

$$\mathbf{F} = \hat{\mathbf{D}}_x \left(\mathbf{U} + \mathbf{K}_p \mathbf{E}_f + \mathbf{K}_i \int_0^t \mathbf{E}_f dt \right) + \hat{\mathbf{H}}_x + \mathbf{F}_e \quad (6.27)$$

where $\hat{\mathbf{H}}_x$ is simply the estimation of \mathbf{H}_x , which is given in Eq. (5.11). The control structure of Scheme II is shown in Fig. 6.3. If there is friction along the position controlled degrees of freedom, the same strategy as for Scheme I can be applied, i.e., the components of \mathbf{F}_e in the position controlled degrees of freedom are measured and assigned to the corresponding components of \mathbf{F}_d .

The previous impedance controllers usually minimize the impedance error such that the input force command is tracked. However, the existence of the randomly changing unpredictable external disturbances usually cannot be accounted for. The proposed two combined impedance/direct control laws combine the advantages of both the impedance control and the direct force control. By properly incorporating a force error based PI-type compensator into the impedance controller, the model uncertainties and the external

disturbances are handled directly, which is the advantage of the direct force control. On the other hand, since $\mathbf{E}_f = \mathbf{0}$ holds in free space motion, the proposed controllers act as pure impedance controllers in the free space motion. Therefore, it does not need to switch the control modes when the end-effector transmits between the unconstrained and the constrained conditions, which is the advantage of impedance control.

6.3 Stability Analysis

In this section, the stability analysis of the proposed control Scheme II is performed. The stability of Scheme I can be analyzed in a similar manner.

By combining Eqs. (5.25), (6.19), and (6.25), the closed-loop equation can be rewritten as

$$\begin{aligned} & \left(\mathbf{M}_t^{-1} \mathbf{K}_t \mathbf{K}_{eq}^{-1} + \mathbf{K}_p \right) \left(\mathbf{F}_d - \mathbf{F}_e \right) + \mathbf{K}_i \int_0^t \left(\mathbf{F}_d - \mathbf{F}_e \right) dt \\ &= \mathbf{M}_t^{-1} \left(\mathbf{M}_t + \mathbf{M}_e - \mathbf{K}_t \mathbf{K}_{eq}^{-1} \mathbf{M}_e \right) \ddot{\mathbf{X}} \\ &+ \mathbf{M}_t^{-1} \left(\mathbf{B}_t + \mathbf{B}_e - \mathbf{K}_t \mathbf{K}_{eq}^{-1} \mathbf{B}_e \right) \dot{\mathbf{X}} + \mathbf{F}_{dist}'' \end{aligned} \quad (6.28)$$

where \mathbf{F}_{dist}'' represents the combination of the model uncertainty ($\Delta \mathbf{D}_x$ and $\Delta \mathbf{H}_x$) related disturbances and the external disturbances \mathbf{F}_{dist} , which is given by

$$\mathbf{F}_{dist}'' = \hat{\mathbf{D}}_x^{-1} \left(\Delta \mathbf{D}_x \ddot{\mathbf{X}} + \Delta \mathbf{H}_x - \mathbf{F}_{dist} - \Delta \mathbf{W}_x \right) \quad (6.29)$$

Under the assumption that \mathbf{F}_{dist}'' is bounded and linear for a sufficiently small deviation, Eq. (6.28) can be expressed in frequency domain as

$$\begin{aligned} & \left(\mathbf{M}_t^{-1} \mathbf{K}_t \mathbf{K}_{eq}^{-1} + \mathbf{K}_p + \frac{1}{s} \mathbf{K}_i \right) \left(\mathbf{F}_d(s) - \mathbf{F}_e(s) \right) \\ &= \mathbf{M}_t^{-1} \left(\mathbf{M}_t + \mathbf{M}_e - \mathbf{K}_t \mathbf{K}_{eq}^{-1} \mathbf{M}_e \right) s^2 \mathbf{X}(s) \\ &+ \mathbf{M}_t^{-1} \left(\mathbf{B}_t + \mathbf{B}_e - \mathbf{K}_t \mathbf{K}_{eq}^{-1} \mathbf{B}_e \right) s \mathbf{X}(s) + \mathbf{F}_{dist}''(s) \end{aligned} \quad (6.30)$$

where $\mathbf{F}_d(s)$, $\mathbf{F}_e(s)$, $\mathbf{F}_{dist}''(s)$, and $\mathbf{X}(s)$ are the Laplace transforms of \mathbf{F}_d , \mathbf{F}_e , \mathbf{F}_{dist}'' , and \mathbf{X} , respectively.

Next, taking the Laplace transform of Eq. (5.19) yields

$$\mathbf{F}_e(s) = \left(\mathbf{M}_e s^2 + \mathbf{B}_e s + \mathbf{K}_e \right) \left(\mathbf{X}(s) - \mathbf{X}_{eo}(s) \right) \quad (6.31)$$

Since all the matrices in Eq. (6.30) are diagonal, there is no coupling between the degrees of freedom. Without loss of generality, in the following, the stability is analyzed for a single degree of freedom. By virtue of Eqs. (6.30) and (6.31), we have

$$\begin{aligned} & \left[\left(k_p m_e + \frac{m_e}{m_t} + 1 \right) s^2 + \left(k_p b_e + k_i m_e + \frac{b_t + b_e}{m_t} \right) s \right. \\ & \left. + \left(k_p k_e + k_i b_e + \frac{k_t + k_e}{m_t} \right) + \frac{k_i k_e}{s} \right] X(s) \\ & = \left(k_p + \frac{k_i}{s} + \frac{k_t + k_e}{m_t k_e} \right) (m_e s^2 + b_e s + k_e) X_{eo}(s) \\ & \quad + \left(k_p + \frac{k_i}{s} + \frac{k_t + k_e}{m_t k_e} \right) F_d(s) - F''_{dist}(s) \end{aligned} \quad (6.32)$$

where $X(s)$, $X_{eo}(s)$, $F_d(s)$, and $F''_{dist}(s)$ are the Laplace transforms of one of the components of vectors \mathbf{X} , \mathbf{X}_{eo} , \mathbf{F}_d , and \mathbf{F}''_{dist} , respectively; and k_p , k_i , m_e , b_e , k_e , m_t , b_t , and k_t are the components of their corresponding matrices. Since the closed-loop system is linear, its stability can be discussed in terms of the stability of the unforced system. To achieve asymptotic stability, according to Hurwitz stability criteria, the parameters should satisfy

$$k_i k_e > 0 \quad (6.33)$$

$$k_p m_e + \frac{m_e}{m_t} + 1 > 0 \quad (6.34)$$

$$k_p b_e + k_i m_e + \frac{b_t + b_e}{m_t} > 0 \quad (6.35)$$

$$\left(k_p b_e + k_i m_e + \frac{b_t + b_e}{m_t} \right) \left(k_p k_e + k_i b_e + \frac{k_t + k_e}{m_t} \right) > k_i k_e \left(k_p m_e + \frac{m_e}{m_t} + 1 \right) \quad (6.36)$$

Inequality (6.36) can be rearranged as

$$\begin{aligned} & k_p b_e \left(\frac{k_t + 2k_e}{m_t} + k_p k_e + k_i b_e \right) + \frac{b_e}{m_t^2} (k_t + k_e) + \frac{k_i b_e}{m_t} (b_t + b_e) \\ & + k_i m_e \left(\frac{k_t}{m_t} + k_i b_e \right) + \frac{b_t}{m_t} \left(\frac{k_t + k_e}{m_t} + k_p k_e \right) - k_i k_e > 0 \end{aligned} \quad (6.37)$$

which implies a sufficient condition for asymptotic stability, i. e., all the parameters are positive, and inequality

$$\frac{b_t}{m_t} \left(\frac{k_t + k_e}{m_t} + k_p k_e \right) > k_i k_e \quad (6.38)$$

or

$$k_i m_t^2 - (k_p m_t + 1) b_t < \frac{b_t k_t}{k_e} \quad (6.39)$$

holds. Condition (6.39) is satisfied for any environment stiffness if

$$k_i m_t^2 < (k_p m_t + 1) b_t \quad (6.40)$$

Therefore, for the situations that the external disturbances and model uncertainties are bounded, and the environment can be modeled as a linear mass-damper-spring system, the proposed combined impedance/direct controller is asymptotically stable provided that all the control parameters are positive and inequality (6.40) is satisfied.

6.4 Computer Simulations

The effectiveness and advantages of the proposed combined impedance/direct control laws, both Schemes I and II, are demonstrated by computer simulations in this section. The same robot finger model (shown in Fig. 5.2) as in Chapter 5 is considered in this section. Similarly, the reaction surface of the environment is oriented normal to the x axis and is located such that $\mathbf{X}_{eo} = [0, 0]^T$. A spring-damper model is used for the environment along the x axis. While along the y axis, a damper model is used to simulate the friction force when the fingertip moves along the surface. The initial robot configuration is assigned to be $\mathbf{q} = [0.9515, 2.1686]^T$ (which corresponds to the Cartesian position $\mathbf{X} = [0, 0]^T$), and $\dot{\mathbf{q}} = [0, 0]^T$, such that the fingertip contacts the surface with zero initial force. Same as in the simulations of the impedance controller in Chapter 5, $\Delta \mathbf{D}_x = \mathbf{0}$ and $\Delta \mathbf{H}_x = \mathbf{0}$ are also assumed. The force commands for all the simulation tasks are set as $\mathbf{F}_d = [100, 0]^T$.

6.4.1 Results of Control Scheme I

Firstly, a constant disturbance $\mathbf{F}_{dist} = [2, 2]^T$ is assumed. Other parameters are set as $\mathbf{K}_e = \text{diag}[10^3, 0]$, $\mathbf{B}_e = \text{diag}[2, 0.1]$, $\mathbf{M}_t = \text{diag}[1, 1]$, $\mathbf{B}_t = \text{diag}[50, 30]$, $\mathbf{K}_t =$

$diag[200, 10^4]$, $\mathbf{K}_p = diag[50, 50]$, and $\mathbf{K}_i = diag[10, 10]$. Figure 6.4 shows the responses by the basic impedance controller and Scheme I of the proposed controller, respectively. It can be seen that the response of the proposed controller tracks the force command ($f_d = 100$) well, but the response of the basic impedance controller has a steady state error $e_{f_{ss}} \approx 19$ mN.

Secondly, the disturbance is assumed to be a randomly changing force signal $\mathbf{F}_{dist} = [r, r]^T$, where r is a random function with the amplitude of 10. Other parameters are set as $\mathbf{K}_e = diag[10^4, 0]$, $\mathbf{B}_e = diag[2, 0.1]$, $\mathbf{M}_t = diag[1, 1]$, $\mathbf{B}_t = diag[10^3, 30]$, $\mathbf{K}_t = diag[200, 10^4]$, $\mathbf{K}_p = diag[50, 50]$, and $\mathbf{K}_i = diag[10, 10]$. The responses of both controllers are shown in Fig. 6.5. It is clearly shown that the response of the proposed control law is superior to that of the basic impedance controller.

Finally, it is assumed that $\mathbf{F}_{dist} = \mathbf{0}$, $\mathbf{K}_e = diag[10^2, 0]$, $\mathbf{B}_e = diag[2, 0.1]$, and the environmental stiffness is estimated 50% higher than the real value. Set the parameters as $\mathbf{M}_t = diag[1, 1]$, $\mathbf{B}_t = diag[100, 30]$, $\mathbf{K}_t = diag[300, 10^4]$, $\mathbf{K}_p = diag[50, 50]$, and $\mathbf{K}_i = diag[10, 10]$. The responses shown in Fig. 6.6 demonstrate the robustness of the proposed control law to the environmental stiffness uncertainty.

6.4.2 Results of Control Scheme II

The performance of the proposed control Scheme II is studied by simulations in this section. Firstly, a constant disturbance is assumed, which is $\mathbf{F}_{dist} = [2, 2]^T$. Other parameters are set as $\mathbf{B}_e = diag[2, 0.1]$, $\mathbf{M}_t = diag[1, 1]$, $\mathbf{B}_t = diag[50, 30]$, $\mathbf{K}_t =$

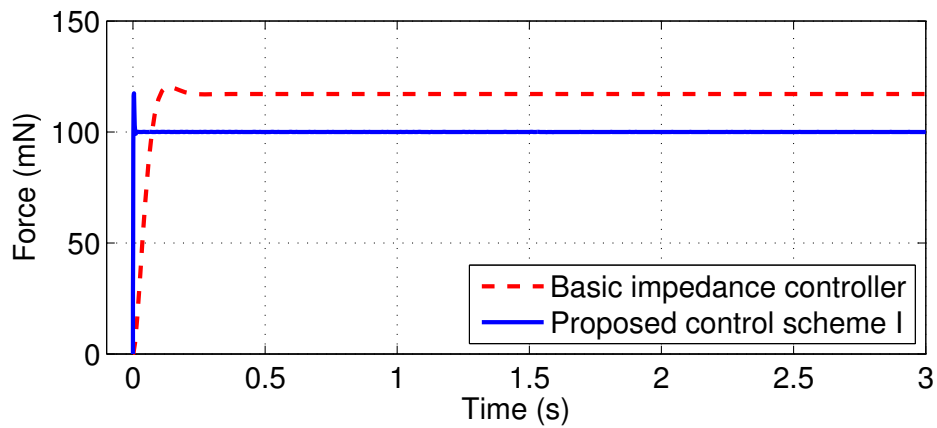


Figure 6.4: Responses of the combined impedance/direct control Scheme I in the case of constant external disturbances ($\mathbf{K}_e = diag[10^3, 0]$, $\mathbf{B}_e = diag[2, 0.1]$, $\mathbf{M}_t = diag[1, 1]$, $\mathbf{B}_t = diag[50, 30]$, $\mathbf{K}_t = diag[200, 10^4]$, $\mathbf{K}_p = diag[50, 50]$, $\mathbf{K}_i = diag[10, 10]$, $\mathbf{F}_{dist} = [2, 2]^T$).

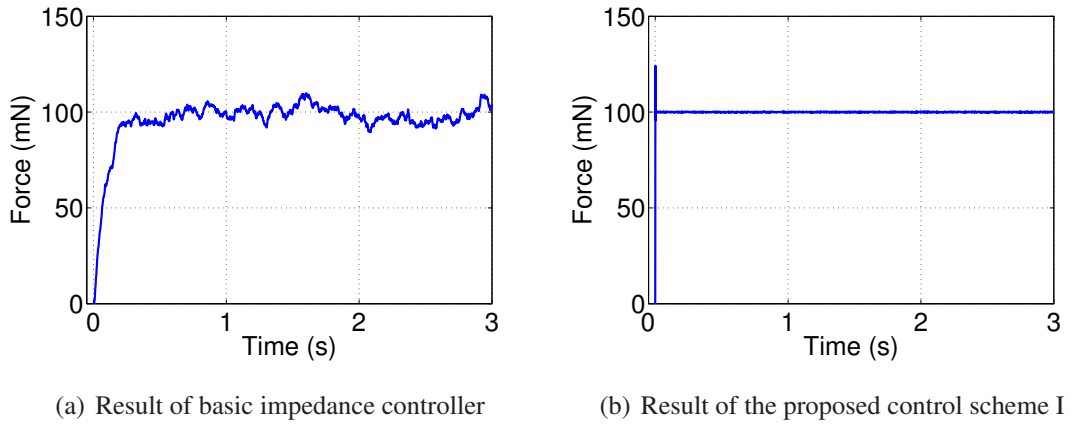


Figure 6.5: Responses of the combined impedance/direct control Scheme I in the case of hard environments and random disturbances ($\mathbf{K}_e = \text{diag}[10^4, 0]$, $\mathbf{B}_e = \text{diag}[2, 0.1]$, $\mathbf{M}_t = \text{diag}[1, 1]$, $\mathbf{B}_t = \text{diag}[10^3, 30]$, $\mathbf{K}_t = \text{diag}[200, 10^4]$, $\mathbf{K}_p = \text{diag}[50, 50]$, $\mathbf{K}_i = \text{diag}[10, 10]$, $\mathbf{F}_{dist} = [r, r]^T$, where r is a random function with the amplitude of 10).

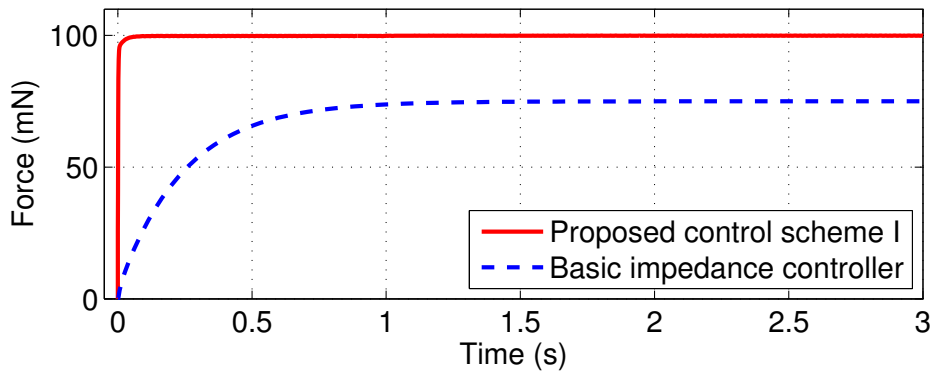
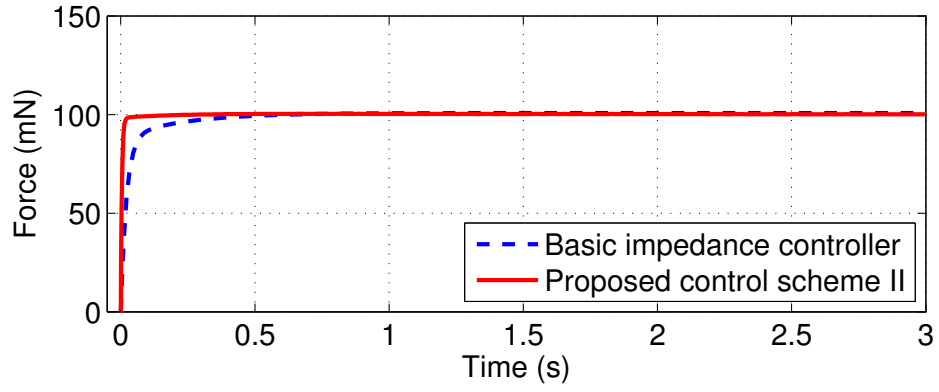
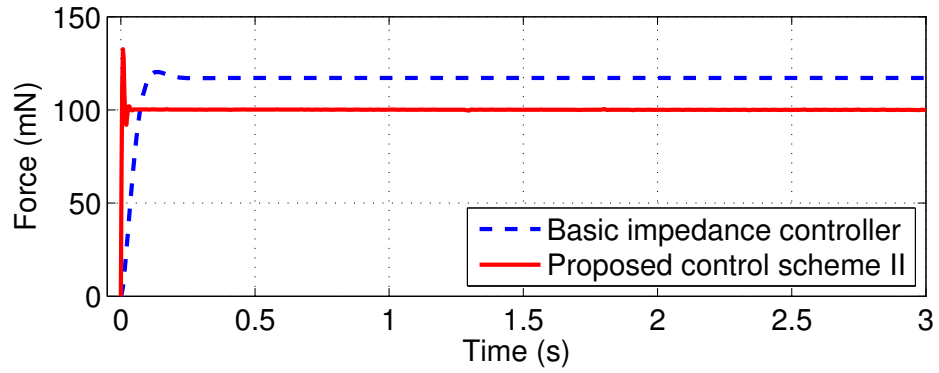


Figure 6.6: Responses of the combined impedance/direct control Scheme I in the case of environmental stiffness uncertainty ($\mathbf{K}_e = \text{diag}[10^2, 0]$ with 50% estimation uncertainty, $\mathbf{B}_e = \text{diag}[2, 0.1]$, $\mathbf{M}_t = \text{diag}[1, 1]$, $\mathbf{B}_t = \text{diag}[100, 30]$, $\mathbf{K}_t = \text{diag}[300, 10^4]$, $\mathbf{K}_p = \text{diag}[50, 50]$, $\mathbf{K}_i = \text{diag}[10, 10]$, $\mathbf{F}_{dist} = [0, 0]^T$).



(a) $k_e = 10$



(b) $k_e = 10^3$

Figure 6.7: Responses of the combined impedance/direct control Scheme II in the case of constant external disturbances ($\mathbf{B}_e = \text{diag}[2, 0.1]$, $\mathbf{M}_t = \text{diag}[1, 1]$, $\mathbf{B}_t = \text{diag}[50, 30]$, $\mathbf{K}_t = \text{diag}[200, 10^4]$, $\mathbf{K}_p = \text{diag}[100, 100]$, and $\mathbf{K}_i = \text{diag}[80, 80]$, $\mathbf{F}_{dist} = [2, 2]^T$).

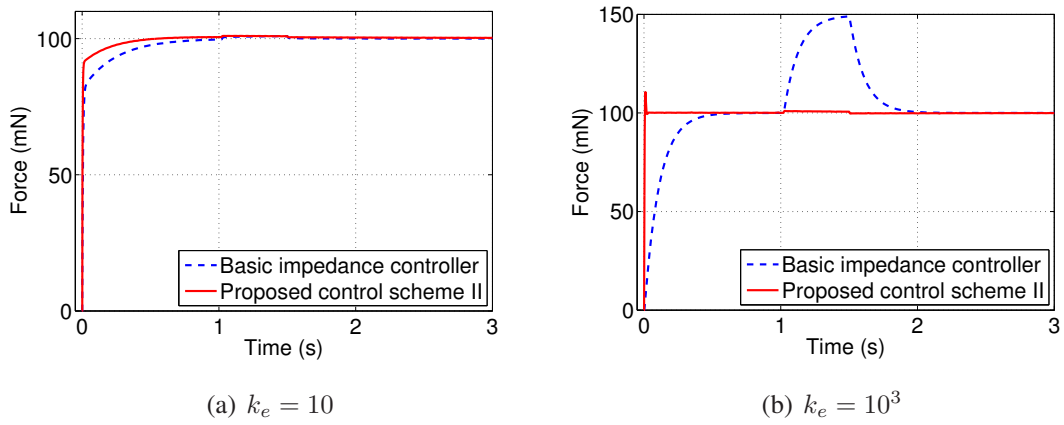


Figure 6.8: Responses of the combined impedance/direct control Scheme II in the case of a pulse external disturbance ($\mathbf{B}_e = \text{diag}[2, 0.1]$, $\mathbf{M}_t = \text{diag}[1, 1]$, $\mathbf{B}_t = \text{diag}[200, 30]$, $\mathbf{K}_t = \text{diag}[800, 10^4]$, $\mathbf{K}_p = \text{diag}[100, 100]$, and $\mathbf{K}_i = \text{diag}[80, 80]$, $\mathbf{F}_{dist} = [p, 0]^T$, where p is a pulse function with the amplitude of 10 between $t = 1$ s and $t = 1.5$ s).

$\text{diag}[200, 10^4]$, $\mathbf{K}_p = \text{diag}[100, 100]$, and $\mathbf{K}_i = \text{diag}[80, 80]$. Figure 6.7 shows the responses by the basic impedance controller and the proposed controller for $k_e = 10$ and $k_e = 10^3$, respectively. It can be seen that the responses of the proposed controller track the force command ($f_d = 100$) well. The performance of the impedance controller is satisfactory when the environment is soft ($k_e = 10$). However, the basic impedance controller results in steady state error $e_{fss} \approx 20$ mN when $k_e = 10^3$.

Secondly, a pulse disturbance is assumed, which is $\mathbf{F}_{dist} = [p, 0]^T$, where p is a pulse function with the amplitude of 10 starting at $t = 1$ s and ending at $t = 1.5$ s. Other parameters are set as $\mathbf{B}_e = \text{diag}[2, 0]$, $\mathbf{M}_t = \text{diag}[1, 1]$, $\mathbf{B}_t = \text{diag}[200, 30]$, $\mathbf{K}_t = \text{diag}[800, 10^4]$, $\mathbf{K}_p = \text{diag}[100, 100]$, and $\mathbf{K}_i = \text{diag}[80, 80]$. Figure 6.8 shows the responses for $k_e = 10$ and $k_e = 10^3$, respectively. As shown in Fig. 6.8(a), both controllers can reject the pulse disturbance if the environment is soft ($k_e = 10$). Nevertheless, unlike the proposed controller, the basic impedance controller fails to reject the pulse disturbance when $k_e = 10^3$, as shown in Fig. 6.8(b).

Thirdly, the disturbance is assumed to be a randomly changing force signal $\mathbf{F}_{dist} = [r, r]^T$, where r is a random function with the amplitude of 10. Setting the parameters the same as in the pulse disturbance simulation, the responses of both controllers for $k_e = 10$ and $k_e = 10^4$ are shown in Figs. 6.9 and 6.10, respectively. Similar to the case of pulse disturbance, both controllers work well for the soft environment, for example $k_e = 10$ (Fig. 6.9). While for the hard environment, such as $k_e = 10^4$, the response of

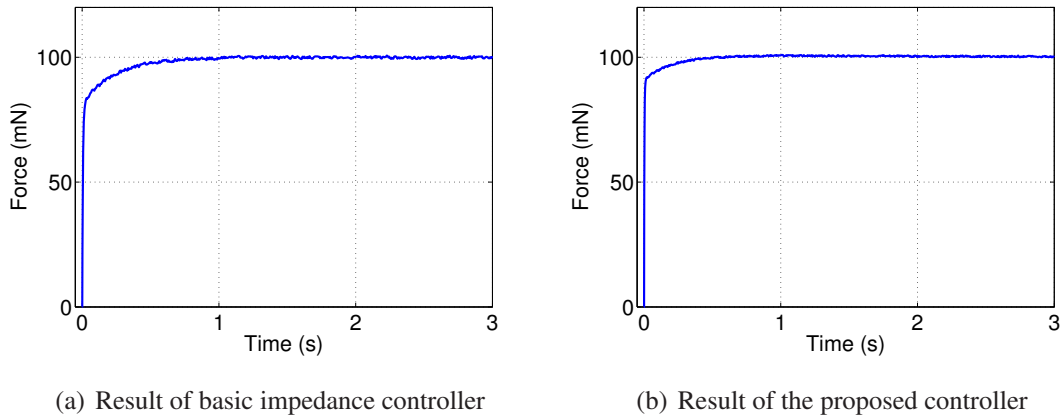


Figure 6.9: Responses of the combined impedance/direct control Scheme II in the case of the soft environment and random disturbances ($\mathbf{K}_e = \text{diag}[10, 0]$, $\mathbf{B}_e = \text{diag}[2, 0.1]$, $\mathbf{M}_t = \text{diag}[1, 1]$, $\mathbf{B}_t = \text{diag}[200, 30]$, $\mathbf{K}_t = \text{diag}[800, 10^4]$, $\mathbf{K}_p = \text{diag}[100, 100]$, and $\mathbf{K}_i = \text{diag}[80, 80]$, $\mathbf{F}_{dist} = [r, r]^T$, where r is a random function with the amplitude of 10).

the proposed controller is superior to that of the basic impedance controller, as shown in Fig. 6.10.

The above simulation results reveal that, in the case of disturbances, the performance of the basic impedance controller will deteriorate when the environmental stiffness increases. While the proposed controller works well for both soft and hard environments.

Let us now assume that $\mathbf{F}_{dist} = \mathbf{0}$, and set the target impedance and the compensator parameters as $\mathbf{M}_t = \text{diag}[1, 1]$, $\mathbf{B}_t = \text{diag}[100, 30]$, $\mathbf{K}_t = \text{diag}[300, 10^4]$, $\mathbf{K}_p = \text{diag}[100, 100]$, and $\mathbf{K}_i = \text{diag}[80, 80]$. For the environmental impedance $\mathbf{K}_e = \text{diag}[3, 0]$, $\mathbf{B}_e = \text{diag}[2, 0]$, with the assumption that the environmental stiffness is estimated 50% higher than the real value, Figure 6.11(a) shows the responses of the basic impedance controller and the proposed controller, respectively. The basic impedance controller has an error of about 33 mN; while the error by the proposed controller is about 6 mN. The same trends are also shown for $\mathbf{K}_e = \text{diag}[10, 0]$, $\mathbf{K}_e = \text{diag}[10^2, 0]$ and $\mathbf{K}_e = \text{diag}[10^3, 0]$, respectively, in Figs. 6.11(b) to 6.11(d).

Therefore, the proposed controller has higher degree of robustness to the environmental stiffness uncertainty than the basic impedance controller.

6.5 Experiments

In this section, a set of experiments are conducted on a 2-DOF planar parallel manipulator to further validate the effectiveness of the proposed combined impedance/direct

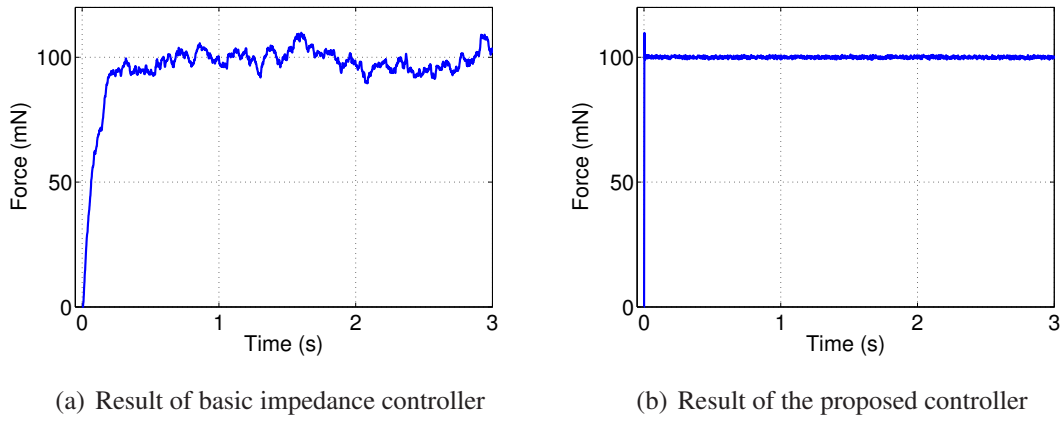


Figure 6.10: Responses of the combined impedance/direct control Scheme II in the case of the hard environment and random disturbances ($\mathbf{K}_e = \text{diag}[10^4, 0]$, $\mathbf{B}_e = \text{diag}[2, 0.1]$, $\mathbf{M}_t = \text{diag}[1, 1]$, $\mathbf{B}_t = \text{diag}[200, 30]$, $\mathbf{K}_t = \text{diag}[800, 10^4]$, $\mathbf{K}_p = \text{diag}[100, 100]$, and $\mathbf{K}_i = \text{diag}[80, 80]$, $\mathbf{F}_{dist} = [r, r]^T$, where r is a random function with the amplitude of 10).

control scheme.

6.5.1 Experimental Platform

Figure 6.12 shows the photograph of the constructed platform, which consists of two electric motors equipped with amplifiers and encoders, the manipulator, the force sensor, and the environment. The EmoteqTM direct drive brushless DC motors (QB03400) with the continuous torque up to 0.81 Nm are selected to drive the manipulator. The encoders with 2000 pulses per revolution are mounted at the end of the motor shafts to measure the angular position. The AMCTM servo amplifiers (B15A) are used to output current commands to the motors. A simple HoneywellTM one-axis force sensor (FSG15N1A) is attached on the environment, which is connected to an amplifier circuit to measure the interaction force. The environment adopts a mass-damper-spring system, which consists of a moving plate mounted on two sliders, and several spring components.

The xPC Target from MatlabTM is used to implement the control system with the sampling frequency at 1 kHz. In this environment, the Simulink is used to program the control algorithms. The Real Time Workshop and C/C++ compiler then convert the Simulink blocks into C code and build a target application, which is downloaded to the target PC and executed in real-time. The Sensoray I/O board (Model 626) is used to read the sensor readings into the control software running in the target PC, and to output commands to the motors through the amplifiers. More detailed description of xPC Target

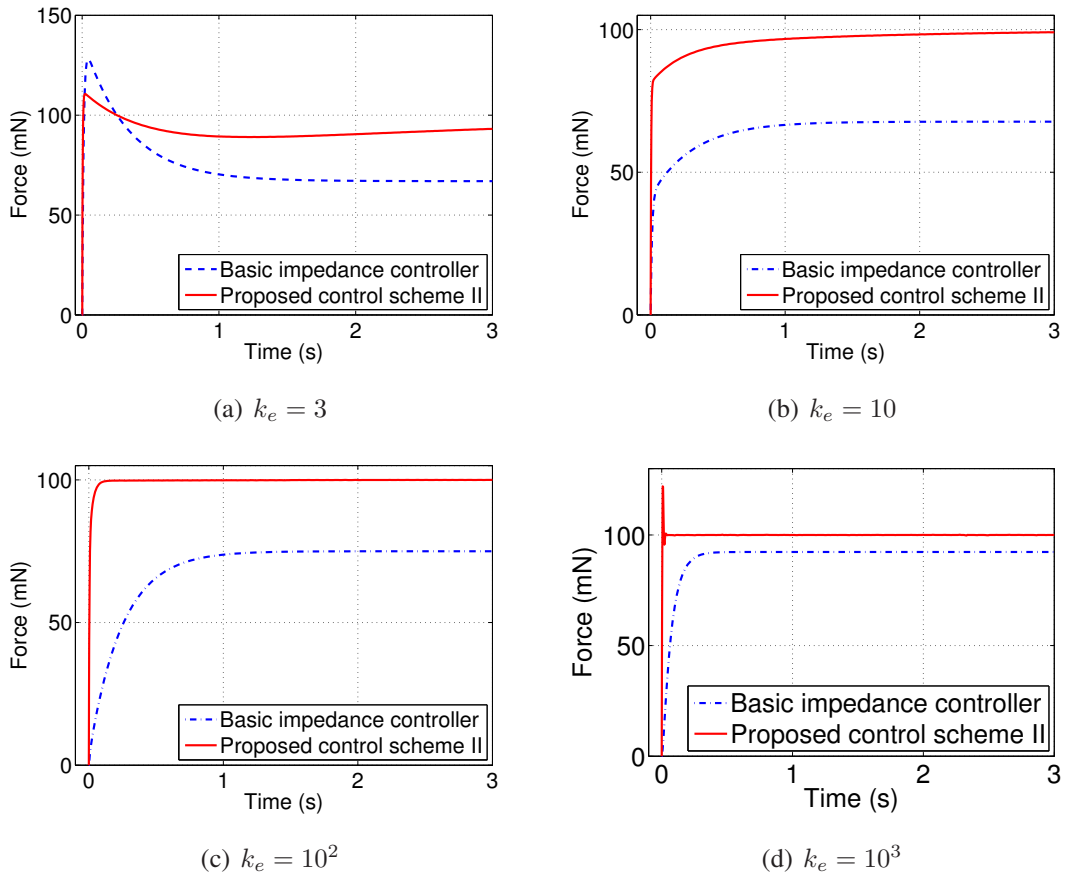


Figure 6.11: Responses of the combined impedance/direct control Scheme II in the case of environmental stiffness uncertainty (50% k_e uncertainty, $\mathbf{B}_e = \text{diag}[2, 0.1]$, $\mathbf{M}_t = \text{diag}[1, 1]$, $\mathbf{B}_t = \text{diag}[100, 30]$, $\mathbf{K}_t = \text{diag}[300, 10^4]$, $\mathbf{K}_p = \text{diag}[100, 100]$, and $\mathbf{K}_i = \text{diag}[80, 80]$, $\mathbf{F}_{dist} = [0, 0]^T$).

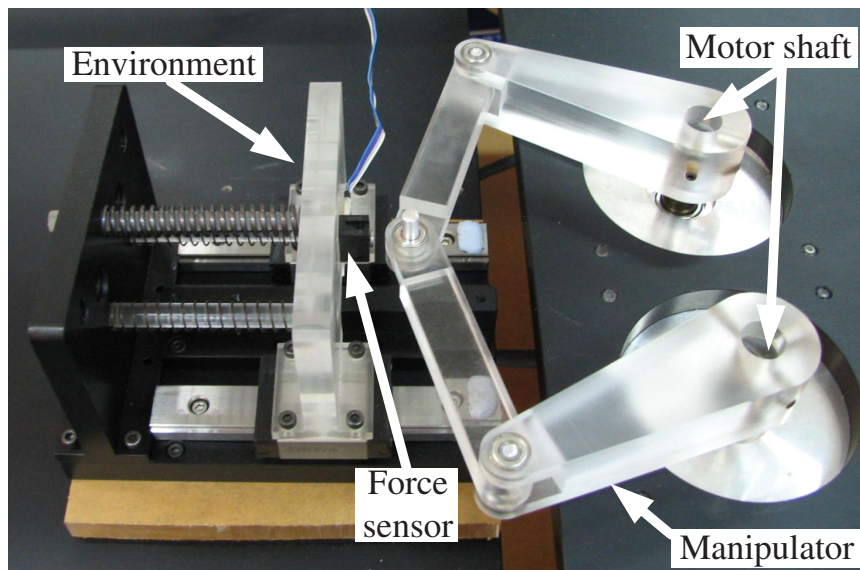


Figure 6.12: The experimental platform.

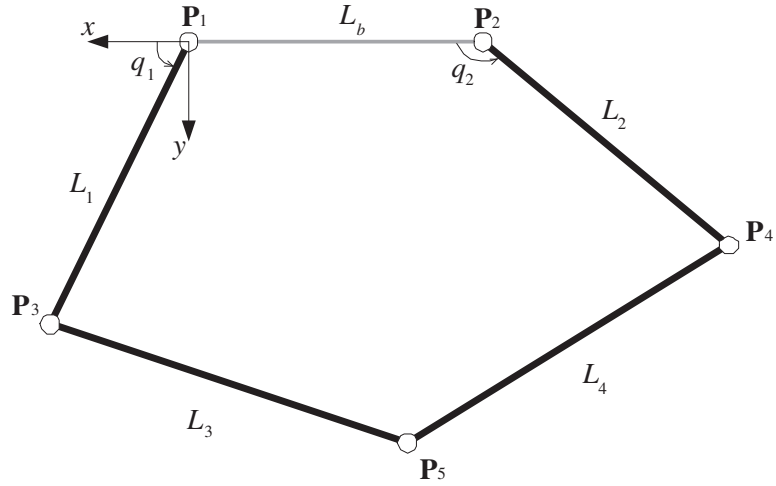


Figure 6.13: Structure of the parallel manipulator.

can be found in Appendix A.

Figure 6.13 shows the kinematic model of the manipulator. The manipulator has a planar parallel structure, which is basically a five-bar linkage mechanism. All the four moving links are made of acrylics, and have the same length, i.e., $l_1 = l_2 = l_3 = l_4 = l = 80$ mm, and $l_b = 86.9$ mm. The forward kinematics analysis generates the end tip position $\mathbf{P}_5(x_5, y_5)$ as

$$\begin{aligned} x_5 = & \frac{1}{2}l \cos q_1 + \frac{1}{2}l \cos q_2 - \frac{1}{2}l_b \\ & + \frac{1}{2} \sqrt{4l^2 - (l \cos q_1 - l \cos q_2 + l_b)^2 - (l \sin q_1 - l \sin q_2)^2} \\ & (l \sin q_2 - l \sin q_1) / \\ & \sqrt{(l \cos q_1 - l \cos q_2 + l_b)^2 + (l \sin q_1 - l \sin q_2)^2} \end{aligned} \quad (6.41)$$

$$\begin{aligned} y_5 = & \frac{1}{2}l \sin q_1 + \frac{1}{2}l \sin q_2 - \frac{1}{2} \\ & + \frac{1}{2} \sqrt{4l^2 - (l \cos q_1 - l \cos q_2 + l_b)^2 - (l \sin q_1 - l \sin q_2)^2} \\ & (l \cos q_2 - l \cos q_1 - l_b) / \\ & \sqrt{(l \cos q_1 - l \cos q_2 + l_b)^2 + (l \sin q_1 - l \sin q_2)^2} \end{aligned} \quad (6.42)$$

The Jacobian matrix J can then be obtained through

$$J(\mathbf{q}) = \begin{bmatrix} \partial x_5 / \partial q_1 & \partial x_5 / \partial q_2 \\ \partial y_5 / \partial q_1 & \partial y_5 / \partial q_2 \end{bmatrix} \quad (6.43)$$

Detailed kinematics and dynamics analysis of the manipulator is given in Appendix B. Due to the parallel structure, the chosen mechanism for the experiments inherently has a complex dynamic equation, which is hard to be implemented in the control system. Therefore, proper approximations of the dynamics are made when implementing the control algorithms. In fact, the mechanism is chosen purposely to show the robustness of the proposed control schemes to the dynamics uncertainties. Toward this end, the inertias of links L_3 and L_4 , and the friction force are neglected, and thus the dynamics is dominated by the inertias of links L_1 and L_2 (including the inertias of the motor shafts). As a result, we have $\mathbf{C}(\mathbf{q}, \dot{\mathbf{q}}) = \mathbf{G}(\mathbf{q}) = \mathbf{0}$, and

$$\mathbf{D}(\mathbf{q}) = \begin{bmatrix} 20.5 & 0 \\ 0 & 20.5 \end{bmatrix} \times 10^{-5} \text{kgm}^2 \quad (6.44)$$

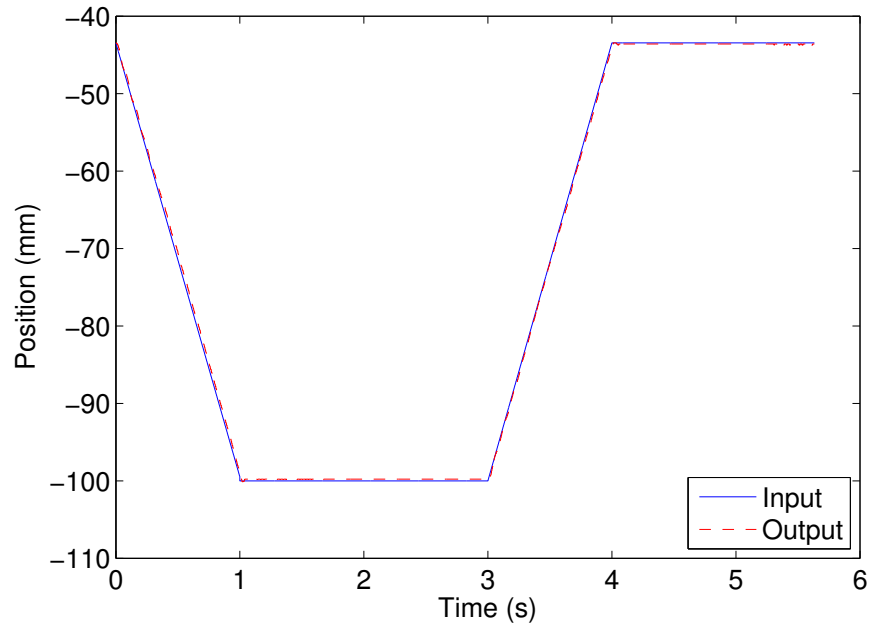
In such a way, the un-modeled dynamics are treated as the disturbance forces.

6.5.2 Experimental Results

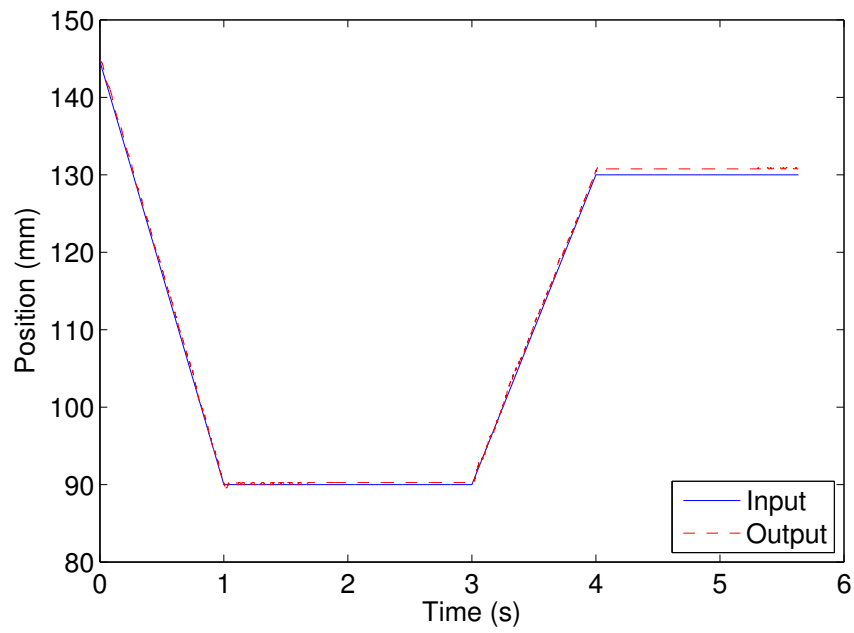
Both Scheme I (Eq. (6.8)) and Scheme II (Eq. (6.27)) are implemented on the experimental platform. The results are presented as follows.

6.5.2.1 Results of Position Tracking

The first set of experiments are performed to examine the position tracking ability of Schemes I and II in free space motion. In the experiments, the end tip of the manipulator is commanded to follow a designed trajectory with the target parameters set as $\mathbf{M}_t = \text{diag}[1, 1] \text{ N} \cdot \text{s}^2/\text{m}$, $\mathbf{B}_t = \text{diag}[30, 30] \text{ N} \cdot \text{s}/\text{m}$, $\mathbf{K}_t = \text{diag}[10^4, 10^4] \text{ N}/\text{m}$. Both Schemes I and II generate the same results, as shown in Fig. 6.14. Figure 6.14(a) shows that the end tip follows the trajectory well in x -axis. While for the y -axis response, there is an error less than 1 mm in the final position. A possible cause of the larger error in y -axis than that in x -axis is due to the kinematic structure of the manipulator. For this specific manipulator structure, a large variation of the y -axis position can be produced by small angular variations of q_1 and q_2 . Therefore, the practical issues, such as encoder resolution, mechanism backlash, etc., may pose more difficulties to position tracking in y -axis than in x -axis. Note that the proposed control schemes are the same as the impedance control in free space motion. Therefore, the position tracking performance can always be improved by increasing the value of \mathbf{K}_t with proper setting of \mathbf{B}_t according to the impedance control technique in free space motion. In practice, however, one should consider the saturation effect of the actuators.

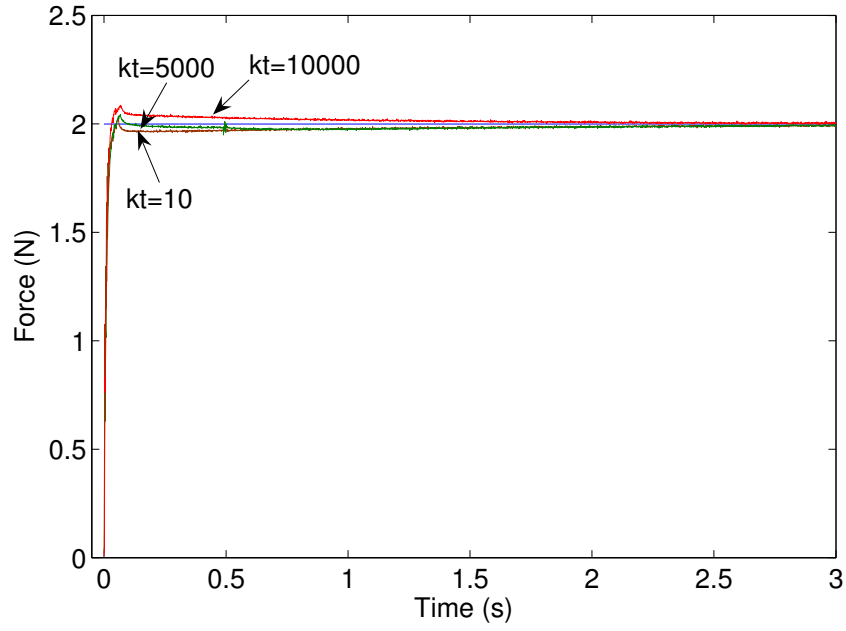


(a) x-axis response

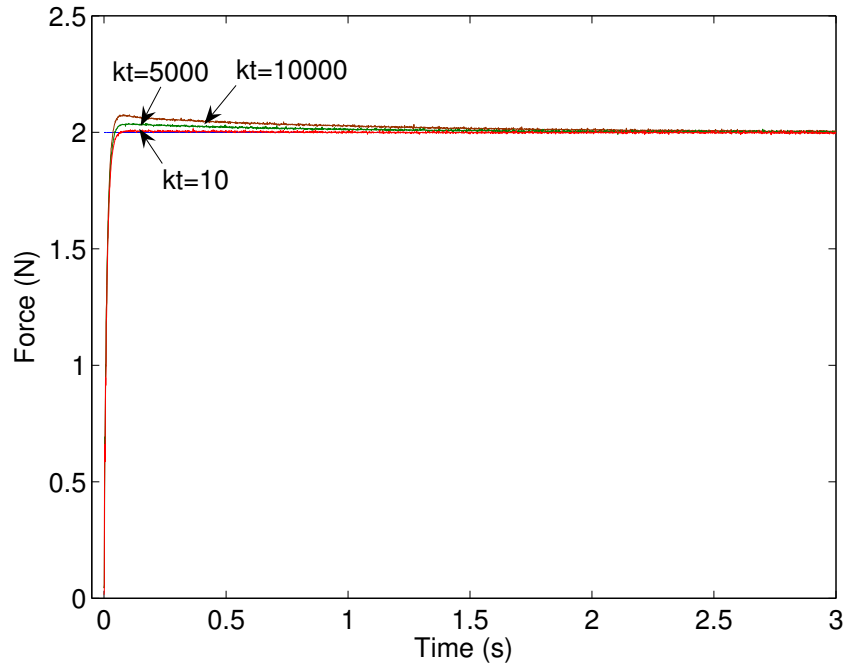


(b) y-axis response

Figure 6.14: Typical position tracking results in free space motion. The control parameters are set as $\mathbf{M}_t = \text{diag}[1, 1] \text{ N} \cdot \text{s}^2/\text{m}$, $\mathbf{B}_t = \text{diag}[30, 30] \text{ N} \cdot \text{s}/\text{m}$, and $\mathbf{K}_t = \text{diag}[10^4, 10^4] \text{ N}/\text{m}$.

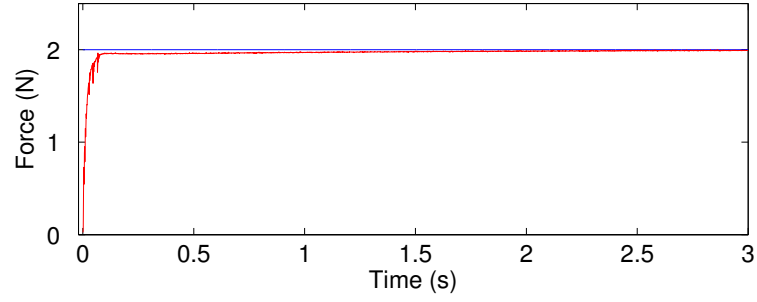


(a) $k_e = 600$ N/m

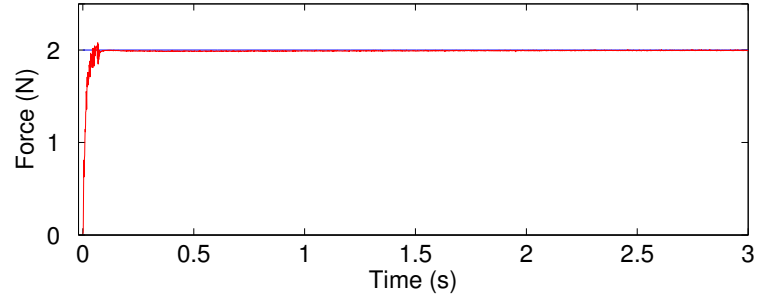


(b) $k_e = 10^4$ N/m

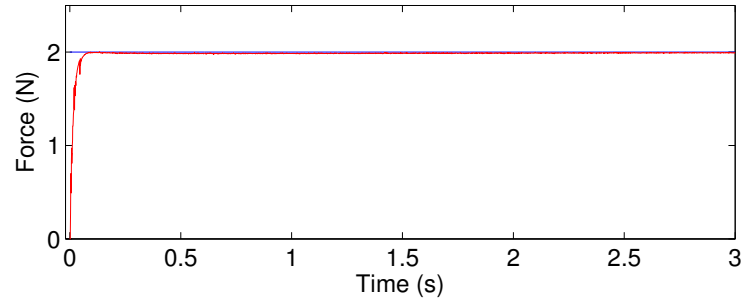
Figure 6.15: Responses to step force input $f_d = 2$ N in contact condition by Scheme I. The control parameters are set as $\mathbf{M}_t = \text{diag}[1, 1]$ N \cdot s²/m, $\mathbf{B}_t = \text{diag}[30, 30]$ N \cdot s/m, $\mathbf{K}_t = \text{diag}[10^4, k_t]$ N/m, $\mathbf{K}_p = \text{diag}[1, 1]$, and $\mathbf{K}_i = \text{diag}[1, 1]$.



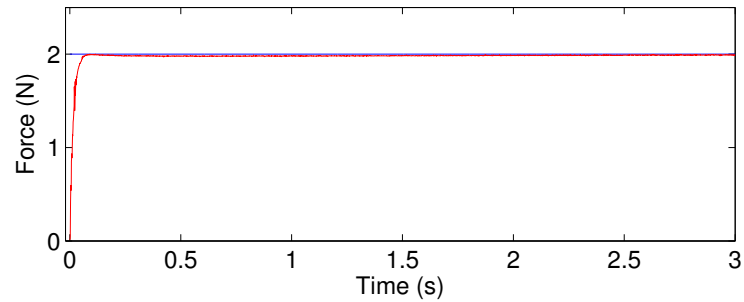
(a) $k_t = 10 \text{ N/m}$, $k_e = 600 \text{ N/m}$



(b) $k_t = 10^4 \text{ N/m}$, $k_e = 600 \text{ N/m}$



(c) $k_t = 10 \text{ N/m}$, $k_e = 10^4 \text{ N/m}$



(d) $k_t = 10^4 \text{ N/m}$, $k_e = 10^4 \text{ N/m}$

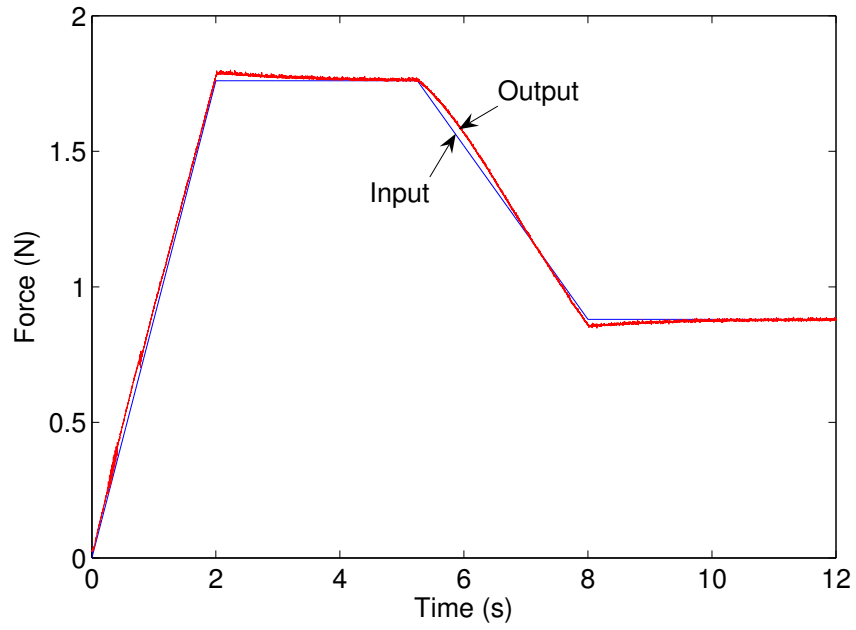
Figure 6.16: Responses to step force input $f_d = 2 \text{ N}$ in contact condition by Scheme II. The control parameters are set as $\mathbf{M}_t = \text{diag}[1, 1] \text{ N} \cdot \text{s}^2/\text{m}$, $\mathbf{B}_t = \text{diag}[30, 300] \text{ N} \cdot \text{s}/\text{m}$, $\mathbf{K}_t = \text{diag}[10^4, k_t] \text{ N/m}$, $\mathbf{K}_p = \text{diag}[100, 100]$, and $\mathbf{K}_i = \text{diag}[80, 80]$.

6.5.2.2 Results of Force Control

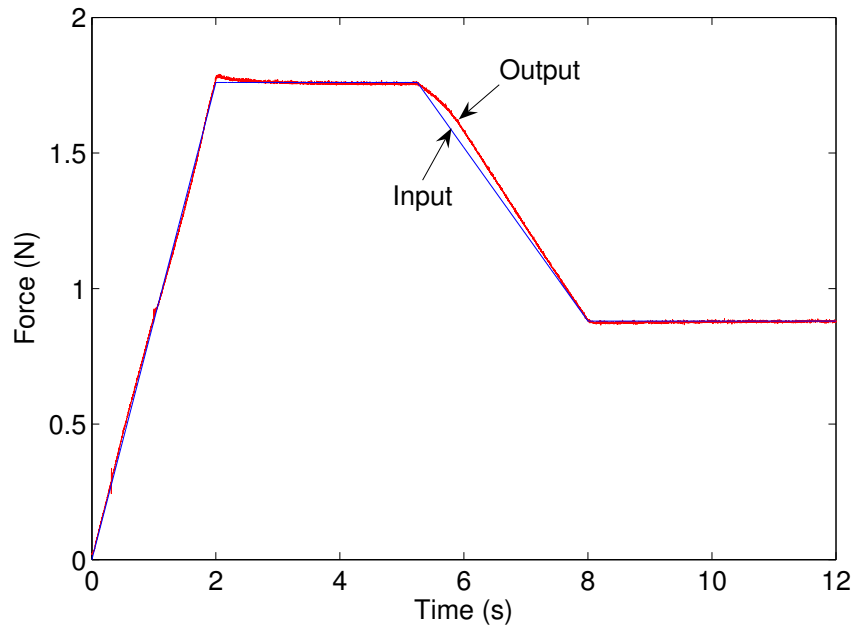
The second set of experiments is on the performance of force control in contact condition. Both Schemes I and II are examined. Before the experiments, the end tip of the manipulator is located at the initial position of the environment $\mathbf{X}_{eo} = [x_{eo}, y_{eo}] = [-43.45, 100.65]^T$ mm. A step input command $f_d = 2$ N is then applied along the y-axis direction, and the interaction force is measured by the force sensor. At the same time, the robot end tip is commanded to keep the position in x-axis at $x = -43.45$ mm.

Firstly, it is assumed that the stiffness of the environment is known or estimated accurately. Figure 6.15 shows the typical responses by the proposed Scheme I for both the soft (Fig. 6.15(a)) and the hard (Fig. 6.15(b)) environments. The control parameters are set as $\mathbf{K}_p = \text{diag}[1, 1]$, and $\mathbf{K}_i = \text{diag}[1, 1]$, $\mathbf{M}_t = \text{diag}[1, 1]$ N · s²/m, $\mathbf{B}_t = \text{diag}[30, 30]$ N · s/m, and $\mathbf{K}_t = \text{diag}[10^4, k_t]$ N/m, where k_t is varied from 10 to 10^4 . It can be seen that, for both $k_e = 600$ N/m and $k_e = 10^4$ N/m, the responses approach the step input in a fast way with a small transient error. The overshoot of the response is increased when the target stiffness k_t is set at a higher value. However, the increase is insignificant, which is around 5% for both environments when k_t is increased from 10 to 10^4 . The responses by Scheme II are shown in Fig. 6.16 with the control parameters set as $\mathbf{K}_p = \text{diag}[100, 100]$, $\mathbf{K}_i = \text{diag}[80, 80]$, $\mathbf{M}_t = \text{diag}[1, 1]$ N · s²/m, $\mathbf{B}_t = \text{diag}[30, 300]$ N · s/m, and $\mathbf{K}_t = \text{diag}[10^4, k_t]$ N/m. The curves shown in Figs. 6.16(a) to 6.16(d) demonstrate similar desirable responses for both $k_e = 600$ N/m and $k_e = 10^4$ N/m with k_t set as 10 and 10^4 . The increase of the value of the target stiffness almost does not affect the responses. The results in Figs. 6.15 and 6.16 show that the force control of the robot manipulator can be achieved by the proposed control Scheme I or II, with the presence of model uncertainties. Furthermore, for both Schemes I and II, the control action by the PI type compensator dominates the responses, and that by the impedance control portion does not affect the responses much for k_p increased to the value as high as 10^4 N/m. As a result, the target stiffness k_p can always be set as 10^4 N/m, such that there is no need to adjust the value of the target stiffness when the robot transits between the free space motion and the constrained motion. Note that the values of the control parameters should be chosen with the consideration of the saturation of the motors. In view of the small inertia of the manipulator, larger values of \mathbf{K}_p and \mathbf{K}_i have been chosen in Scheme II than in Scheme I.

Next, it is assumed that the stiffness of the environment is unknown. With the parameter setting $\mathbf{K}_p = \text{diag}[1, 1]$, and $\mathbf{K}_i = \text{diag}[1, 1]$, $\mathbf{M}_t = \text{diag}[1, 1]$ N · s²/m,

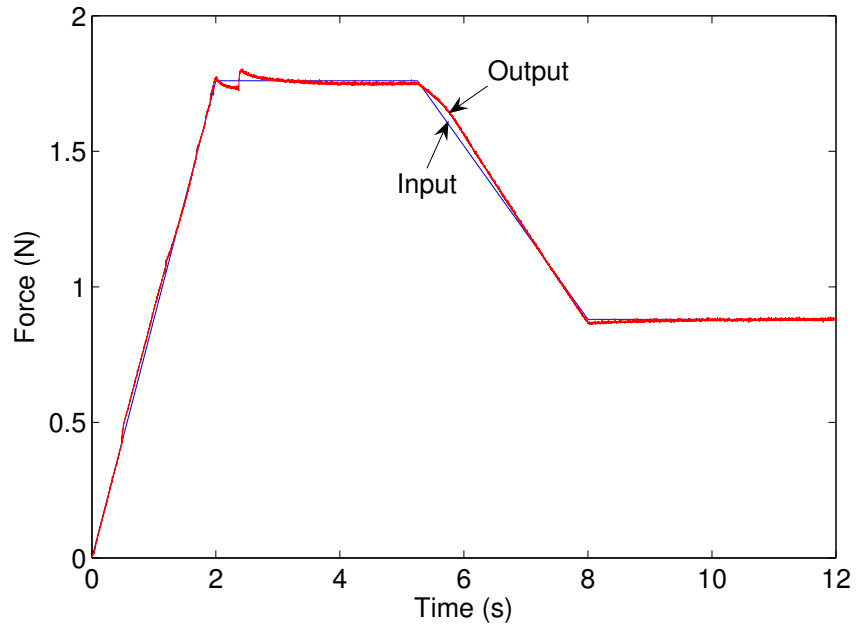


(a) $k_e = 800 \text{ N/m}$, $\hat{k}_e = 1200 \text{ N/m}$

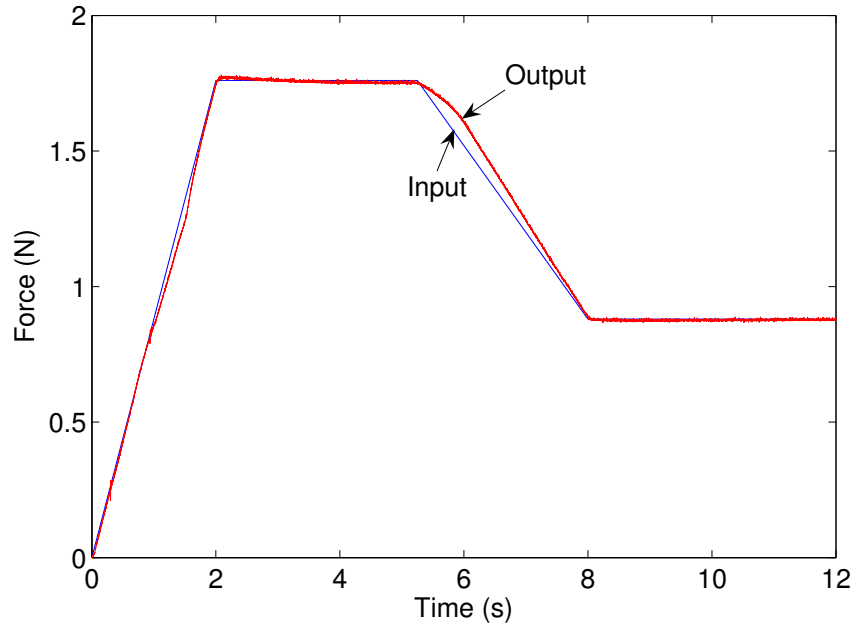


(b) $k_e = 1.2 \times 10^4 \text{ N/m}$, $\hat{k}_e = 6000 \text{ N/m}$

Figure 6.17: Force tracking results by Scheme I with environment impedance uncertainties. The control parameters are set as $\mathbf{M}_t = \text{diag}[1, 1] \text{ N} \cdot \text{s}^2/\text{m}$, $\mathbf{B}_t = \text{diag}[30, 30] \text{ N} \cdot \text{s}/\text{m}$, $\mathbf{K}_t = \text{diag}[10^4, 10^4] \text{ N}/\text{m}$, $\mathbf{K}_p = \text{diag}[1, 1]$, and $\mathbf{K}_i = \text{diag}[1, 1]$.



(a) $k_e = 800 \text{ N/m}$, $\hat{k}_e = 1200 \text{ N/m}$



(b) $k_e = 1.2 \times 10^4 \text{ N/m}$, $\hat{k}_e = 6000 \text{ N/m}$

Figure 6.18: Force tracking results by Scheme II with environment impedance uncertainties. The control parameters are set as $\mathbf{M}_t = \text{diag}[1, 1] \text{ N} \cdot \text{s}^2/\text{m}$, $\mathbf{B}_t = \text{diag}[30, 30] \text{ N} \cdot \text{s}/\text{m}$, $\mathbf{K}_t = \text{diag}[10^4, 10^4] \text{ N}/\text{m}$, $\mathbf{K}_p = \text{diag}[100, 100]$, and $\mathbf{K}_i = \text{diag}[80, 80]$.

$\mathbf{B}_t = \text{diag}[30, 30] \text{ N} \cdot \text{s}/\text{m}$, and $\mathbf{K}_t = \text{diag}[10^4, 10^4] \text{ N}/\text{m}$, Fig. 6.17 shows two typical force tracking results by Scheme I. In particular, Fig. 6.17(a) shows the result of contacting the soft environment $k_e = 800 \text{ N}/\text{m}$, where the estimated stiffness \hat{k}_e is 50% higher than the actual value, i.e., $\hat{k}_e = 1200 \text{ N}/\text{m}$; while for the result of contacting the hard environment $k_e = 1.2 \times 10^4 \text{ N}/\text{m}$ shown in Fig. 6.17(b), the stiffness is estimated 50% lower than the actual value, i.e., $\hat{k}_e = 6000 \text{ N}/\text{m}$. Similarly, the force tracking results by Scheme II are shown in Fig. 6.18, with the parameter setting $\mathbf{M}_t = \text{diag}[1, 1] \text{ N} \cdot \text{s}^2/\text{m}$, $\mathbf{B}_t = \text{diag}[30, 30] \text{ N} \cdot \text{s}/\text{m}$, $\mathbf{K}_t = \text{diag}[10^4, 10^4] \text{ N}/\text{m}$, $\mathbf{K}_p = \text{diag}[100, 100]$, and $\mathbf{K}_i = \text{diag}[80, 80]$. For both proposed control Schemes I and II, the results show that the outputs track the input well, and thus demonstrate the robustness to the environment stiffness uncertainty.

6.5.2.3 Results of Transition of Motion

The last set of experiments are focused on the transition of motion between the free space condition and the constrained condition. In the experiments, the robot end tip is commanded to move from the initial position ($\mathbf{X}_{\text{initial}} = [-43.45, 92.67]^T \text{ mm}$) toward the resting position of the environment ($\mathbf{X}_{\text{eo}} = [-43.45, 128.37]^T \text{ mm}$) at the speed of 35.7 mm/s. Once the end tip contacts the environment, a command of force trajectory is then applied to the end tip, which starts at 0 N, increases to 2 N gradually, maintains at 2 N for a while, and finally decreases to 0 N gradually. As the reading of the force sensor becomes zero, the end tip is commanded to move to the position $\mathbf{X}_{\text{final}} = [-43.45, 100]^T \text{ mm}$ at the speed of 17.85 mm/s. An environment with the stiffness as $k_e = 3000 \text{ N}/\text{m}$, and unknown mass and damping coefficients are used in the experiment. The stiffness of the environment is estimated 33.3% lower than the actual value, i.e., $\hat{k}_e = 2000 \text{ N}/\text{m}$.

With the control parameter setting $\mathbf{M}_t = \text{diag}[1, 1] \text{ N} \cdot \text{s}^2/\text{m}$, $\mathbf{B}_t = \text{diag}[30, 30] \text{ N} \cdot \text{s}/\text{m}$, $\mathbf{K}_t = \text{diag}[10^4, 10^4] \text{ N}/\text{m}$, $\mathbf{K}_p = \text{diag}[1, 1]$, and $\mathbf{K}_i = \text{diag}[1, 1]$, a typical result by Scheme I is shown in Fig. 6.19. Figure 6.19(a) shows the y-axis position history of the end tip, and Fig. 6.19(b) shows the robot-environment interaction force history. It can be observed that the robot end tip moves smoothly in the first second, and contacts the environment at $t = 1 \text{ s}$. During the transition from the free space motion to the constrained motion, the interaction force chatters for a small time period, due to the impact between the fast moving end tip and the environment. After the transition, the environment is compressed for about 7 seconds (refer to Fig. 6.19(a)), and the interaction force follows the commanded force trajectory (refer to Fig. 6.19(b)). At $t = 8 \text{ s}$,

the environment returns to the resting position, and the interaction force turns to zero. The robot thus transits from the constrained motion to the free space motion. Finally, the end tip moves to $\mathbf{X}_{final} = [-43.45, 100]^T$ mm. The result by Scheme II is similar to that by Scheme I, and is shown in Fig. 6.20, where the control parameters are set as $\mathbf{M}_t = \text{diag}[1, 1]$ N · s²/m, $\mathbf{B}_t = \text{diag}[30, 30]$ N · s/m, $\mathbf{K}_t = \text{diag}[10^4, 10^4]$ N/m, $\mathbf{K}_p = \text{diag}[50, 50]$, and $\mathbf{K}_i = \text{diag}[40, 40]$. In addition, the result with a hard environment ($k_e = 1.2 \times 10^4$ N/m) by Scheme II is shown in Fig. 6.21. Interestingly, no chattering effect during the transition is observed.

All the above results in Figs. 6.19 to 6.21 have shown that the proposed combined impedance/direct control schemes I and II can achieve the transition between the free space motion and the constrained motion without switching the control modes, even without tuning the parameter values during the transitions. In addition, the commanded position and force trajectories are tracked with satisfactory accuracy in the presence of environment impedance uncertainties, and robot model dynamics uncertainties. Note that the dynamics of the manipulator is not known precisely, and an approximation is utilized in the experiments, as addressed in Sec. 6.5.1.

6.6 A Comparison of the Control Schemes

The simulation and experimental results have shown that, if compared to the basic impedance control, both of the proposed schemes can improve the performance. The features of the direct control, impedance control, and the combined impedance/direct control (schemes I and II) are summarized in Table 6.1.

The comparison between schemes I and II is then performed. In Scheme I, the force error based compensation is included directly. The advantage of Scheme I is that the implementation requires less computing resources. However, to reduce the steady state error, the value of \mathbf{K}_p should be carefully selected such that the condition shown in Eq. (6.6) can be guaranteed. To do this, according to Eq. (6.6), one may need to know the information of the environment stiffness and the position/orientation that the end effector will reach during the operation. Requiring to know more information for the controller design is the disadvantage of Scheme I.

Compared with Scheme I, the error based compensation in Scheme II is achieved in an indirect way, where the estimate of the robot Cartesian inertia matrix $\hat{\mathbf{D}}_x$ is pre-multiplied with the compensator. In this way, the steady state force tracking error is definitely reduced by any parameter setting for $k_p > 0$ and $k_i > 0$ if compared to the

Table 6.1: Comparison of the control schemes.

Control Scheme	Advantages	Disadvantages/Limitations
Direct Control	More robust to robot model uncertainties and environment uncertainties than impedance control	Requiring control mode switch during transition of motion
Impedance Control	Not requiring control mode switch during transition of motion	Decreased performance with the presence of disturbance force or environment stiffness uncertainties
Combined Impedance/Direct Control	1. Not requiring control mode switch; 2. More robust to model uncertainties, disturbances, and environment uncertainties than impedance control	Requiring more computing resource than direct control and impedance control

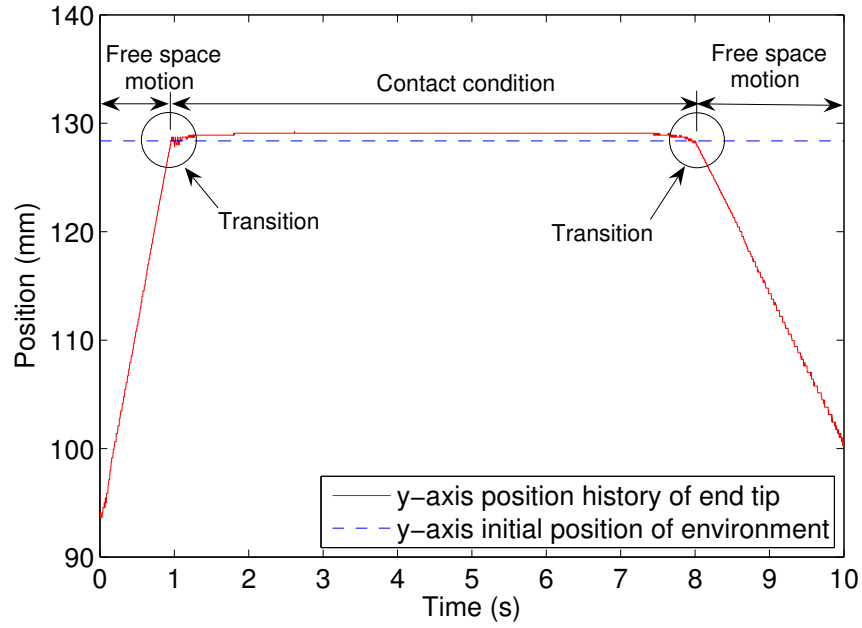
basic impedance control, where k_p and k_i are the components of \mathbf{K}_p and \mathbf{K}_i , respectively. In other words, Scheme II has a less requirement on the information of the environment and the manipulator, which is the advantage of Scheme II. The disadvantage, if compared to Scheme I, is that it uses more computing resources than Scheme I.

In the free space motion, both schemes I and II are the same as the basic impedance control, and result in the same performance as shown in Fig. 6.14. It is worth comparing the performance by the two schemes in contact condition. First of all, both the simulations and the experiments show similar results by the two schemes. The two schemes both improve the performance, if compared to the basic impedance control. However, if compare the experimental results by the two schemes, it can be found that the performance by Scheme II is slightly better than that by Scheme I. Firstly, for different values of \mathbf{K}_t , Fig. 6.15 shows that the transient responses by Scheme I differ slightly, whereas Fig. 6.16 shows that the responses by Scheme II are almost the same. In other words, Response by Scheme I is more sensitive to the control parameter \mathbf{K}_t . Secondly, Figs. 6.15 and 6.16 also show better transient responses by Scheme II. Thirdly, the comparison of Figs. 6.19 and 6.20 reveals that, during the transition of motion, Scheme II has less chattering effect than Scheme I.

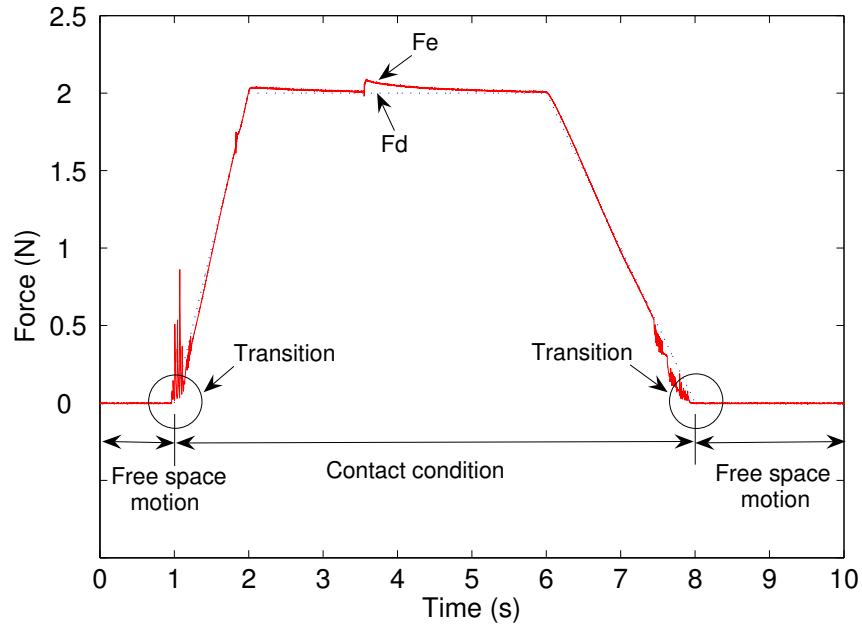
In a word, Scheme II outperforms Scheme I. Therefore, Scheme II is recommended for implementation, as long as the computing resources are sufficient.

6.7 Concluding Remarks

The idea of combined impedance/direct control has been presented with two schemes of implementation, each of which is composed of two parts, namely the direct force control action and the impedance control action. In fact, the combined impedance/direct control combines the advantages of both the impedance control (i.e., no need to switch the control modes) and the hybrid position/force control (i.e., more robust than impedance control to the environment uncertainties and disturbances). A sufficient stability condition is given to Scheme II with the assumption that the environment can be modeled as a linear mass-damper-spring system. Both the theoretical analysis and the computer simulations have shown the superiority of the proposed controllers (both schemes I and II) over the impedance control and the hybrid position/force control. The experiments have also been conducted to validate the effectiveness of the proposed control schemes I and II. Finally, a comparison between the proposed two schemes is presented, based on which the recommendation is made on Scheme II over Scheme I.

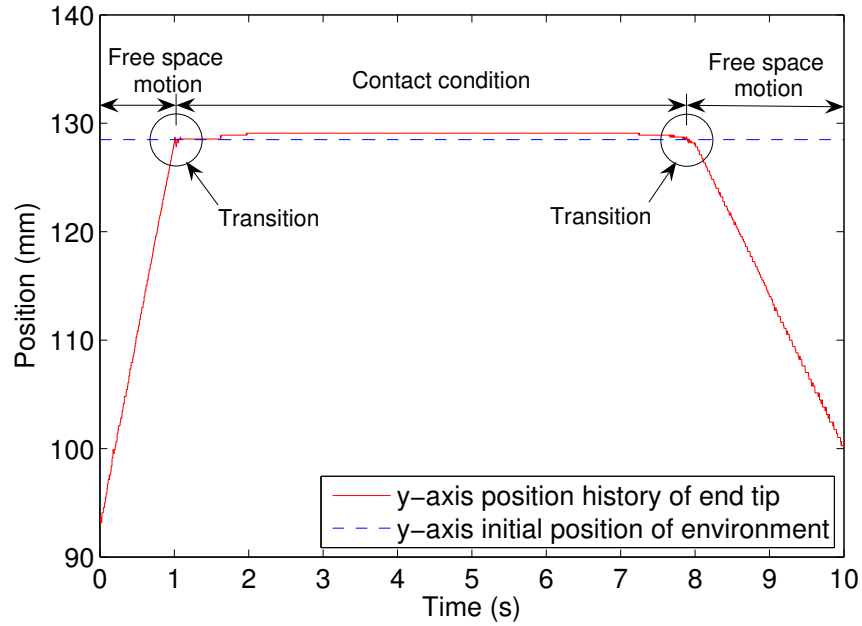


(a) y-axis position profile

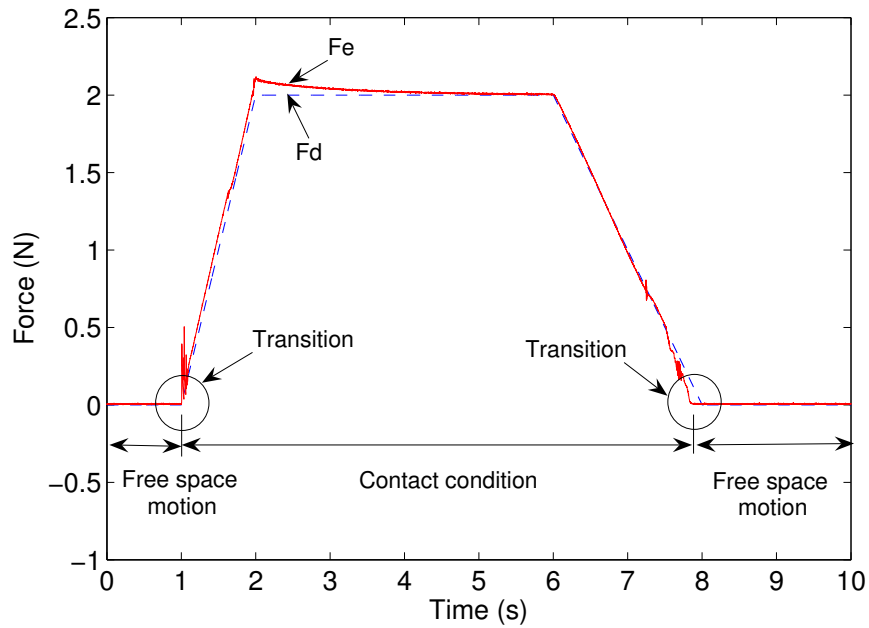


(b) interaction force profile

Figure 6.19: Typical results of transition between the free space motion and the constrained motion by Scheme I. The environment stiffness is $k_e = 3000 \text{ N/m}$, which is estimated to be $\hat{k}_e = 2000 \text{ N/m}$. The control parameters are set as $\mathbf{M}_t = \text{diag}[1, 1] \text{ N} \cdot \text{s}^2/\text{m}$, $\mathbf{B}_t = \text{diag}[30, 30] \text{ N} \cdot \text{s}/\text{m}$, $\mathbf{K}_t = \text{diag}[10^4, 10^4] \text{ N/m}$, $\mathbf{K}_p = \text{diag}[1, 1]$, and $\mathbf{K}_i = \text{diag}[1, 1]$.

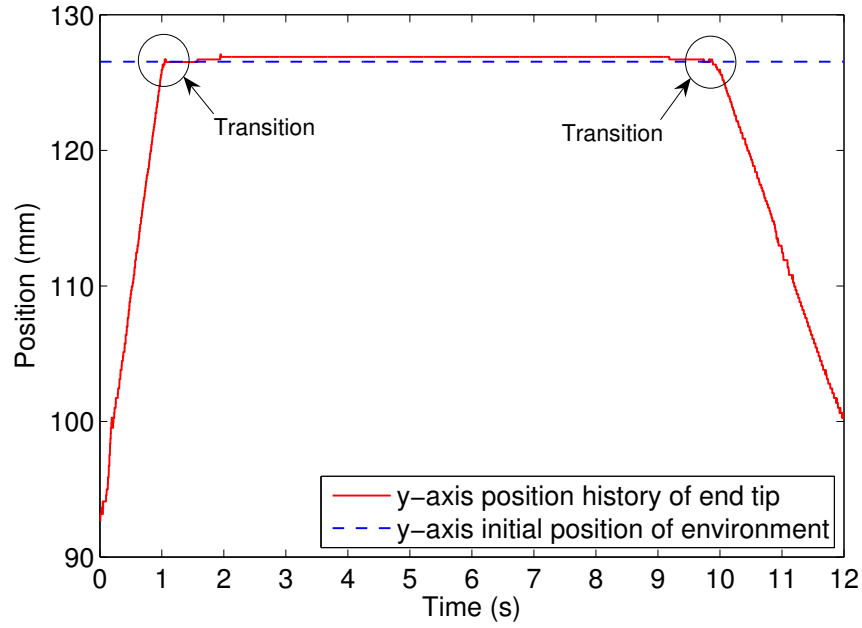


(a) y-axis position profile

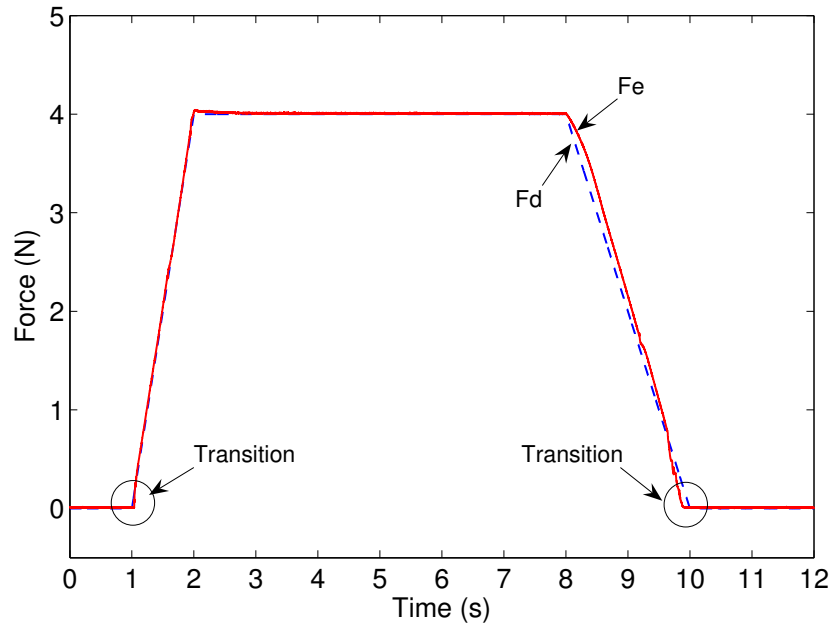


(b) interaction force profile

Figure 6.20: Typical results of transition between the free space motion and the constrained motion by Scheme II. The environment stiffness is $k_e = 3000 \text{ N/m}$, which is estimated to be $\hat{k}_e = 2000 \text{ N/m}$. The control parameters are set as $\mathbf{M}_t = \text{diag}[1, 1] \text{ N} \cdot \text{s}^2/\text{m}$, $\mathbf{B}_t = \text{diag}[30, 30] \text{ N} \cdot \text{s}/\text{m}$, $\mathbf{K}_t = \text{diag}[10^4, 10^4] \text{ N/m}$, $\mathbf{K}_p = \text{diag}[50, 50]$, and $\mathbf{K}_i = \text{diag}[40, 40]$.



(a) y-axis position profile



(b) interaction force profile

Figure 6.21: Typical results of transition between the free space motion and the constrained motion by Scheme II. The environment stiffness is $k_e = 1.2 \times 10^4$ N/m, which is estimated to be $\hat{k}_e = 2 \times 10^4$ N/m. The control parameters are set as $\mathbf{M}_t = \text{diag}[1, 1]$ N · s²/m, $\mathbf{B}_t = \text{diag}[30, 30]$ N · s/m, $\mathbf{K}_t = \text{diag}[10^4, 10^4]$ N/m, $\mathbf{K}_p = \text{diag}[50, 50]$, and $\mathbf{K}_i = \text{diag}[40, 40]$.

Chapter 7

Bilateral Control Scheme Design

Most of the previous works on the telemanipulation control schemes were conducted based on the network model, where the system is idealized as the linear one. Plentiful insights and observations associated with the system performance have been obtained through these work. In particular, it has been well known that the stability and the transparency are the two major issues when designing the bilateral controllers. The passivity and the absolute stability concepts have been widely used to derive the stability conditions¹. Transparency is a measure of how well the impedance felt by the operator matches the impedance of the environment. In a perfect transparent system, the operator feels exactly the same impedance as that of the environment. The quantitative description of the attainable transparency has been well established through the analysis based on the network model and the four-channel architecture representation, which has been reviewed in Sec. 2.4.1. In addition, the transparency conditions of two-channel systems will be reviewed next in Sec. 7.1.

Since the master and slave manipulators usually have complex coupled nonlinear dynamics, the progress of the manipulator control technologies make it advantageous to apply the well developed manipulator control schemes to the telemanipulation systems. Some research efforts have been made toward this end. In [12], a three-channel bilateral controller is proposed, where the impedance controller is designed for the master, and the slave is controlled by the sliding-mode-based impedance control. In the two-channel position-force framework, the impedance control was applied to control the slave for experimental study of shared control in [32]. A control scheme, named as Naturally Transitioning Rate-to-Force Control, was employed for experimental evaluation

¹Instead of the network model, Fite *et al.* [23, 24] address the transparency and stability of a two-channel system from a frequency-domain perspective by applying the loop-shaping methods.

of telemanipulation tasks in [99]. Impedance control was also applied to design the telemanipulation controller presented in [79]. However, the transparency was not discussed in these work [12, 32, 79, 99]. The parallel force/position control [10] and the the hybrid position/force control [80] for single manipulator control have been applied to telemanipulation systems in [36] and [55], respectively. In these two works, the developed bilateral controllers were compared with the classical four-channel representation, and the transparency and the stability were studied. Note that the four-channel representation has been reviewed in Sec. 2.4.2.

The transition of motion between the free space condition and the constrained condition has gained attention in the work on single robot control. However, to our best knowledge, this issue has not been explicitly addressed in the previous work on control of telemanipulation systems. The analysis and experiments in Chapter 6 have shown that the proposed combined impedance/direct control does not require to switch the control modes during the transition between the constrained and unconstrained motions, and is more robust to the un-modeled robot dynamics than impedance control. Therefore, it is promising to apply the combined impedance/direct control scheme in the bilateral controller design of telemanipulation systems.

Considering the transition of motion between the free space (unconstrained) and the contact (constrained) conditions, a two-channel bilateral controller is proposed in this chapter by applying the combined impedance/direct control. Perfect transparency can be achieved in the ideal situation. In addition, no control mode switch is required during the transition of motion. It should be noted that the work presented in this chapter does not consider the scale factor, and the presence of time delay in the communication channels.

Note that the proposed bilateral controller can be applied in the systems, where the slave is either a single manipulator, or a robotic hand.

In the following sections, the transparency conditions of the two-channel control architectures are first reviewed. The bilateral controller is then proposed with transparency and stability analysis. Next, the experimental study is presented. Finally, the concluding remarks are addressed.

7.1 Transparency Conditions of Two-Channel Systems

Lawrence [60] has proven that perfect transparency can be achieved by transmitting both master and slave positions and forces, based on the four-channel system structure shown

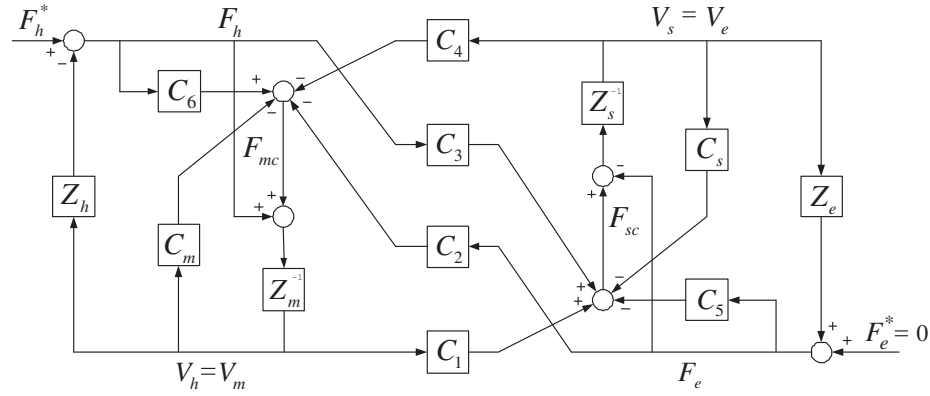


Figure 7.1: Four-channel architecture with local force feedback [37, 55].

in Fig. 2.3. Hashtrudi-Zaad and Salcudean [37] later expanded the four-channel architecture by including the local force feedback as shown in Fig. 7.1, with the parameters defined in Fig. 2.3. The authors showed that the architecture with only three channels can realize perfect transparency. Recently, by analyzing the four-channel architecture with local force feedback, Kim, *et al.* [55] showed that perfect transparency can be achieved in the position-force and force-position two-channel architectures. This result conforms to the work by Fite, *et al* [23, 24]. This section reviews the previous achievements on the quantitative description of the transparency based on the network model, which provides the basis for the bilateral controller evaluation.

To obtain the transparency conditions for the two-channel architectures, the form of the hybrid parameters in Eq. (2.9) are first expressed by the system parameters. From Fig. 7.1, the closed-loop dynamic equations of the master and the slave can be obtained as follows

$$(Z_m + C_m)V_h + C_4V_e + C_2F_e - (1 + C_6)F_h = 0 \quad (7.1)$$

$$(Z_s + C_s)V_e - C_1V_h - C_3F_h + (1 + C_5)F_e = 0 \quad (7.2)$$

By combining Eqs. (2.6), (7.1), and (7.2), the hybrid parameters can be expressed by the control parameters and the impedances of the master and slave as follows [55]

$$h_{11} = \frac{(Z_m + C_m)(Z_s + C_s) + C_1C_4}{(1 + C_6)(Z_s + C_s) - C_3C_4} \quad (7.3)$$

$$h_{12} = \frac{C_2(Z_s + C_s) - C_4(1 + C_5)}{(1 + C_6)(Z_s + C_s) - C_3C_4} \quad (7.4)$$

$$h_{21} = -\frac{C_3(Z_m + C_m) + C_1(1 + C_6)}{(1 + C_6)(Z_s + C_s) - C_3C_4} \quad (7.5)$$

$$h_{22} = \frac{(1 + C_5)(1 + C_6) - C_2C_3}{(1 + C_6)(Z_s + C_s) - C_3C_4} \quad (7.6)$$

It has been shown in [55] that the transparent telemanipulation in P-P and F-F architectures is impossible. While in P-F and F-P architectures, the transparency conditions can be obtained by using the hybrid parameters (7.3)-(7.6) and the perfect transparency condition (2.9) as [55]

$$\begin{cases} C_1 = Z_s + C_s \neq 0 \\ C_2 = 1 + C_6 \neq 0 \\ C_5 = -1 \\ C_m = -Z_m \end{cases} \quad (7.7)$$

for P-F architecture, and

$$\begin{cases} C_3 = 1 + C_5 \neq 0 \\ C_4 = -(Z_m + C_m) \neq 0 \\ C_6 = -1 \\ C_s = -Z_s \end{cases} \quad (7.8)$$

for F-P architecture. Note that the above derivation is based on a single DOF system.

7.2 Bilateral Control Scheme Design

The control schemes for single robot manipulator control usually has either position or force command as the input². Since perfect transparency is achievable in two-channel control architectures, the well developed single robot control schemes can be applied to design the bilateral controller. In the unconstrained condition, slave is controlled to follow the motion of the master, and therefore the P-P architecture is employed.

For the constrained condition, Sec. 7.1 has shown that P-F and F-P architectures have advantages over the P-P and F-F architectures in terms of the achievable transparency. In this work, the combined impedance/direct controller is employed on the slave manipulator, such that smooth transition of motion without switching the control modes at the slave can be achieved. In addition, according to the results in Chapter 6, the combined

²An exception is the parallel force/position control, which has both the force and the position as the inputs.

impedance/direct controller at the slave is expected to minimize the effects of the unmodeled robot dynamics. Since the combined impedance/direct controller receives the force command as the single input, the F-P architecture is thus employed. In other words, the force command is sent to the slave from the master, and the position information is fed back from the slave to the master.

7.2.1 F-P Architecture in Constrained Condition

It is assumed that the slave contacts the environment along all the degrees of freedom in this section. In practice, the slave most likely contacts the environment along a single degree of freedom, which is normal to the environment. In this case, the controller for free space motion presented in the next section is applied along other degrees of freedom.

Both P-F and F-P architectures are capable of obtaining perfect transparency. Considering the fact that controlling the force is the primary requirement in the constrained motion, the F-P architecture is thus employed in this work ($C_1 = C_2 = 0$), where the force information is transmitted from the master to the slave, and the position information is transmitted from the slave to the master. Actually, it is the proper force value, rather than the perfect transparency, that guarantees the manipulated object, or the exploited environment from being damaged. Toward this end, the combined impedance/direct control scheme proposed in Chapter 6 is applied on the slave. While a position control scheme with local force compensation is employed on the master.

7.2.1.1 Master and Slave Controller Design

Recall the robot dynamic equation (5.12), without considering the disturbance force, the master and slave dynamics are modeled as

$$\mathbf{F}_{mc} = \mathbf{D}_{xm} \ddot{\mathbf{X}}_m + \mathbf{H}_{xm} - \mathbf{F}_h \quad (7.9)$$

$$\mathbf{F}_{sc} = \mathbf{D}_{xs} \ddot{\mathbf{X}}_s + \mathbf{H}_{xs} + \mathbf{F}_e \quad (7.10)$$

where \mathbf{D}_{xm} and \mathbf{D}_{xs} represent the master and slave inertia matrices, respectively; \mathbf{H}_{xm} and \mathbf{H}_{xs} denote the master and slave terms corresponding to \mathbf{H}_x of Eq. (5.12), respectively; \mathbf{X}_m and \mathbf{X}_s are the master and slave positions; \mathbf{F}_h and \mathbf{F}_e are the force exerted on the master by the operator, and the force applied on the environment by the slave; and \mathbf{F}_{mc} and \mathbf{F}_{sc} denote the control inputs of the master and the slave, respectively.

Same as in Chapters 5 and 6, the environment is modeled as LTI mass-damper-spring

system, which is expressed in frequency domain as

$$\mathbf{F}_e = (\mathbf{M}_e s^2 + \mathbf{B}_e s + \mathbf{K}_e)(\mathbf{X}_s - \mathbf{X}_{eo}) \quad (7.11)$$

where \mathbf{M}_e , \mathbf{B}_e , and \mathbf{K}_e are the diagonal matrices representing the environment mass, damping, and stiffness coefficients, respectively. The operator dynamics is also modeled as LTI mass-damper-spring system, which is expressed in frequency domain as

$$\mathbf{F}_h = \mathbf{F}_h^* - \mathbf{Z}_h \mathbf{V}_h \quad (7.12)$$

where $\mathbf{X}_h = \mathbf{X}_m$ is the human position, \mathbf{F}_h^* is the operator exogenous input force, and \mathbf{Z}_h denotes the operator impedance matrix, which is defined as

$$\mathbf{Z}_h = \mathbf{M}_h s + \mathbf{B}_h + \frac{\mathbf{K}_h}{s} \quad (7.13)$$

with \mathbf{M}_h , \mathbf{B}_h , and \mathbf{K}_h representing the operator mass, damping, and stiffness matrices, respectively.

In the constrained motion, we have $\mathbf{F}_{ed} = \mathbf{F}_h$, where \mathbf{F}_{ed} denotes the desired force applied on the environment by the slave robot. According to the combined impedance/direct controller represented by Eq. (6.26), the following controller is proposed for the slave

$$\mathbf{F}_{sc} = \mathbf{D}_{xs} \left(\mathbf{U}_s + \mathbf{K}_{ps} \mathbf{E}_{fs} + \mathbf{K}_{is} \int_0^t \mathbf{E}_{fs} dt \right) + \mathbf{H}_{xs} + \mathbf{F}_e \quad (7.14)$$

where

$$\mathbf{E}_{fs} = \mathbf{F}_h - \mathbf{F}_e \quad (7.15)$$

$$\mathbf{U}_s = \mathbf{M}_{ts}^{-1} (\mathbf{B}_{ts} \dot{\mathbf{E}}_{xs} + \mathbf{K}_{ts} \mathbf{E}_{xs} - \mathbf{F}_e) \quad (7.16)$$

$$\mathbf{E}_{xs} = \mathbf{X}_{rs} - \mathbf{X}_s \quad (7.17)$$

$$\mathbf{X}_{rs} = \mathbf{X}_{eo} + \mathbf{K}_e^{-1} (\mathbf{K}_e + \mathbf{K}_{ts}) \mathbf{K}_{ts}^{-1} \mathbf{F}_h \quad (7.18)$$

The nomenclature is basically the same as that defined in Chapters 5 and 6, with the adding letter s in the subscript representing the *slave*. Note that the slave acceleration is not needed to implement the slave controller.

For the master, we have $\mathbf{X}_{md} = \mathbf{X}_s$, where \mathbf{X}_{md} is the desired master position. A position error based controller with local force compensation is employed, which is

$$\mathbf{F}_{mc} = \mathbf{D}_{xm} \left[\ddot{\mathbf{X}}_s + \mathbf{K}_{vm} \dot{\mathbf{E}}_{ms} + \mathbf{K}_{pm} \mathbf{E}_{xm} + \mathbf{K}_{im} \int_0^t \mathbf{E}_{xm} dt \right] + \mathbf{H}_{xm} - \mathbf{F}_h \quad (7.19)$$

where

$$\mathbf{E}_{xm} = \mathbf{X}_s - \mathbf{X}_m \quad (7.20)$$

and the letter m in the subscript representing the *master*, the diagonal matrices \mathbf{K}_{vm} , \mathbf{K}_{pm} and \mathbf{K}_{im} are the master control parameters. To implement the master controller (7.19), the slave acceleration is needed. In the case that the acceleration signal is noisy due to the numerical differentiation of the digital encoder readings, the terms with acceleration can be ignored at the penalty of transparency decrease at high frequencies.

By combining Eqs. (7.9) and (7.19), (7.10) and (7.14), the closed-loop dynamic equations can be obtained as

$$\ddot{\mathbf{X}}_s - \ddot{\mathbf{X}}_m + \mathbf{K}_{vm}(\dot{\mathbf{X}}_s - \dot{\mathbf{X}}_m) + \mathbf{K}_{pm}(\mathbf{X}_s - \mathbf{X}_m) + \mathbf{K}_{im} \int_0^t (\mathbf{X}_s - \mathbf{X}_m) dt = \mathbf{0} \quad (7.21)$$

for the master, and

$$\begin{aligned} & \left(\mathbf{M}_{ts}^{-1} \mathbf{K}_{ts} \mathbf{K}_{eqs}^{-1} + \mathbf{K}_{ps} \right) (\mathbf{F}_h - \mathbf{F}_e) + \mathbf{K}_{is} \int_0^t (\mathbf{F}_h - \mathbf{F}_e) dt \\ &= \mathbf{M}_{ts}^{-1} \left(\mathbf{M}_{ts} + \mathbf{M}_e - \mathbf{K}_{ts} \mathbf{K}_{eqs}^{-1} \mathbf{M}_e \right) \ddot{\mathbf{X}}_s + \mathbf{M}_{ts}^{-1} \left(\mathbf{B}_{ts} + \mathbf{B}_e - \mathbf{K}_{ts} \mathbf{K}_{eqs}^{-1} \mathbf{B}_e \right) \dot{\mathbf{X}}_s \end{aligned} \quad (7.22)$$

for the slave.

Taking Laplace transform of Eqs. (7.21) and (7.22), and without loss of generality, the closed-loop dynamics can be expressed in frequency domain for a single degree of freedom as

$$(X_s - X_m)s^2 + k_{vm}(X_s - X_m)s + k_{pm}(X_s - X_m) + k_{im}(X_s - X_m)\frac{1}{s} = 0 \quad (7.23)$$

for the master, and

$$\begin{aligned} & \left(\frac{k_{ts}}{m_{ts}k_{eqs}} + k_{ps} + \frac{k_{is}}{s} \right) (F_h - F_e) \\ &= \left(1 + \frac{m_e}{m_{ts}} - \frac{m_e k_{ts}}{m_{ts}k_{eqs}} \right) s^2 X_s + \left(\frac{b_{ts}}{m_{ts}} + \frac{b_e}{m_{ts}} - \frac{b_e k_{ts}}{m_{ts}k_{eqs}} \right) s X_s \end{aligned} \quad (7.24)$$

for the slave, where the parameters in small letters are the components of their corresponding matrices in Eqs. (7.21) and (7.22), and X_m , X_s , F_h , and F_e are the Laplace transform of x_m , x_s , f_h , and f_e , respectively.

Assume that the environment initially rests at $x_{eo} = 0$, and f_h^* is constant, then the steady state analysis of Eqs. (7.11), (7.12), (7.23), and (7.24) yields

$$\bar{x}_h \equiv \bar{x}_m = \bar{x}_s \equiv \bar{x}_e = \frac{f_h^*}{k_h + k_e} \quad (7.25)$$

$$\bar{f}_h = \bar{f}_e = \frac{k_e f_h^*}{k_h + k_e} \quad (7.26)$$

where $(\bar{\cdot})$ denotes the steady state value of the argument. Equations. (7.25) and (7.26) show that the master and slave steady state position and force are decided by the operator and environment stiffness coefficients and the operator exogenous force input. It is also easy to verify that $\bar{f}_h/\bar{x}_h = k_e$, i.e., the transparency is fully achieved in steady state.

7.2.1.2 Transparency Analysis

The transparency attainability is further analyzed in this section. For the master, by comparing the closed-loop dynamics of the proposed master controller and the four-channel architecture, i.e., Eqs. (7.1) and (7.23), and considering $V_e(s) = V_s(s) = sX_s(s)$ and $V_h(s) = V_m(s) = sX_m(s)$, one obtains

$$\begin{cases} C_4 = -(Z_m + C_m) = -\left(s^2 + k_{vm}s + k_{pm} + \frac{k_{im}}{s}\right) \neq 0 \\ C_2 = 0 \\ C_6 = -1 \end{cases} \quad (7.27)$$

Similarly, comparing Eqs. (7.2) and (7.24) yields

$$\begin{cases} C_s + Z_s = \frac{1}{m_{ts}} \left(m_{ts} + m_e - \frac{k_{ts}}{k_{eqs}} m_e \right) s + \frac{1}{m_{ts}} \left(b_{ts} + b_e - \frac{k_{ts}}{k_{eqs}} b_e \right) \\ C_3 = 1 + C_5 = \left(\frac{k_{ts}}{m_{ts} k_{eqs}} + k_{ps} + \frac{k_{is}}{s} \right) \\ C_1 = 0 \end{cases} \quad (7.28)$$

By comparing Eqs. (7.27) and (7.28) with the transparency condition of the F-P architecture represented by Eq. (7.8), it can be seen that the perfect transparency can be

achieved if $\frac{k_{ts}}{m_{ts}k_{eqs}} + k_{ps} + \frac{k_{is}}{s} \neq 0$, and

$$m_{ts} + m_e - \frac{k_{ts}}{k_{eqs}}m_e = 0 \quad (7.29)$$

$$b_{ts} + b_e - \frac{k_{ts}}{k_{eqs}}b_e = 0 \quad (7.30)$$

By substituting $k_{eqs} = k_e k_{ts} / (k_e + k_{ts})$ into Eqs. (7.29) and (7.30), a simple condition set for perfect transparency can then be derived as

$$\begin{cases} \frac{k_{ts}}{m_{ts}} = \frac{k_e}{m_e}; & \frac{k_{ts}}{b_{ts}} = \frac{k_e}{b_e} \\ k_{pm} \neq 0 \end{cases} \quad (7.31)$$

Therefore, in theory, transparent telemanipulation is attainable in the F-P two-channel architecture with the combined impedance/direct controller employed for the slave, and the position error based controller with local force compensation for the master, provided that the condition set (7.31) is satisfied. It can be shown that, if $\mathbf{K}_{im} = \mathbf{0}$, the transparency condition is the same as Eq. (7.31).

By observing the perfect transparency condition (7.31), it can be found that the force error based compensator at the slave does not contribute to the system transparency. In other words, ideally there is no difference whether the combined impedance/direct controller or the basic impedance controller is employed at the slave in terms of attainable transparency. However, in practice, un-modeled dynamics may exist. The combined impedance/direct control is more robust to the model uncertainties than impedance control. Therefore, in the discussed bilateral control system, the force error based PI-type compensator $k_{ps} + \frac{k_{is}}{s}$ in C_3 is expected to improve the performance by minimizing the effects of un-modeled dynamics.

Another observation is that the environment impedance is required to be known to achieve the perfect transparency according to Eq. (7.31). In fact, the environment impedance information has the same function as a force or position information channel, and that is why two-channel control architectures can achieve perfect transparency. It will be shown in Sec. 7.3 that, when the environment stiffness is estimated with error, the resulting bilateral controller will produce poor force tracking results, and thus the system is not transparent.

7.2.1.3 Stability Analysis

Based on the network model and four-channel architecture, passivity theory has been employed to design stable telemanipulation systems [3, 60]. A less conservative condition for stability is the Llewellyn's stability criteria, which provides the necessary and sufficient conditions for the absolute stability [38], and has been employed in [12, 35, 74]. A perfectly transparent system is marginally absolutely stable according to the Llewellyn's criteria. Therefore, the transparency may be sacrificed partially for increased stability, if passivity or absolute stability is employed for stability analysis. Nevertheless, Fite *et al.* [23] have used frequency-domain loop shaping method to show that both transparency and stability can be improved in the P-F two-channel architecture. This result has implied that transparency and stability are not conflicting design objectives, if right stability analysis tools are employed, such as the transfer function concept.

In this section, we analyze the stability conditions of the proposed bilateral controller with optimized transparency (i.e., condition set (7.31) is satisfied) using the recent results by Hashtrudi-Zaad and Salcudean [37], who have showed that for the transparency-optimized telemanipulation systems, the characteristic equation may be written as

$$[C_2(Z_s + C_s) + C_3(Z_m + C_m)](Z_h + Z_e) = 0 \quad (7.32)$$

which indicates that the system is stable if

$$C_2(Z_s + C_s) + C_3(Z_m + C_m) = 0 \quad (7.33)$$

has all roots in the left half-plane. Substituting Eqs. (7.27) and (7.28) into Eq. (7.33), and combining Eq. (7.31) yields the characteristic equation

$$a_4 s^4 + a_3 s^3 + a_2 s^2 + a_1 s + a_0 = 0 \quad (7.34)$$

where

$$a_0 = k_{im} k_{is} m_e k_{ts} \quad (7.35)$$

$$a_1 = k_{im} k_{ts} + k_{im} k_{ps} m_e k_{ts} + k_{pm} k_{is} m_e k_{ts} + k_{im} k_e \quad (7.36)$$

$$a_2 = k_{vm} k_{is} m_e k_{ts} + k_{pm} k_e + k_{pm} k_{ts} + k_{pm} k_{ps} m_e k_{ts} \quad (7.37)$$

$$a_3 = k_{vm}k_{ts} + k_{vm}k_{ps}m_e k_{ts} + k_{is}m_e k_{ts} + k_{vm}k_e \quad (7.38)$$

$$a_4 = k_e + k_{ts} + k_{ps}m_e k_{ts} \quad (7.39)$$

The stability condition can then be derived according to Hurwitz criteria. A problem is that the stability condition of the fourth-order system is more or less complex. The selected parameter values should be verified to satisfy the stability condition.

Let us consider the situation that the master controller has no integral term of the position error, i.e., $\mathbf{K}_{im} = \mathbf{0}$. It is easy to verify that the transparency condition (7.31) maintains the same as the situation with integral term, while the order of characteristic equation (7.34) reduces by one. As a result, according to Hurwitz criteria, the asymptotic stability of the system can be achieved, if the control parameters satisfy the following conditions: $k_e + k_{ts} + k_{ps}m_e k_{ts} > 0$, $k_{vm}k_{ts} + k_{vm}k_{ps}m_e k_{ts} + k_{is}m_e k_{ts} + k_{vm}k_e > 0$, $k_{pm}k_{is}m_e k_{ts} > 0$, and

$$(k_{vm}k_{ts} + k_{vm}k_{ps}m_e k_{ts} + k_{is}m_e k_{ts} + k_{vm}k_e)(k_{pm}k_e + k_{pm}k_{ts} + k_{pm}k_{ps}m_e k_{ts} + k_{vm}k_{is}m_e k_{ts}) > (k_e + k_{ts} + k_{ps}m_e k_{ts})k_{pm}k_{is}m_e k_{ts} \quad (7.40)$$

which can be simplified to

$$\begin{aligned} & 2k_{vm}k_{ts}k_{pm}k_e + k_{vm}k_{ts}^2k_{pm} + 2k_{vm}k_{ts}^2k_{pm}k_{ps}m_e + k_{vm}^2k_{ts}^2k_{is}m_e \\ & + 2k_{vm}k_{ps}m_e k_{ts}k_{pm}k_e + k_{vm}k_{ps}^2m_e^2k_{ts}^2k_{pm} + k_{vm}^2k_{ps}m_e^2k_{ts}^2k_{is} \\ & + k_{is}^2m_e^2k_{ts}^2k_{vm} + k_{vm}k_e^2k_{pm} + k_{vm}^2k_e k_{is}m_e k_{ts} > 0 \end{aligned} \quad (7.41)$$

Obviously, the system is stable for all positive control parameters. The above analysis shows that, in theory, the bilateral controller without the integral term of the position error at the master has the same transparency condition as that with the integral term, and has a looser stability condition. However, due to the non-ideal condition in practice, a noticeable position tracking error can be observed if the controller has no integral term at the master. With the addition of the integral term, the performance can be improved, which will be seen in Sec. 7.3.

7.2.2 P-P Architecture in Unconstrained Condition

In the unconstrained motion, the slave robot moves in free space, and $\mathbf{Z}_e = \mathbf{0}$. Therefore, the system is transparent if the operator does not feel the force, and the slave accurately

follows the motion of the master. Without the interaction between the slave and the environment, the kinematic correspondence between the master and the slave becomes the primary concern. This situation is much simpler than the constrained motion. Intuitively, the position information, rather than the force information, should be transmitted between the master and the slave. As a result, a P-P architecture is suggested in this work for unconstrained motion telemanipulation. In addition, it is suggested that the force exerted by the operator to the master is compensated for, such that the feeling of force of the operator in free space is minimized. In this case, the master controller considering both constrained and unconstrained motion can be expressed as

$$\mathbf{F}_{mc} = \mathbf{D}_{xm} \left[\ddot{\mathbf{X}}_s + \mathbf{K}_{vm} \dot{\mathbf{E}}_{ms} + \mathbf{K}_{pm} \mathbf{E}_{xm} + \mathbf{K}_{im} \int_0^t \mathbf{E}_{xm} dt \right] + \mathbf{H}_{xm} - \text{sgn}(\mathbf{F}_e) \mathbf{F}_h \quad (7.42)$$

where in this work the function $\text{sgn}(\cdot)$ is defined as

$$\text{sgn}(x) = \begin{cases} 1 & x \neq 0 \\ -1 & x = 0 \end{cases} \quad (7.43)$$

As demonstrated in Chapter 6, the combined impedance/direct control scheme does not require to switch the control modes during the transition of motion. Therefore, the same controllers for the master and the slave as in the constrained motion are used in the unconstrained motion. Specifically, when employing the combined impedance/direct control for the slave, the reference trajectory for the slave is simply set as the master position, i.e., $\mathbf{X}_r = \mathbf{X}_h$, and $\mathbf{F}_h = \mathbf{0}$. Since $\mathbf{F}_e = \mathbf{0}$ in free space motion, the slave controller is basically the impedance controller, or PD controller. Complete transparency is generally not attainable in the P-P architecture [55]. However, in the extreme situation with $\mathbf{Z}_e = \mathbf{0}$, according to Ni and Wang's [74] result about P-P architecture, we can choose high gains for the slave controller, and low gains for the master controller, such that the transmitted impedance $\mathbf{Z}_t \rightarrow \mathbf{0}$. Therefore, the extreme condition for the master parameters $\mathbf{K}_{vm} = \mathbf{K}_{pm} = \mathbf{K}_{im} = \mathbf{0}$ is set for the unconstrained motion.

7.2.3 Transition of Motion

The transition of motion between the unconstrained and constrained conditions is common during most manipulation tasks. The proposed bilateral controller requires no control mode switch of both the master and the slave controllers during the transition of motion. Once the designed controllers are implemented, they can work in both the constrained and unconstrained conditions. The only difference between the constrained and

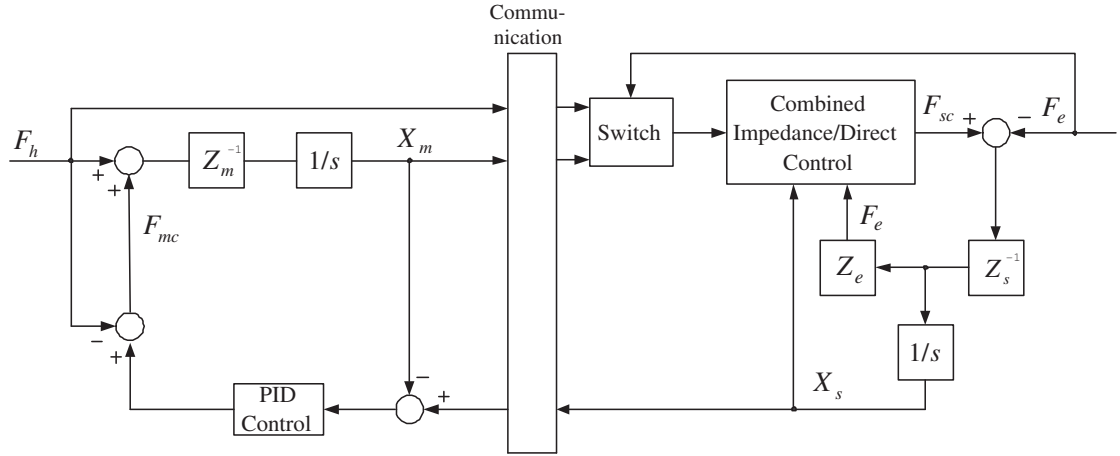


Figure 7.2: Block diagram of the proposed bilateral control scheme (Refer to Fig. 6.3 for the details of the combined impedance/direct control block).

unconstrained conditions is that different communication channels are used. Since the transparency condition in F-P and P-P architectures are different, the values of the control parameters K_{ts} , K_{pm} , K_{vm} and K_{im} need to be switched when the transition of motion takes place, in order to achieve the perfect transparency. In fact, the value of K_{ts} can be remained unchanged for both constrained and unconstrained motions, which will be shown in Sec. 7.3. The bilateral controller considering both the constrained and unconstrained motions is thus designed, and the block diagram is shown in Fig. 7.2.

7.3 Experimental Study

In this section, experiments are conducted on a system with two identical 1-DOF slider-crank mechanisms to validate the effectiveness of the proposed bilateral controller.

7.3.1 Experimental Platform

Figure 7.3 shows the photograph of the constructed platform. Both the master and the slave are driven by the EmoteqTM direct drive brushless DC motors (QB03400) with the continuous torque up to 0.81 Nm. The encoders with 2000 pulses per revolution are mounted at the end of the motor shafts to measure the angular position. The AMCTM servo amplifiers (B15A) are used to output current commands to the motors. Two simple HoneywellTM one-axis force sensor (FSG15N1A) are attached on the master and the slave, respectively, which are connected to an amplifier circuit to measure the interaction force. The Sensoray I/O board (Model 626) is used to read the sensor readings and to output commands to the motors through the amplifiers. The xPC Target from

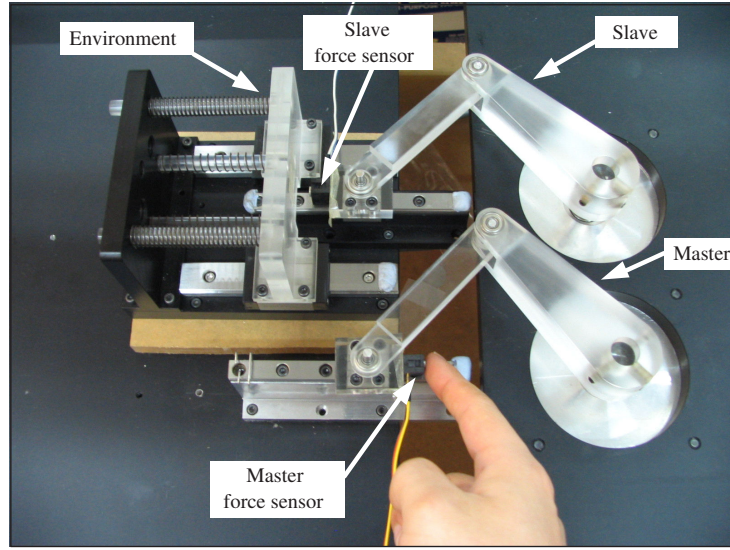


Figure 7.3: Telemanipulation experimental platform.

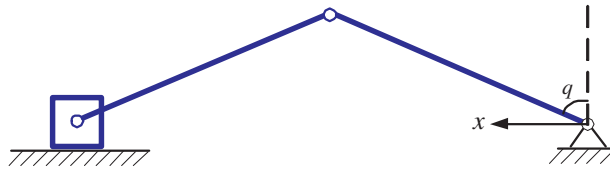


Figure 7.4: Slider crank mechanism used in the experiments.

MatlabTM is used to implement the control system with the sampling frequency set at 1 kHz. Detailed description of xPC Target can be found in Appendix A.

The slider crank mechanism with the coordinate system of the master and slave is shown in Fig. 7.4. Without considering the Coulomb and viscous frictions, the dynamic equation can be obtained by applying Euler-Lagrange method as

$$d(q)\ddot{q} + c(q)\dot{q} = \tau \quad (7.44)$$

where the parameters are estimated to be $d(q) = (7.10 \cos^2 q + 2.58) \times 10^{-4} \text{ kgm}^2$, and $c(q) = 3.55 \times 10^{-4} \dot{q} \sin(2q) \text{ kgm}^2/\text{s}$. Note that there are errors between the estimations and the real values. The environment adopts a mass-damper-spring system, which consists of a moving plate mounted on two sliders, and several spring components. The values of the impedance parameters are $m_e = 0.14 \text{ kg}$, $k_e = 400 \text{ N/m}$, and b_e is small and unknown.

As addressed, the parameters of the dynamic equation are not known precisely and have uncertainties. One of the objectives of the experiments is to show the robustness of the proposed bilateral controller to the robot dynamics uncertainties. The acceleration

term is dropped from the master controller in the experiments. For all the following experiments, $k_{ps} = 90$, $k_{is} = 80$, $m_{ts} = 1 \text{ N} \cdot \text{s}^2/\text{m}$, and $b_{ts} = 10 \text{ N} \cdot \text{s}/\text{m}$. During the constrained motion, the parameters of the master controller are set as $k_{pm} = 1.8 \times 10^4$, $k_{vm} = 10$, and $k_{im} = 10^4$. While during the unconstrained motion, $k_{pm} = k_{vm} = k_{im} = 0$. Note that in practice, due to the noise of differentiating the encoder signals, especially in the constrained motion, parameters b_{ts} and k_{vm} should be assigned with relatively small values. In the experiments, it has been found that when b_{ts} is increased to $100 \text{ N} \cdot \text{s}/\text{m}$, most likely the system goes to be unstable.

7.3.2 Results of Constrained Motion

The first set of experiments studies the system performance in the constrained motion. Before the experiments, the slider of the slave locates at the initial position of the environment $x_{eo} = 122.32 \text{ mm}$. The master locates correspondingly. During the experiments, the human operator pushes the master slider along the x -axis direction and then releases gradually.

Firstly, the controller without the integral term of the position error at the master is implemented. According to the perfect transparency condition (7.31), the slave target stiffness is set as $k_{ts} = 3000 \text{ N}/\text{m}$, such that the system is regarded to be quasi transparent. The results are shown in Fig. 7.5. The force profiles of the master and the slave (see Fig. 7.5(b)) show that the interaction force f_e can follow the command f_h with high accuracy. However, a relatively large position error between the master and the slave exists, when the operator pushes the master slider and keeps it at a constant position. The results reveal that, in practice, it is hard to construct perfect transparent systems, if the controller has no integral term of the position error at the master. Nevertheless, the resulting system is expected to work well in the case that the master-slave position correspondence is not a critical requirement.

Secondly, the integral term of the position error is included in the master controller, and the results are shown in Fig. 7.6. The force profiles show a similar or a little better tracking result, and the position error is reduced greatly, if compared to the results without the integral term at the master. It can be observed that the transient position error still exists, especially during the restoring stage of the environment. This phenomena can be explained as follows. At the stage of pushing, the term $(x_s - x_m)$ is negative, and thus the integral term builds up negative control actions of the master continuously. When the operator releases the master slider gradually, the resulting negative control actions by the integral term will drive the master to move faster than the slave. Another possible reason

is that the Coulomb and viscous frictions may dominate the environment dynamics at the restoring stage, which slow the restoring of the environment. The transient error decreases gradually to zero at the steady state. Another observation is that the integral term introduces a small oscillation into the master position, the amplitude of which is about one encoder count. Note that in the experimental platform, the motors are driven directly without gear-head connected. Overall, the transparency of the system is increased by incorporating the integral term of the position error into the master controller.

Next, the slave target stiffness is set as $k_{ts} = 1.8 \times 10^4 \text{ N/m}$, and therefore the system is nontransparent. The results for this system are shown in Fig. 7.7. The position profiles are similar to those of the quasi transparent system shown in Fig. 7.6(a). Although the force tracking error increases a little bit, if compared to the quasi transparent system (see Fig. 7.6(b)), the error is small and can be neglected normally. In this case, the value of k_{ts} can be kept unchanged during the transition of motions.

Finally, it is assumed that the environment stiffness is unknown and estimated to be $\hat{k}_e = 2500 \text{ N/m}$. The slave target stiffness is thus designed to be $k_{ts} = 1.8 \times 10^4 \text{ N/m}$, in order to achieve perfect transparency. Figure 7.8 shows the results. Interestingly, the position error is reduced. However, the force tracking performance deteriorates drastically. The results comply with the analysis in Sec. 7.2.1 that for the F-P two channel control architecture, the information of the environment impedance is required to be known to achieve perfect transparency.

7.3.3 Results of Transition of Motion

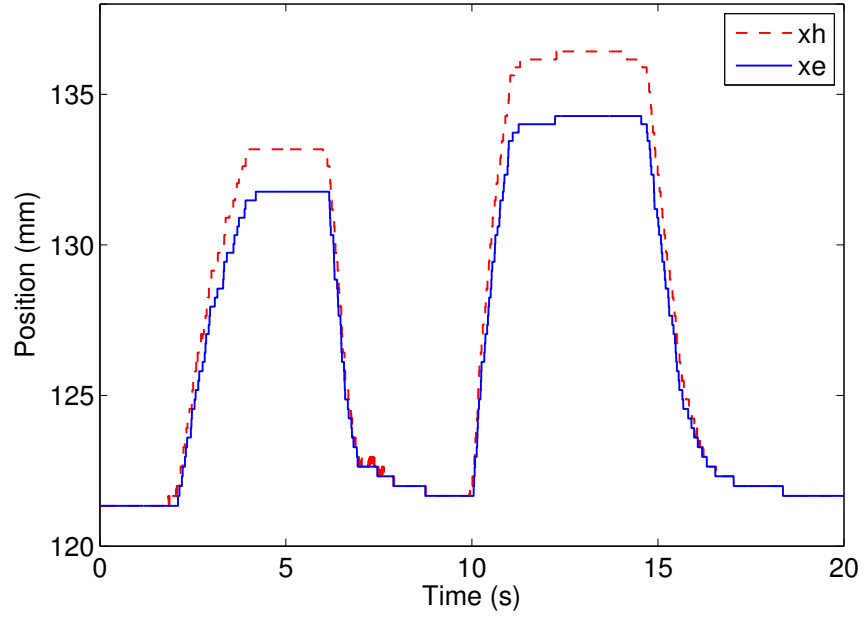
In the second set of experiments, the slave slider is initially located at $x = 113.10 \text{ mm}$. So does the master slider. During the experiment, the operator pushes the master slider along the x -axis direction. The free space motion transits to the constrained motion when the slave slider contacts the environment at $x = 122.32 \text{ mm}$. Afterwards, the operator repeats to push and then release the master several times, followed by the transition from the constrained motion to the free space motion.

The slave target stiffness is set as $k_{ts} = 1.8 \times 10^4 \text{ N/m}$. Therefore, during the transition of motion, it does not need to switch the control modes and the values of the control parameters of the slave controller. For the master, the control mode is also kept un-switched, while the values of the control parameters should be switched from $k_{pm} = k_{vm} = k_{im} = 0$ to $k_{pm} = 1.8 \times 10^4$, $k_{vm} = 10$, and $k_{im} = 10^4$ in order for transparency. Note that the transparency conditions of F-P and P-P architectures are different (refer to Sections. 7.2.1 and 7.2.2). As shown in Fig. 7.9, the motion transits

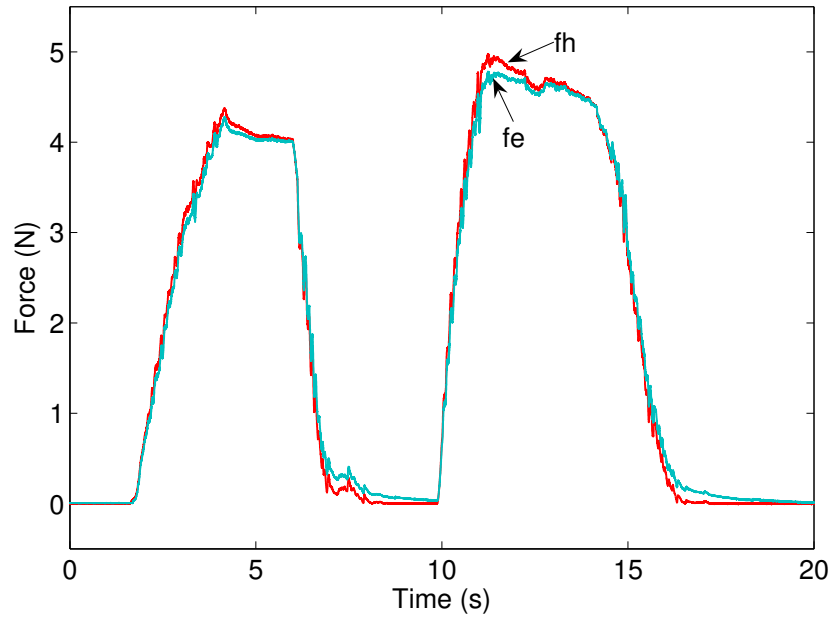
smoothly. In addition, the kinematic correspondence is maintained when the motion transits from the contact condition to the free space, which is important for repetitive and consecutive manipulations. High transparency in both constrained and unconstrained motions has been demonstrated by the results.

7.4 Concluding Remarks

By applying the combined impedance/direct control scheme, a two-channel bilateral controller is proposed for telemanipulation systems in this chapter. A control architecture is constructed considering both the free space motion and the constrained motion. Specifically, the F-P architecture is applied in the constrained motion, while the P-P architecture is applied in the free space motion. The proposed bilateral control scheme has the following features. Firstly, perfect transparency can be achieved in the two-channel control architecture in theory. Secondly, the interaction force F_e can be controlled with high accuracy in the case of robot dynamic uncertainties. Thirdly, although different control architectures are employed for the constrained and unconstrained motions, it does not need to switch the control modes of the master and the slave controllers during the transition of motion. Note that different communication channels are used in the constrained and unconstrained conditions, i.e., F-P architecture for constrained condition, and P-P architecture for the unconstrained condition. The effectiveness of the proposed bilateral control scheme has been demonstrated by the experiments.

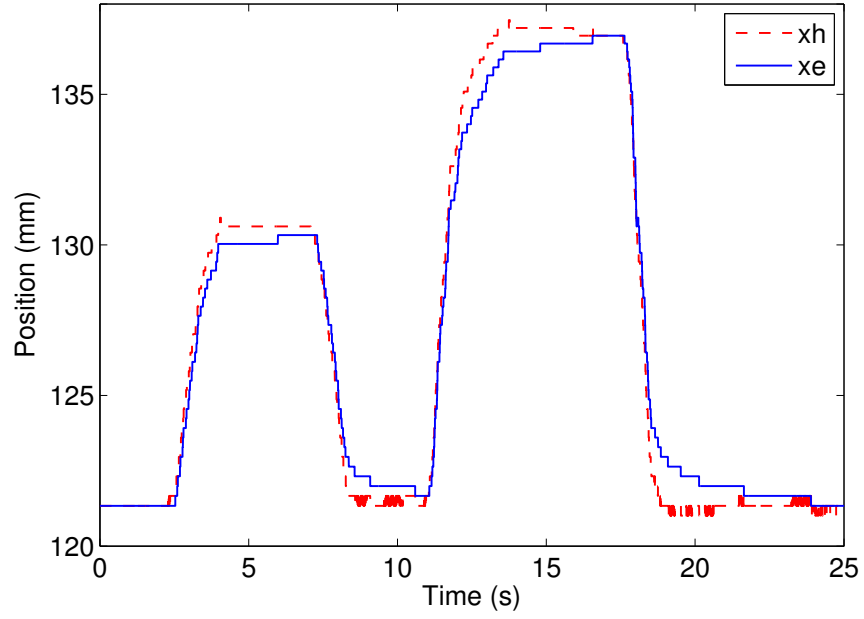


(a) Position

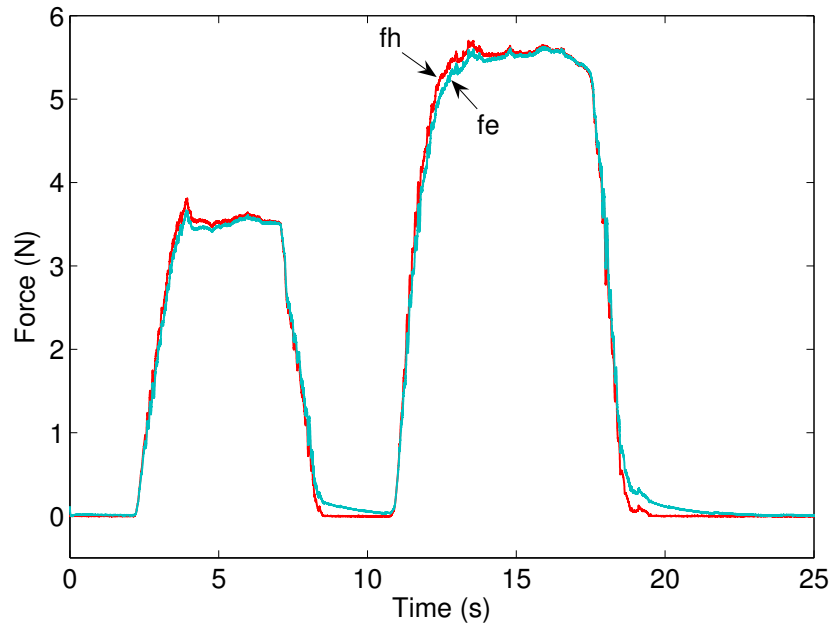


(b) Force

Figure 7.5: Results of the quasi transparent system without integral term of position error at the master. The environment impedance parameters are $k_e = 400$ N/m, $m_e = 0.14$ kg, and b_e unknown. The control parameters are set as $m_{ts} = 1$ N \cdot s²/m, $b_{ts} = 10$ N \cdot s/m, $k_{ts} = 3000$ N/m, $k_{ps} = 90$, $k_{is} = 80$, $k_{pm} = 1.8 \times 10^4$, and $k_{vm} = 10$.

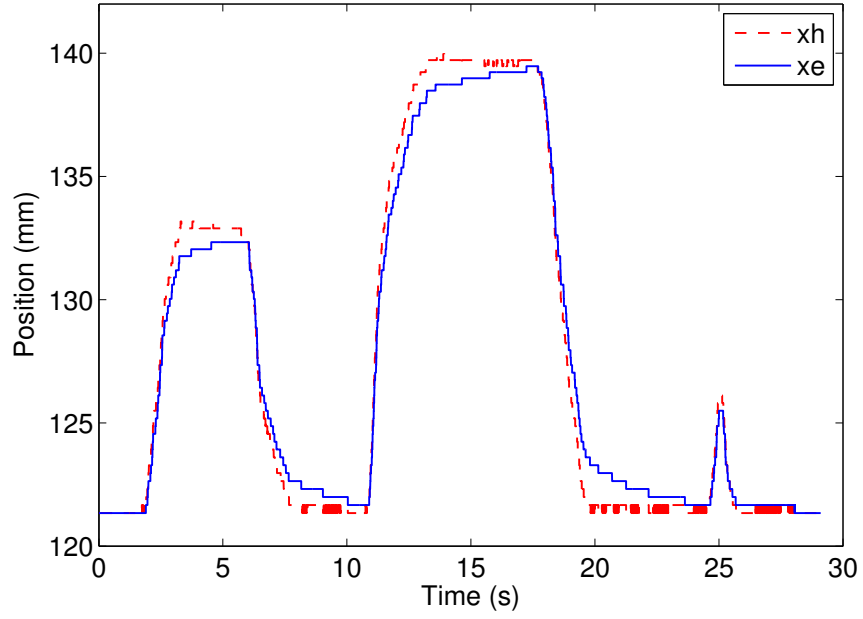


(a) Position

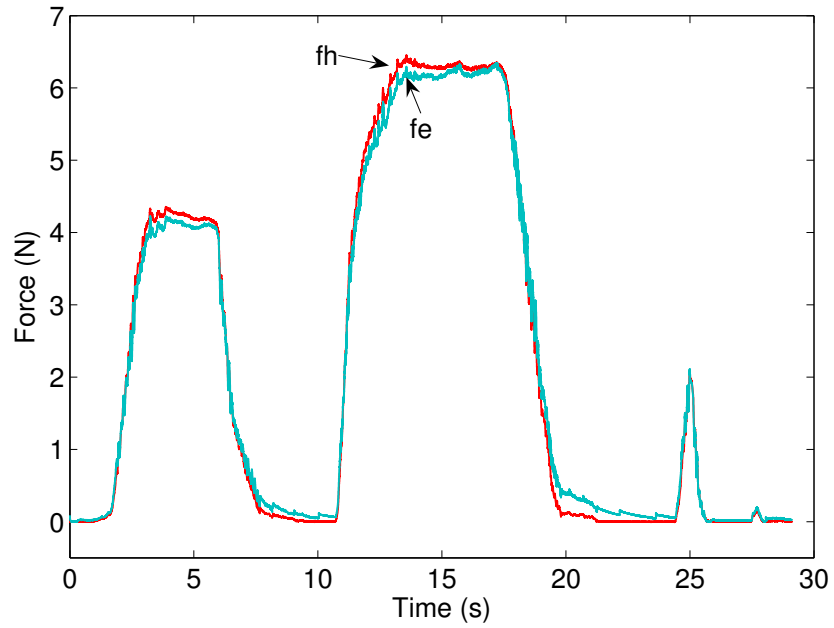


(b) Force

Figure 7.6: Results of the quasi transparent system with integral term of position error at the master. The environment impedance parameters are $k_e = 400$ N/m, $m_e = 0.14$ kg, and b_e unknown. The control parameters are set as $m_{ts} = 1$ N · s²/m, $b_{ts} = 10$ N · s/m, $k_{ts} = 3000$ N/m, $k_{ps} = 90$, $k_{is} = 80$, $k_{pm} = 1.8 \times 10^4$, $k_{vm} = 10$, and $k_{im} = 10^4$.

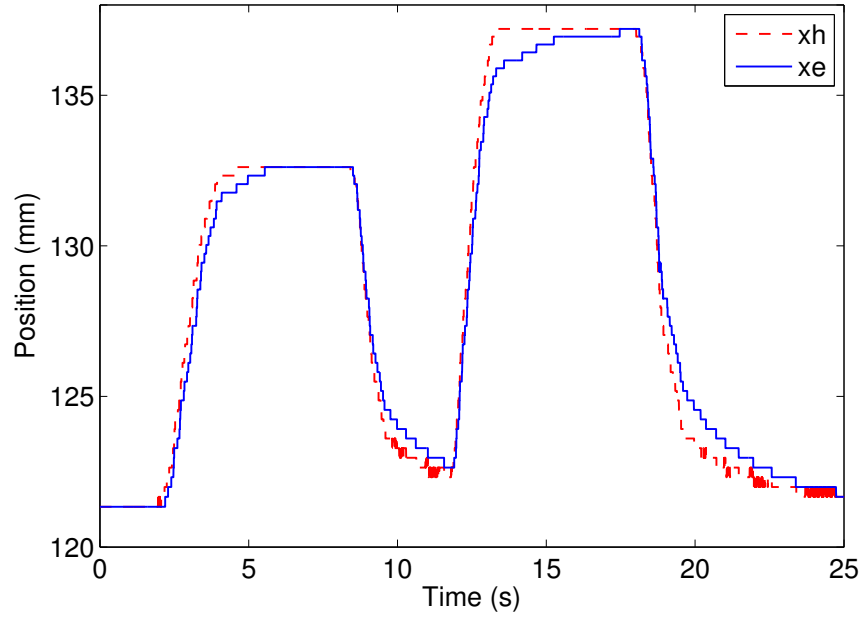


(a) Position

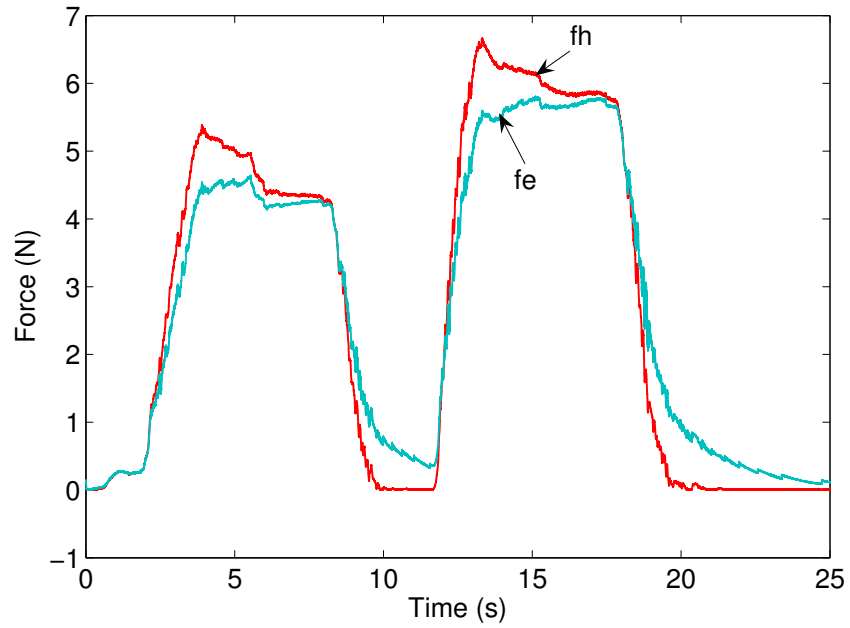


(b) Force

Figure 7.7: Results of nontransparent system with integral term of position error at the master. The environment impedance parameters are $k_e = 400 \text{ N/m}$, $m_e = 0.14 \text{ kg}$, and b_e unknown. The control parameters are set as $m_{ts} = 1 \text{ N} \cdot \text{s}^2/\text{m}$, $b_{ts} = 10 \text{ N} \cdot \text{s}/\text{m}$, $k_{ts} = 1.8 \times 10^4 \text{ N/m}$, $k_{ps} = 90$, $k_{is} = 80$, $k_{pm} = 1.8 \times 10^4$, $k_{vm} = 10$, and $k_{im} = 10^4$.

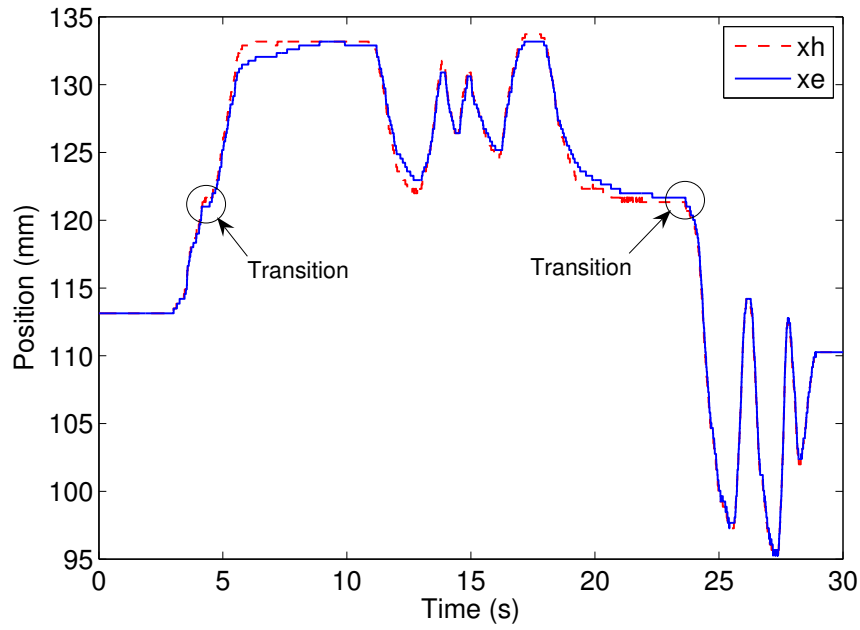


(a) Position

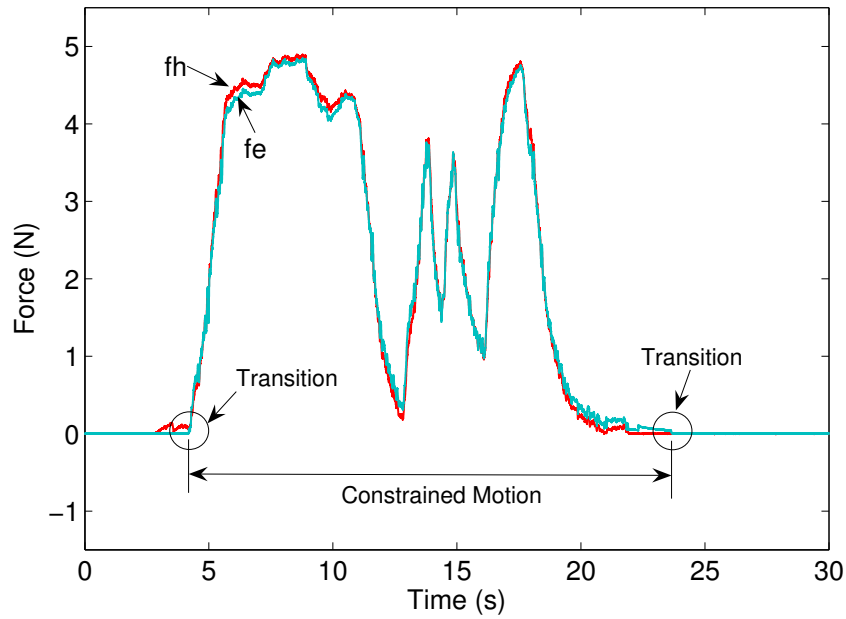


(b) Force

Figure 7.8: Results in the case that the environment stiffness is estimated with error. The environment impedance parameters are $k_e = 400$ N/m, $m_e = 0.14$ kg, and b_e unknown. k_e is estimated as $\hat{k}_e = 2500$ N/m. The control parameters are set as $m_{ts} = 1$ N \cdot s²/m, $b_{ts} = 10$ N \cdot s/m, $k_{ts} = 1.8 \times 10^4$ N/m, $k_{ps} = 90$, $k_{is} = 80$, $k_{pm} = 1.8 \times 10^4$, $k_{vm} = 10$, and $k_{im} = 10^4$.



(a) Position



(b) Force

Figure 7.9: Results of an operation including transition between the free space motion and the constrained motion. The environment impedance parameters are $k_e = 400$ N/m, $m_e = 0.14$ kg, and b_e unknown. k_e is known. The control parameters are set as $m_{ts} = 1$ N · s²/m, $b_{ts} = 10$ N · s/m, $k_{ts} = 1.8 \times 10^4$ N/m, $k_{ps} = 90$, $k_{is} = 80$, $k_{pm} = 0$ (free space motion) or 1.5×10^4 (constrained motion), $k_{vm} = 10$, and $k_{im} = 0$ (free space motion) or 10^4 (constrained motion).

Chapter 8

Conclusions and Future Work

This chapter first presents possible overall structures, which connect the kinematic mapping addressed in Part I and the controller design addressed in Part II. The contributions of the thesis are then summarized, followed by the discussion of future work. Finally, the conclusion is given.

8.1 Structures Combining Mapping and Control

The work on the kinematic mapping and the control scheme design are both related to telemanipulation. A good system with high degree of telepresence requires both a suitable mapping scheme and a proper controller. This section provides two possible overall structures to combine the proposed mapping and control schemes in a telemanipulation system. Note that the virtual circle mapping method proposed in Part I can be combined with the control schemes other than the one proposed in Part II. Similarly, the bilateral controller proposed in Part II can be implemented in a system with any mapping schemes applied.

8.1.1 Structure I

The P-F two-channel architecture is widely used in the telemanipulation systems. In the first structure, the virtual circle mapping method is combined with the P-F control architecture. Under the given structure, the virtual circle mapping scheme can be integrated into the systems with any P-F bilateral controller applied.

A typical operation of a telemanipulation system can be divided into two parts, namely the free space operation and the object manipulation operation. In the free space operation, none of the slave fingers contact the object. Positions of the human fingertips are measured and used to compute the desired slave fingertip positions according to the

virtual circle mapping scheme. The desired slave fingertip positions are then sent to the slave controller as the position input to the slave fingers. Since the slave hand moves in free space, no force information is fed back to the master. The object manipulation operation starts once the slave fingers get in contact with the object. During the object manipulation operation, the desired slave fingertip positions are computed according to the human fingertip positions by the virtual circle mapping scheme, and then sent to the slave. The actual slave fingertip positions are obtained by the sensor readings of the slave. The differences between the desired and the actual positions, i. e., the position errors, can then be used by the slave controller to derive the driving forces for the slave fingers. At the same time, the contact force between the slave fingers and the object is fed back to the master, which is used to derive the driving forces for each of the master fingers, such that the operator feels the contact force.

8.1.2 Structure II

Before the description of the second structure, the reverse of the virtual circle mapping is first defined. Recall that the fundamental idea of the virtual circle mapping is to construct a relationship between two virtual circles, which are decided by the human and robot hands, respectively. The method presented in Chapter 4 is a forward way of the mapping, i. e., mapping from the human to the robot. In a similar way, the mapping from the slave hand to the human hand can also be constructed, which can be named as reverse of virtual circle mapping.

In the second structure, the virtual circle mapping scheme and the proposed bilateral controller in Part II, which is a F-P architecture, are combined. In the free space operation, same as in Structure I, the virtual circle mapping produces the desired slave positions, which are then sent to the slave controller. The slave controller controls the slave fingers to follow the desired position. While in the object manipulation operation, the force applied by the human fingers to the master device are measured and sent from the master to the slave. The slave controller, which is a combined impedance/direct controller, generates the driving force for each of the slave fingers according to the received force information. At the same time, the positions of the slave fingers are measured, according to which the desired human fingertip positions are generated by the reverse of virtual circle mapping method. The desired human fingertip positions are then fed back to the master controller, which commands the human fingers to follow the desired positions.

Two sample structures combining the mapping and control are thus given. It is worth

pointing out that the virtual circle mapping and the proposed bilateral controller are basically two schemes for the telemanipulation systems, which aim to improve the telepresence from different perspectives. They can be combined as described in the second structure. In addition, Each of them can also be applied in a system with other mapping or control schemes, as described in the first structure. In other words, more combination schemes are possible. The detailed development work are not discussed in this work though.

8.2 Summary of Contributions

The major contributions of this thesis are summarized as follows:

- The problem of tele-controlling a non-anthropomorphic robot hand is put forward. The classical fingertip position mapping has been implemented in the system with a three-fingered non-anthropomorphic robot hand. The system performance has been investigated by simulations and experiments. It has been found that the fingertip position mapping method fails to provide satisfactory degree of intuitiveness and workspace matching between the master and the slave hands, and new mapping methods should be developed for the systems with non-anthropomorphic robot hands.
- A virtual circle mapping method is proposed for tele-controlling the three-fingered slave robot hands. The concept of the method has been introduced. An algorithm for a specific three-fingered robot hand has been presented. The simulation results of the workspace matching have shown that the proposed method can account for the dissimilarities between the human hand and the robot hand, and therefore more effective for tele-controlling the non-anthropomorphic robot hands. The experiments demonstrates the feasibility of the proposed method. Although the presented algorithm is specific for the non-anthropomorphic robot hand introduced in Sec. 3.1.2, the idea of virtual circle mapping is applicable for all kinds of three-fingered robot hands, both anthropomorphic and non-anthropomorphic.
- By developing the test-bed for the mapping methods, a mechatronic design approach to manipulator control in free space is presented. Different from the normal design procedure, in which the mechanical system and the electrical system are treated separately, the presented mechatronic approach takes into account all

the dynamics of the manipulator, actuators, amplifiers, and I/O boards in a united manner. The method can be extended to design the motion control system of other mechanical systems.

- The force tracking performance of the impedance control subjecting to model uncertainties and random external disturbances is investigated. Several insights have been obtained through the investigation. It is also found that the model and environment uncertainties affect the performance of the impedance control. The investigation provides the basis for proposing new control schemes, which can improve the robustness to the disturbances and uncertainties, and maintains the advantage of the impedance control at the same time.
- The combined impedance/direct control scheme for control of robot manipulators has been proposed. The controller is composed of two parts, namely the direct force control action and the impedance control action. A sufficient stability condition is given. The theoretical analysis, simulations and experiments have shown the superiority of the proposed controller over the impedance control and the hybrid position/force control. The combined impedance/direct control combines the advantages of both the impedance control (i.e., no need to switch the control modes for all tasks) and the hybrid position/force control (i.e., higher robustness to the environmental uncertainties and disturbances).
- By applying the combined impedance/direct control scheme, a two-channel bilateral controller is proposed for telemanipulation systems. A control architecture is constructed considering both the free space motion and the constrained motion. In theory, perfect transparency can be achieved in the proposed control architecture. In addition, it does not need to switch the control modes of the master and the slave controllers during the transition of motion. Once the designed controllers are implemented, they can work in both the constrained and unconstrained conditions. One more advantage is that the controller is robust to un-modeled dynamics and uncertainties. Experiments have been conducted to verify the effectiveness of the proposed bilateral control architecture.

8.3 Suggestions for Future Work

There are several possible directions for future work in the areas of research presented in this thesis. Some suggestions are as follows:

- The application of the virtual circle mapping method to other three-fingered robot hands. The concept of the virtual circle mapping has been introduced in Sec. 4.1. A detailed algorithm has also been developed for a specific three-fingered robot hand. Since a different robot hand usually has a different structure, it can be expected that the mapping algorithms developed for other systems from the virtual circle mapping concept should be altered from the one presented in Chapter 4 to a certain extent. Therefore, it is worth developing specialized mapping algorithms for other three-fingered robot hands based on the one presented in this thesis by applying the virtual circle mapping concept. For instance, the concept can be applied to the robot hands shown in Figs. 2.1(b) and 2.1(c).
- Development of new mapping methods for the four-fingered non-anthropomorphic robot hands. The mapping for the four-fingered non-anthropomorphic robot hands is remained unaddressed. Due to the same reason given in Chapter 3, it can be expected that the traditional mapping methods also cannot produce satisfactory mapping results if the slave robot hand is a four-fingered one and has a symmetric structure. The proposed virtual circle mapping method is an extension of the Griffin's virtual object based mapping method [31] from 2-D to 3-D. The two methods basically transmit the information of the relative position between the fingertips from the master to the slave. Therefore, they can be named as the relative position based mapping. A possible direction of mapping is then to extend the relative position based mapping concept to the four-fingered non-anthropomorphic robot hands. Toward this end, it is desired to find a *carrier* to carry the information of the relative position between the four fingertips. Note that the *carrier* in the virtual circle mapping method is a circle, and that of the virtual object based mapping [31] is a sphere.
- Applying the combined impedance/direct control scheme to construct other types of control architectures for telemanipulation systems. Besides the bilateral controller proposed in Chapter 7, other types of bilateral controllers, such as two-channel P-F architecture, three-channel architectures, and four-channel architecture, can be developed by applying the combined impedance/direct control scheme.

8.4 Conclusions

As introduced in Chapter 1, a good telemanipulation system should provide high degree of telepresence to the operator, such that he/she feels physically present at the remote site. This thesis presents the efforts aiming to improve the telepresence of the telemanipulation systems from two aspects, which are the kinematic mapping and the control scheme design. Specifically, part I deals with the kinematic mapping between a human and a robot hand. The rules of mapping are explored and the superiority of the proposed virtual circle mapping is demonstrated. In particular, the systems with three-fingered non-anthropomorphic robot hands are considered. The objective is to develop new mapping methods to improve the degree of intuitiveness experienced by the human operator. The main focus of part II is on the control scheme design. The objective is to apply the well developed single manipulator control schemes to the telemanipulation systems, such that the problem of the bilateral controller design can be simplified, and at the same time, the robot nonlinear dynamics and uncertainties are properly dealt with. The simulation and experimental results have demonstrated the inefficiency of the previous methods, and the effectiveness of the proposed methods.

The last part of the thesis summarizes the contributions, and addresses several possible research directions to extend the ideas and methods presented in this work.

Bibliography

- [1] *xPC Target Getting Started Guide*. MA, USA: MathWorks, Inc., 2005.
- [2] R. Anderson and M. Spong, “Hybrid impedance control of robotic manipulators,” *IEEE Journal of Robotics and Automation*, vol. 4, no. 5, pp. 549–556, Oct. 1988.
- [3] R. Anderson and M. Spong, “Bilateral control of teleoperators with time delay,” *IEEE Transactions on Automatic Control*, vol. 34, no. 5, pp. 494–501, May 1989.
- [4] M. Bouzit, “Design, implementation and testing of a data glove with force feedback for virtual and real objects telemanipulation,” Ph.D. dissertation, Laboratoire de Robotique de Paris, University of Pierre Et Marie Curie, Paris, France.
- [5] M. Bouzit, G. C. Burdea, G. Popescu, and R. Boian, “The rutgers master II—New design force-feedback glove,” *IEEE/ASME Transactions on Mechatronics*, vol. 7, no. 2, pp. 256–263, June 2002.
- [6] G. C. Burdea, *Force and Touch Feedback for Virtual Reality*. New York: John Wiley & Sons, 1996.
- [7] G. Campion, Q. Wang, and V. Hayward, “The pantograph Mk-II: A haptic instrument,” in *Proceedings of the IEEE/RSJ International Conference on Intelligent Robots and Systems (IROS’05)*, Edmonton, Alberta, Canada, Aug. 2005, pp. 723–728.
- [8] M. C. Çavuşoğlu, D. Feygin, and F. Tendick, “A critical study of the mechanical and electrical properties of the phantom(tm) haptic interface and improvements for high performance control,” *Presence*, vol. 11, no. 6, pp. 555–568, Dec. 2002.
- [9] C. C. Cheah and D. Wang, “Learning impedance control for robotic manipulators,” *IEEE Transactions on Robotics and Automation*, vol. 14, no. 3, pp. 452–465, June 1998.

- [10] S. Chiaverini and L. Sciavicco, "The parallel approach to force/position control of robotic manipulators," *IEEE Transactions on Robotics and Automation*, vol. 9, no. 4, pp. 361–373, Aug. 1993.
- [11] S. Chiaverini, B. Siciliano, and L. Villani, "A survey of robot interaction control schemes with experimental comparison," *IEEE/ASME Transactions on Mechatronics*, vol. 4, no. 3, pp. 273–285, Sept. 1999.
- [12] H. C. Cho and J. H. Park, "Stable bilateral teleoperation under a time delay using a robust impedance control," *Mechatronics*, vol. 15, no. 5, pp. 611–625, June 2005.
- [13] B. H. Choi and H. R. Choi, "SKK hand master-hand exoskeleton driven by ultrasonic motors," in *Proceedings of the IEEE/RSJ International Conference on Intelligent Robots and Systems (IROS'00)*, Takamatsu, Japan, Oct. 2000, pp. 1131–1136.
- [14] W. S. Chou, T. M. Wang, and L. Hu, "Design of data glove and arm type haptic interface," in *Proceedings of the IEEE 11th Symposium on Haptic Interfaces for Virtual Environment and Teleoperator Systems (HAPTICS'03)*, Los angeles, CA, USA, Mar. 2003, pp. 422–427.
- [15] J. J. Craig, *Introduction to Robotics: Mechanics and Control*, 2nd ed. Reading, MA: Addison Wesley, 1989.
- [16] M. Cutkosky and R. Howe, "Human grasp choice and robotic grasp analysis," *Dextrous Robot Hands*, Venkataraman and T. Iberall Eds., pp. 5–31, 1990.
- [17] R. W. Daniel and P. R. McAree, "Fundamental limits for force reflecting teleoperation," *The International Journal of Robotics Research*, vol. 17, no. 8, pp. 811–830, Aug. 1998.
- [18] R. V. Dubey, T. F. Chan, and S. E. Everett, "Variable damping impedance control of a bilateral telerobotic system," *IEEE Control System Magazine*, vol. 17, no. 1, pp. 37–44, Feb. 1997.
- [19] R. V. Dubey, S. E. Everett, N. Pernalet, and K. A. Manocha, "Teleoperation assistance through variable velocity mapping," *IEEE Transactions on Robotics and Automation*, vol. 17, no. 5, pp. 761–766, Oct. 2001.

- [20] G. Ferretti, G. Magnani, P. Rocco, F. Cecconello, and G. Rossetti, “Impedance control for industrial robots,” in *Proceedings of the IEEE International Conference on Robotics and Automation (ICRA’00)*, Francisco, CA, USA, Apr. 2000, pp. 4027–4032.
- [21] M. Fischer, P. Smagt, and G. Hirzinger, “Learning techniques in a dataglove based telemanipulation system for the DLR hand,” in *Proceedings of the IEEE International Conference on Robotics and Automation (ICRA’98)*, Leuven, Belgium, May 1998, pp. 1603–1608.
- [22] W. D. Fisher and M. S. Mujtaba, “Sufficient stability condition for hybrid position/force control,” in *Proceedings of the IEEE International Conference on Robotics and Automation (ICRA’92)*, Nice, France, May 1992, pp. 1336–1341.
- [23] K. B. Fite, L. Shao, and M. Goldfarb, “Loop shaping for transparency and stability robustness in bilateral telemanipulation,” *IEEE Transactions on Robotics and Automation*, vol. 20, no. 3, pp. 620–624, June 2004.
- [24] K. B. Fite, J. E. Speich, and M. Goldfarb, “Transparency and stability robustness in two-channel bilateral telemanipulation,” *Journal of Dynamic Systems, Measurement, and Control*, vol. 123, no. 3, pp. 400–407, Sept. 2001.
- [25] J. G. Frankel, M. E. Kontz, and W. J. Book, “Design of a testbed for haptic control of hydraulic systems,” in *Proceedings of the ASME International Mechanical engineering congress and Exposition (IMECE’04)*, Anaheim, CA, USA, Nov. 2004.
- [26] A. Frisoli, E. Sotgiu, C. Avizzano, D. Checcacci, and M. Bergamasco, “Force-based impedance control of a haptic master system for teleoperation,” *Sensor Review*, vol. 24, no. 1, pp. 42–50, 2004.
- [27] B. E. Fritz, W. Yu, N. Pernalet, M. Jurczyk, and R. V. Dubey, “Enhancing the manipulation capabilities of persons with disabilities using sensor assisted teleoperation,” in *The 15th Florida Conference on Recent Advances in Robotics, FCRAR’02*, Miami, FL, USA, May 2002.
- [28] R. C. Goertz, “Mechanical master-slave manipulators,” *Nucleonics*, vol. 12, no. 11, pp. 45–46, Nov. 1954.
- [29] R. C. Goertz and W. M. Thompson, “Electronically controlled manipulators,” *Nucleonics*, vol. 12, no. 11, pp. 46–47, Nov. 1954.

- [30] P. Gorce and N. Rezzoug, "A method to learn hand grasping posture from noisy sensing information," *Robotica*, vol. 22, no. 3, pp. 309–318, May 2004.
- [31] W. B. Griffin, "Shared control for dexterous telemanipulation with haptic feedback," Ph.D. dissertation, Department of Mechanical Engineering, Stanford University, Stanford, CA, USA.
- [32] W. B. Griffin, W. R. Provancher, and M. R. Cutkosky, "Feedback strategies for telemanipulation with shared control of object handling forces," *Presence*, vol. 14, no. 6, pp. 720–731, Dec. 2005.
- [33] B. Hannaford, L. Wood, D. A. McAfee, and H. Zak, "Performance evaluation of a six-axis generalized force-reflecting teleoperator," *IEEE Transactions on Systems, Man, and Cybernetics*, vol. 21, no. 3, pp. 620–633, 1991.
- [34] B. Hannaford, "A design framework for teleoperators with kinesthetic feedback," *IEEE Transactions on Robotics and Automation*, vol. 5, no. 4, pp. 426–434, Aug. 1989.
- [35] K. Hashtrudi-Zaad and S. E. Salcudean, "Analysis of control architectures for teleoperation systems with impedance/admittance master and slave manipulators," *The International Journal of Robotics Research*, vol. 20, no. 6, pp. 419–445, June 2001.
- [36] K. Hashtrudi-Zaad and S. E. Salcudean, "Bilateral parallel force/position teleoperation control," *Journal of Robotic Systems*, vol. 19, no. 4, pp. 155–167, Apr. 2002.
- [37] K. Hashtrudi-Zaad and S. E. Salcudean, "Transparency in time-delayed systems and the effect of local force feedback for transparent teleoperation," *IEEE Transactions on Robotics and Automation*, vol. 18, no. 1, pp. 108–114, Feb. 2002.
- [38] S. S. Haykin, *Active Network Theory*. Addison-Wesley, 1970.
- [39] V. Hayward, O. R. Astley, M. Cruz-Hernandez, D. Grant, and G. Robles-De-La-Torre, "Haptic interfaces and devices," *Sensor Review*, vol. 24, no. 1, pp. 16–29, 2004.

- [40] N. Hogan, "Impedance control: An approach to manipulation. parts i, ii and iii," *ASME Journal of Dynamic Systems, Measurement and Control*, vol. 107, no. 1, pp. 1–24, Mar. 1985.
- [41] J. Hong and X. Tan, "Calibrating a VPL DataGlove for teleoperating the Utah/MIT hand," in *Proceedings of the IEEE International Conference on Robotics and Automation (ICRA'89)*, Scottsdale, AZ, USA, May 1989, pp. 1752–1757.
- [42] T. C. Hsia, T. A. Lasky, and Z. Y. Guo, "Robust independent robot joint control: design and experimentation," in *Proceedings of the IEEE International Conference on Robotics and Automation (ICRA'1988)*, Philadelphia, USA, 1998, pp. 1329–1334.
- [43] H. Hu, X. Gao, J. Li, J. Wang, and H. Liu, "Calibrating human hand for teleoperating the hit/dlr hand," in *Proceedings of the IEEE International Conference on Robotics and Automation (ICRA'04)*, New Orleans, LA, USA, Apr. 2004, pp. 4571–4576.
- [44] H.-P. Huang and Y.-F. Wei, "Control of dexterous hand master with force feedback," in *Proceedings of the IEEE International Conference on Robotics and Automation (ICRA'98)*, Leuven, Belgium, May 1998, pp. 687–692.
- [45] L. Huang, S. S. Ge, and T. H. Lee, "Neural network based adaptive impedance control of constrained robots," in *IEEE Proceedings of the International Symposium on Intelligent Control (ISIC'02)*, Vancouver, Canada, Oct. 2002, pp. 615–619.
- [46] Z.-H. Jiang, "Impedance control of flexible robot arms with parametric uncertainties," *Journal of Intelligent and Robotic Systems*, vol. 42, no. 2, pp. 113–133, Feb. 2005.
- [47] S. Jung and T. C. Hsia, "Neural network impedance force control of robot manipulator," *IEEE Transactions on Industrial Electronics*, vol. 45, no. 3, pp. 451–461, June 1998.

- [48] S. Jung, T. C. Hsia, and R. G. Bonitz, "Force tracking impedance control for robot manipulators with an unknown environment: Theory, simulation, and experiment," *The International Journal of Robotics Research*, vol. 20, no. 9, pp. 765–774, Sept. 2001.
- [49] S. B. Kang and K. Ikeuchi, "Toward automatic robot instruction from perception–mapping human grasps to manipulator grasps," *IEEE Transactions on Robotics and Automation*, vol. 13, no. 1, pp. 81–95, Feb. 1997.
- [50] H. Kawasaki, K. Nakayama, T. Mouri, and S. Ito, "Virtual teaching based on hand manipulability for multi-fingered robots," in *Proceedings of the IEEE International Conference on Robotics and Automation (ICRA'01)*, Seoul, Korea, May 2001, pp. 1388–1393.
- [51] H. Kawasaki, J. Takai, and Y. Tanaka, "Control of multi-fingered haptic interface opposite to human hand," in *Proceedings of the IEEE/RSJ International Conference on Intelligent Robots and Systems (IROS'03)*, Las Vegas, Nevada, USA, Oct. 2003, pp. 2707–2712.
- [52] H. Kazerooni, P. K. Houpt, and T. B. Sheridan, "Robust compliant motion for manipulators," *IEEE Journal of Robotics and Automation*, vol. 2, pp. 83–105, 1986.
- [53] H. Kazerooni, T.-I. Tsay, and K. Hollerbach, "A controller design framework for telerobotic systems," *IEEE Transactions on Control Systems Technology*, vol. 1, no. 1, pp. 50–62, Mar. 1993.
- [54] O. Khatib, "A unified approach for motion and force control of robot manipulators: the operational space formulation," *IEEE Journal of Robotics and Automation*, vol. 3, no. 1, pp. 43–53, Feb. 1987.
- [55] J. Kim, P. H. Chang, and H.-S. Park, "Transparent teleoperation using two-channel control architectures," in *Proceedings of the IEEE/RSJ International Conference on Intelligent Robots and Systems (IROS'05)*, Edmonton, Alberta, Canada, Aug. 2005, pp. 2824–2831.
- [56] K. Kim, J. Jun, H. Kwon, C. Oh, and J. Park, "A bilateral force reflecting teleoperation system for wiping operation," in *Proceedings of the IEEE/RSJ International Conference on Intelligent Robots and Systems (IROS'02)*, Lausanne, Switzerland, Oct. 2002, pp. 2899–2904.

- [57] K. J. Kyriakopoulos, J. V. Riper, A. Zink, and H. E. Stephanou, “Kinematic analysis and position/force control of the anthrobot dexterous hand,” *IEEE Transactions on Systems, Man and Cybernetics, Part B*, vol. 27, no. 1, pp. 95–104, Oct. 1997.
- [58] T. Lasky and T. C. Hsia, “On force-tracking impedance control of robot manipulators,” in *Proceedings of the IEEE International Conference on Robotics and Automation (ICRA’91)*, Sacramento, CA, USA, Apr. 1991, pp. 274–280.
- [59] H. Y. K. Lau and L. C. C. Wai, “Implementation of position-force and position-position teleoperator controllers with cable-driven mechanisms,” *Robotics and Computer-Integrated Manufacturing*, vol. 21, no. 2, pp. 145–152, Apr. 2005.
- [60] D. A. Lawrence, “Stability and transparency in bilateral teleoperation,” *IEEE Transactions on Robotics and Automation*, vol. 9, no. 5, pp. 624–637, Oct. 1993.
- [61] S. S. Lee and J. M. Lee, “Design of a general purpose 6-dof haptic interface,” *Mechatronics*, vol. 13, no. 7, pp. 697–722, Sept. 2003.
- [62] G. Liu and A. A. Goldenberg, “Robust hybrid impedance control of robot manipulators,” in *Proceedings of the IEEE International Conference on Robotics and Automation (ICRA’91)*, Sacramento, CA, USA, Apr. 1991, pp. 287–292.
- [63] J. Liu and Y. R. Zhang, “Dataglove based grasp planning for multi-fingered robot hand,” in *Proceedings of the 11th World Congress in Mechanism and Machine Science*, Tianjin, China, Apr. 2004, pp. 1827–1831.
- [64] L. Love and W. Book, “Force reflecting teleoperation with adaptive impedance control,” *IEEE Transactions on Systems, Man, and Cybernetics—Part B: Cybernetics*, vol. 34, no. 1, pp. 159–165, Feb. 2004.
- [65] K. H. Low, *Robotics: Principles and Systems Modeling*, 2nd ed. Singapore: Prentice Hall, 2004.
- [66] M. Spinner, M. D., *Kaplan’s Functional and Surgical Anatomy of the Hand*. Philadelphia, PA: J. B. Lippincott Company, 1984.

- [67] K. A. Manocha, N. Pernalet, and R. V. Dubey, "Variable position mapping based assistance in teleoperation for nuclear cleanup," in *Proceedings of the IEEE International Conference on Robotics and Automation (ICRA'01)*, Seoul, Korea, May 2001, pp. 374–379.
- [68] S. Manorotkul and H. Hashimoto, "Virtual impedance with position error correction for teleoperator with time delay," in *Proceedings of the IEEE International Workshop on Advanced Motion Control (AMC'96)*, Japan, Mar. 1996, pp. 524–528.
- [69] M. T. Mason, "Compliance and force control for computer controlled manipulators," *IEEE Transactions on Systems, Man and Cybernetics*, vol. 11, pp. 418–432, 1981.
- [70] T. H. Massie and J. K. Salisbury, "The PHANTOM haptic interface: A device for probing virtual objects," in *Proceedings of the ASME Winter Annual Meeting, Symposium on Haptic Interfaces for Virtual Environment and Teleoperator System*, Chicago, IL, USA, Nov. 1994.
- [71] M. Matinfar and K. Hashtrudi-Zaad, "Optimization-based robot compliance control: Geometric and linear quadratic approaches," *The International Journal of Robotics Research*, vol. 24, no. 8, pp. 645–656, Aug. 2005.
- [72] J. K. Mills and A. A. Goldenberg, "Force and position control of manipulators during constrained motion tasks," *IEEE Transactions on Robotics and Automation*, vol. 5, no. 1, pp. 30–46, Feb. 1989.
- [73] T. Mouri, H. Kawasaki, and K. Umebayashi, "Developments of new anthropomorphic robot hand and its master slave system," in *Proceedings of the IEEE/RSJ International Conference on Intelligent Robots and Systems (IROS'05)*, Edmonton, Alberta, Canada, Aug. 2005, pp. 3474–3479.
- [74] L. Ni and D. W. L. Wang, "A gain-switching control scheme for position-error-based bilateral teleoperation system: Contact stability analysis and controller design," *The International Journal of Robotics Research*, vol. 23, no. 3, pp. 255–274, Mar. 2004.
- [75] M. Otsuka, N. Matsumoto, T. Idogaki, K. Kosuge, and T. Itoh, "Bilateral telemanipulator system with communication time delay based on force-sum-driven

- virtual internal models,” in *Proceedings of the IEEE International Conference on Robotics and Automation (ICRA '95)*, Stanford, CA, USA, May 1995, pp. 344–350.
- [76] L. Pao and T. H. Speeter, “Transformation of human hand positions for robotic hand control,” in *Proceedings of the IEEE International Conference on Robotics and Automation (ICRA '89)*, Scottsdale, AZ, USA, May 1989, pp. 1758–1763.
- [77] H. Park and J. M. Lee, “Adaptive impedance control of a haptic interface,” *Mechatronics*, vol. 14, no. 3, pp. 237–253, Apr. 2004.
- [78] J. H. Park and H. C. Cho, “Impedance control with varying stiffness for parallel-link manipulators,” in *Proceedings of the American Control Conference (ACC '98)*, Philadelphia, PA, USA, June 1998, pp. 478–482.
- [79] A. Peer, B. Stanczyk, and M. Buss, “Haptic telemanipulation with dissimilar kinematics,” in *Proceedings of the IEEE/RSJ International Conference on Intelligent Robots and Systems (IROS '05)*, Edmonton, Alberta, Canada, Aug. 2005, pp. 2483–2488.
- [80] M. H. Raibert and J. J. Craig, “Hybrid position/force control of robot manipulators,” *ASME Journal of Dynamic Systems, Measurement and Control*, vol. 102, no. 2, pp. 126–133, June 1981.
- [81] R. N. Rohling and J. M. Hollerbach, “Optimized fingertip mapping for teleoperation of dexterous robot hands,” in *Proceedings of the IEEE International Conference on Robotics and Automation (ICRA '93)*, Atlanta, GA, USA, May 1993, pp. 769–775.
- [82] J.-H. Ryu, D.-S. Kwon, and B. Hannaford, “Stable teleoperation with time-domain passivity control,” *IEEE Transactions on Robotics and Automation*, vol. 20, no. 2, pp. 365–373, Apr. 2004.
- [83] J. D. Schutter and H. V. Brussel, “Compliant robot motions. part i-ii,” *The International Journal of Robotics Research*, vol. 7, no. 4, pp. 3–33, 1988.
- [84] H. Seraji and R. Colbaugh, “Force tracking in impedance control,” *The International Journal of Robotics Research*, vol. 16, no. 1, pp. 97–117, 1997.

- [85] M. Shah and R. V. Patel, "Inverse jacobian based hybrid impedance control of redundant manipulators," in *Proceedings of the IEEE International Conference on Mechatronics and Automation (ICMA'05)*, Niagara Falls, Canada, July 2005, pp. 55–60.
- [86] Y. Shen and K. Huper, "A joint space formulation for compliant motion control of robot manipulators," in *Proceedings of the IEEE International Conference on Mechatronics and Automation (ICMA'05)*, Niagara Falls, Canada, July 2005, pp. 362–369.
- [87] T. B. Sheridan, *Telerobotic, Automation, and Human Supervisory Control*. Cambridge, MA: The MIT Press, 1992.
- [88] M. W. Spong and M. Vidyasagar, *Robot Dynamics and Control*. New York: John Wiley & Sons, 1989.
- [89] S. Tafazoli, S. E. Salcudean, K. Hashtrudi-Zaad, and P. D. Lawrence, "Impedance control of a teleoperated excavator," *IEEE Transactions on Control Systems Technology*, vol. 10, no. 3, pp. 355–367, May 2002.
- [90] N. A. Tanner and G. Niemeyer, "Improving perception in time-delayed telerobotics," *The International Journal of Robotics Research*, vol. 24, no. 8, pp. 631–644, Aug. 2005.
- [91] R. Taylor and D. Stoianovici, "Medical robotics in computer-integrated surgery," *IEEE Transactions on Robotics and Automation*, vol. 19, no. 5, pp. 765–781, Oct. 2003.
- [92] M. L. Turner, "Programming dexterous manipulation by demonstration," Ph.D. dissertation, Department of Mechanical Engineering, Stanford University, Stanford, CA, USA.
- [93] B. J. Unger, R. L. Klatzky, and R. L. Hollis, "A telemanipulation system for psychophysical investigation of haptic interaction," in *Proceedings of the IEEE International Conference on Robotics and Automation (ICRA'03)*, Taipei, Taiwan, China, Sept. 2003, pp. 1253–1258.

- [94] D. Šurdilović and Ž. Čojbašić, “Robust robot compliant motion control using intelligent adaptive impedance approach,” in *Proceedings of the IEEE International Conference on Robotics and Automation (ICRA’99)*, Detroit, MI, USA, May 1999, pp. 2128–2133.
- [95] M. K. Vukobratovic and Y. Ekalo, “New approach to control of robotic manipulators interacting with dynamic environment,” *Robotica*, vol. 14, no. 1, pp. 31–393, Jan. 1996.
- [96] X. Wang, P. X. Liu, D. Wang, B. Chebbi, and M. Meng, “Design of bilateral teleoperators for soft environments with adaptive environmental impedance estimation,” in *Proceedings of the IEEE International Conference on Robotics and Automation (ICRA’05)*, Barcelona, Spain, Apr. 2005, pp. 1127–1132.
- [97] A. Wege, K. Kondak, and G. Hommel, “Mechanical design and motion control of a hand exoskeleton for rehabilitation,” in *Proceedings of the IEEE International Conference on Mechatronics and Automation (ICMA’05)*, Niagara Falls, Canada, July 2005, pp. 155–159.
- [98] J. T. Wen and S. Murphy, “Stability analysis of position and force control for robot arms,” *IEEE Transactions on Automatic Control*, vol. 36, no. 3, pp. 365–371, Mar. 1991.
- [99] R. L. Williams II, J. M. Henry, and D. W. Repperger, “Evaluation of rate-based, force-reflecting teleoperation in free motion and contact,” *Presence*, vol. 9, no. 1, pp. 25–36, Feb. 2000.
- [100] T. Wojtara, K. Nonami, H. Shao, R. Yuasa, S. Amano, and Y. Nobumoto, “Master-slave hand system of different structures, grasp recognition by neural network and grasp mapping,” *Robotica*, vol. 22, no. 4, pp. 449–454, Aug. 2004.
- [101] A. K. Wright and M. M. Stanisic, “Kinematic mapping between the EXOS Hand-master exoskeleton and the Utah/MIT dexterous hand,” in *Proceedings of the IEEE International Conference on Systems Engineering (ICSE’90)*, Aug. 1990, pp. 101–104.
- [102] J. Yan and S. Salcudean, “Teleoperation controller design using H_∞ -optimization with application to motion-scaling,” *IEEE Transactions on Control Systems Technology*, vol. 4, no. 3, pp. 244–258, May 1996.

- [103] Y. Yokokohji, Y. Iida, and T. Yoshikawa, “‘toy problem’ as the benchmark test for teleoperation systems,” *Advanced Robotics*, vol. 17, no. 3, pp. 253–273, Jan. 2003.
- [104] Y. Yokokohji and T. Yoshikawa, “Bilateral control of master-slave manipulators for ideal kinematic coupling-formulation and experiment,” *IEEE Transactions on Robotics and Automation*, vol. 10, no. 5, pp. 605–620, Oct. 1994.
- [105] W.-K. Yoon, T. Goshozono, H. Kawabe, M. Kinami, Y. Tsumaki, M. Uchiyama, M. Oda, and T. Doi, “Model-based space robot teleoperation of ETS-VII manipulator,” *IEEE Transactions on Robotics and Automation*, vol. 20, no. 3, pp. 602–612, June 2004.
- [106] T. Yoshikawa, “Dynamic hybrid position/force control of robot manipulators— description of hand constraints and calculation of joint driving force,” *IEEE Journal of Robotics and Automation*, vol. 3, no. 5, pp. 386–396, Oct. 1987.
- [107] G. Zeng and A. Hemami, “An overview of robot force control,” *Robotica*, vol. 15, no. 5, pp. 473–482, Sept. 1997.
- [108] (2007) The Immersion Corporation website. [Online]. Available: <http://www.immersion.com/3d/products/cyber-grasp.php>
- [109] (2007) The Fifth Dimension Technologies website. [Online]. Available: <http://www.5dt.com/hardware.html#glove>
- [110] (2007) Website of Dexterous Manipulation Lab, Stanford University. [Online]. Available: http://bdml.stanford.edu/DML/tele_projects/index.html
- [111] (2007) Website of Laboratoire de Robotique, University LAVAL. [Online]. Available: <http://robot.gmc.ulaval.ca/en/research/industry101.html>
- [112] (2007) Website of Laboratory for Intelligent Robots & Vision Systems, Kyushu University. [Online]. Available: <http://fortune.is.kyushu-u.ac.jp/index-e.html>

Appendix A - A Mechatronic Approach to Manipulator Controller Design

A mechatronic design approach to manipulator control in free space is presented in this appendix, which is applied to develop the test-bed for the mapping methods addressed in Chapters 3 and 4. Different from the normal design procedure, in which the mechanical system of the electrical system are treated separately, the presented mechatronic approach takes into account all the dynamics of the manipulator, actuators, amplifiers, and I/O Board in a united manner. The controller is then applied to control the slave robot hand introduced in Sec. 3.1.2 according to the input from the *5DT* data glove.

A.1 Introduction

The robot manipulator/hand is a non-linear system with coupled effects among each joint or translation variables. In control practice, it is convenient to use a suitable linear model to replace the non-linear one. The frequency response method is widely used to derive the approximate linear model of the dynamic systems [8, 25]. With the linear model, the controller can be designed and simulated by virtual of the classical and modern control theories. The widely used software MATLAB/Simulink makes it a simple task.

The implementation of the control hardware and software for the robotic system could be quite complex [13, 14, 44, 93]. The MATLAB toolbox xPC Target provides us a a solution for prototyping, testing, and deploying real-time control systems using standard PC hardware [1]. It is unnecessary to incorporate too many different chips together and to develop the custom interface codes.

In the following sections, the hardware and software used in the proposed work are first introduced. The modeling process and controller design are then presented. Finally, the designed motion control system is validated by experiments.

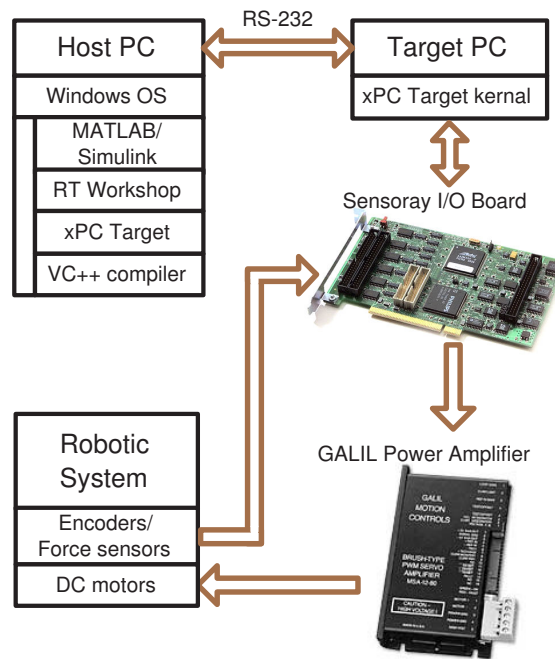


Figure A.1: Control system architecture of the test-bed for mapping.

A.2 Hardware and Software

xPC Target uses a host-target environment to deploy the real time control system. The software is running in two PCs, host and target. The host PC runs Microsoft Windows operating system and the required software packages: MATLAB, Simulink, Real-Time Workshop (RTW), xPC Target, and C/C++ compiler. MATLAB is the host software environment of Simulink, RTW, and xPC Target. The Simulink is used to model the physical systems (robotic systems in our work) and controller design. RTW and C/C++ compiler convert Simulink blocks into C code and build a target application, which is downloaded to the target PC and executed in real-time. The communication between the host and target PCs is through RS-232 or TCP/IP. The target PC is booted by a boot disk, which is easily created in MATLAB on the host PC. Subsequently, the target PC runs the highly optimized xPC target kernel loaded from the boot disk. The executable code generated from the Simulink block in the host PC is then running in real-time on the target PC.

xPC Target supports quite a few standard I/O boards, which are simply plugged into the PCI or ISA slots of the target PC. By including the driver block into the Simulink model, the analog and digital data flow between the physical system and the control software (executable codes in the target PC) in real time. Therefore, the physical system is controlled in the manner of hardware-in-the-loop (HIL) simulation. The Sensoray

model 626 card is used in this work. It has four analog outputs (13 bit resolution), sixteen differential analog input (14 bit resolution), forty-eight digital I/O channels, and six counters for encoder reading.

The overall architecture of the host-target HIL real-time robotic control system is shown in Fig. A.1, where the GALIL power amplifier is interfaced with the I/O board to generate proper command signals for DC motors. The developed control system setup has been shown in Fig. 4.17 of Chapter 4.

A.3 Modeling and Control

The modeling and control process of the lower joint (joint R_{lower}) of the right finger is presented for the illustration purpose. The same procedure is performed for the other joints.

A.3.1 Transfer Function Model for Joint R_{lower}

Consider a DC motor driving a load, the transfer function of the joint of the output shaft angle to the input voltage of the motor can be expressed by

$$T_1(s) = \frac{Q(s)}{V(s)} = \frac{\eta^2 k_{tc}}{(J_{all}s^2 + b_{all}s)(L_{aw}s + R_{aw}) + \eta^2 k_{tc}k_{emf}s} \quad (A.1)$$

where k_{tc} is the motor torque constant. k_{emf} is the back *emf* constant of the motor. R_{aw} and L_{aw} are the resistance and the inductance of the armature windings. J_{all} and b_{all} are the inertia and the viscous friction coefficient of the combination of the motor rotor, gear train, timing belt transmission and the load referred to the output shaft of the gearing, respectively. η is the gear ratio.

Since L_{aw} is usually small, it can be neglected. Thus Eq. (A.1) can be written as

$$T_2(s) = \frac{\frac{\eta k_{tc}}{R_{aw}J_{all}}}{s^2 + \frac{1}{J_{all}} \left(b_{all} + \frac{\eta^2 k_{tc}k_{emf}}{R_{aw}} \right) s} \quad (A.2)$$

For our slave robot hand, the gear reduction ratio is high. The normal operating velocities and accelerations are limited. Plus, the motion range of each joint is relatively small, since the robotic hand usually grasps or manipulates the object in a limited area. Therefore, guiding by Eq. (A.2), it is feasible to model each joint of the hand by a linear

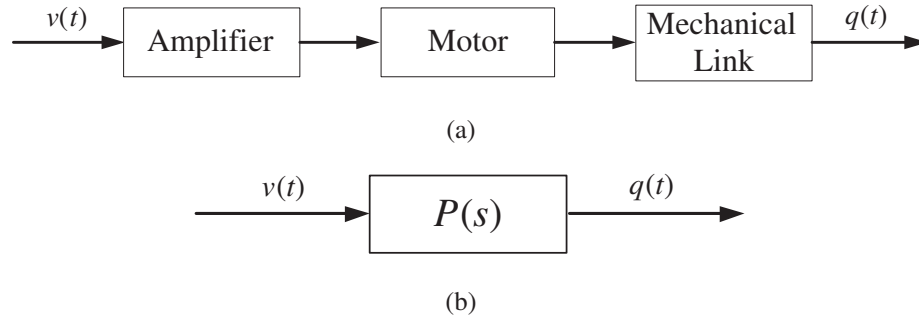


Figure A.2: The input-output relation of joint R_{lower} .

transfer function in the form

$$P(s) = \frac{C}{s^2 + as} \quad (\text{A.3})$$

where C and a are unknown parameters. Through this way, coupling effects between joints due to varying configurations during the motion are treated as disturbances. Note that if an amplifier gain is included into the open loop transfer function, Eq. (A.3) still holds. We now show the way of determining the values of C and a by the frequency response method.

Figure A.2(a) shows the input-output relation of joint R_{lower} , where a voltage level $v(t)$ (output of the D/A channel of the I/O board) is the input to the amplifier. The motor drives the lower link of the right finger to rotate to joint position $q(t)$. The open loop transfer function $P(s)$ takes into account all the dynamics between $v(t)$ and $q(t)$ (see Fig. A.2(b)), such that

$$Q(s) = P(s)V(s) \quad (\text{A.4})$$

where $V(s)$ and $Q(s)$ are the Laplace transform of $v(t)$ and $q(t)$, respectively.

If the input to such a system is a sinusoidal signal of certain frequency, the output in steady state will also be a sinusoid with the same frequency. Suppose that the input is

$$v(t) = A\sin(\omega t) \quad (\text{A.5})$$

where A is the amplitude and ω is the radian frequency of the sinusoid. The output in steady state is of the form

$$q(t) = B\sin(\omega t + \phi) \quad (\text{A.6})$$

Also,

$$|P(j\omega)| = B/A \quad (\text{A.7})$$

which states that the magnitude of $P(j\omega)$ is the ratio of the steady state output amplitude to the input amplitude.

With the background knowledge addressed above, the frequency response method can be performed to obtain the transfer function for joint R_{lower} describing its dynamics approximately.

Firstly, a sinusoidal input voltage signal $v(t) = A\sin(\omega t)$ is applied to drive the motor. As a result, the link swings in a sinusoidal fashion and the steady state output is in the form $q(t) = B\sin(\omega t + \phi)$. Measure the amplitude B , and record the results. Repeat the above process for a number of different values of ω ($\omega_i, i = 1, 2, \dots$) with A kept fixed. The corresponding amplitudes of the output sinusoids B_i are measured and recorded. From these data the ratios B_i/A are computed corresponding to each ω_i . Draw the Bode plot of the experimental data of B_i/A versus ω_i for all i .

Secondly, the guideline of the transfer function (Eq. A.3) is fit with the measured data such that specific values for the parameters in model $P(s)$ are determined. By plotting Bode plot of the transfer function $P(s)$ (Eq. A.2) with some trials in MATLAB, the proper values of C and a can be determined. The set of (C, a) that makes $P(s)$ best fit the experimental data is $C = 48500$, and $a = 2.89$. The equivalent transfer function of joint R_{lower} will thus be

$$P(s) = \frac{48500}{s^2 + 2.89s} \quad (\text{A.8})$$

Figure A.3 shows the Bode plot of $P(s)$ versus ω for all frequencies, superimposed on the corresponding plot of the experimental data. As shown in the figure, the transfer function model agrees well with the experimental data.

A.3.2 Controller Design by Simulation

A digital PID controller is designed to improve the dynamic behavior of the system. Figure A.4 shows the Simulink block diagram of the feedback loop control scheme of joint R_{lower} with the digital PID controller. By virtual of Control System Design Tool [4] from MATLAB, the coefficients K_P , K_I , and K_D are modified so as to make the system obtain a pretty high bandwidth and crossover frequency. The overshoot and steady-state error of the system are also assured to be in an acceptable range. The simulation response

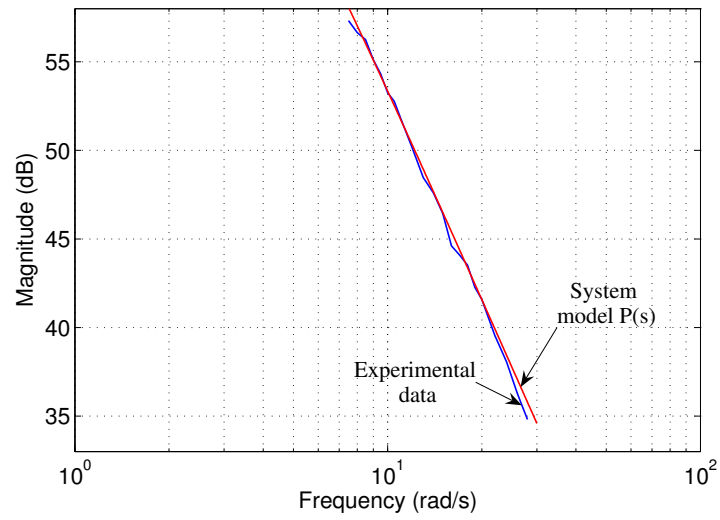


Figure A.3: Bode plot of experimental data and system model $P(s)$.

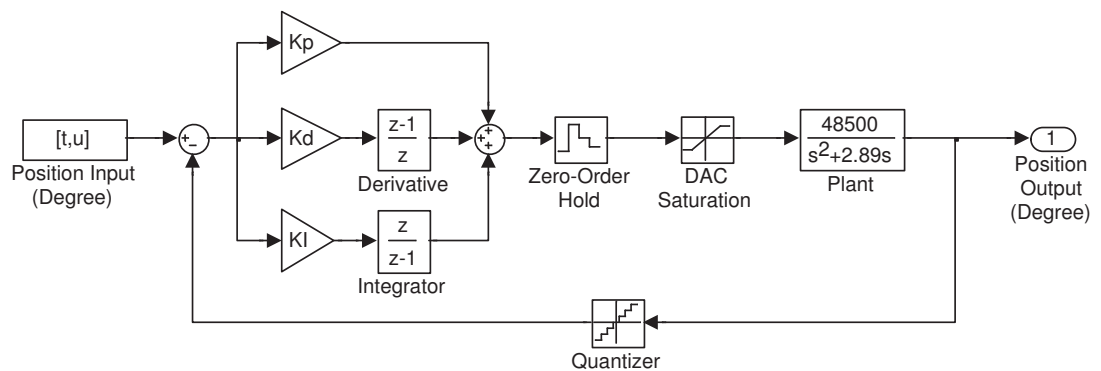


Figure A.4: Block scheme of joint R_{lower} with PID controller for simulation.

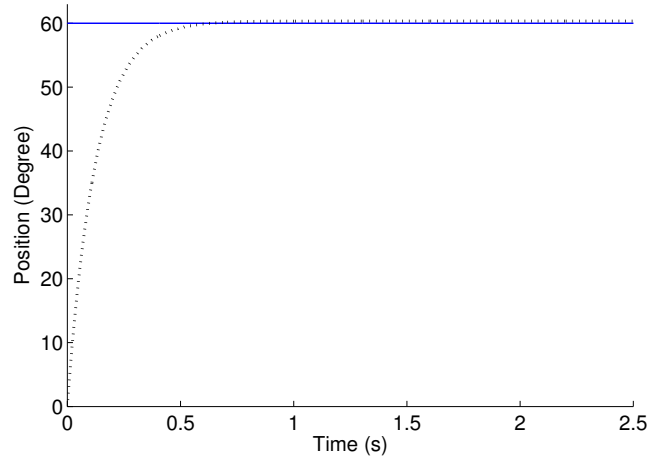


Figure A.5: Step input response of joint R_{lower} by simulation.

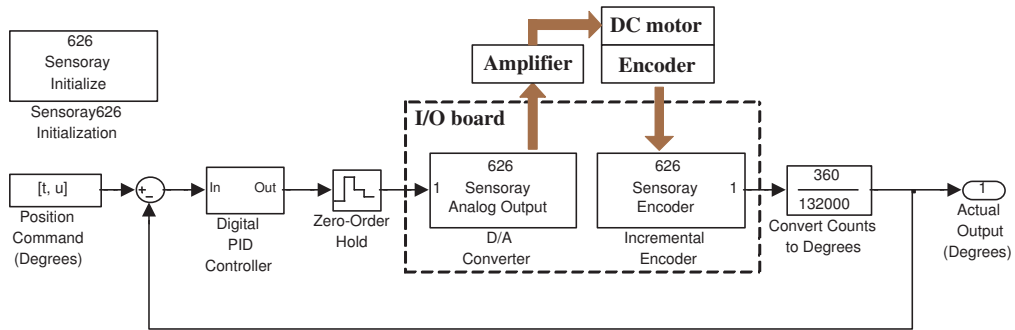


Figure A.6: Block scheme of joint R_{lower} with real system in the loop.

to a step input is shown in Fig. A.5, which shows that the PID controller is well designed for the system.

A.3.3 Control System Implementation

Once suitable PID gains are obtained in the simulation stage, the control system is implemented by the hardware and software shown in Fig. A.1. The physical system is easily included in the control loop by substituting the I/O board blocks for the plant model, as shown in Fig. A.6. The I/O board, which is plugged into the PCI slot of the target PC, connects the amplifier and encoder through proper channels.

To run the control application developed in Simulink, the constructed graphical model is compiled into executable code and then downloaded to the target PC through RS-232 connection. Joint R_{lower} can then be controlled in real time when the executable code is commanded to execute from the host PC.

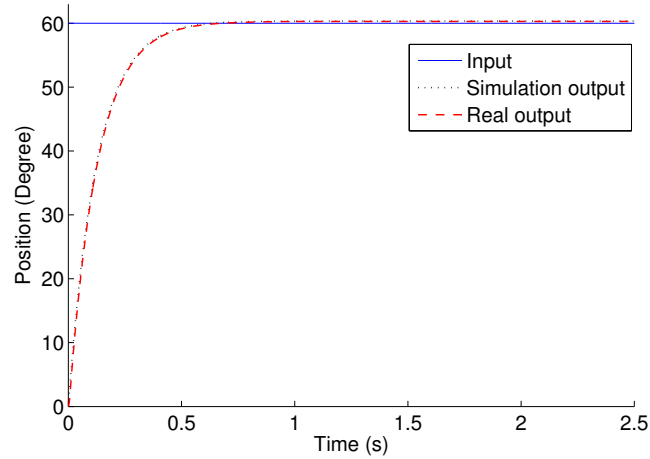


Figure A.7: Step input response of real system and simulation.

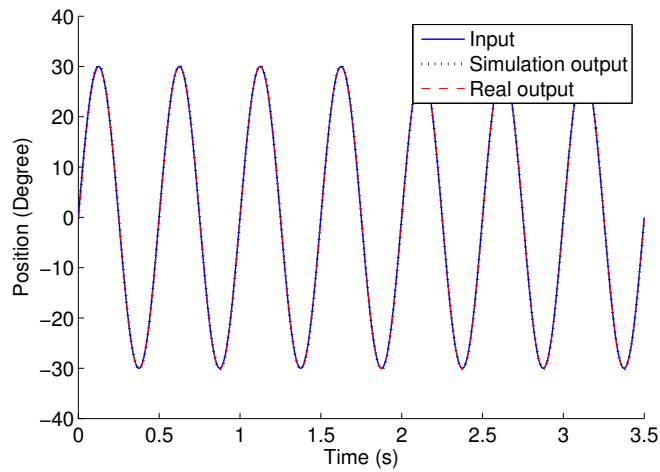


Figure A.8: Sine wave (2 Hz) response of real system and simulation.

Figure A.7 shows the step input response of the real system together with the simulation result for comparison purpose. As shown in the figure, the output of the real physical system is almost the same as that of the simulation. This also happens in Fig. A.8, which shows the response to a 2 Hz sine wave input. Therefore, the feasibility of the obtained transfer function is validated, and the control system is thus constructed by performing the design procedure for each joint of the robot hand. The developing procedure shows a convenient way to implement a robotic real time control system.

Appendix B - Kinematics and Dynamics of the Parallel Manipulator

The kinematics and dynamics of the planar parallel five-bar manipulator is addressed in this appendix. The computation is performed by using MapleTM software.

B.1 Kinematics

The kinematic structure of the manipulator is shown in Fig. B.1. This five-bar mechanism consists of four moving links L_i , $i = 1$ to 4, and a fixed link L_b . The tip point of the manipulator is located at point P_5 , and moves in the plane. The motors and the encoders are located at point P_1 and P_2 . The base frame is located at point P_1 . The kinematic analysis aims to construct the relationship between the position of the tip point P_5 and the two angles q_1 and q_2 .

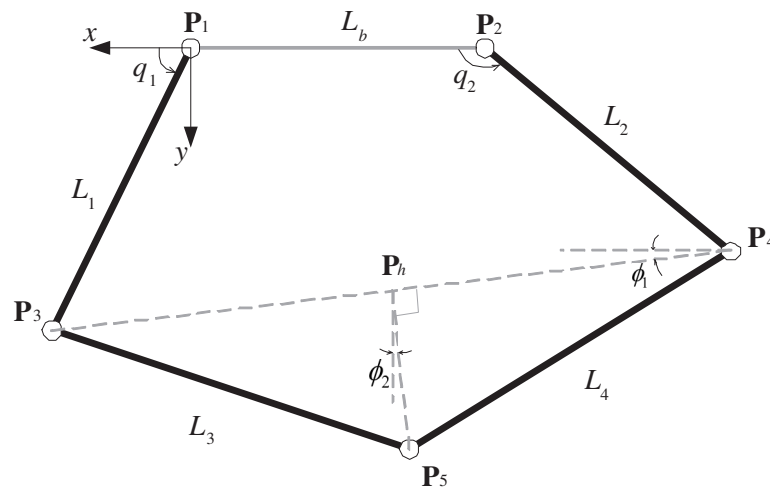


Figure B.1: Kinematic structure of the parallel manipulator.

B.1.1 Forward Kinematics

The forward kinematics is to find the position of point \mathbf{P}_5 according to the measured joint angles q_1 and q_2 . The base frame is defined as shown in Fig. B.1. The approach used here is basically the same as the geometry method presented by Campion *et al.* [7].

The positions of point \mathbf{P}_3 and \mathbf{P}_4 are computed as

$$\mathbf{P}_3(x_3, y_3) = \begin{Bmatrix} L_1 \cos q_1 \\ L_1 \sin q_1 \end{Bmatrix} \quad (\text{B.1})$$

$$\mathbf{P}_4(x_4, y_4) = \begin{Bmatrix} L_2 \cos q_2 - L_b \\ L_2 \sin q_2 \end{Bmatrix} \quad (\text{B.2})$$

Express $\mathbf{P}_5 = (x_5, y_5)$, and $\mathbf{P}_h = (x_h, y_h)$, which is the intersection between the segment $\mathbf{P}_3\mathbf{P}_4$ and the height of triangle $\mathbf{P}_3\mathbf{P}_4\mathbf{P}_5$. Then

$$\|\mathbf{P}_h - \mathbf{P}_3\| = \frac{L_3^2 - L_4^2 + \|\mathbf{P}_4 - \mathbf{P}_3\|^2}{2 \|\mathbf{P}_4 - \mathbf{P}_3\|} \quad (\text{B.3})$$

$$\mathbf{P}_h = \mathbf{P}_3 + \frac{\|\mathbf{P}_h - \mathbf{P}_3\|}{\|\mathbf{P}_4 - \mathbf{P}_3\|}(\mathbf{P}_4 - \mathbf{P}_3) \quad (\text{B.4})$$

$$\|\mathbf{P}_5 - \mathbf{P}_h\| = \sqrt{L_3^2 - \|\mathbf{P}_h - \mathbf{P}_3\|^2} \quad (\text{B.5})$$

Considering $\phi_1 = \phi_2$ in Fig. B.1, the end tip position $\mathbf{P}_5(x_5, y_5)$ can then be computed by

$$x_5 = x_h + \frac{\|\mathbf{P}_5 - \mathbf{P}_h\|}{\|\mathbf{P}_4 - \mathbf{P}_3\|}(y_4 - y_3) \quad (\text{B.6})$$

$$y_5 = y_h - \frac{\|\mathbf{P}_5 - \mathbf{P}_h\|}{\|\mathbf{P}_4 - \mathbf{P}_3\|}(x_4 - x_3) \quad (\text{B.7})$$

All the four moving links of the mechanism have the same length L . By performing the following set of Maple instructions,

```
P2:=Vector([-Lb,0]);
P3:=Vector([L*cos(q1),L*sin(q1)]);
P4:=Vector([L*cos(q2)-Lb,L*sin(q2)]);
d:=sqrt((P3[1]-P4[1])^2+(P3[2]-P4[2])^2);
b:=(L^2-L^2+d^2)/(2*d);
h:=sqrt(L^2-b^2);
Ph:=P3+b/d*(P4-P3);
```

```
x5:=Ph[1]+h/d*(P4[2]-P3[2]);
y5:=Ph[2]-h/d*(P4[1]-P3[1]);
P5:=Vector([x5,y5]);
```

the end tip position $P_5(x_5, y_5)$ can be obtained as

$$x_5 = \frac{1}{2}L \cos q_1 + \frac{1}{2}L \cos q_2 - \frac{1}{2}L_b + \frac{1}{2} \sqrt{4L^2 - (L \cos q_1 - L \cos q_2 + L_b)^2 - (L \sin q_1 - L \sin q_2)^2} (L \sin q_2 - L \sin q_1) / \sqrt{(L \cos q_1 - L \cos q_2 + L_b)^2 + (L \sin q_1 - L \sin q_2)^2} \quad (B.8)$$

$$y_5 = \frac{1}{2}L \sin q_1 + \frac{1}{2}L \sin q_2 - \frac{1}{2}L_b + \frac{1}{2} \sqrt{4L^2 - (L \cos q_1 - L \cos q_2 + L_b)^2 - (L \sin q_1 - L \sin q_2)^2} (L \cos q_2 - L \cos q_1 - L_b) / \sqrt{(L \cos q_1 - L \cos q_2 + L_b)^2 + (L \sin q_1 - L \sin q_2)^2} \quad (B.9)$$

B.1.2 Differential Kinematics

Without considering the end tip angular velocity, the Jacobian matrix J_v can be found by direct differentiation of the forward kinematics of Eqs. B.8 and B.9 with respect to q_1 and q_2 , i.e.,

$$J_v(\mathbf{q}) = \begin{bmatrix} \partial x_5 / \partial q_1 & \partial x_5 / \partial q_2 \\ \partial y_5 / \partial q_1 & \partial y_5 / \partial q_2 \end{bmatrix} \quad (B.10)$$

where $\mathbf{q} = [q_1, q_2]^T$.

B.1.3 Inverse Kinematics

Inverse kinematics aims to find the actuating angles q_1 and q_2 according to the position P_5 . Due to the parallel structure of the manipulator, the inverse kinematics is easier to be derived than the forward kinematics. Refer to Fig. B.2, given $P_5(x_5, y_5)$, q_1 and q_2 can be derived by using Campion's *et al.* method [7] as

$$q_1 = \pi - \alpha_1 - \beta_1 \quad (B.11)$$

$$q_2 = \alpha_2 + \beta_2 \quad (\text{B.12})$$

where

$$\alpha_1 = \arccos \left(\frac{L_1^2 - L_3^2 + \|\mathbf{P}_5 - \mathbf{P}_1\|^2}{2L_1\|\mathbf{P}_5 - \mathbf{P}_1\|} \right) \quad (\text{B.13})$$

$$\beta_1 = \text{atan2}(y_5, -x_5) \quad (\text{B.14})$$

$$\alpha_2 = \arccos \left(\frac{L_2^2 - L_4^2 + \|\mathbf{P}_5 - \mathbf{P}_2\|^2}{2L_2\|\mathbf{P}_5 - \mathbf{P}_2\|} \right) \quad (\text{B.15})$$

$$\beta_2 = \text{atan2}(y_5, x_5 + L_b) \quad (\text{B.16})$$

B.2 Dynamics

The Euler-Lagrange method is used to derive the dynamics equation. Specifically, the approach introduced by Spong and Vidyasagar [88] for the equation of motion of robot manipulators is applied to derive the matrices $\mathbf{D}(\mathbf{q})$ and $\mathbf{C}(\mathbf{q}, \dot{\mathbf{q}})$. Note that matrix $\mathbf{G}(\mathbf{q}) = \mathbf{0}$ due to the planar configuration.

Firstly, q_3 and q_4 (refer to Fig. B.2) are computed as

$$q_3 = \pi - \arccos \left(\frac{L_1^2 + L_3^2 - \|\mathbf{P}_5 - \mathbf{P}_1\|^2}{2L_1L_3} \right) \quad (\text{B.17})$$

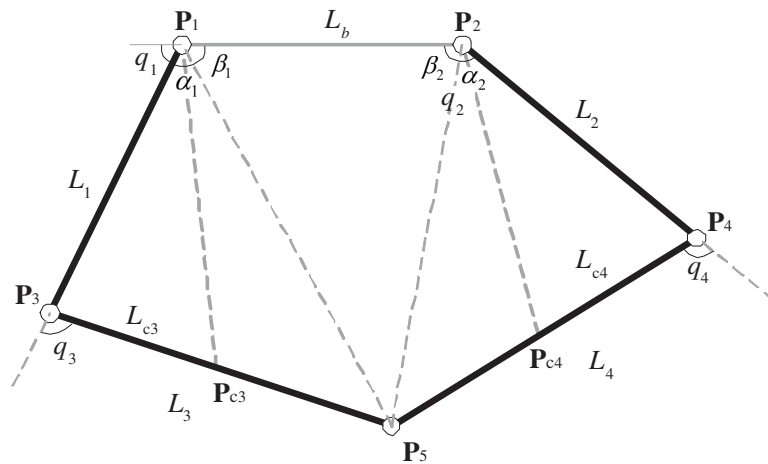


Figure B.2: Kinematic structure for deriving the inverse kinematics and dynamics equations.

$$q_4 = \pi - \arccos\left(\frac{L_2^2 + L_4^2 - \|\mathbf{P}_5 - \mathbf{P}_2\|^2}{2L_2L_4}\right) \quad (\text{B.18})$$

Let \mathbf{P}_{c3} and \mathbf{P}_{c4} denote the mass center of links L_3 and L_4 , respectively, then

$$\mathbf{P}_{c3} = \mathbf{P}_3 + \frac{L_{c3}}{L_3}(\mathbf{P}_5 - \mathbf{P}_3) \quad (\text{B.19})$$

$$\mathbf{P}_{c4} = \mathbf{P}_4 - \mathbf{P}_2 + \frac{L_{c4}}{L_4}(\mathbf{P}_5 - \mathbf{P}_4) \quad (\text{B.20})$$

where L_{c3} and L_{c4} are the distances between \mathbf{P}_{c3} and \mathbf{P}_3 , and \mathbf{P}_{c4} and \mathbf{P}_4 , respectively.

The Jacobian matrices of \mathbf{P}_{c3} and \mathbf{P}_{c4} can then be obtained via

$$J_{c3}(\mathbf{q}) = \begin{bmatrix} \frac{\partial \mathbf{P}_{c3}}{\partial q_1} & \frac{\partial \mathbf{P}_{c3}}{\partial q_2} \end{bmatrix} \quad (\text{B.21})$$

$$J_{c4}(\mathbf{q}) = \begin{bmatrix} \frac{\partial \mathbf{P}_{c4}}{\partial q_1} & \frac{\partial \mathbf{P}_{c4}}{\partial q_2} \end{bmatrix} \quad (\text{B.22})$$

Next, define $\mathbf{q}_{13} = [0, 0, q_1 + q_3]^T$, and $\mathbf{q}_{24} = [0, 0, q_2 - q_4]^T$. The Jacobian matrices associated with the angular velocities of the four links can be easily obtained via

$$J_{\omega 1}(\mathbf{q}) = \begin{bmatrix} 0 & 0 \\ 0 & 0 \\ 1 & 0 \end{bmatrix} \quad (\text{B.23})$$

$$J_{\omega 2}(\mathbf{q}) = \begin{bmatrix} 0 & 0 \\ 0 & 0 \\ 0 & 1 \end{bmatrix} \quad (\text{B.24})$$

$$J_{\omega 3}(\mathbf{q}) = \begin{bmatrix} \frac{\partial \mathbf{q}_{13}}{\partial q_1} & \frac{\partial \mathbf{q}_{13}}{\partial q_2} \end{bmatrix} \quad (\text{B.25})$$

$$J_{\omega 4}(\mathbf{q}) = \begin{bmatrix} \frac{\partial \mathbf{q}_{24}}{\partial q_1} & \frac{\partial \mathbf{q}_{24}}{\partial q_2} \end{bmatrix} \quad (\text{B.26})$$

Let m_i and I_i denote the mass and the moment of inertia of link L_i , respectively, and I_{1e} and I_{2e} represent the moment of inertia of links L_1 and L_2 (the motor rotor inertia included) with respect to the rotating axis. The inertia matrix of the manipulator can then be derived through

$$\mathbf{D}(\mathbf{q}) = \sum_{i=1}^2 [I_{ie} J_{\omega i}(\mathbf{q})^T J_{\omega i}(\mathbf{q})] + \sum_{i=3}^4 [m_i J_{ci}(\mathbf{q})^T J_{ci}(\mathbf{q}) + I_i J_{\omega i}(\mathbf{q})^T J_{\omega i}(\mathbf{q})] \quad (\text{B.27})$$

The corresponding Maple instructions of the above equations are as follows.

```
Pc3:=P3+Lc3/L3*(P5-P3);
Pc4:=P4-P2+Lc4/L4*(P5-P4);
Jc3:=Jacobian(Pc3,[q1, q2]);
Jc4:=Jacobian(Pc4,[q1, q2]);
q13:=q1+q3;
q24:=q2-q4;
q13:=Vector([0,0,q13]);
q24:=Vector([0,0,q24]);
Jomega1:=Matrix([[0,0],[0,0],[1,0]]);
Jomega2:=Matrix([[0,0],[0,0],[0,1]]);
Jomega3:=Jacobian(q13,[q1, q2]);
Jomega4:=Jacobian(q24,[q1, q2]);
Dq:=ScalarMultiply( Multiply(Transpose(Jc3),Jc3), m3)
+ScalarMultiply( Multiply(Transpose(Jc4),Jc4), m4)
+ScalarMultiply( Multiply(Transpose(Jomega3),Jomega3), l3)
+ScalarMultiply( Multiply(Transpose(Jomega4),Jomega4), l4)
+ScalarMultiply( Multiply(Transpose(Jomega1),Jomega1), l1e)
+ScalarMultiply( Multiply(Transpose(Jomega2),Jomega2), l2e);
```

The elements of matrix $C(\mathbf{q}, \dot{\mathbf{q}})$ can then be obtained through

$$c_{kj} = \sum_{i=1}^2 c_{ijk}(\mathbf{q})\dot{q}_i = \sum_{i=1}^2 \frac{1}{2} \left\{ \frac{\partial d_{kj}}{\partial q_i} + \frac{\partial d_{ki}}{\partial q_j} - \frac{\partial d_{ij}}{\partial q_k} \right\} \dot{q}_i \quad (\text{B.28})$$

and the corresponding Maple instructions are as follows.

```
d[11]:=D(q)[1,1]; d[12]:=D(q)[1,2]; d[21]:=D(q)[2,1]; d[22]:=D(q)[2,2];
c[111]:=1/2*diff(d[11], q1);
c[211]:=1/2*diff(d[11], q2);
c[121]:=c[211];
c[221]:=diff(d[12], q2)-1/2*diff(d[22], q1);
c[212]:=1/2*diff(d[22], q1);
c[122]:=c[212]; c[222]:=1/2*diff(d[22], q2);
c[112]:=diff(d[21], q1)-1/2*diff(d[11], q2);
c[11]:=c[111]*diff(q1(t), t) + c[211]*diff(q2(t), t);
c[12]:=c[121]*diff(q1(t), t) + c[221]*diff(q2(t), t);
c[21]:=c[112]*diff(q1(t), t) + c[212]*diff(q2(t), t);
c[22]:=c[122]*diff(q1(t), t) + c[222]*diff(q2(t), t);
C(q,diff(q(t),t)):=Matrix([[c[11], c[12]], [c[21], c[22]]]);
```


Finally, it should be pointed out that, although computer program can generate the dynamics equation within a few seconds, the equation is too involved to be implemented in the control system. The situation is formed mainly due to the closed loop structure of the mechanism. Proper approximations of the dynamics equation should be made to implement the control algorithms.